Scalability and modularity for transmon-based quantum processors

Dickel, Christian

DOI
10.4233/uuid:78155c28-3204-4130-a645-a47e89c46bc5

Publication date
2018

Document Version
Final published version

Citation (APA)
Dickel, C. (2018). *Scalability and modularity for transmon-based quantum processors*. [Dissertation (TU Delft), Delft University of Technology]. https://doi.org/10.4233/uuid:78155c28-3204-4130-a645-a47e89c46bc5

Scalability and modularity for transmon-based quantum processors

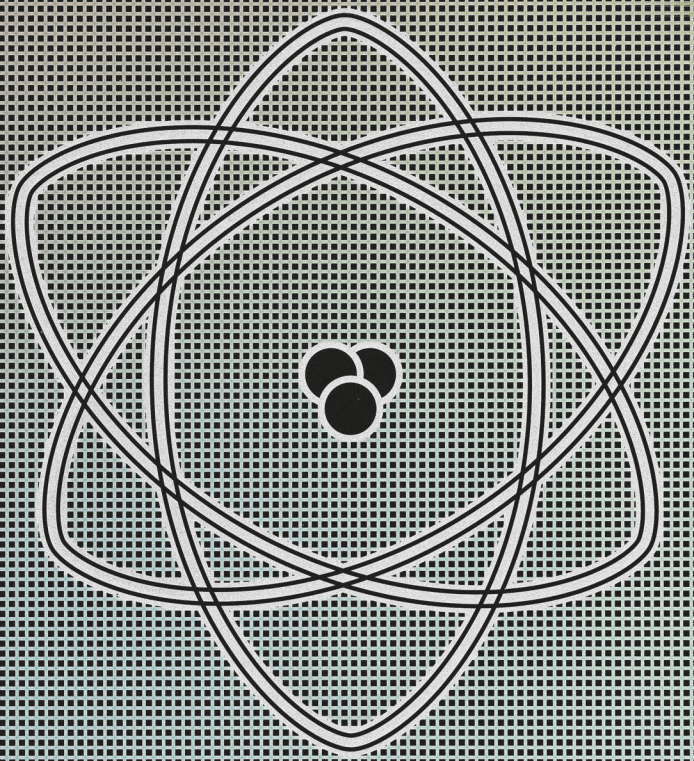

Christian Dickel

Propositions

accompanying the dissertation

Scalability and modularity for transmon-based quantum processors

by

Christian Dickel

1. The transmon qubit is the most promising superconducting qubit for medium-scale integration due to its simplicity and the flexibility of cQED architectures (Chapter 2).
2. Large-scale superconducting quantum computers will use traveling photons as interconnects and switchboard-like devices to increase connectivity (Chapter 6).
3. Large-scale quantum computers will not be monolithic systems, they will be composed of identical modules for economical as well as design reasons (Chapter 5).
4. The current focus on quantum hardware hides that in the race for building a quantum computer, the code base and software-architecture become important factors in addition to the system architecture and the classical computer hardware (Chapter 4).
5. The quantum computer will not be a disruptive technology.
6. Analog quantum simulations without error correction will not lead to trustworthy new insights into the underlying models but they might motivate scientists to look for analogies.
7. Discussions about the ultimate scalability of quantum computing platforms are mostly unproductive, lacking in honesty, clarity and better universal metrics, especially for fabrication yield and accuracy.
8. Very soon, the academic efforts will no longer be competitive with industry efforts in quantum computing and the field will undergo a major transition.
9. The quantum internet will be used for adult content, for example to allow customer privacy without requiring trust in the providers.
10. Quantum coherence is not essential to the information processing of the human brain.

These propositions are regarded as opposable and defendable, and have been approved as such by the promotor Prof. dr. L. DiCarlo.

Scalability and modularity for transmon-based quantum processors

Scalability and modularity for transmon-based quantum processors

Dissertation

for the purpose of obtaining the degree of doctor
at Delft University of Technology
by the authority of the Rector Magnificus Prof. Dr. Ir. T.H.J.J. van der Hagen,
Chair of the Board for Doctorates,
to be defended publicly on Tuesday 25 september 2018 at 10:00 o'clock

by

Christian Dickel

Master of Science in Physics,
Rheinisch-Westfälische Technische Hochschule, Aachen, Germany,
born in Herten, Germany.

This dissertation has been approved by the promotors.

Composition of the doctoral committee:

Rector Magnificus,	chairperson
Prof. dr. L. DiCarlo,	Technische Universiteit Delft, promotor
Prof. dr. ir. R. Hanson,	Technische Universiteit Delft, promotor
Independent members:	
Prof. dr. B. M. Terhal	Technische Universiteit Delft
Prof. dr. ir. J. E. Mooij	Technische Universiteit Delft
Prof. dr. W. Tittel	Technische Universiteit Delft
Prof. dr. G. Rempe	Max-Planck-Institut für Quantenoptik, Germany

Printed by: Gildeprint, Enschede

Cover: **Front:** SEM image of chip with CPWs forming a Rutherford atom symbol. The thesis title is written in my handwriting as is my name. A slight rainbow like false color around the holey ground is adapted from optical pictures of chips, which are very photogenic due to the diffraction grating created by the holey ground. **Back:** Generic single-qubit chip, with a transmon coupled to a resonator with annotations.
The idea to put my handwriting on a chip came to me when I looked at other people using the python design package I wrote for their chips and noticing the personal styles manifesting in different devices.

Casimir PhD Series, Delft-Leiden 2018-34 ISBN 978-90-8593-363-2

DON’T PANIC

CONTENTS

SUMMARY

This thesis mainly summarizes two experiments that relate to building a quantum computer out of superconducting transmon qubits. Transmon qubits have emerged as one of the foremost solid state qubits, realizing processors with more than ten qubits and demonstrating small scale quantum algorithms as well as quantum error correction schemes. Right now, there is a race between different academic and industry research groups to scale up transmon qubit processors.

The first experiment was a demonstration of qubit control by selective broadcasting in order to reduce the scaling of expensive electronics with the number of qubits for individual single-qubit control. We demonstrated that we can bring two transmon qubits to the same frequency (combining fabrication accuracy and in-situ fine tuning) and use the same hardware to control both, routing the pulses with a nanosecond-timescale vector switch matrix. Despite the compromises required by this technique, we show a scalable path to single qubit control beyond the threshold required for quantum error correction. In benchmarking, we take into account gate leakage due to the fact that transmons are fundamentally multi-level systems.

SAMENVATTING

Dit proefschrift vat voornamelijk twee experimenten samen die betrekking hebben op het bouwen van een kwantumcomputer uit supergeleidende transmon qubits. Transmon qubits zijn naar voren gekomen als een van de belangrijkste vastestofqubits, met verwerkers met meer dan tien qubits en demonstraties van kleinschalige kwantumalgoritmen en kwantumfoutcorrectieschema's. Op dit moment is er een race tussen verschillende academische en industriële onderzoeksgroepen om transmon qubit-processors op te schalen.

Het eerste experiment was een demonstratie van qubit-controle door selectieve uitzending om de schaal van dure elektronica te verminderen met het aantal qubits voor individuele single-qubit-controle. We hebben aangetoond dat we twee transmon qubits op dezelfde frequentie kunnen brengen (door combineren van productie nauwkeurigheid en in-situ fijnafstemming) en dezelfde hardware gebruiken om beide te sturen, waarbij de pulsen worden gerouteerd met een nanoseconde tijdschaal vector schakelmatrix. Ondanks de compromissen die deze techniek vereist, laten we een schaalbaar pad zien naar een enkele qubit-controle die de drempel overschrijdt die nodig is voor kwantumfoutcorrectie. Bij benchmarking houden we rekening met poortlekkage vanwege het feit dat trans-

In the second experiment we establish entanglement between two transmon qubits on different chips. We use an entanglement by measurement scheme and demonstrate that we can overcome minor fabrication imperfections by shaping our measurement pulses. Ultimately, performance is mainly limited by photon loss between the chips and up to the amplification chain. This entanglement mediated by traveling photons could be used to make a distributed transmon processor where computations are spread across several chip modules. This modularity could enable connectivities that cannot be realized on chip and ease fabrication requirements, as modules could be individually fabricated and selected.

Thus, both of these experiments fit into the larger effort to converge on the hardware, control equipment and architecture of a future large-scale transmon quantum computer. Other experiments I contributed to are summarized in the conclusion chapter to show the diverse physics that can be studied in cQED experiments.

mons fundamenteel multi-level systemen zijn.

In het tweede experiment leggen we verstrikking vast tussen twee transmon qubits op verschillende chips. We gebruiken een verstrikking door middel van het meetschema en tonen aan dat we kleine fabricage onvolkomenheden kunnen overwinnen door onze meetpulsen vorm te geven. Uiteindelijk wordt de prestatie voornamelijk beperkt door fotonenverlies tussen de chips en tot aan de versterkingsketen. Deze verstrengeling gemedieerd door bewegende fotonen zou kunnen worden gebruikt om een gedistribueerde transmon processor te maken, waarbij berekeningen over verschillende chipmodules worden verspreid. Deze modulariteit zou connectiviteiten mogelijk maken die niet op een chip kunnen worden gerealiseerd en fabricagevereisten vereenvoudigen, omdat modules individueel kunnen worden gefabriceerd en geselecteerd.

Beide experimenten passen dus in de grotere inspanning om te convergeren op de hardware, besturingsapparatuur en architectuur van een toekomstige grootschalige transmon kwantumcomputer. Andere experimenten waaraan ik heb bijgedragen zijn samengevat in het conclusiehoofdstuk om de diverse fysica te tonen die in cQED-experimenten kunnen worden bestudeerd.

PREFACE

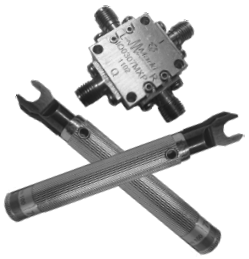

This preface is mainly a mission statement which will hopefully guide me through the process of writing. My ambition is to write a thesis that I would have liked to have read before starting this PhD. Naturally this target audience of one is in sharp contrast to the committee that is going to evaluate this thesis; my apologies for that to the experts. But writing for that specific audience which I know intimately might help make the thesis useful beyond the goal of getting a title. I also hope I can find my own voice instead of always maintaining the impersonal style of scientific writing to convey how deeply personal any scientific work ultimately is. Lastly, I will not hold back on opinion when the facts are not clear to me and I will at times indulge a narrative style. Thus, this thesis will reflect my knowledge and opinions at the time of writing as well as the journey that lead me here.

Christian Dickel
Delft, January 2018

1

QUANTUM PROCESSORS AT THE BRINK OF MEDIUM SCALE INTEGRATION

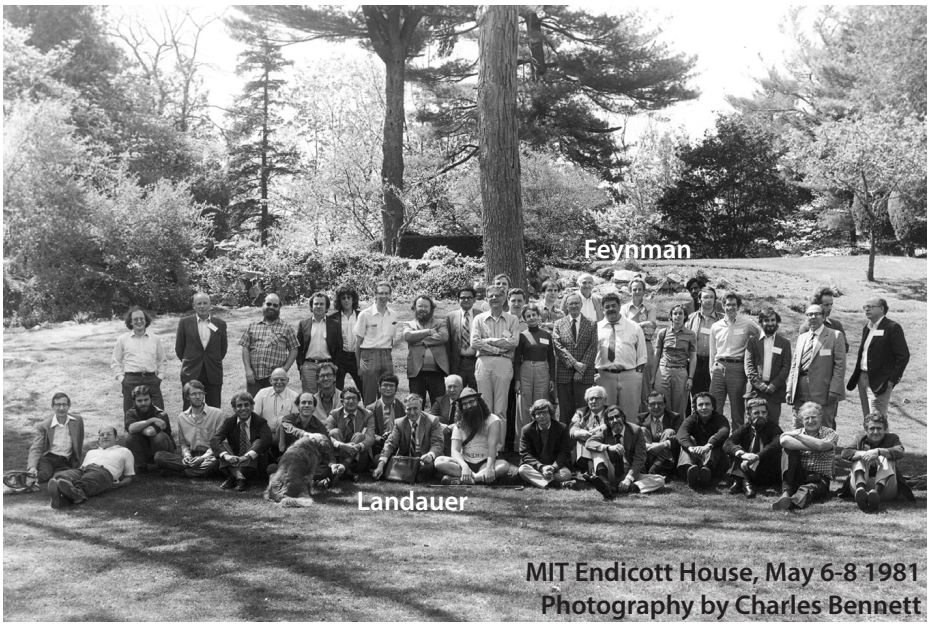

Figure 1.1: *Group picture of the Physics of Computation Conference organized by MIT and IBM in 1981. Picture courtesy of the Archives, California Institute of Technology.*

This chapter is an introduction to the state of the quantum computing field at the time of writing with a focus on scaling up to a "useful" quantum computer, because the experiments presented in this thesis make sense in this context. Rolf Landauer will be quoted several times, exploring his connection to the large-scale integration program for classical computers, his career at the intersection of academia and industry and his skeptical view of alternatives to the transistor-based digital computer. In the end, the results presented in this thesis will be related to the larger quantum computer project.

1.1 TRUTH AND ADVERTISING IN QUANTUM COMPUTING

Rolf Landauer is often quoted by quantum computer enthusiasts repeating his mantra "Information is physical" [1]. The argument is simple: at the smallest scale, nature behaves according to the laws of quantum mechanics. Therefore, at this level we will encounter quantum information. As computers are miniaturized, one would naturally run into quantum systems, making the quantum computer a natural development.

Landauer's name carries an additional subtext, because it is connected to the Large Scale Integration (LSI) program at IBM Research, which would ultimately lead to a classification for the scale of transistor-based integrated circuits. He is credited with coining the term LSI in a memo from 1962. [2] Putting more components on each chip makes electronics more powerful, cheaper and, counter-intuitively, the metal-oxide-semiconductor transistors can be improved by shrinking them, creating strong driving forces to develop miniaturization technology. Integrated circuits with up to ten transistors would be classified as small-scale integration (SSI) and devices with up to 500 transistors as medium-scale integrated (MSI) devices and devices up to 20000 transistors as LSI devices.[1] The increasingly complex integrated circuits were the key factor for Moore's Law [3], which predicted that the number of components on a chip would double every two years. It was this development which lead to the powerful and cheap digital computers today.

But Landauer's connection with our field of quantum information processing goes deeper and is more complex[2]. With the current development of larger and larger quantum information processors, our field can benefit from looking back at his work and his career, because quantum information processing is rapidly developing from an abstract idea to a reality. Landauer's background both in science and engineering is a requirement for anyone who wants to build a useful computing machine – quantum computing is becoming more interdisciplinary with computer scientists and electronics engineers getting involved to an ever-increasing degree. His position within industry at IBM did not keep him from doing fundamental research but it enabled him to play a key role in what might soon be called the *classical* computer revolution.

Later, Landauer was present at the conference where Feynman gave his famous talk introducing the idea of simulating quantum mechanics on quantum hardware [4] (see Figure 1.1). However, he did not become a believer. A decade later, he wrote the article "Is quantum mechanics useful?" [5], where useful was meant in an information processing context. In this article, he warns that the quantum computing paradigm might be flawed. Landauer points out two main problems with quantum computer proposals:

1. The computation is likely to suffer from localization which reflects it from the computational trajectory and causes it to turn around.

[1] According to the integrated circuit article on Wikipedia.

[2] Both his work on quantum transport in mesoscopic systems and his work on the thermodynamics of information processing are ultimately underpinning todays quantum computing effort.

2. Small errors will accumulate and cause the computation to go off track.

While technically both of these points are related to noise in an essentially analog simulation, these were reasonable objections at the time. The digital computers, that Landauer was very familiar with had thresholds between the zeros and ones, which exceeded the noise, a strategy that would not work for quantum computers. In his article, he also mentions the Josephson Junction, which will be introduced later as the crucial component in the quantum computer prototypes central to this thesis. Many of Landauer's objections have been resolved, but the title question of the article has not been answered conclusively, yet.

In a more provocative article titled "Advanced technology and truth in advertising" Landauer starts [6]:

> "Most proposals for new technological approaches fail, and that is reasonable. Despite that, most of the technological proposals arising from basic science are promoted unhesitantly, with little attention to critical appraisal, even little opportunity for the presentation of criticism."

The article goes on to talk about alternative computing technologies and so far his skepticism was warranted: the transistor-based digital computer remains almost unchallenged.

As a new researcher in this buzzing field of quantum information processing, the skeptical attitude resonates with me. Especially because the fascinating theoretical question of the feasibility of a quantum computer is often muted by press releases that uncritically proclaim a quantum computer revolution comparable to the digital computer revolution. Doing research in the era of the quantum computer hype is a very interesting experience, but I often wonder if the quantum computer will be able to deliver on the list of promises that are being made across the research landscape. Long-shot applications in chemistry, material science, medicine and artificial intelligence are often mentioned when quantum computers are introduced, but while plausible in theory, they will likely not be realized in the next ten years. Despite this, the quantum computer is already becoming a household prop in advertising as many companies publicly invest in the technology. For me personally, making and interacting with quantum mechanical systems through my classical computer that controls the experiment was the main motivator for doing research. Controlling nature at this level with a few keystrokes is invigorating and by realizing and controlling larger quantum systems we will naturally answer the question of the feasibility and technological viability of quantum computers.

1.2 THE BLUEPRINT FOR A QUANTUM COMPUTER

Since Landauer's articles, there have been several developments that dispel his doubts and provide hope that the effort to build a quantum computer is not doomed to fail:

1. The theoretical foundation of the fault-tolerant quantum computer, proving that an arbitrarily good quantum computer can be build from imperfect hardware.

2. The experimental demonstration of larger and larger controlled quantum systems that successfully perform small computations.

2017 saw two papers claiming quantum simulations with > 50 qubits [7, 8] and IBM announcing the first data from a 50-qubit superconducting quantum processor[3]. Intel, with collaboration of our research group in QuTech, announced the fabrication of a 49-qubit chip, Google announced a 72-qubit chip and Rigetti Computing announced plans for a 128-qubit chip. The current phase could be seen as the MSI phase of quantum computing. Alternatively, John Preskill classifies the current time as the noisy intermediate-scale quantum technology (NISQ) era [9], focusing more on the fact that currently there is effort to explore near-term advantages of quantum simulators and quantum processors on the road to a fault-tolerant quantum computer. The fault-tolerant quantum computer will be a large-scale machine where noise can be greatly reduced using redundancy. Landauer saw the potential in the integrated circuit before the metal-oxide field-effect transistor had been mastered. The quantum computer today is in a similar stage; several hardware platforms show promise but none are sufficiently mastered for a useful quantum computer.

What makes a quantum system a quantum computer and how is it different from a quantum simulator? A quantum computer is a calculation machine and for most applications it can be thought of as a classical input, classical output device, just like a regular computer. However, the states of the quantum computer are quantum mechanical states of a controllable quantum system. Any quantum mechanical system will have distinct eigenstates of an underlying Hamiltonian that describes the full system and its dynamics. An open quantum system has additional coupling to quantum or classical baths. In order to build a quantum computer, we need a system that exhibits coherent and controllable quantum behavior, as well as having ways to get classical information in and out. The input of information depends on initializing the system in a well-defined state, while measurements are used to extract information. A universal quantum computer is a machine, where any quantum operation on a register of qubits can be produced efficiently (polynomially in resources) via controlling the Hamiltonian or the input/output behavior. For a quantum simulator, a well defined initial state and readout of the final state are also necessary, but in between, the system just undergoes an evolution that resembles a known Hamiltonian to better understand its properties. Naturally the simulator should be more controllable or accessible than the system itself.

During a computation, the quantum states – essentially analog objects – have to be preserved and manipulated. Already the coupling of the system to the outside world, that is necessary to read out and operate the quantum computer, introduces a minimum of noise, which leads to decoherence turning pure quantum mechanical

[3] To my knowledge, there is no publication related to the 50-qubit processor, yet.

states into mixed states. Additional system specific noise sources are usually also present in quantum computer prototypes. Once in a completely mixed state, a qubit is indistinguishable from a classical random bit. Therefore, the coupling of the qubits to the outside world needs to be precisely engineered, ideally to be switched on and off on demand. Decoherence melts away the advantage quantum computers have over classical ones, at least for standard algorithms in the gate model of quantum computing.

To make a quantum computer work in the presence of decoherence, quantum error correction was developed [10]. The price for creating more coherent systems is redundancy: one qubit worth of information, the logical qubit, can be encoded in several physical qubits. The encoding is chosen such that the logical qubit can be made robust against local noise on the physical qubits. Quantum error correction is based on the peculiar way measurements work in quantum mechanics, described by the Born Rule [11], which states that a measurement will project a system to an eigenstate of the measured observable and give a corresponding output. The process is probabilistic and the probability of outcomes (and corresponding projection of the state) is given by the overlap of the wave function with the different eigenstates of the observable. The trick of quantum error correction is to use measurements that do not learn the state of individual qubits, but rather collective qualities of a many-qubit system such as the parity[4]. Repeatedly measuring a set of collective measurements that commute with each other on a qubit register can constrain the states of those qubits to a lower dimensional subspace corresponding to the measurement results. Under measurement, a quantum system with gradual errors will be projected into a state of no error, or a state where a specific error has occurred, together with the corresponding error signature. Thus, analog noise on the physical qubits is turned into digital noise, ideally along with the information which error has occurred. The collective measurements need to be chosen such that the leading errors in the system are distinguishable. Then, specific errors can be identified and fixed.

Eventually schemes were proposed, where the analog errors can be arbitrarily reduced even in the presence of noisy operations on the qubits and occasional faulty measurements [12]. The levels of noise that such a scheme can tolerate while still improving with more redundancy defines the error-correction threshold.[5] It was this breakthrough that turned quantum computing from an interesting academic topic of speculation into the multi-million dollar research field it is today. Quantum error correction is essential to building a real world quantum computer, thus creating a system beyond the threshold is part of the DiVincenzo criteria [13] that became a road map for the development of the quantum computer.

The first codes that were proposed had logical qubits encoded in 5 [14, 15], 7 [16] and 9 [10] physical qubits. They all have a code-distance of 3, meaning

[4] Whether the qubit register has an even or an odd number of ones.

[5] Technically, noisy measurements and noisy gates will have a different impact, such that it is not really a single threshold but rather the aggregate system performance that counts.

that a minimum of 3 errors on physical qubits are required in order to change the state of the logical qubit. These codes have error thresholds far beyond the overall qubit performance that has been reached in any system to date and were considered impractical in one of the pioneering fault-tolerance publications [17]. On the theory side, the concept of multi-qubit measurements for error correction was quickly generalized to stabilizer codes [12], a way of constructing the multi-qubit measurement operators for codes of arbitrary distance. On the experimental side, the required repeated measurements of the multi-qubit operators for quantum error correction became a focus in the field. They can be implemented by applying gates between data qubits, which encode the logical qubit, and ancilla qubits, onto which the multi-qubit measurement operators are mapped. The ancilla qubits are then read out. Thus, an error correcting code produces as many bits of information per round as it has measurement operators. From these it has to be inferred whether an error has occurred and in a process referred to decoding the error syndrome the most likely error has to be identified.

Amongst the different stabilizer codes, a code on a two dimensional lattice of physical qubits with nearest neighbor interactions was proposed: the surface code [6]. The lattice contains data and ancilla qubits and the gates within a cycle of error correction have been worked out in way that scales to arbitrary lattice sizes. It currently stands out for several reasons: First, a 2D lattice of qubits with nearest-neighbor coupling can easily be realized on chips in a scalable manner. Second, its high error-correction threshold has been reached in several quantum systems. Third, an efficient scheme for decoding the error syndrome is known. The task of infering the underlying error from the syndrome is non-trivial for large systems, such that decoding quantum error correcting codes has also become an active area of research.

1.3 CURRENT PLATFORMS FOR QUANTUM COMPUTING

Above, theoretical considerations of the potential of the quantum computer were discussed, but the theory underlying a fault-tolerant quantum computer is widely accepted by now. The main question is whether we will find the right hardware to realize it. Are we in the situation of Charles Babbage, who tried to construct computing machines but ultimately failed because technology was not yet ready, or is the current effort similar to the one of Alan Turing who succeeded? An intriguing parallel is that, for a long time, the main selling point for quantum computers was that Shor's algorithm could break modern day encryption [20], just like the development of classical computers was tied to breaking encryption in the Second World War.

Currently only a few quantum hardware platforms have demonstrated the ability to execute small quantum algorithms. Performing algorithms is a way to demonstrate all requirements for a quantum computer in a single self-contained experiment.

[6] First proposed in [18]. A detailed explanation in the context of superconducting qubits can be found in [19].

Therefore, it is more demanding than just demonstrating individual requirements, such as good qubit readout or realizing a coupling between pairs of qubits. There was pioneering work in nuclear magnetic resonance systems [21, 22], trapped ions [23] and optical systems [24]. The first realization in a solid-state system was based on superconducting transmon qubits [25], the platform used in this work. Recently, the first realization of quantum algorithms with quantum dots in semiconductors has been presented [26] and qubits based on NV centers in diamond have shown multi-qubit control [27] aimed at quantum error correction. In ion traps, a five-qubit programmable quantum computer was put forward, already providing the ability to quickly and easily perform different algorithms [28]. A step further, IBM has made small quantum computers available on the cloud and even offers a commercial option [29]. This leads to the first calls to commercialize quantum technologies in the near term [30].

1.4 THE ANSWER TO LANDAUER'S QUESTION

So are we on track to practically answer Landauer's question whether quantum mechanics is useful? More importantly, how will we do it? I am going to discuss two milestones that relate to the question in different ways but fall short of creating a commercially viable computer that would solve interesting problems.

The milestone of the first quantum chip that would be competitive with classical supercomputers was (unfortunately) named quantum supremacy [31]. The current world record of simulating a full Hamiltonian on a state-of-the-art supercomputer is 45 qubits [32][7] and each additional qubit at least doubles the required memory to store the state. The consequences for the actual calculations that simulate the qubits are more complicated, because the computation needs to be cleverly distributed on a supercomputer, which is why the run for new records is driving real innovation. With different methods, IBM researchers claim to be able to simulate the behavior of a 56-qubit system [33]. This simulation race shows that the emergence of quantum computing also challenges the classical computer community. Current ~ 50 qubit quantum computers are not very coherent and do not necessarily have full connectivity, which will make it easier to simulate them, because the matrix that stores the qubit state can be more sparse if the qubits lose their quantum information. Still, even a classical supercomputer will likely have problems imitating the next generation of quantum processors. It is not unlikely that within this year or the next, there will be the first claims of reaching the supremacy milestone. Without algorithmic breakthroughs, classical computers add a qubit every two years at best, assuming Moore's law holds and the connectivity of supercomputers can keep up. As long as the quantum computer prototypes grow more quickly, quantum computing will be established as a technology that surpasses the classical computers on its own turf.

[7] There is an unpublished claim of a 46 qubit simulation from FZ Julich.

The second important milestone, which is being pursued is the demonstration of fault-tolerant quantum systems. Demonstrating fault tolerance is about showing improved performance of logical qubits in a quantum-error-correction scheme with increased redundancy, an aggregate performance beyond the error-correction threshold. Step one is realizing a quantum memory, which can preserve quantum information longer by encoding the logical qubit in more physical qubits. Step two is creating a processor that shows higher fidelity when doing operations with more redundancy, a fault-tolerant quantum computer. The second step is harder for several reasons: First, the logical operations are interleaved with the quantum-error-correction cycle, thus the gates on the physical qubits are faster which makes it harder to beat them. Second, our operations are imperfect, such that doing nothing well, as in a memory, is harder than doing something well in a computation. On top of that, the operations on a larger system that make up logical operations become more complicated, thus more prone to error.

The surface code is a good platform for this demonstration as it is an arbitrarily scalable framework for making logical qubits. One could encode logical qubits with different redundancy in a large lattice to demonstrate fault tolerance, therefore making a lattice where several codes of different distance can be realized is an important goal in the community. Once we can show that adding more redundancy improves the processor, the "perfect" quantum system would be reached in the asymptotic case of infinite redundancy. Interestingly, it is easier to show a positive scaling of operation fidelity with redundancy than it is to beat the constituent physical qubits with a logical qubit. The performance requirements to beat the constituent physical qubit performance with a logical qubit depends on the code distance and for small codes, they are more stringent than the requirements for a beneficial scaling with redundancy.

For transmon qubits as used in this thesis, simulations indicate that 17 qubits with current performance could be made into a one-qubit quantum memory that outperforms the constituting qubits, and with 49 qubits, one could make a logical qubit, which has higher-fidelity operations then the constituting qubits [34]. More importantly, in a 49-qubit surface-code lattice, both a distance-3 and a distance-5 logical qubit could be encoded. If current performance in few-qubit chips can be reproduced at the larger scale, the fault-tolerance scaling can be demonstrated. This milestone might be more meaningful, because a practical demonstration would mean that a powerful universal quantum computer could be realized by simply scaling up the system that demonstrated it to a larger number of qubits. In order to make this scaling plausible, ideally a unit-cell chip design should be used such that even larger lattices could just be realized by copy pasting the unit cell to form a larger lattice [35]. This would be a clear path to unlock all the quantum speedups that have been discovered so far and maybe some that have not yet been discovered.

Both of these milestones can likely be reached with less than 100 qubits and several groups in the world are participating in the "quantum space race"[8] to reach them.

1.5 HOW DOES THIS WORK FIT INTO THIS? A THESIS OVERVIEW

I hope to not have left the impression of being grandiose with this lengthy introduction. This thesis does not answer the question of the quantum computer's usefulness, nor did I attempt to when I started working on my experiments. But the ongoing worldwide research to realize a quantum computer influenced my decisions as a researcher, they influence our research group as a whole as well as the agencies and corporations that provide our funding and the referees that evaluate our manuscripts. In this thesis, two experiments are presented that contribute to the bigger picture of building a quantum computer:

Firstly, the qubit control via selective broadcasting experiment (Chapter 5) was a proof-of-principle demonstration of a more economical control architecture for a many-qubit quantum processor. We showed that we can share hardware for single-qubit control, to achieve economies of scale in a bigger quantum computer. The shared control hardware only leads to a constant overhead for arbitrary single qubit control and we can still achieve single-qubit gates beyond the surface code threshold. In addition to meeting the thresholds for a fault-tolerant quantum computer in a many-qubit system, there is an economic threshold to meet: the quantum computer needs to solve interesting problems at a cost that the people interested in the solutions can afford. The price for the economies of scale is that the qubits sharing the hardware need to be at the same frequencies, leading to a repeating pattern of same frequency qubits on the quantum processor.

Secondly, the chip-to-chip entanglement experiment (Chapter 6) was a step towards modular architectures where qubits are not entangled with on-chip interaction but via a measurement that leaves qubits on different chips entangled. Ultimately, a quantum computer could be constructed from several on-chip modules that are connected with flying photons. While there is currently a big effort to monolithically scale up superconducting quantum processors, modularity will likely be crucial for achieving large-scale-integrated quantum devices. Eventually fabrication yield and accuracy will require the quantum computer to be put together from pieces that can be handpicked. This could be done by implementing the photonic chip-to-chip quantum connections that we showed to connect the modules.

In addition, I will introduce the basics of cQED quantum processors in Chapter 2 and outline their design and fabrication in Chapter 3. Chapter 4 is a personal look at building a programming framework for the control of superconducting quantum processors, which will ultimately need to be capable of easily performing different algorithms and handle quantum error correction. Building an extensible framework is necessary to manage the growing complexity of experiments. Summarizing some of

[8] title of the John Martinis Talk at the QIP conference in Delft 2018

the lessons from failures and successes in this context might be helpful for following generations. Finally, Chapter 7 contains an outlook on the main experiments in this thesis and a summary of experiments where I played a supporting role along with some personal take-away messages.

2 CQED QUANTUM PROCESSORS WITH TRANSMON QUBITS

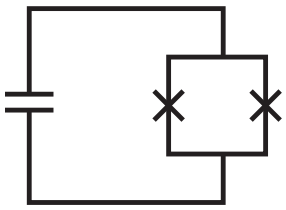

Figure 2.1: *Simplified circuit diagram of the transmon qubit*

This chapter provides a brief introduction to circuit Quantum Electrodynamics (cQED) with transmon qubits. The basic Jaynes-Cummings Hamiltonian is introduced and the basic theory for qubit readout and control is summarized. The theory for qubit performance metrics, such as coherence time as well as gate fidelity and quantum state tomography, is briefly introduced. A brief overview of architectures for transmon quantum processors is provided. In-depth circuit diagrams and design will be provided in Chapter 3.

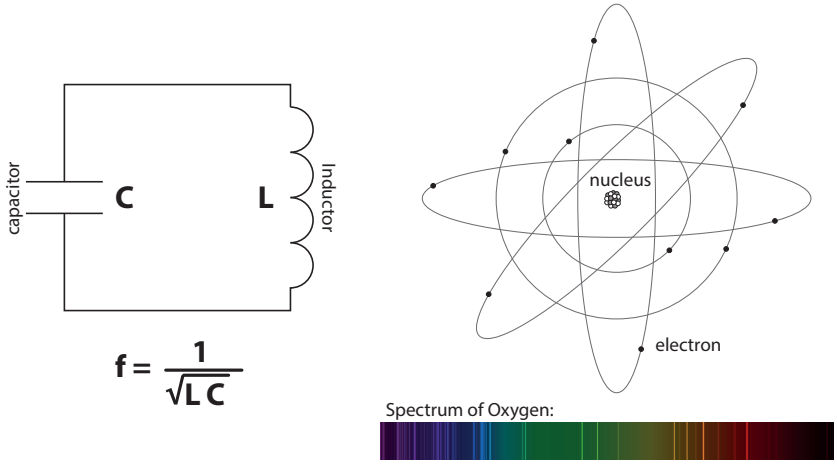

Figure 2.2: *The analogy between the spectral lines of an atom and the resonance frequency of an LC circuit.*

2.1 SUPERCONDUCTING CIRCUITS AS ARTIFICIAL ATOMS

The first quantum behavior was recognized in atomic spectra and light-matter interaction, but quantum theory essentially became a new fundamental theory of nature for systems in the limit of low temperatures and few degrees of freedom. On a macroscopic scale, superconductivity was one of the first consequences of quantum mechanics that were observed. Naturally then, it requires low temperatures. Due to an effective attractive interaction between conducting electrons in some metals (and insulators), the conducting electrons in a piece of superconductor collapse into one joint quantum state — the Cooper pair condensate. In this state, currents flow without resistance, because the condensate is decoupled from lattice vibrations in the crystal around it and does not scatter on local defects, the two causes of electrical resistance. The temperature at which this phase transition occurs is related to the strength of the effective electron-electron attraction, its energy scale determines the superconducting gap.

Using superconducting materials, we can now make a dissipationless electrical circuit. The degrees of freedom of this circuit will behave quantum mechanically if we choose their energy scales to be above the energy scale associated with temperature. But superconductors require very low temperatures anyway. In our case, most of our experiments take place around 20 mK, a temperature that can be reached with commercially available dilution refrigerators. The energies at which we can operate our circuits are bounded by temperature from below and the superconducting gap from above as shown in Figure 2.3.

Superconducting electrical circuits exhibit quantum behavior and can no longer be described by the classical Kirchhoff laws. However, capacitors and inductors are linear

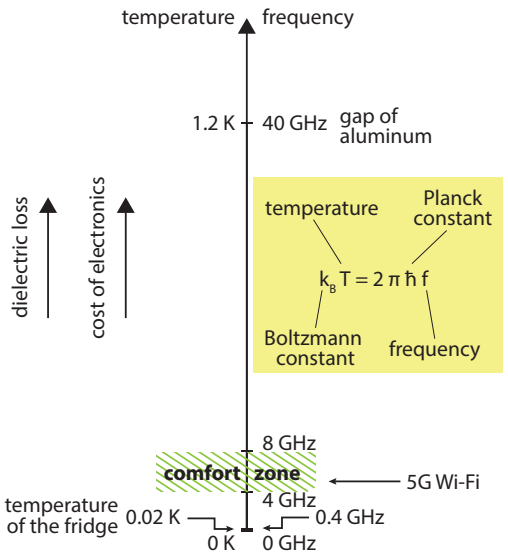

Figure 2.3: *Schematic of the energy scales for our experiments. The* 4 GHz-8 GHz *band falls roughly in the middle between the limits imposed by temperature on the low end and the superconducting gap of alluminum on the high end. In addition, this band is used in telecommunication, such that amplifiers and control electronics for the qubits are readily available.*

circuit elements, so while circuits comprised only of these elements will be described by quantum mechanics, their behavior will correspond to the behavior of classical circuits. The only modification from quantum mechanics arises in the noise behavior of these circuits, which at very low temperatures will be limited by the Heisenberg uncertainty principle.

2.1.1 *The Josephson junction*

To realize more exotic quantum behavior, a nonlinear circuit element with low dissipation is needed. A coherent nonlinear circuit element based on the properties of superconductors was discovered in 1962: the Josephson junction [36].[1] An island of superconductor is described only by the number of Cooper pairs and by the phase of the condensate, very few degrees of freedom for a potentially macroscopic system. When two of these islands are weakly coupled, such that Cooper pairs can tunnel from one side to the other, this tunneling gives rise to a current. Josephson derived the relationship between the tunneling current I, and the voltage difference and superconducting phase difference between the islands V and ϕ, respectively:

$$\begin{aligned} I &= I_c \sin \phi, \\ V &= \frac{\Phi_0}{2\pi} \frac{\partial \phi}{\partial t}. \end{aligned} \tag{2.1}$$

Here, I_c is a critical current that is a parameter of any Josephson junction and Φ_0 is the superconducting flux quantum, a natural constant. Using these Josephson relations and basic relations between current and voltage, one can come to realize

[1] In superconducting circuits, other nonlinear circuit elements can be realized using kinetic inductance or nanomechanical oscillators.

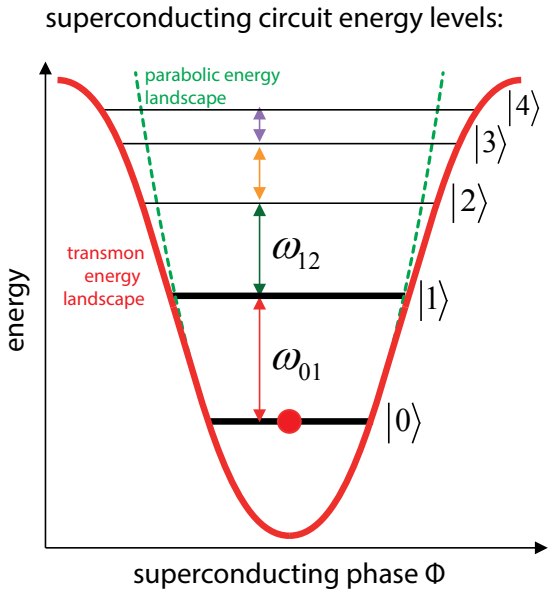

Figure 2.4: *Schematic of the energy levels of the transmon circuit. A slight deviation from the parabolic energy landscape leads to unequal spacing of the levels. Generally the qubit is encoded in the lower two levels.*

that the Josephson junction can be interpreted as an inductor – inductance being the quantity that relates voltage to the time derivative of the current:

$$V = L_J \frac{\partial I}{\partial t} \implies L_J = \frac{\Phi_0}{2\pi I_c \cos\phi}. \tag{2.2}$$

But the Josephson inductance L_J implicitly depends on the current I itself via the phase ϕ, which a normal inductance does not. The Josephson junction is a non-linear inductor. Because of the superconducting gap, the two superconducting condensates on the islands are virtually decoupled from their environments, such that there is very little dissipation. Thus, the discovery of the Josephson junction as a circuit element made it possible to realize circuits that exhibit interesting quantum behavior. The first observation of quantized levels in a circuit at microwave frequencies then opened up the field of artificial atoms in quantum circuits [37]. A detailed explanation of how to derive the Hamiltonian of such circuits that predates the first superconducting qubits can be found in [38] and more recent introductions to circuit quantization include [39, 40].

2.1.2 *The transmon*

The transmon circuit (Figure 2.1) is the first circuit one would come up with when given a non-linear inductor and the goal to design a system with distinct level spacing. The simplicity is certainly part of its success. However, it took a few years of research to find the right regime of circuit parameters for a high-coherence qubit. While we have good recipes for turning a circuit into a Hamiltonian and derive its

quantum behavior, making a circuit to achieve the perfect Hamiltonian for a given task, for example parity checks in quantum error correction, is apparently not as easy, such that most research in superconducting qubits focuses on a very limited number of elementary circuits. Here, I will try to give an easy and intuitive introduction to the transmon Hamiltonian.

To understand the behavior of the circuit in Figure 2.1, consider the quantum states of the system. We will make the assumption that all conduction electrons in the two islands are paired up to Cooper pairs. Any residual unpaired electrons, so-called quasiparticles, form an additional dissipative system in the Hamiltonian that can couple to the Cooper pairs and causes energy loss. While these quasiparticles are present in higher numbers than the temperature of the dilution refrigerator would suggest, they usually are not the leading cause of dissipation [41–43]. The Cooper pairs are all collapsed into one macroscopic quantum state on each island that just has two parameters: the number of Cooper pairs on each island and the superconducting phase. As the number of conduction electrons is comparable to the number of atoms, the number of Cooper pairs in the system is a macroscopically big number. However, for symmetric islands and in the absence of strong voltage biasing, the imbalance of Cooper pairs on the islands is small, usually only few Cooper pairs. The Hamiltonian is a function of the charging energy E_C and the Josephson energy E_J, and the variables are the Cooper-pair difference $\hat{n}$ and the superconducting phase difference ϕ:

$$H = 4E_C \left(\hat{n} - n_g\right)^2 - E_J \cos\phi. \tag{2.3}$$

n_g is an offset in the Cooper-pair difference that can for example be caused by a voltage gate next to one of the islands. Even this simple circuit can be operated in different parameter regimes and at first it was used as a Cooper-pair box [44], where a qubit would be stored in superpositions of states that differ by a single Cooper pair on the islands. However, this Cooper-pair box qubit is highly sensitive to the charge environment and was therefore not very coherent. Later, it was realized, that the ratio E_J/E_C determines the charge sensitivity, as well as the anharmonicity, the difference between the f_{01} and f_{12} (energy levels are numbered ascending from the ground state) [45]. With $E_J/E_C \approx 50$, the charge sensitivity becomes negligible as a source of decoherence: this is the transmon regime. A comprehensive introduction to the transmon including the coupling to microwave resonators can be found in reference 45 from where the following formulas are derived. The qubit is charge insensitive, because the capacitor becomes very big, at the cost of bringing the higher levels of the system closer together. In this regime, the cosine term in Equation (2.4) results in a small deviation from the harmonic oscillator potential, giving the potential landscape sketched in Figure 2.4. The transmon anharmonicity $\alpha = f_{12} - f_{01}$ is approximately given by $-E_C$, which is usually chosen between 200 MHz and 300 MHz, enough to make pulses that can address the f_{01} transition

to manipulate the qubit without off-resonantly driving f_{12} too much. The qubit transition f_{01} and f_{12} approximately given by

$$\begin{aligned} hf_{01} &\approx \sqrt{8E_J E_C} - E_C, \\ hf_{12} &\approx hf_{01} - E_C. \end{aligned} \tag{2.4}$$

f_{01} is usually chosen in the 4−8 GHz window by adjusting E_J. For exactly extracting the parameters of the Hamiltonian, the approximations above are too imprecise, it is best to measure f_{01} and f_{12} and find the parameters of the numerically diagonalized Hamiltonian that give those transition frequencies. Diagonalizing the Hamiltonian in the charge basis going up to Cooper pair differences $n = 30$ is computationally easy. To give an example, for a qubit with $E_J/h = 22.25$ GHz and an $E_C/h = 270.8$ MHz, the approximation would give $f_{01} = 6.672$ GHz and an $\alpha = -E_C$, while diagonalizing the Hamiltonian gives $f_{01} = 6.660$ GHz and $\alpha = -300.0$ MHz. Note that the relative error on f_{01} is acceptable, while the relative error on the anharmonicity is 10%.

The resulting transmon qubit [45][2] has been arguably the most successful superconducting qubit, while the original Cooper-pair box has been largely abandoned as a qubit. Importantly the transmon, despite being charge insensitive, retains a sizable electric dipole moment for coupling it to lines that drive it, to resonators to read it out, and to other transmons. For most purposes, only the bottom two levels are used, but the other levels need to be taken account in control sequences or when designing circuits, because their presence leads to corrections.

2.1.3 *The SQUID loop as a tuneable Josephson junction*

In many cases, single Josephson junctions are replaced by a loop with two Josephson junctions in parallel, a Superconducting Quantum Interference Device (SQUID) loop[3]. Embedded in the transmon circuit, SQUID loops behave like a single Josephson junction that is tunable by the flux through the loop, due to the quantization of the flux through the loop. Thus, we can realize a transmon with a frequency tuning knob.

The two junctions each have a Josephson energy $E_{J,1}$ and $E_{J,2}$. Without net flux through the loop, one can view them as one bigger Josephson junction with $E_J = E_{J,1} + E_{J,2}$. This gives a maximum transmon frequency $f_{max} \approx \sqrt{8\,(E_{J,1} + E_{J,2})\,E_C} - E_C$ [45], because the E_J in the presence of a net flux will

[2] The "mon" signifies that the qubit is encoded in a plasmon (a plasma oscillation, meaning an interplay of the electromagnetic field and the superconducting electrons). The "trans" could come from the transmission line resonator that couples to the qubit. However, a transmission line is not an essential part of the transmon. It could also mean that the Hamiltonian is operated beyond the charge-qubit regime.

[3] The effect was discovered two years after the Josephson effect [46], the whimsical name appears another two years later [47]

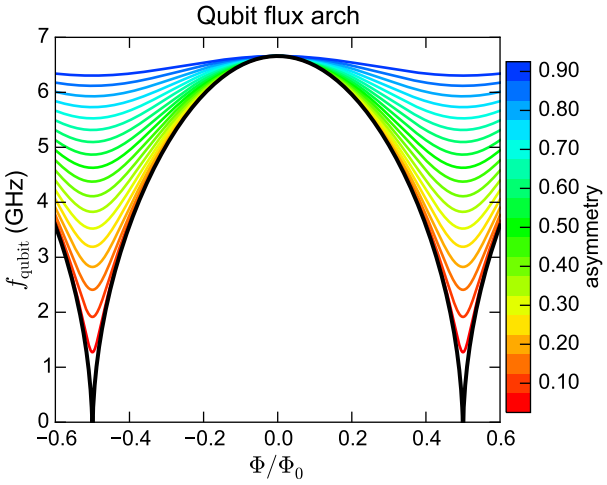

Figure 2.5: *Frequency as a function of reduced flux through the SQUID loop for a transmon with* $f_{\mathrm{max}} = 6.66$ GHz *varying the SQUID loop asymmetry. The reduced tuning range as well as the reduced flux gradient are clearly evident. Based on the accuracy of junction fabrication and the tuneability needed, the asymmetry should be chosen for optimum performance.*

be reduced. Introducing the junction asymmetry $\alpha_{\mathrm{JJ}} = |E_{\mathrm{J},1} - E_{\mathrm{J},2}|/(E_{\mathrm{J},1} + E_{\mathrm{J},2})$, the frequency dependence on flux Φ can be written as

$$f(\Phi) \approx (f_{\mathrm{max}} + E_{\mathrm{C}}) \left[\alpha_{\mathrm{JJ}}^2 + (1 - \alpha_{\mathrm{JJ}}^2)\cos^2(\pi\Phi/\Phi_0)\right]^{1/4} - E_{\mathrm{C}}, \qquad (2.5)$$

with the flux quantum Φ_0. Figure 2.5 shows the frequency dependence on flux for different junction asymmetry given a qubit with a top sweet spot of $f_{\mathrm{max}} = 6.66$ GHz. The asymmetry reduces the overall tuning range, which in the symmetric case goes all the way to 0 GHz[4] , however it also reduces the flux gradient. In the presence of flux noise, which is usually $1/f$ noise on the order of $\sim 10\ \mu\Phi_0/\sqrt{\mathrm{Hz}}$, the effective tuning range where the qubit exhibits sufficient coherence can be enhanced [48]. Several experiments during my PhD consequently made use of the asymmetric SQUID loop [49–51] to optimize qubit coherence for the required tunability.

2.2 CAVITIES AND THE JAYNES-CUMMINGS HAMILTONIAN

In the exploration of quantum mechanics, cavities played a key role. The coupling of single atoms to single photons is weak, therefore the quantum behavior of single atoms (or ions, or any other elementary quantum systems) is difficult to study. Cavities enhance the light-atom interaction and enable fast light-based readout and manipulation of quantum states. It is for this reason that strong coupling to cavities has been an important result for many quantum systems [52–54].

The most important Hamiltonian in this context is the Jaynes Cummings Hamiltonian [55]. The Jaynes Cummings Hamiltonian has become the basis of transmon readout and, in some architectures, two-qubit gates. In the qubit approximation, it can be written down using creation and annihilation operators of the resonator mode ($\hat{a}^\dagger = \sum_{n=0}^{\infty} \sqrt{n+1}\,|n+1\rangle\langle n|$ and $\hat{a} = \sum_{n=0}^{\infty} \sqrt{n+1}\,|n\rangle\langle n+1|$) and

[4] however, the transmon regime eventually breaks down, such that Equation (2.5) is no longer valid.

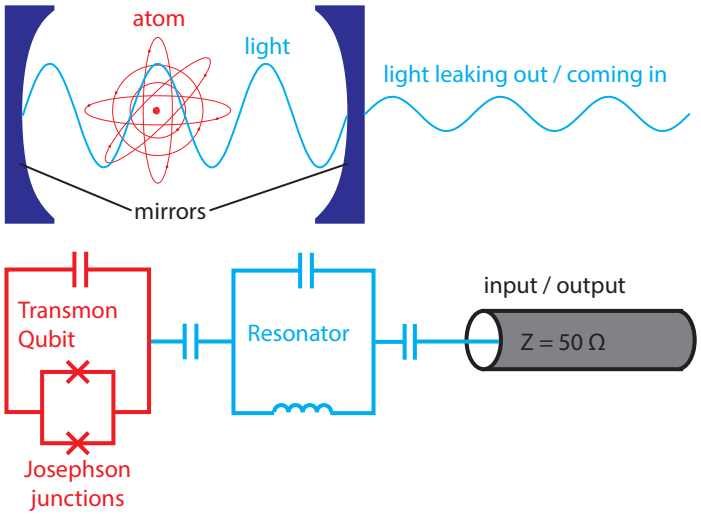

Figure 2.6: *Analogy between Cavity Quantum Electrodynamics, where atoms couple to optical cavities, and circuit Quantum Electrodynamics, where transmons (or other qubits) take the roles of the atoms and LC-like resonator circuits take the roles of the cavities. The enhanced coupling of the transmons to photons in the resonator is used to readout the transmon, or, in more complicated settings to couple two or more transmons via the resonator for two-qubit gates.*

of the qubit ($\hat{\sigma}_- = |g\rangle\langle e|$ and $\hat{\sigma}_+ = |e\rangle\langle g|$), as well as the Pauli-z operator $\hat{\sigma}_z = |g\rangle\langle g| - |e\rangle\langle e|$[5]:

$$\frac{H}{\hbar} = \omega_r \hat{a}^\dagger \hat{a} + \frac{\omega_q}{2}\hat{\sigma}_z + g\left(\hat{a}^\dagger \hat{\sigma}_- + \hat{a}\hat{\sigma}_+\right). \tag{2.6}$$

ω_q and ω_r are the resonator and qubit frequencies and g is the qubit-resonator coupling. In the limit of detunings $\Delta = \omega_q - \omega_r$ that are large compared to g, the

[5] I used the intuitive Dirac notation [56], to define the actions of the operators. $|g\rangle$ denotes the ground state of the qubit, $|e\rangle$ the qubit excited state and $|n\rangle$ an n-photon state of the resonator mode.

Figure 2.7: *Dispersive shift of a resonator as a function of the qubit state. The chip 2 resonator from Chapter 6 was measured in transmission with a short integration window with and without an initial π-Pulse on the qubit. Due to the short integration window to avoid qubit relaxation, the resonator linewidth κ is slightly wider than measured in continuous wave.*

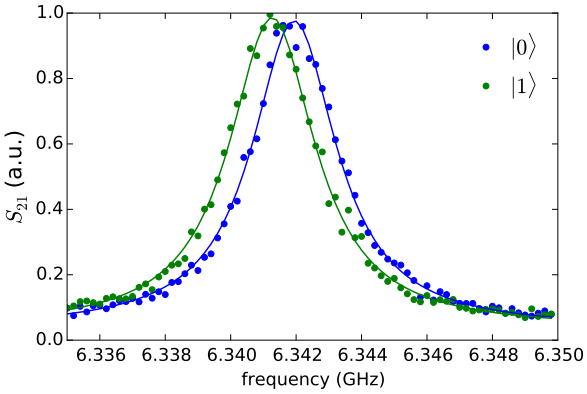

dispersive approximation is applied, reducing the resonator qubit interaction to a qubit dependent shift of the resonance frequency and a photon number dependent shift of the qubit frequency. This approximation is only valid for low photon numbers, it starts breaking down around a critical photon number $n_{\mathrm{crit}} = \Delta^2/4g^2$. Introducing the dispersive shift $\chi = g^2/\Delta$, the Hamiltonian becomes

$$\frac{H_{\mathrm{JC}}}{\hbar} = \omega_{\mathrm{r}}\hat{a}^\dagger\hat{a} + \frac{\omega_{\mathrm{q}}}{2}\hat{\sigma}_{\mathrm{z}} + \chi\hat{a}^\dagger\hat{a}\hat{\sigma}_{\mathrm{z}}. \tag{2.7}$$

Particularly for qubit readout this is a very useful Hamiltonian. The resulting system exhibits a qubit dependent resonator frequency shift that can be detected with transmission or reflection measurements. However, the transmon is not a two-level system and the higher levels result in a modification of the dispersive shift $\chi = g^2\alpha/[\Delta(\Delta+\alpha)]$ [45] that contains the anharmonicity α. These kinds of corrections exemplify why the qubit approximation should be used with caution for transmons. Additionally, the coupling to the transmon imprints some nonlinearity on the resonators, another critical photon number $n_{\mathrm{crit,Kerr}} = \kappa\Delta/\chi^2$ was introduced to estimate the size of the effect. In most of our experiments, $n_{\mathrm{crit,Kerr}}$ is usually negligible, while n_{crit} is an important factor in transmon readout, limiting the power that can be used.

There are also some effects on qubit coherence to consider, where the finite resonator linewidth κ plays a role. The resonator coupling imposes a limit on the qubit relaxation time $T_1^{\mathrm{Purcell}} = \Delta^2/(g^2\kappa)$ as the qubit hybridizes with the resonator which loses photons, both by leaking them into lines coupled to the resonator and by intrinsic resonator losses. In case there are photons in the resonator, for example thermal photons, an average photon number $\bar{n}$ also impose a limit on qubit coherence time $T_2^{\mathrm{photon}} = (\kappa^2+4\chi^2)/(4\chi^2\kappa\bar{n})$ [57].

2.3 OPERATING THE TRANSMON AS A GOOD QUBIT

The first step to turning a quantum system into a quantum information processor is to define how information is encoded, usually this means designating certain pairs of levels as qubits. These two-level systems need to be individually controlled and read out, which will be described for transmon qubits below. Technically, some measure of qubit control is required in order to calibrate the readout and a good readout is required in order to calibrate the control pulses. Thus, turning a transmon-resonator system into a useful qubit is a bootstrapping procedure. Traditional transmon two-qubit gates were not performed in the main experiments of this thesis, so they will not be introduced in detail. I will also try to summarize qubit performance metrics that we use to ascertain that our qubit operations make sense.

2.3.1 *Dispersive qubit readout*

Qubit readout is based on the dispersive Jaynes Cummings Hamiltonian. While the frequency domain picture of a qubit-dependent resonator shift that we detect is

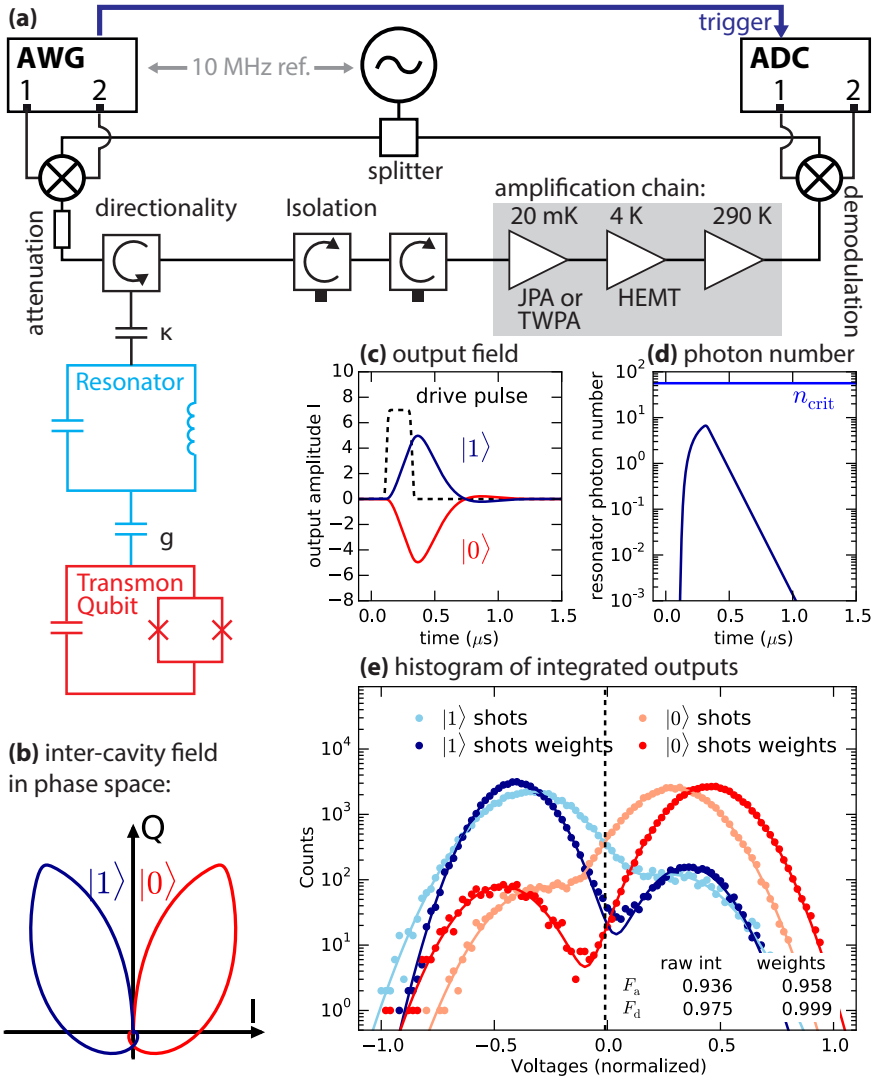

Figure 2.8: ***(a)*** *Schematic of transmon readout electronics and wiring. The readout pulse can be realized with a microwave source and an AWG. On the way down attenuation reduces the room-temperature noise. A circulator can be used to direct all photons that bounce on the microwave resonator to the amplification chain. Isolators are used to shield from noise coming from the amplification chain without compromising the signal. The following data is simulated using a stochastic master equation as described Chapter 6. A quantum efficiency of* 0.5 *is used. The* $2\chi = \kappa$ *condition is simulated for good SNR with* $\kappa = 2$ MHz. ***(b)*** *Phase-space diagram of the inter-cavity state evolution with a square pulse drive. Simulation has a drive in the middle between the* $|0\rangle$ *and* $|1\rangle$ *resonator frequencies. In case of symmetric driving, one quadrature contains the qubit information.* ***(c)*** *Readout signal in the relevant quadrature. The difference between the* $|0\rangle$ *and* $|1\rangle$ *outputs can be used as a weight function on single-shot traces.* ***(d)*** *Resonator photon number as a function of time.* ***(e)*** *Histograms of the outputs integrated from* 0 *to* 1 μs *with and without the integration weights.*

intuitive, it is useful to look at the problem in time domain simply because with lossy qubits, everything is time critical. Similarly to the single-qubit gates, we use pulsing equipment to generate the readout pulses as seen in the schematic in Figure 2.8**(a)**. If mixers are used, imperfections should be digitally corrected where possible, both for the mixer generating the pulses and for the mixer demodulating the signal. For most measurements in reflection, input and output can be separated by a circulator, a three-port device that behaves like a roundabout for the radiation. This ensures that all photons carrying state information are transmitted to the amplification chain. The experiment in Chapter 5 used a feedline setup instead, where the readout resonators couple to a transmission line and reflect the signal on resonance. Then, only about half the photons make it to the detection, leading to a loss in quantum efficiency.

For high-fidelity measurements, the most essential factor is usually not the hardware generating the pulses and digitizing them, nor is it usually the qubit-cavity system, but the amplification chain. Particularly, the first amplifier usually limits the noise performance [58]. For high-fidelity measurements, the nonlinearity of Josephson junctions has been used to implement parametric amplifiers. First, Josephson parametric amplifiers (JPAs) were realized [59], essentially resonators with one or multiple Josephson junctions that provide some nonlinearity. A good recent introduction to the Hamiltonian and the different operating regimes can be found in [60]. In the experiment in Chapter 6, we used a JPA. Higher bandwidth parametric amplifiers have been realized by making transmission lines that include Josephson junctions, so called travelling-wave parametric amplifiers (TWPAs) [61]. The second amplifier in the chain is usually a transistor-based amplifier at the 4K stage which has a typical noise temperature of ~ 2.K. This alone would limit the quantum efficiency η_m to about $\eta_m = \hbar\omega/k_B T_{noise} \approx 0.1$. With TWPAs and JPAs, $\eta_m \approx 0.5$ can be realized, as for example reported in Chapter 6 of this thesis. Recently, $\eta_m \approx 0.8$ has been achieved by coupling a qubit directly to a nonlinear resonator to get in-situ parametric amplification and using a JPA as well as a TWPA as subsequent amplification stages [62]. Additional amplifiers at room temperature are used to achieve signal levels appropriate for the measurement hardware, but they should not influence the quantum efficiency.

The data points in Figure 2.8**(b-e)** are simulated using a stochastic master equation to model the qubit-cavity system readout dynamics. This simulation hopefully provides a good intuition for the crucial requirements for good dispersive readout. A Polaron approximation [63] is used, which assumes that the cavity always stays in a coherent state when it is exposed to a coherent driving field (e.g. the readout tone). This simplifies the cavity modeling to tracking the center of the coherent state $\alpha(t)$ instead of doing a full Fock-state simulation. Classical equations of motion for the cavity describe the cavity field trajectory $\alpha(t)$ as a response to the readout tone with the qubit merely shifting the cavity frequency by the dispersive shift. Single-qubit readout modeling methods are nicely described in [63] and [64]. For a two-qubit-two-cavity system, the full derivation can be found in Chapter 6.

It is generally advantageous to chose a measurement frequency at the symmetry point between the $f_{\mathrm{res},|0\rangle}$ and $f_{\mathrm{res},|1\rangle}$, because then, all the qubit information will be encoded in one quadrature of the resonator field as seen in Figure 2.8**(b)**. If the cavity is kept at a steady photon number $\bar{n}$, the signal-to-noise ratio in this symmetry condition is given by [63]:

$$SNR = \eta_{\mathrm{m}} \bar{n} \frac{\kappa T_1 \chi^2}{\kappa^2/4 + \chi^2}, \tag{2.8}$$

which for a Purcell-limited qubit lifetime gives an optimum for $\kappa = 2\chi$. This condition was chosen in the simulation. A $\kappa/2\pi = 2$ MHz was chosen as a realistic parameter that allows for relatively fast measurements. For a qubit-resonator coupling $g/2\pi = 50$ MHz, this gives a qubit resonator detuning 750 MHz, which results in $T_1^{\mathrm{Purcell}} = 18$ μs and a critical photon number of $n_{\mathrm{crit}} = 56$. Qubit $T_1 = 12$ μs was chosen in simulation, to reflect other losses. The readout pulse is a slightly-smoothed square pulse of 200 ns length. The maximum photon number reached during the measurement is more than a factor of five below n_{crit}. This simple simulation shows how many parameters have to be taken into account when designing chips. Many parameters represent compromises and in design many assumptions have to be made as to what can realistically be achieved.

High-fidelity readout pulses with durations down to 48 ns [65] or 140 ns [66] have been realized, but more generally readout pulses are on the order of 200 ns – 1 μs. While there are the pulse-time and the integration time to consider, the most interesting time for readout is the time the cavity remains populated – in our simulation a 1 μs window in which the qubit cannot be operated coherently [Figure 2.8**(d)**]. For fast readout κ can be increased without compromising the qubit lifetime by using a Purcell filter [67]. The filter after the cavity has to permit signals at the readout frequency to pass but has to make it impossible for the qubit to relax via this path. Readout pulses can be generated similar to the qubit control pulses with a microwave source, a mixer and an AWG, but some microwave sources can also be pulsed with digital markers, as done in Chapter 5. In the latter case, only square pulses can be realized. For faster readout, the pulses will be shaped to ramp up the cavity photon number quicker and especially to drive it back to the vacuum state quicker [68, 69].

A mixer is usually used to downconvert the readout signal from the GHz frequency of the readout resonator to a MHz frequency that can be easily digitized with an analog to digital converter (ADC) that has 1 ns resolution. The finite quantum efficiency and low power of measurements leads to noisy output traces that can be integrated over time. Integration weights can be used to better distinguish the states, for example the difference between the average readout traces for $|0\rangle$ and $|1\rangle$ in each quadrature [70].

To show the effect of the integration weights, Figure 2.8**(e)** gives normalized histograms of the integrated readout signal with and without the weights for an

$\eta_m = 0.5$. As shown in [71], the weights are also crucial when trying to estimate the quantum efficiency of a detection chain correctly in the transient regime, where the resonator is not in the steady state for most of the readout time. The assignment fidelity F_a given by the overlap of the raw probability distributions The discrimination fidelity F_d given by the overlap of the main Gaussians for $|0\rangle$ and $|1\rangle$. F_d is a better figure of merit to characterize the readout than F_a because the latter is influenced by relaxation and thermal excitation of the qubit. Both fidelity definitions are given for both cases showing a clear improvement due to the integration weights. Here, the readout information is in one quadrature and a simple threshold can be drawn to convert the shots into bits representing the most likely qubit state. In Chapter 6, the readout information for two qubits is given by complex numbers and a machine-learning classifier is used to infer the most likely state.

2.3.2 *Qubit initialization*

For most purposes it is also important to initialize qubits in a well defined pure state, usually the ground state. The combination of our qubits finite lifetime and the fact that their transitions energies are much larger than the temperature of our dilution refrigerators suggests initialization by waiting several multiples of T_1 between runs of the experiment, which was done for the experiments in Chapter 5 and Chapter 6. The main drawback is that it puts a limit of the repetition rate of experiments. Additionally, the qubits often have a few percent thermal excitation, much more than predicted by the $\sim$ 10mK temperature of the dilution refrigerator, partially caused by coupling to a quasiparticle bath in the superconductor that is generally not at thermal equilibrium [43], but also by imperfect filtering of room-temperature noise. The thermal excitation can be estimated from single-shot histograms with high readout fidelity [Figure 2.8**(e)**] assuming that measurement induced excitation is negligible. For the simulated data, with weights we estimate 2.8% and without we coincidentally get 3.0%, exactly the simulated amount.

However, particularly in Chapter 6, good state preparation is a crucial problem because it can skew qubit tomography results which makes it difficult to assess the quality of our experimental result. To improve the initialization, we perform an initial measurement and reject data where the qubits are measured to be in the excited state. For many qubits, this strategy does not scale as the overall ground state probability will tend towards zero. With low-latency feedback on the measurement results, it is possible to initialize the qubits by measurement [72], performing a conditional π pulse for $|1\rangle$ state outcomes. Then, the repetition time would ultimately be limited to the experiment time including the initialization procedure.

2.3.3 *Qubit control*

For single qubit control, we generally use the dipole moment of the qubit to couple it to the voltage fluctuation in a microwave line. It is also possible to send single

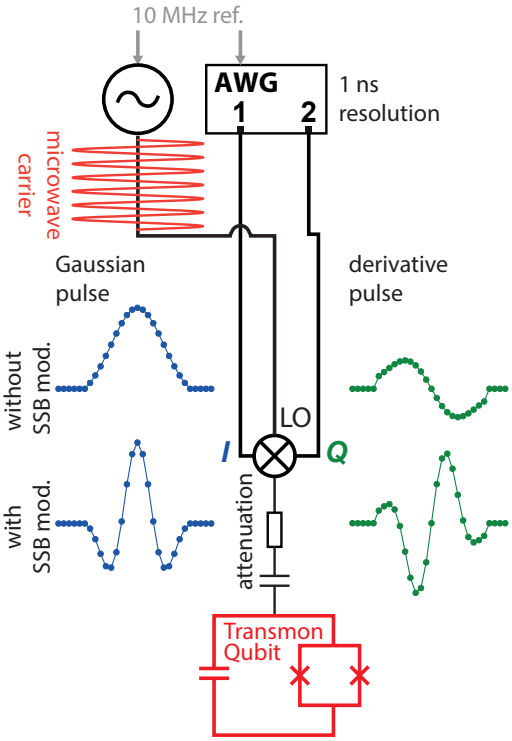

Figure 2.9: *Pulses for single qubit gates. A microwave source is used to provide a stable and clean microwave carrier usually slightly detuned from the qubit frequency by a sideband modulation frequency. AWG generates pulses that time-shape the carrier signal. AWG and microwave source are synchronized by a common reference oscillator (usually* 10 MHz*). We apply a Gaussian that is cut off after 2 standard deviations on the I quadrature and the derivative of the Gaussian on the Q quadrature. A scaling factor between the two can be used to minimize leakage. Here the AWG has* 1 ns *resolution and the pulses are* 20 ns *long. Pulses are given both without and with the* $\sim$ 100 MHz *sideband modulation used in the experiments in this thesis.*

qubit control pulses to the resonator instead of a dedicated drive line, as long as pulses are strong enough.

A drive resonant with ω_{01} induces transitions $|0\rangle \leftrightarrow |1\rangle$. We generally use a microwave carrier to generate a stable continuous wave signal close to the qubit frequency and arbitrary waveform generator (AWG) to shape control pulses in time, realizing qubit rotations of the right angle around an axis in the x-y-plane. The axis is controlled by the relation between the pulse and the carrier phase, while the angle is controlled by the amplitude. Therefore, the microwave source and AWG need to be synchronized to a common reference oscillator. Recently, high-fidelity gates have been realized using direct synthesis on an AWG without a microwave carrier and a mixer [73], but the high-bandwidth electronics are currently more expensive and the phase-stability does not yet reach the performance of the mixer-based pulses.

In order to shape the GHz-frequency carrier with the MHz frequency AWG voltages, we use IQ mixers as shown in Figure 2.9. Mixers lead to a complex multiplication of the LO input with the I and Q inputs. Several imperfections in the mixers can be digitally corrected by adjusting the control pulses:

1. **Carrier leakage:** Even with no input on the I and Q channels, some of the carrier signal leaks through the mixer. This effect can be corrected by DC voltages on I and Q that are adjusted while monitoring the carrier leakage on

a spectrum analyzer. In addition, using a sideband modulation, the carrier can be chosen to be off-resonant, leading to a smaller effect of carrier leakage.

2. **Phase skewness:** The phase of the signal on I and the signal on Q is ideally 90 deg, but in practice this does not hold perfectly due to unequal cables, attenuation on the mixer inputs and imperfections in the mixer itself.

3. **Amplitude imbalance:** Ideally, the I and Q inputs require identical amplitudes, but in practice there is an imbalance, again due to the setup and the mixer itself.

4. **Non-linearity:** Ideally, the output power of the mixer will scale with the square of the amplitude on I and Q, however, this scaling only holds for small voltages. Eventually, the output power usually saturates. This effect can be measured in advance and corrected. In particular, π pulses usually require slightly more than twice the $\pi/2$ pulse amplitude.

To correct the latter two effects, one can use a spectrum analyzer to monitor the unwanted sideband and minimize it, by varying a phase shift and amplitude imbalance on the AWG pulses. The digital corrections will usually only hold at a given LO frequency and sideband modulation frequency.

A quick tuneup of single-qubit control pulses is done as follows: By measuring Rabi oscillations, varying the pulse amplitude for a fixed pulse length, the amplitude corresponding π pulse can be found approximately and a $\pi/2$ pulse has half of that amplitude if non-linearities are calibrated well. Ramsey measurements can be performed, using a first $\pi/2$ pulse to create a superposition state and a second $\pi/2$ pulse to map the phase evolution on the computational basis for readout. The qubit resonance frequency can then be estimated by varying the idling time between the two $\pi/2$ pulses and fitting the oscillation frequency with accuracy ideally set by the qubit dephasing time T_2^*. On resonance, the amplitudes might have to be adjusted again. Example measurements are shown in Chapter 5. Tuning up good qubit pulses is a bootstrapping procedure, eventually pulse sequences that amplify specific errors can be used for fine tuning, as described in Chapter 5 for the pulse amplitude. Another method is to simply use an optimization algorithm on a cost function, for example the randomized benchmarking fidelity as done in [74, 75].

For fast high-fidelity control pulses, the higher levels of the transmon need to be taken into account. It is possible to achieve control pulses of length 10 ns – 20 ns, but due to the localization in time, those pulses will have frequency contributions at ω_{12} of the transmon, leading to leakage. Accordingly, the control pulses need to be designed with at least a qutrit in mind such that this leakage can be minimized. It was derived [76] and experimentally demonstrated [77] that this is possible with DRAG (derivative removal by adiabatic gate) pulses, where a Gaussian pulse is applied to one quadrature and the derivative of the Gaussian in the other (Figure 2.9). In Chapter 5, the DRAG parameter, the ratio between the Gaussian and derivative amplitudes is

varied to fix phase errors and it is not optimized for leakage.[6] Reference 78 shows how the phase error can be fixed with slight detunings from the qubit frequency, such that the DRAG parameter can be used as intended to minimize leakage.

For transmon qubits we make use of the SQUID loop as a frequency control knob. The experiments in Chapter 5 and Chapter 6 only use static bias currents to adjust the frequencies of the qubits. However, it can be used to implement rotations around the z axis, or to bring the qubit (or higher transitions of the transmon) on resonance with microwave resonators or other qubits. This is one common way to implement two-qubit gates [25].

2.3.4 *Qubit performance metrics*

The quest for a viable quantum information processing technology has expanded the metrics for quantum bits in recent years. While qubit coherence times were very short compared to the time of operations, the qubit relaxation time and coherence time were the most important metrics for qubit performance. For our qubits, we generally find qubit relaxation times T_1 in the range of 10 μs $-$ 30 μs and qubit dephasing times $T_{2,\text{echo}}$ (with a single symmetric Hahn-echo pulse [79]) on the order of T_1 at the qubit's flux sweetspot. $T_{2,\text{echo}}$ is usually the more important metric than T_2^*, the dephasing time without any echo pulses, because dynamical decoupling techniques [80] can be used to eliminate slowly varying noise on the qubit frequency for most applications. The transmon qubits with SQUID loops are subject to flux noise, which is relatively slowly varying as well as charge-parity fluctuations due to quasiparticles [81] which happen on a millisecond timescale.

With the focus on error correction, fidelity of operations on the qubits and the single-shot readout fidelity became the most important numbers. They depend on the coherence time but also on how fast operations (or readout) on the qubits can be performed and how much additional noise is added by the operations. Improving In Chapter 5, randomized benchmarking [82] (RB) is performed to access the underlying gate fidelities excluding errors in the qubit initialization and measurements. Essentially RB aims at testing the self consistency of a set of gates that forms a mathematical group, in general the Clifford group, but other groups can be chosen [83]. The properties of a mathematical group are that the combined action of sequences of gates is within the group and that every group element has an inverse that is also part of the group. Random sequences of gates of different length are performed, followed by a final gate that inverts the combined action of the previous ones. Thus, ideally the system remains in the starting state. Due to gate errors, the system, averaged over many different random gate-sequences, approaches a completely mixed state for long random gate sequences. The gate fidelity can be inferred from fitting an exponential curve to the decay to a mixed state, providing a simple way to extract a gate fidelity.

[6] We still observe low leakage per gate but could have likely achieved better results.

More refined techniques to access gate fidelities have been proposed and implemented. Examples are gate set tomography [84], as demonstrated in [75] on a transmon qubit, and purity benchmarking [85] to distinguish coherent and incoherent errors. All of these techniques rely on checking if the qubit gates behave self-consistently and varying the number of gates until the qubit state is randomized.

In Chapter 6, we perform quantum state tomography [86], to reconstruct the density matrix from readout outcomes in different bases. Checking whether target states can be prepared with high fidelity is another way to assess performance, but care needs to be taken to avoid state-preparation and measurement (SPAM) errors, which can skew the tomography result. We also show that our model accurately predicts the system's behavior in the qubit subspace, another consistency check.

2.4 OTHER SUPERCONDUCTING QUBITS

While the transmon is currently the most popular superconducting qubit, there is competition that is worth mentioning. A review of the field up to the arrival of the transmon can be found in [87]. Since then, only a few qubit types have remained competitive for building quantum processors. With the exception of the D-Wave quantum processors, which operate within the quantum annealing paradigm and not in a circuit model of universal quantum computers, the most complicated superconducting quantum processors have been transmon based.

The flux qubit [88, 89] has been produced in great quantities for D-Wave quantum annealers. Processors with nominally up to 2048 qubits have been made, and even in the face of imperfect yield, they have demonstrated experiments involving hundreds of qubits [90, 91]. Signatures of coherence have been shown in many-qubit contexts, but the D-Wave flux qubits only show coherence times on the order of ~ 10 ns. However, an upgraded version of the flux qubit shunted with a large capacitor [92, 93] has recently matched transmon qubit performance for a single qubit [57]. It generally has a larger relative anharmonicity than a transmon and it will be interesting to see how it performs in a multi-qubit context.

The fluxonium qubit [94] is a qubit that has a significantly larger anharmonicity than a transmon and it is insensitive to charge offsets. Fluxonium qubits have shown record T_1 of several milliseconds for superconducting circuits [95, 96], but coherence times, gate and readout fidelities have not yet matched transmon overall performance. An honorable mention goes to the 0-π qubit [97]. It is a fascinating proposal promising great coherence times [98] but it has yet to be realized.

2.5 TRANSMON ARCHITECTURES

The transmon qubit might ultimately not be the best qubit at any one thing, but its simplicity and promising overall performance makes it a good choice to build larger processors. With transmon qubits and resonators as the main building blocks,

there are still many possible choices for quantum processor architectures. The transmon community is currently exploring them and so far there is no convergence to an optimum. Qubits can have dedicated or shared readout resonators and a longitudinal qubit-resonator interaction has been proposed in order to eliminate the Purcell effect [99] with different ways to realize it in a circuit have being explored theoretically [100].

Coupling the qubits to achieve reliable multi-qubit gates is at the heart of building powerful quantum processors. The pioneering work on coupling two transmon qubits used a resonator to mediate the interaction [101]. However, the first entanglement shown with superconducting qubits used phase qubits with direct capacitive coupling [102]. Direct capacitive coupling of transmons was subsequently used to achieve two-qubit gates at the surface code threshold [103]. Additionally, more complicated tunable couplers have been explored [104, 105], such as the one we demonstrated in [51]. In our realization, different coupling regimes (longitudinal and transverse coupling in the qubit subspace) can be achieved. While the current capacitive coupling is transverse, circuits for longitudinal coupling have been proposed as a more scalable scheme for large lattices [106, 107].

For two-qubit gates, there are all-microwave schemes [108] and schemes using lower frequency pulses changing the flux through the SQUID loop [25]. Periodically modulating SQUID loop flux with higher frequencies has also been explored. Two-qubit gates can be realized both by modulating tuneable couplers [105, 109, 110] or modulating the qubit frequency [111]. With these techniques it is also possible to use a transmon to encode qubits in multiple coupled resonators [112]. The exploration of the vast space of possible circuits and ways to drive them will keep superconducting qubits an interesting field of research for years to come.

Ultimately, one might redesign circuit elements specifically for error correction and maybe the best qubits for that will not be transmon qubits. The fact that superconducting circuits offer so much flexibility in designing Hamiltonians for a purpose makes them an outstanding platform for building quantum computers. However, the transmon will likely be the workhorse for the first experiments that demonstrate genuine quantum advantages and fault-tolerant medium-scale quantum processors.

DESIGN AND FABRICATION OF TRANSMON PROCESSORS 3

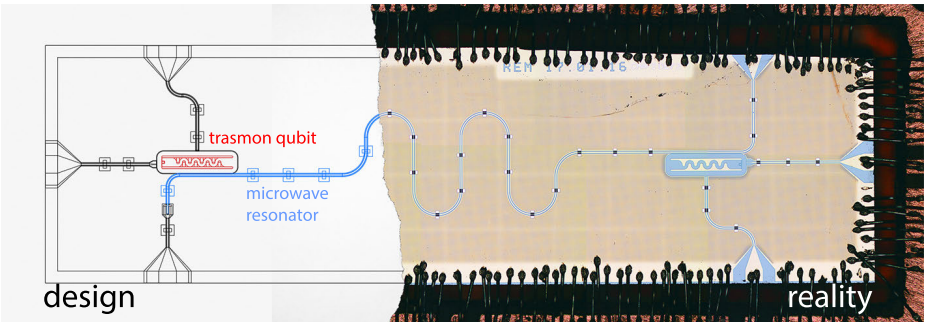

While Chapter 2 was concerned with the system on an abstract Hamiltonian level, here the details of designing a chip that realizes the Hamiltonian will be discussed. In addition, the fabrication and packaging which are essential for the performance will be described.

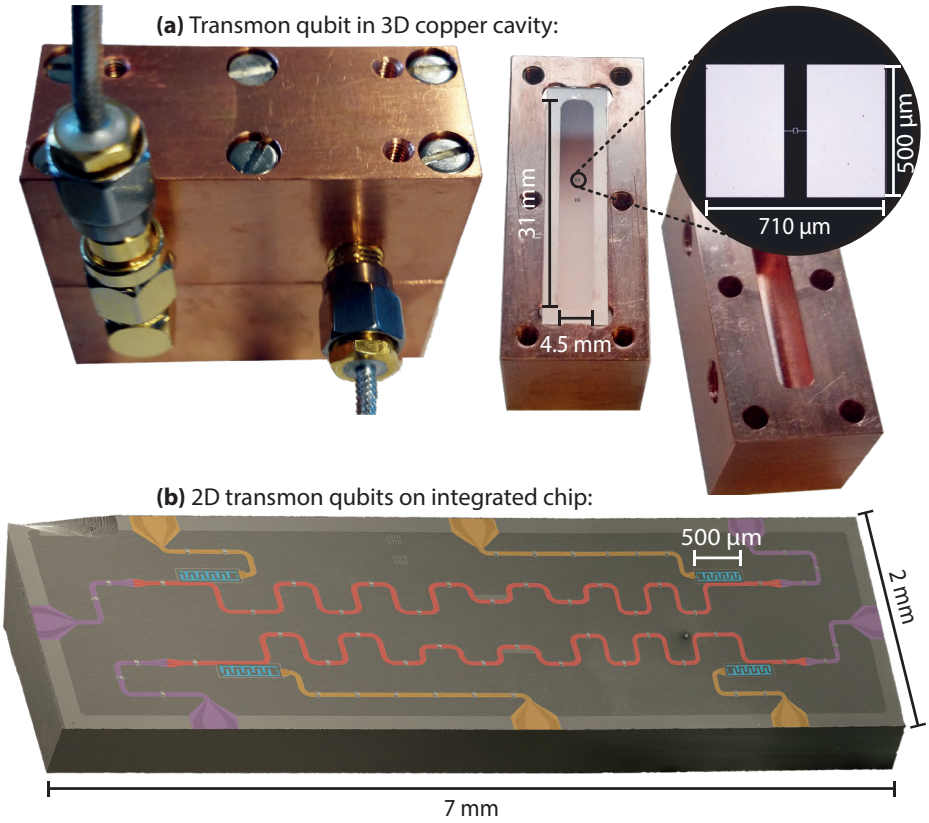

Figure 3.1: *Pictures and micrographs of 3D cavities and planar cQED chips with transmons comparing the sizes.* ***(a)*** *3D cavity closed with connectors to deliver signals and open with inset showing the magnified qubit on the saphire chip resting in the cavity.* ***(b)*** *2D chip with four qubits (blue) and two microwave resonators (red). Flux-bias lines for each qubit (yellow) can be used to change the flux through the qubit SQUID loops. Microwave lines couple to the two ends of each resonator (violet).*

3.1 2D AND 3D TRANSMONS

The publications that became part of this thesis, only deal with planar cQED transmons devices, but my initial experiments were conducted with transmons in 3D cavities, building on previous work in the group. The 3D cavities can be made of aluminum [113] or copper [114]. In those architectures, transmon qubits are fabricated on chips that are placed within the cavity. In planar cQED chips, the resonators are integrated on the same chip as the transmons, as done in the very first transmon experiments [115, 116].

In Figure 3.1, example pictures from my experiments are shown. The difference in lengthscales is evident, as the 3D cavities vastly exceed the size of a single 2D chip that can contain multiple qubits and cavities even when taking into account connectors and PCBs. The advantage of the larger 3D designs is that increased

Table 3.1: *Qubit performance for different attempts of the entanglement experiment (Chapter 6). The first attempt had aluminum qubits on sapphire in 3D cavities. The second attempt had the two resonators and qubits on the same chip, sample can be seen in Figure 3.1. The last attempt had the worst qubit coherence times but the more important transient matching for the experiment was better. Results of the experiment are reported on in Chapter 6. All coherence times are reported at* f_{max}

Qubit	f_{max}	T_1	$T_{2,echo}$
3D transmons			
Q_1	5.128 GHz	27 μs	34 μs
Q_2	5.165 GHz	38 μs	32 μs
2D transmons on same chip			
Q_1	5.791 GHz	26 μs	24 μs
Q_2	5.817 GHz	27 μs	20 μs
2D transmons on different chips			
Q_1	5.230 GHz	18 μs	27 μs
Q_2	5.240 GHz	9 μs	15 μs

mode-volume leads to reduced electric field strength which means lower coupling to and therefore lower influence from the dielectric losses of the surrounding materials. Increasing the mode volume - making the qubit capacitors bigger - is also beneficial on chip until radiation loss due to the now larger structures become a comparable limiting factor.

The underlying motivation to use 2D transmons in the experiments was that on-chip flux-bias lines are a promising route to fast two-qubit gates [25]. If there are multiple qubits they also allow for easier individual control of the flux through the SQUID loops. In addition, the quality factors of on-chip resonators ($Q \approx 10^6$ [117]) were exceeding the intrinsic quality factors we achieved with copper cavities ($Q \approx 10^4$), 3D cavities that allowed for slow tuneability with SQUID devices. In fact, in our group, several 2D samples with qubits that match the performance of 3D qubits in copper cavities have been fabricated, for example in [49]. However, the $T_1 > 100$ μs [41] that have been achieved for qubits in aluminum 3D cavities could not be reproduced in 2D in our group.

In the meantime, 3D transmon architectures are capitalizing on the high intrinsic quality factors ($Q \approx 10^9$) of superconducting cavities, using them to become the information carriers. The non-linearity provided by transmon qubits is only used to manipulate cavity states [118]. Encoding qubits in the cavities [119] has since shown quantum error correction at the break-even point for a quantum memory, meaning that the encoded qubit has a longer lifetime than any of the components [120]. The 3D approach represents an alternative to the current race to monolithic small-scale realizations of surface code with transmon qubits. One of the most interesting open questions will be which quantum hardware will be most scalable.

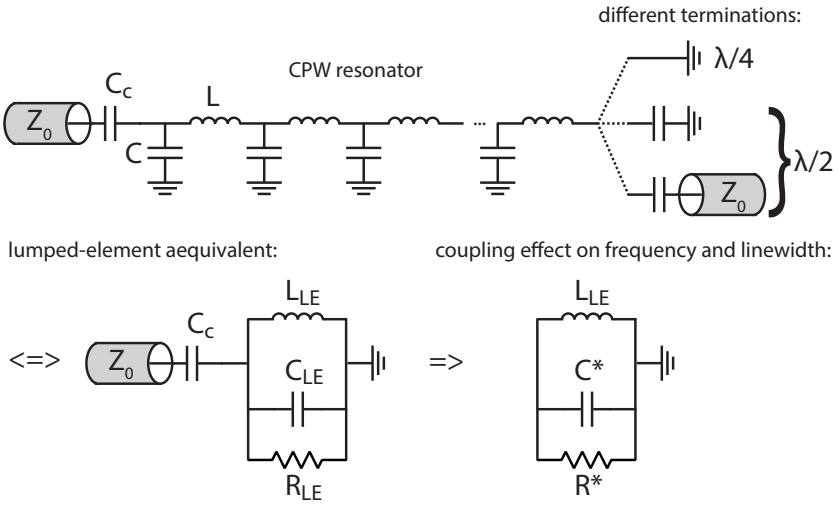

Figure 3.2: *Circuit diagram of a CPW resonator capacitively coupled to an environment with impedance Z_0. The resonator can be terminated in different ways: shorted to ground on one end to become a $\lambda/4$-resonator, it can be open with a different ground capacitance at the end, or it can have another capacitively coupled port. Close to resonance the circuit can be replaced with an equivalent RLC circuit from the point of view of the coupled transmission line. For coupling to the qubit, the position of the coupler with respect to the end of the CPW resonator needs to be taken into account, because the voltage fluctuations are naturally strongest at the open end and disappear at nodes. From the point of view of the resonator, the capacitive coupling to a line with impedance Z_0 can be absorbed into the resistance and capacitance of the RLC circuit.*

3.2 COPLANAR WAVEGUIDE RESONATORS

In Chapter 2, we assumed to have a harmonic oscillator that couples to the qubit, but there are different ways of realizing harmonic oscillators in practice. The 3D cavities mentioned above can be realized in different geometries, for example rectangular boxes or stub cavities. On-chip resonators can be made either in lumped-element form, connecting an on-chip capacitor to an on-chip inductor, or as coplanar waveguide resonators (CPWs), essentially an on-chip coaxial cable that has a standing wave corresponding to its length. In this work only CPW resonators were used, partially because their linear nature is practical when using them to connect different elements on a chip, for example transmons. A good introduction for CPWs for cQED can be found in [121].

As illustrated in Figure 3.2, there is a center conductor with an inductance per unit length and a capacitance to ground per unit length. In addition to the geometric inductance, we have to take into account the kinetic inductance because the thin superconducting films we use have a low charge-carrier density. Therefore, the few charge carriers need to be accelerated more, giving rise to an additional inductance related to the charge carrier inertia. The kinetic inductance contribution is influenced

by the film thickness and the material properties, but it can be estimated from the room temperature resistivity of the film, which is related to the charge-carrier density in the normal state.

Thus, a CPW resonator has a phase velocity $v_{ph} = 1/\sqrt{\mathcal{C}_g(\mathcal{L}_g+\mathcal{L}_k)}$ depending on the kinetic inductance per unit length $\mathcal{L}_k$ and the geometric capacitance and inductance per unit length $\mathcal{C}_g$ and $\mathcal{L}_g$. The CPW can be terminated in different ways, either with a short to ground or an open end or capacitively coupling to another CPW (Figure 3.2). Depending on whether the termination is a short or an open, there is a phase jump or not. Thus, a resonator with two open ends will be a $\lambda/2$ resonator and a resonator with one open and one short end will be a $\lambda/4$ resonator. The phase velocity, together with the length L of the resonator gives the resonance frequency:

$$\omega_0 = \begin{cases} 2\pi v_{ph}/2L, & \lambda/2 \\ 2\pi v_{ph}/4L, & \lambda/4. \end{cases} \tag{3.1}$$

The phase velocity can be estimated by making resonators of different length. Once the phase velocity is known, it can be used to precisely target the frequencies of resonators. We can usually get within $\sim$ 50 MHz of the target value and are mainly limited by the strong dependence of the kinetic inductance contribution on film thickness. The cables we use to couple to the chips are standard 50 Ω cables. For the input and output of microwave signals, we impedance match the on-chip lines to 50 Ω as well. The characteristic impedance is also a function of the capacitance and inductance per unit length: $Z_0 = \sqrt{(\mathcal{L}_g+\mathcal{L}_k)/\mathcal{C}_g}$. To target both the phase velocity and impedance precisely, we need to estimate the kinetic inductance contribution and we need to know the dielectric constant of silicon at cold temperatures.

Resonators do not necessarily have to be at the same impedance, because the coupling to the in and output lines, be it capacitive or inductive, represents an impedance mismatch anyway. However, the coupling, if capacitive, introduces some extra capacitance such that the resonance frequency will be reduced. Capacitive coupling to the qubits also changes the resonator capacitance (and the qubit capacitance), thus making a resonator with a specific coupling the coupler needs to be taken into account. One solution is to simulate the entire resonator including the coupling and adjusting the parameters until the simulated resonator has the right properties.

A more common technique is to simplify the circuit, replacing the resonator with a lumped element resonator of the same frequency[1] and impedance (see Figure 3.2) as explained in detail in [121]. This gives two equations with two unknowns, the inductance L_{LE} and capacitance C_{LE} of the lumped element resonator. On resonance, this approximates the CPW resonator closely, but the resonances at higher multiples of the wavelength are neglected. A resistance R_{LE} in parallel to

[1] Usually the fundamental frequency, but it would also work for higher modes.

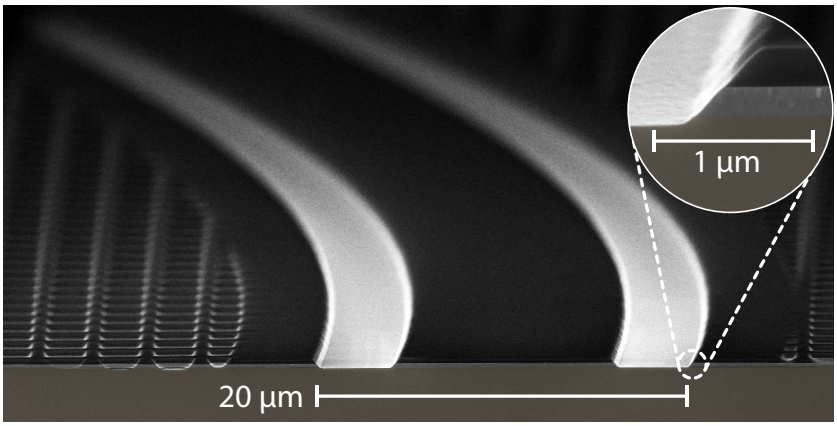

Figure 3.3: *False-color SEM picture of a CPW resonator cross-section. The chip was cleaved to investigate feature etching. For this picture the resist defining the etch was not removed. Nonetheless the figure gives a clear sense of the real CPW dimensions and the etch profile will probabaly weakly influence the CPW properties. The profile can be changed by varying the plasma acceleration voltage and composition. It weakly depends on the size of the resist-free area that will be etched.*

the inductance and capacitance is added to make loss part of the model for the resonator, giving it a finite linewidth. From the point of view of resonator photons, the coupled circuit with a capacitor and a line of impedance Z_0 can be rewritten, absorbing the additional capacitance and the loss channel into the capacitance C^* and resistance R^*. The resonance frequency and linewidth can be calculated from the values of L_{LE}, C^* and R^*. These series-parallel transformations and approximations are important tricks to simplify circuits and develop simple models to design chips to specifications.

3.3 FEEDLINES, FLUX-BIAS LINES AND DRIVE LINES

We do not only use CPW resonators, but also CPW lines on chip. In order to control the transmon we make use of two different tuning knobs. There is a flux-bias line that can control the flux through a squid-loop by applying a current through an on-chip line. In addition, drive pulses to the qubit can be applied through a microwave line with capacitive coupling. These lines are 50 Ω CPWs, in order to avoid reflections and resonances due to impedance mismatches. Similarly, the lines carrying the readout signals are 50 Ω CPWs that capacitively couple to the readout resonators.

3.4 FROM HAMILTONIAN TO A CIRCUIT TO A CHIP LAYOUT

In the beginning of designing a quantum experiment, there is the target Hamiltonian with certain parameters that the experimentalist can control. It is chosen to observe

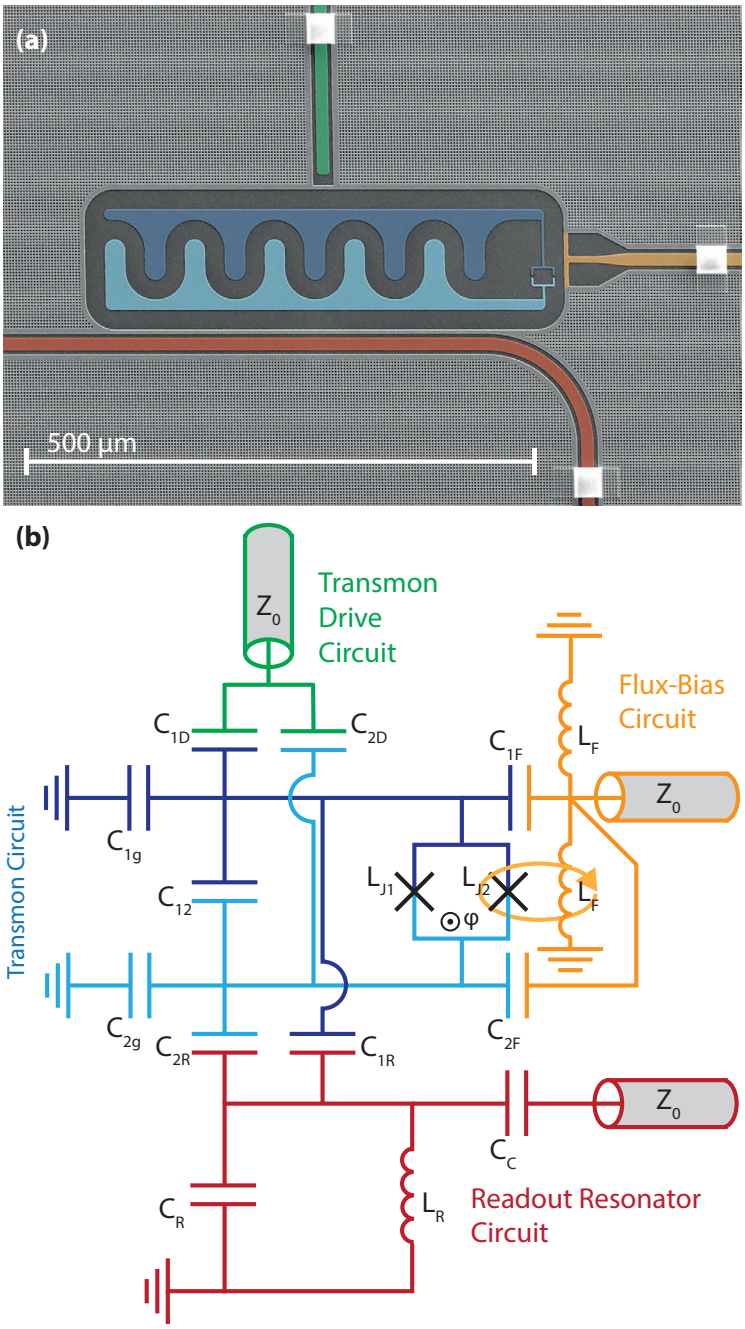

Figure 3.4: *(a) Scanning electron micrograph of the transmon on the chip. False color indicates the transmon islands (blue and cyan), the microwave drive line (green), the flux bias line (yellow) and the CPW readout resonator (red). Airbridge crossovers and a thin ground plane strip in the coupling section realize a connected groundplane around the transmon. (b) The full circuit diagram for the transmon with additional circuits for microwave driving, flux biasing and readout through a resonator. For design, the capacitance matrix can be simulated with electrostatics simulation software. Most circuit parameters can be derived from it.*

an interesting effect or to build a quantum processor. The latter case requires enough parameters for qubit control. Circuit quantization techniques can be used to find the Hamiltonian for a given circuit, but we usually are interested in the reverse first.

Most design is done at the level of circuit diagrams, but translating a circuit into a chip layout introduces many additional degrees of freedom. Thus, rules of thumb and intuition play a role in creating circuit layouts. It also leads to conservative designs, which share features with previously working ones. The conservative approach is the reason why the devices I have worked are so similar to previous chips of the DiCarlo group and the Yale group, with the interdigitated transmon capacitor shown in Figure 3.4 **(a)**. We did however start rounding the edges, which is supposed to avoid strong fields that would arise from convex corners.

There are expensive software tools to take a drawing of metal islands on chip and get the capacitance matrix or even the high-frequency behavior. We usually use a 3D electrostatics solver to take a parameterized model of metal plates on silicon similar to the device in Figure 3.4 **(a)** and use it to extract the capacitances in our circuit [Figure 3.4 **(b)**]. Using these capacitances, the inductances and the Josephson energies of the junctions, we can use circuit quantization techniques to arrive at the Hamiltonian and then iteratively try to realize the system that we want. As experiments become more sophisticated, approximations such as neglecting the effect of a coupling capacitor on the transmon qubit or the CPW resonator have to be dropped. Eventually even the capacitance of airbridge crossovers on CPW resonators might have to be taken into account.

3.5 2D TRANSMON FABRICATION PROCESS

The planar or 2D transmon fabrication is done in several steps using standard micro- and nano-fabricaton techniques. In this section, I will describe the fabrication process, point out guiding principles and mention possible ways to improve in the future. A schematic summary of the fabrication process can be found in Figure 3.5, but in the following I will give more details for the different steps and explain some of the fabrication choices made for our chips.

3.5.1 *Choosing the substrate*

Fabrication starts with an empty wafer which is usually made of undoped silicon or sapphire. In our group, initial experiments used sapphire chips [122–125], but we switched to silicon substrates which are used for all experiments in this thesis. In choosing between silicon and sapphire, one needs to consider several factors. Generally, undoped substrates are preferred, as dopants can lead to a more noisy charge environment. In case of undoped silicon, that can mean that the wafers and dies are brittle and prone to breaking in different stages in the process. Sapphire chips are less prone to break. While both substrates are good insulators at cryogenic temperatures, silicon is more conductive at room temperature. This means that electron-beam

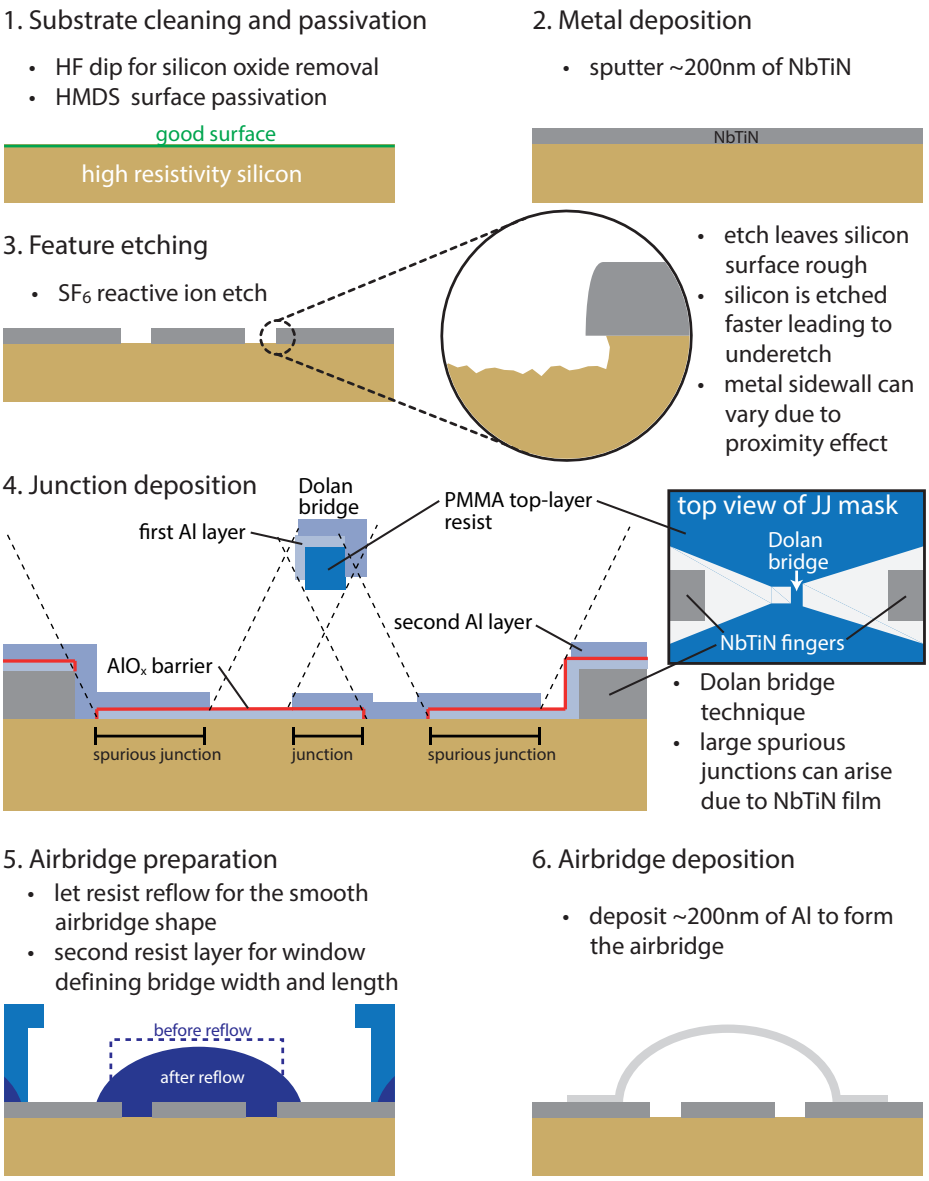

Figure 3.5: *Schematic of the fabrication process. There are 4 electron beam lithography steps: one for the definition of the base-layer features, one for the definition of the Josephson junctions and two for the airbridge crossovers. Only the Josephson junctions require nanometer precision, the other steps could in principle be done with optical lithography.*

writing and scanning-electron micrographs that are taken for diagnostic purposes can leave parts of sapphire chips charged or even lead to electrostatic explosions. More importantly, sapphire wafers are more expensive and not available in sizes above 4 inches, making silicon more promising for large-scale fabrication. Additionally, the silicon can be etched, which opens additional options for 3D fabrication and scalability.

For our group, the switch to silicon was mostly motivated by improved CPW resonators using surface cleaning techniques and the ability to etch into the substrate [117]. CPW resonators with trenches such that the electric field is stored in vacuum were a first step. Afterwards the etching was used to create through-the-silicon vias [35], that can provide control lines from the bottom of the chip and improve the grounding. Thus we invested in the silicon process as a group and therefore even devices that did not make use of the etching were fabricated on silicon.

The cleaning procedure for the silicon wafer is a dip into diluted hydrofluoric (HF) acid to remove the native silicon oxide that forms on the surface, followed by a surface passivation with hexamethyldisilazane (HMDS) [117]. For the passivation, the wafer is placed on a hot plate at 110°C for 2 minutes and exposed to an HMDS-nitrogen atmosphere. HMDS is generally used to improve resist adhesion, but the hope is that it will form an ordered stable monolayer on the silicon surface preventing the formation of disordered dangling bonds. However, the HF dip should technically also lead to an H-terminated silicon surface where the HMDS monolayer might not form, still the HMDS might also avoid the accumulation of water between the passivation step and the metal deposition. In order to keep surface oxydation minimal, we try to minimize sample exposure to air between the cleaning step and the metal deposition.

3.5.2 *The superconducting base layer and feature etching*

Most cQED processors do not have multiple layers, as dielectrics that can be deposited on-chip are usually lossy and can show increased levels of charge noise. Future processors with higher density could instead use flip-chip technology [126] to achieve devices with multiple layers and higher connectivity. All devices in this thesis have a single layer of superconducting thin film in which all features are etched.

Similar to the substrate, there are several choices for the superconducting thin film used to make the cQED processors. Relaxation times $T_1 > 20$ μs have been achieved with aluminum [127], niobium [128], TiN [129] and NbTiN [69]. For the samples in this thesis, we used of NbTiN film deposited by sputtering [130] (300 nm for the sample in Chapter 5 and 200 nm for the sample in Chapter 6).

Immediately after the substrate preparation mentioned above, a superconducting base layer is deposited everywhere on the wafer to optimize film quality and the substrate-metal interface. The high-quality substrates usually have an electrically

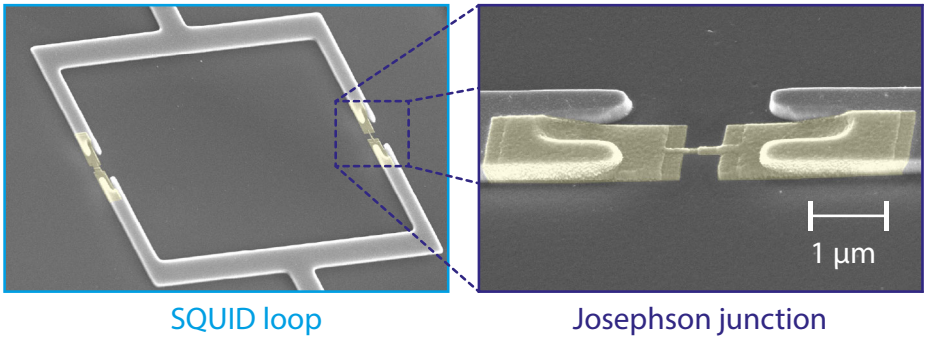

Figure 3.6: *False-color SEM images of the squid loop (20µmx15µm inner dimensions) and zoom in on the Josephson junction. This is an asymmetric SQUID. A close look reveals that the two Josephson junctions have very different overlap areas. Figure adapted from [49].*

quiet bulk, thus most of the electrical noise comes from defects and adsorbents at the interfaces. The substrate-metal interface is the most critical interface, because it has the highest participation ratio due to the high field strength there. Etching the features into the film instead of using a lift-off procedure has two main advantages: No resist is introduced when the critical substrate-metal interface is formed and the sidewalls of the superconducting films are well behaved.

Features are etched into the wafer with a reactive ion etch. In the course of this work I tried both a SF_6 etch and a CF_4 etch. Here, the choice of silicon as a substrate lead to complications, as the etch is not selective to the superconductor, leading to a rough silicon surface and possible underetch (see Figure 3.5). Thus, the etch stop is essential. A set of qubits fabricated with the CF_4 etch showed reduced coherence even though the surface roughness was visibly reduced. However, we did not thoroughly investigate this but instead focused on optimizing the SF_6 etch. During the etching, a laser is used to monitor the progress. As soon as the metal layer is etched through, the reflected laser power is reduced. We managed to develop a process that keeps the underetch small and surface roughness tolerable while making sure that all NbTiN is removed.

3.5.3 *Josephson Junction fabrication*

The Josephson junctions are the only truly nano-scale objects on our chips. We relied on the workhorse Al-AlO_x-Al Josephson junctions made by double-angle evaporation and using the Dolan bridge technique [131]. The concept is illustrated in step 3 of Figure 3.5. We use a 570 nm PMGI layer as a spacer, which is removed below the junction area and a 150 nm PMMA layer that will form the Dolan bridge. PMGI (Polymethylglutarimide) and PMMA (Polymethylmethacrylaat) are different polymers which form the two-layer mask for the evaporation and their different reaction to electron-beam exposure and the different developers make the bridge process possible.

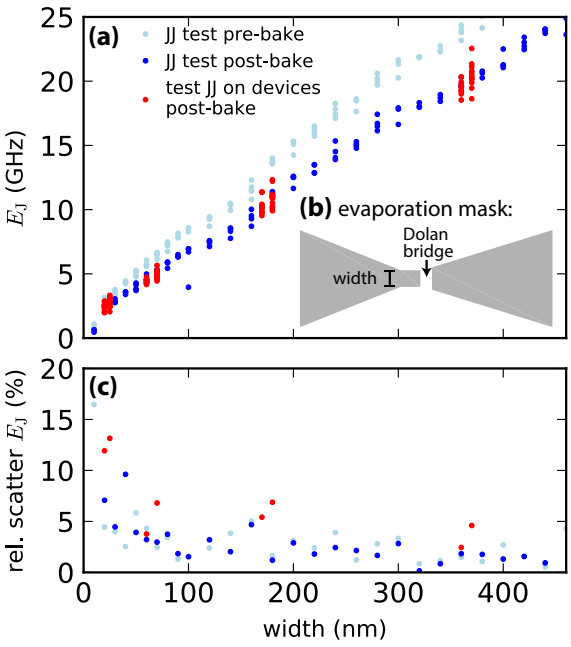

Figure 3.7: ***(a)*** *E_J values based on room-temperature resistances of a Josephson junction test before the bake necessitated by the airbridge step (light blue) and after (dark blue). E_Js measured on the test-junction arrays of final devices made in a subsequent evaporation show good agreement.* ***(b)*** *Birds-eye view of the junction evaporation mask. On both ends, contact to the NbTiN is made. The first evaporation comes in under a slight angle from right to left, the second from left to right.* ***(c)*** *Relative scatter of the E_J values at each junction width. Scatter is bigger for the final devices due to the bigger overall writing area. Generally, statistical fluctuations are $\sim$ 5%, but below 100 nm the junctions are less reliable.*

Before the aluminum evaporation we perform an oxygen plasma and an HF-dip to clean the exposed silicon surface and ensure good contact to the NbTiN fingers of the SQUID loop. An under-etch into the silicon can become a problem at this point, because it can lead to contacting problems between the NbTiN base layer and the aluminum. We therefore etched a bay into the NbTiN fingers where the Al layers make contact hoping to have less underetch and a more gently sloped contact area as well as to simply increase the contact area (see Figure 3.6). In the double-angle evaporation, we use $\pm 11.5^\circ$ angles for the two evaporations. After the first evaporation (30 nm of aluminum), an oxidation step (8 minutes at 0.5mBar) creates the thin AlO_x barrier. After the oxidation, we evaporate the second layer of aluminum (50 nm) without exposing the sample to air in between. Before exposing the sample, we controllably grow the first AlO_x layer on the second aluminum layer (8 minutes at 0.5mBar). Long lift-off times and mixing of the NMP liftoff-solvent with water are avoided, as the aluminum on chip is easily attacked, resulting in open junctions.

A critical advantage of the Al-AlO_x-Al Josephson junction technology is that the Ambegaokar-Baratoff formula [132] holds, which allows associating the room temperature resistance R_N with the Josephson energy for a known superconducting gap Δ_{Al} $E_J = \hbar\Delta_{Al}/(8e^2 R_N) \approx 140.3\,\mathrm{GHz/k\Omega}\cdot 1/R_N$. Thus, junctions can be tested with a room-temperature resistance measurement, which allows estimating the Josephson

energy. It also allows making junction tests, sweeping the width of the area where the two aluminum layers overlap in order to target qubit frequencies. On the bottom end this area is limited by lithographic precision and the grain size of aluminum, while on the top end it is eventually limited by the stability of the Dolan bridge.

A typical junction test curve is given in Figure 3.7. The junction step requires a flat chip for reliable resist spinning, therefore it has to precede the airbridge step. The airbridge step explained in the next section requires heating the chips to reflow the resist. This bake influences the junctions (see Figure 3.7), likely reordering the thin AlO_x layer or leading to further oxygen incorporation, it usually results in an increased resistance. Thus, for good targeting, the junction tests need to undergo the same processing as the final device to anticipate the effect. As Figure 3.7**(b)** shows, the baking alters the junctions but does not significantly increase the statistical fluctuations. As reported in [133], the bake also seems to reduce junction aging, a slow increase in resistance over time that is often observed.

Shorted or open junctions are not included in the figure. In this test 14 out of 120 junctions were either shorted (in case of large junctions) or open (mainly the smallest junctions). In the most relevant 30 nm – 350 nm regime, we find a yield of $\sim 95\%$. Based on the test, junction width for the final devices were chosen. Test junctions on the final devices allow consistency checks between evaporations. In this data set, test and final devices are relatively consistent, however, on different occasions we found systematic differences of up to 5% between subsequent evaporations. Data are not included here but around 500 nm bridge width our particular junction recipe becomes unstable.

Current $\sim 5\%$ statistical and systematic fabrication fluctuations in E_J are a major bottleneck for making more complex cQED devices. They translate into frequency uncertainties of ~ 100 MHz, which lead to $\sim 10\%$ errors in usual detunings between transmons and resonators for readout and coupling. The same-frequency transmons for our hardware-saving scheme in Chapter 5 and the symmetry engineering for entanglement experiments in Chapter 6 are both made difficult by junction fabrication. SQUID-tunable transmons allow for about 100 MHz of tunability without compromising coherence times too much for fairly symmetric SQUID loops. With large asymmetries, more than 300 MHz of tunability with fairly constant coherence has been achieved [48], but the fabrication parameters would have to be adapted to allow for large differences in junctions, probably using different mask layouts for the small and large junctions. For large-scale devices, junction yield could also become a problem. Josephson junction fabrication issues can be mediated in a modular architecture as many modules can be fabricated and selected based on the room-temperature resistances.

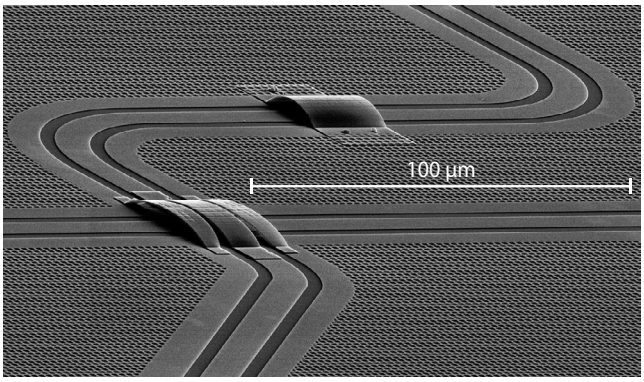

Figure 3.8: *Airbridges can be used as crossovers or to connect ground planes for better microwave hygiene.*

3.5.4 *Airbridge crossovers*

An important part of creating a quiet environment for the qubits is to provide a stable ground plane on chip. Otherwise, additional modes between the different ground plane islands on the chip can couple to the resonators and transmons as well as to the lossy environment and reduce performance. Initially, this problem was solved with on-chip wirebonds across the CPWs [25], but using resist reflow techniques, it is possible to define airbridge crossovers [125]. For the airbridges, a PMGI/PMMA resist stack is used. The reflow requires a 5 minute bake at 220°C, which affects the Josephson junction resistances. Before evaporating 450 nm of aluminum, an oxygen plasma and an HF dip are performed for good contact to the NbTiN base layer. As seen in Figure 3.8, the airbridges can form simple ground crossover or even crossings between CPWs, which can be necessary for connectivity reasons.

For larger chips, additional through the wafer vias and a ground plane on the back of the chip can be used to break the cavity modes inside the dielectric which tend to lower frequencies as the chip sizes grow [35]. Eventually vias can also be used to route microwave signals to the chip from below, as there is ultimately no scalable way to bring in all connections from the sides. However, the chips used for the experiments during my PhD did not have through the wafer vias, yet.

3.6 PACKAGING AND FILTERING

In addition to the effects on the devices themselves, the quantum processors are sensitive to the packaging and to the filtering of the incoming lines. To give some examples: The sample used in [125] has reported T_1 times of 6 μs − 13 μs and $T_{2,\text{echo}}$ times of 3 μs − 13 μs in the corresponding paper. However, later cooldowns with improved radiation shielding and reduced noise in the driving circuit[2] showed T_1 times of 12 μs − 20 μs and $T_{2,\text{echo}}$ times of 13 μs − 19 μs. In the later cooldowns,

[2] In the experiment a microwave amplifier was used to reach the high powers for fast single-qubit gates. But the amplifier was creating photon shot noise reducing the coherence time. Once understood, this problem was solved by adding a stub filter that reduces the noise at the resonator frequencies in later cooldowns.

qubit frequencies were reduced by ~ 70 MHz due to device aging, not enough to account for the T_1 improvements. Similarly, the devices of Chapter 6 were cooled down in two different fridges. An initial cooldown with samples in aluminum boxes directly attached to the mixing chamber showed $T_1 = 10$ μs for the entanglement qubit of device 1. Later cooldowns in another dilution refrigerator with the layers of shielding described below yielded the $T_1 = 18$ μs result reported in Chapter 6. The entanglement qubit of device 2 did not improve as much. $T_{2,\text{echo}}$ times almost doubled for both qubits. These examples show that performance is not necessarily limited by fabrication and design, packaging and filtering are very important as well.

The first goal of the packaging is to create an environment for the chip that is devoid of lossy modes that the transmon or the resonators can couple to via their dipole moment. An important constraint is that the chip needs to be able to thermalize and ideally reach a temperature limited by the dilution refrigerator it is placed in. Therefore, the sample PCB ideally is attached to a piece of copper that is attached to the mixing chamber plate of the dilution refrigerator. For radiation shielding, ideally the higher temperature stages of the fridge have additional shields in order to avoid high-temperature radiation reaching the sample.

In order to minimize SQUID loop offsets and improve the properties of the superconductor, which can be compromised by magnetic fields, the sample is shielded against external magnetic fields. External fields are mainly the field of the earth, however, magnetic components close to the sample need to be avoided as well. Connectors on the PCB that are in close proximity to the sample are especially ordered to not contain nickel. Microwave circulators that use ferromagnets to provide the directionality are enclosed in magnetic shields themselves. The magnetic shields we use are two layers of Cryophy, a ferromagnetic material that is demagnetized that guides the magnetic fieldlines away from the inside of the enclosure due to its large magnetic susceptibility. Cables enter these shields through tubes in order to avoid compromising the shielding. An inner aluminum box should expel the residual fields when it becomes superconducting.

The innermost box is again a radiation shield made of copper for good thermalization. It is coated with a mix of Stycast and silicon carbide powder with diameters between 15 μm and 1000 μm to better absorb radiation at different frequencies [134]. More subtle problems, such as cavity modes between the PCB, chip and cover, as well as cavity modes due to the shields are more difficult to explore and eliminate. Generally care is taken to keep spaces around the qubits small and surfaces superconducting if possible.

The filtering of the incoming lines is to ensure that the wanted coupling of the chip to the outside world, which eventually is at room temperature, does not introduce more noise than necessary. A good introduction to wiring dilution refrigerators for many-qubit experiments including the discussion of cables and the ratio of attenuation at each stage can be found in [135]. For each experiment reported in this thesis, the full wiring diagram is provided in chapters 5 and 6.

A natural complication arises because we want good microwave transmission of signals onto and especially coming from the cold plate of the dilution refrigerator to the detection chain. But good microwave transmission requires good conductors which in turn also conduct heat and would thermally connect the sample with the hotter stages of the refrigerator. There are two options to solve this problem: stainless steel cables which are relatively poor conductors and superconducting cables which are perfect conductors and incidentally poor conductors of heat. Generally, we chose stainless steel cables for input lines, where losses can be compensated by driving the system harder and superconducting cables between the 4 K and 20 mK stage for output lines. The cables are clamped to the different stages of the fridge to thermalize the outer conductor.

Attenuators on the input lines both at the 4 K and 20 mK stage of the fridge are put in to ensure that the thermal noise from room temperature is suppressed and the center conductor of the cable can thermalize to its stage via the resistor in the attenuator. We generally use 20 dB at 4 K and 30 dB at 20 mK. We also use home-made Eccosorb filters for infrared absorption to protect the sample from pair-breaking radiation coming down through the lines [136, 137]. Two varieties are produced, with more lossy ones used for flux-bias lines and less lossy ones used for microwave lines. We also use low-pass filters at cold temperatures. Many commercially available components work even at 20 mK, but they need to be tested. The total attenuation between room temperature and the mixing chamber plate is about 65 dB at 6 GHz when cable losses are included for our microwave lines. The role of the input attenuation for thermalization of the input lines has been reported to matter. To give two recent examples, [138] reports that adding additional 20dB attenuation at the mixing chamber stage improved the $T_{2,\text{echo}}$ of a capacitively shunted flux qubit to $\sim 2T_1$ and [139] uses home-made lossy band-pass cavities at the mixing chamber which thermalize better than commercial attenuators, achieving $T_{2,\text{echo}} \approx 2T_1$ even for a 3D transmon qubit with $T_1 > 100\mu$s. In both of these cases, the qubit coherence time was previously limited by residual thermal population in the readout cavity which was then reduced.

As the signal from the cold stage has to reach the room temperature electronics, the output lines cannot contain attenuation to suppress room-temperature noise. Instead, circulators are used, directional devices that within their bandwidth can be used to let the signal from the cold stage pass upwards, while the noise from above is dissipated in a 50 Ω termination. The circulators have ferromagnetic components to induce the directionality, therefore they have magnetic shields to prevent these magnetic fields from reaching our samples and they are placed outside the magnetic shielding of the sample if possible.

PROGRAMMING FOR THE QUANTUM COMPUTER

4

```
import time
from pycqed import quantum_processor

qp = quantum_processor.quantum_processor(
        initilize_default_setup=True)
qp.calibrate_qubits()
qubit1 = qp.qubit_list[0]

for i in range(10):
        time.sleep(60)
        qubit1.measure_T1(stepsize=2e-6, nsteps=50)

qp.execute_algorithm("algorithm.txt")
```

Caution: this chapter does not contain any physics insights. I want to comment on the software decisions we took in building a framework for the experiments in this thesis and the lessons I learned in contributing to this framework. A flexible framework for measurements is important for any experiments of a certain complexity, but scaling up our quantum processors also requires modularity and abstraction in the codebase such that experiments can build on previous work. I won't have the answer to the age-old question of building a scalable codebase for a complex hardware environment, but I want to share some caveats and some solutions we found during my PhD. A common theme of all the little tips for coding is to have the final result in mind from the start and to not just work on an implementation right away.

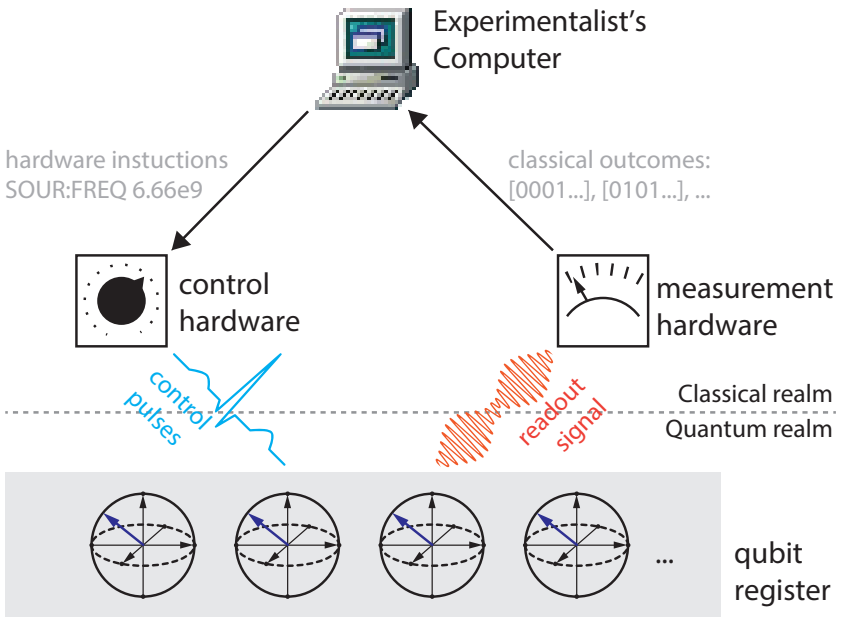

Figure 4.1: *A schematic of a quantum computer experiment.*

Building a quantum computer is different from performing usual physics experiments. In fact, many early qubit experiments were just fundamental research into quantum theory and not aimed at building scalable processors. Now that we wish to scale to more than a few qubits, things are changing:

In early qubit experiments people were building a system and trying to model its behavior. In the beginning, the noise plaguing different qubit types and the exact physics underlying their operation was not fully understood. Currently, several types of qubits are well enough understood that there are attempts to scale up, requiring the qubits to operate more and more like an "idealized" qubit that does not depend upon the implementation. This would then allow them to be more easily integrated into a specific 'computational model' (for the purpose of this article the computational model used is going to be the circuit model of quantum computing, but there are other models such as the adiabatic quantum computer (D-wave) or the one-way quantum computer). Matching the physical system to the model for increasing system sizes leads to a growing complexity in the tune-ups and calibrations required to make each qubit behave as expected. The physical systems where the quantum degrees of freedom reside all have parameters that need to be set, such that they will behave like a 'qubit register' of the computational model. Some of these parameters have to be tuned once, setting up the quantum information processor, but some have to be re-tuned regularly. These calibration processes must be automated, if we are to cross into the many-qubit regime.

The growing complexity in the quantum algorithms run on bigger quantum computer prototypes requires experimental physicists like me to spend our lives manually setting up the quantum computer to adapt. Not unlike the first classical computers that were programmed using reams of punch cards, we need to start setting up our experiments so that the input can be a representation of a quantum algorithm that a theorist develops. Then, we need software that converts the quantum algorithm into instructions for the experimental hardware. I will describe this in more detail below. The representation of a given quantum algorithm in gates is not unique. To squeeze the maximum coherence out of our qubits, we might want to 'decompose' the algorithm into the sequence of gates with the highest fidelity. Let's call the program that turns the abstract quantum algorithm into hardware instructions a quantum compiler. In order to perform these optimizations we will need flexible and powerful quantum compilers.

4.1 THE CHOICE OF PROGRAMMING LANGUAGE

When I started my PhD, experiments in our lab were performed using several programming languages and softwares for different purposes. LabView was used to interface with the hardware and perform the experiments providing live plotting and Igor Pro was used for analysis and visualization. In addition, a toolkit written in Mathematica was used to generate the most complicated parts of the experiments, the waveforms that are loaded into the AWG(s), which are at the heart of all time-domain experiments. Computer-aided chip design was done in python. This combination had grown organically, because different people had written different parts of the software and chosen their favorite language/environment to do it.

While building on an already existing framework is essential for performing more complicated experiments, we eventually decided to find one programming language to do everything. The benefits of having one programming language for everything outweighed the overhead of rewriting code for all the different functions. Firstly, it made it easier for people to join the group, requiring them to only learn one language. Secondly, it enabled writing scripts to combine measurements and analysis without having to interface different programming languages. Interfaces between different languages are fragile: small changes in the code or updates can break them, and they are more difficult to debug.

Data analysis is mostly about fitting and plotting data, which means that any good choice of language has to perform well in these tasks. Occasionally, however, complicated numerical models need to be fitted to experiment. In Chapter 6, we fit simulations with considerable runtime directly to experimental data. Therefore, the language of choice should also be a decent language for numerics.

We chose Python because it is a versatile language with an active user-base, it is easy to learn and easy to debug. It is an object-oriented language, which is very useful because hardware drivers are a main part of the experimental codebase and

they are almost archetypal examples of the usefulness of object oriented programming. We heavily relied on several packages that have made python into arguably the first choice language for physicists today: numpy and scipy for numerics [140], and matplotlib for plotting [141]. For fitting we used lmfit [142] and for plotting density matrices and some other quantum functionalities we used QuTiP [143].

4.2 HOW TO WRITE GOOD CODE AS A TEAM

Research groups are small teams and most experiments we tackle are getting too complicated for a single experimentalists. Therefore it is important to impose guidelines to collaboratively develop a good codebase. The personnel fluctuations in academic groups are high: master students stay less than a year, post docs stay two years on average, PhD students four years. Thus, the code needs to be learnable in about three months and not everyone will be a Donald Knuth.

Unfortunately, we also usually write our code with clear goals in mind, usually to finish an experiment. There is a delicate balance between getting things done and writing code that can scale up for the next experiment. From my experience, these are some important rules that help maintain this balance:

1. Use a version control system, in our case GIT. Thus the different setups in the lab can share the same software and important updates can be shared between experiments. The code can be branched off in case major updates are in progress that are not yet fully working. New code will have to be committed to the remote repository, which is a good point where rules can be enforced, especially the following two items. Unfortunately, this means that all team members need to be competent users of the version management system.

2. Implement unit testing as an automated way to test whether the code works. Thus, any new additions to the software that pass all of the tests usually have not straightforwardly broken any core functionality. The unit testing is most easily introduced while writing new code, because writing tests for already existing code is quite tedious. In addition, if done right, it can speed up new developments. Therefore, it is good practice to require new contributions to have unit tests, even though initially most team members (including me at the time) will object.

3. Enforce a coding style. Writing code together means adopting common standards. For python, PEP 8 is the standard style guideline and there are automatic tools such as autopep8 or linter, which will highlight violations or even fix them automatically.

4. Use descriptive and consistent variable names and **never** have hard-coded numbers in the code. Not everything has to be a function inside a function, but

variable names and function names are the most important form of documentation. If an expression just has a number in it that is not an integer, a constant or π, it will confuse people. The extra line of giving that number a descriptive variable name can make a huge difference for code readability.

5. If there is a widely used piece of code that only a small fraction of the group understands when they try to read it (in our case of about a dozen members, a small fraction would be about three people), it needs to be rewritten. A common wisdom is that code is read much more often than it is written — thus readability is extremely important. A formula can be difficult to grasp, but the flow and the connections in any piece of code have to be understandable. Treating code as a black box is good, code should be modular and we need to trust the input output behavior, but once we look inside the box it needs to be possible to understand the contents more quickly than one could rewrite it, otherwise it is bad code.

6. "Murder your darlings" is famous writing advice of contested origin. It holds for coding as well. Code needs to be constantly revised and rewritten. The true art of coding is probably about knowing when to start over and when to merely rewrite some parts. This process needs to be managed in a group to maintain a good working atmosphere.

7. Coding as a contribution to science needs to be respected. Of course coding it is merely a means to an end. Writing drivers is for example a tedious but very important task. Writing fast code for quantum state tomography on the other hand requires using the right optimization tools. Quantum simulations on classical computers require a good understanding of numerics. Often we just translate existing mathematics into new code. If these contributions are not respected, they will not be performed with the care they require.

4.3 DRIVERS AND SYNCHRONICITY

In order to control a quantum computer, we need drivers that control all the hardware. We only use a few different components in cQED: microwave sources, AWGs, current sources, and ADCs for readout. In addition, we use spectrum analyzers and vector network analyzers for high-quality measurements in the frequency domain and to digitally correct mixer imperfections.

The drivers are objects that store the current state of the different hardware in memory and have functions that send the proper strings to the hardware for communication (usually SCPI). For example, a microwave source `S1` might be set to output 6.66GHz at −10dBm. We can query the object with `S1.frequency.get()` or change it with `S1.frequency.set(6.28)` commands for the different parameters. The objects retain their states unless they are explicitly changed. Our current framework

has a layer on top of the drivers that allows the user to quickly see the current attributes listed to monitor the setup. We initially used the QTlab [144] as a backend for handling the drivers and later switched to QCoDeS [145].

However, if we have multiple pieces of hardware that need to be prepared and possibly need some time to be set, we do it sequentially. Code of the form

```
AWG1.upload_waveforms("entanglement_sequence.awg")
AWG2.upload_waveforms("entanglement_sequence.awg")
AWG3.upload_waveforms("entanglement_sequence.awg")
```

would sequentially upload the files to the AWGs. In an ideal world, we could have the uploading happen in parallel and wait to commence the experiment once everything is ready. Hardware communication delays can add overheads as large as $\sim 50\%$ and with setups becoming more complicated parallelizing communications will be a necessity. To achieve this, we would need to have a python process for each piece of hardware and a master process that manages the flow of the experiment. Currently this is not implemented, but it is an update to the framework of drivers that would eliminate dead time. However, the framework for the drivers needs to be built with this multi-process approach in mind. QCoDeS should actually make it possible with a few modifications.

4.4 HARDWARE VS FIRMWARE

Our qubit readout with ADCs usually relies heavily on digital demodulation, where the readout signal is not a fixed voltage but an oscillating voltage with frequencies on the order of $1\text{MHz} - 10\text{MHz}$. Thus, the signal is more robust to DC fluctuations. The signal is digitized and then demodulated by multiplying it with a weight function and integrating the readout signal over the relevant window resulting in a large data reduction. In case of thresholding, the readout signals are reduced to a single bit giving the declared measurement outcome.

This data reduction, from ns timescale sampling of a 200ns signal to an integrated result that can be thresholded to a 0 or a 1 can be done in the computer that controls the experiment or in the hardware itself. With FPGA technology, programmable hardware where firmware can be adjusted to enable complex data processing pipelines, these operations can be done in real time and greatly reduce the amount of data that is sent back to the experimentalist's computer when doing the experiment. While the experiments in this thesis [50, 146] were still using data reduction on the computer, other experiments in our group were already relying on this more advanced approach [69, 75]. This eases the requirements for the code that is actually run on the experimentalist's computer and hugely reduces the amount of data that is transfered in the runtime of a quantum experiment.

Another example is sideband modulation for qubit pulses. For our transmon qubit pulses, the sideband modulation phase together with the timing of a pulse with

respect to the microwave carrier defines the rotation axis of the gate in the x-y-plane. Therefore, the ability to make a certain gate at a certain time requires getting this reference frame right. In our case, we still uploaded the entire experimental sequence up to the AWGs - tens of microseconds with nanosecond precision for several AWG channels. In our group, custom AWGs are developed where the modulation can be added on-board with respect to a stable reference. Then, simple primitives can be stored in a waveform memory and the only thing that needs to be uploaded are those pulse primitives. Thus, the amount of data that needs to be sent from the experimentalists computer to all the pulse-generation hardware is greatly reduced. But hardware development requires considerable investment which requires experimental groups to partner up with electronics experts.

For now, uploading times are already bottlenecks for randomized benchmarking experiments, but as the number of qubits grows, there will be more AWG channels and readout data. Therefore, a scalable scheme for the overall data rates in experiment is desirable.

4.5 A SIMPLE FRAMEWORK FOR MEASUREMENTS AND ANALYSIS

Most experiments conform to a simple pattern: one parameter is swept and another is read out at every point in the sweep, which can easily be visualized with graphs. Sometimes two parameters are being swept, leading to scans that can still be visualized with color plots. Usually more complicated scans are broken up into 1D or 2D scans for visualization. In addition to this measurement loop, a software needs to provide live plotting, such that the experimentalist can directly monitor the experiment, logging of all relevant hardware settings and unified data saving, such that the scripts for loading measurements and quick plotting can be unified. Nice to have features, such as an interrupt button or an estimate for the remaining measurement time, need to be written only once.

The way this is handled in our software PyCQED [147] is to have a measurement object we call `Measurement_Control` that can have multiple functions to be swept and multiple detector functions. Essentially, this runs loops of the form:[1]

```
def run(self, *kw):
self.initialize_live_plotting()

    self.sweep_function.prepare()
    self.detector_function.prepare()

    self.measured_values = np.zeros(
        self.sweep_points.shape)
```

[1] This is pseudo code that represents the gist of the measurement function. While it seems trivial, writing a `measure` function that can handle all different types of measurements lead to the prepare() and finish() statements, which are often necessary for comunicating with hardware.

```
if self.measurement_type is 'hard':
    self.measured_values = self.detector_function.get_values()

elif self.measurement_type is 'soft'
    for i, sweep_point in enumerate(self.sweep_points):
            self.sweep_function.set_parameter(sweep_point)
            self.measured_values[i] =
                    self.detector_function.acquire_data_point()

self.sweep_function.finish()
self.detector_function.finish()

self.take_snapshot_of_hardware_settings()
self.save_data_to_file()
```

We made a distinction between "hard" measurements, where the measurement loop is performed on the hardware, for example VNA measurements that return the transmission through a line as a function of frequency all at once, and "soft" measurements, where a software loop sets parameters and then measures a parameter. For more complicated measurement loops, for example 2D or higher-dimensional scans, our `Measurement_Control` object in principle allows an arbitrary number of sweep functions. The 2D case is implemented as a special case with a simple nested "for" loop.

All measurements in the experiments I was involved in during my PhD could be performed this way, with a unified live plotting interface, logging of system parameters, data saving (including metadata), and intuitive ways to quickly change the parameters that are swept or the ranges. A measurement can then be run with a few lines of code through the `Measurement_Control` object:

```
import measurement_analysis as ma

Measurement_Control.set_sweep_function(
        awg_swf.T1(pulse_pars=puls_pars, RO_pars=RO_pars))
Measurement_Control.set_sweep_points(
        np.arange(t_start, t_stop, t_step))
Measurement_Control.set_detector_function(
        det.integrated_average_detector(
                        RO_hardware=RO_hardware, AWG=AWG))

Measurement_Control.run(name='T1_qubit_x')

a = ma.T1_analysis(auto=True, close_fig=false)
```

To change the sweep range, one could then for example just set different sweep points and run the measurement again. The `measurement_analysis` module contains standard analysis scripts for different measurements. In our codebase, data taking and analysis are strictly separated. For night runs, scripts containing all scheduled measurements can be written and executed.

Ultimately, we also added the functionality of running a closed-loop optimization on measured data using the optimizers provided by `scipy` and saving every measured point in the process. With a simple flag it was possible to provide the system with a set of parameters to vary and a measurement value to minimize, which proved useful in tuning processes for many of the experiments.

4.6 MODULARITY

As I said, a good codebase is an important asset for a research group. This means not only that there is code that solves the current problems, but it should be written in a way that it can be easily stitched together to solve tomorrows problems. Whenever possible, code should be written in a more general form. As an example, consider the backbone of quantum state tomography: solving an equation system of the form

$$\langle \hat{M}_i \rangle = \mathrm{Tr}\left(\hat{M}_i \rho\right), \tag{4.1}$$

where $\hat{M}_i$ form a set of measurement operators and ρ is the density matrix. Equations can be aditionally weighted by the standard deviation of the estimators for the measurement results. The additional constraint is that ρ is a valid density matrix, meaning that its eigenvalues are all larger or equal to zero and that $\mathrm{Tr}(\rho) = 1$. Code solving this problem can be written for ρ of arbitrary size (even though it quickly becomes computationally intractable) taking the measurement operators and estimators for expectation values as an input. To solve the problem, we simply wrote a wrapper for an existing semidefinite programming algorithm. Now people measuring larger systems can build on our code and ideally do not have to tackle this problem again. The code needs to be broken up into functions that tackle specific general problems rather than scripts that solve specific problems.

Properly modularizing code takes practice and does create overhead in develoepement time. For our purposes, plotting, and fitting of data should be written in more generality, as these tasks have to be performed in many contexts. Other task such as generating sequences of gates for randomized benchmarking or thresholding readout results can have functions for the general problem rather than convoluting them with the pulse generation or readout hardware. While it is always quicker to write a specific solution to a problem, writing good and modular code as a group will be beneficial for everyone in the longer run. The codebase then needs to be organized such that the right module for a task can be found quickly. This seems like common sense, but a well modularized codebase does not arise naturally in

my experience, but a positive feedback loop can be created if the research group predominantly writes good code.

Modularity also ensures that switching hardware (e.g. using an AWG from a different company with a different way that pulse sequences are implemented) does not require changing all other code. With experimental setups that constantly evolve to keep up with state-of-the-art electronics, it is a high priority to have a codebase that does not require constant rewriting - only swapping certain modules that have the same input-output behavior. Nevertheless, long-term planning on the hardware side is needed to keep experiments functional while the hardware is evolving.

4.7 ABSTRACTION

The power of programming comes with abstraction. Any experiment can be written as a long script that contains all the relevant commands, but in order to run complicated experiments, these scripts would quickly become unwieldy. Therefore we need intuitive abstract commands.

4.7.1 *qubit objects*

We used the object orientation in python to build qubit objects. These qubit objects control all the relevant hardware connected to that qubit and store its parameters for control and readout, for example the readout frequency, readout-pulse length and readout power. The qubit object class also contain high-level functions.

```
qubit.calibrate_rabi()
```

will calibrate the amplitude for a π pulse. The measurements are run through the `Measurement_Control` object from inside the qubit object. The new value will be stored in the object.

```
qubit.calibrate_frequency_ramsey()
```

will then perform multiple Ramsey experiments with different stepsize to calibrate the qubit frequency up to the limit imposed by T_2^*.

This lead to a more intuitive interaction with the experiment and made it easier for people who might not know all the details of the functions to perform simple experiments. The qubit object is also a container for all the settings required to run algorithms involving that particular qubit, such that it could be queried by a compiler that needs to make the pulses for this qubit and upload them to an AWG. This strategy made the standard single-qubit experiments very simple. However, in order to move to complex multi-qubit algorithms there are many steps that need to be taken.

4.7.2 *A quantum processor object?*

We did not implement the next level in the hierarchy of our growing quantum computer yet, but I want to briefly outline my thoughts on the matter. Next in line after a qubit object that unifies the main hardware for each qubit, we would need an object that represents the entire processor. This object would contain matrices that represent the connectivity and store the parameters for two-qubit or even multi-qubit gates. This paradigm of an object hierarchy is aimed at organizing the information such that a compiler that turns a quantum algorithm into hardware intructions can easily find all the information it needs. Different container objects that mainly store parameters can be used and modules can be written that operate on these objects.

4.8 THE FULL-STACK APPROACH

As we move to the stage of executing quantum algorithms, we need to create layers of abstraction in the way that they exist for normal computers. When we write down a classical computer algorithm, we do not write down the operations on the bit level. We program in high-level languages that get compiled into assembly code that is executed in the processor. There are proposals for holistic architectures organizing the quantum and classical hardware and different abstraction layers, for example [148]. Once the microarchitecture is decided upon, an executable quantum instruction set architecture can be developed such as the one proposed in [149].

Similarly, there will likely be several layers of compilation from an abstract quantum circuit diagram, to a scheduling diagram to the final concrete instructions that are sent from the experimentalists computer to the hardware. The compilation might need multiple iterations between the three stages. But there are contraints, the single-qubit control architecture in Chapter 5 can perform the same gate on many qubits simultaneously, but different gates would have to be done sequentially. We wrote a Clifford compiler, minimizing the number of pulses to perform certain sequences of Cliffords on two qubits simultaneously. These types of helper routines will be needed for future quantum processors.

I would call a platform that accepts a generic representation of a quantum algorithm as an input, can run this algorithm on the physical quantum processor and return the outcomes, a programmable quantum computer. Currently the first such programmable quantum computers are being realized [28] and sometimes even made available [29]. Eventually the part of my job that was tuning up and writing hardware instructions for a few qubits by hand will be done by a computer automatically. Writing easy to use interfaces for a cloud-based quantum computer is a critical part to the success of quantum computers as a whole. More and more automated quantum platforms in the cloud will allow theorists to try out their ideas themselves on quantum systems that are better than simulations on their notebooks or even supercomputers, hopefully inspiring new quantum algorithms.

5

INDEPENDENT, EXTENSIBLE CONTROL OF SAME-FREQUENCY SUPERCONDUCTING QUBITS BY SELECTIVE BROADCASTING

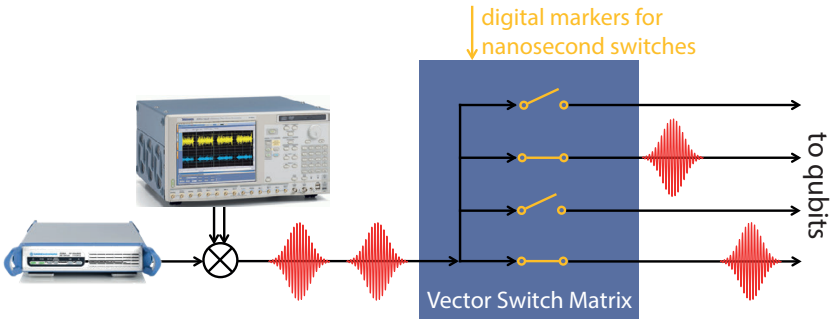

A critical ingredient for realizing large-scale quantum information processors will be the ability to make economical use of qubit control hardware. We demonstrate an extensible strategy for reusing control hardware on same-frequency transmon qubits in a circuit QED chip with surface-code-compatible connectivity. A vector switch matrix enables selective broadcasting of input pulses to multiple transmons with individual tailoring of pulse quadratures for each, as required to minimize the effects of leakage on weakly anharmonic qubits. Using randomized benchmarking, we compare multiple broadcasting strategies that each pass the surface-code error threshold for single-qubit gates. We also monitor gate-induced leakage that could otherwise skew randomized benchmarking results. Shared control hardware comes at the cost of introducing overhead when independent individual control is necessary. We introduce a selective-broadcasting control strategy using five pulse primitives, which allows independent, simultaneous Clifford gates on arbitrary numbers of fixed frequency qubits, showing that this overhead is constant.

This chapter has been published with minor differences in *npj Quantum Information* **2**, 16029 (2016).

5.1 INTRODUCTION

Building a fault-tolerant quantum computer requires the ability to efficiently address and control individual qubits in a large-scale system. Many leading experimental quantum information platforms, among them trapped ions [150], electronic spins in impurities and quantum dots [151], and superconducting circuits [152], employ qubits with level transitions in the microwave frequency domain. Addressing these transitions often involves expensive microwave electronics scaling linearly with the number of qubits. To move beyond the state of the art in microwave-frequency quantum processors, such as those recently used for small-scale quantum error correction in superconducting circuits [125, 153, 154], it is already beneficial to have a hardware-efficient control strategy that harnesses economies of scale. One approach is to use microwave pulses from a single control source for multiple qubits [155], requiring frequency-matched qubits and high-speed routing of pulses to separate control lines. The linear scaling of control equipment could then be reduced to a constant overhead for the most expensive resources. Practically, fan-out can not be achieved without signal degradation, even with active circuits, such that ultimately this strategy will not turn a linear into a constant scaling but rather result in reducing expensive electronics by a factor of $\sim 50 - 100$.

Using control equipment for multiple qubits has previously been demonstrated for optical addressing in atomic systems, where qubits naturally have the same frequency [156–159]. Such frequency reuse also becomes possible in circuit quantum electrodynamics (cQED) [160] in the context of fault-tolerant computation strategies which rely only on local interactions between qubits mediated by bus resonators [161–163]. The natural isolation between different lattice sites allows the use of repeating patterns of qubit frequencies with selectivity provided by spatial separation. A tileable unit cell with a handful of qubit frequencies [164] could therefore provide a promising route towards scalability. Crucially, this also solves the frequency-crowding problem which arises when trying to fit many distinct-frequency qubits within the finite useful bandwidth of the circuit-based devices, particularly for designs based on weakly anharmonic qubits where higher levels must also be avoided [124, 165]. While no qubit experiments have yet shown the viability of this approach, Hornibrook *et al.* have recently demonstrated a cryogenic switching matrix for pulse distribution operating at 20 mK, triggered by a field-programmable gate array at 4 K (ref. 155). Cryogenic control equipment may shorten feedback latency and reduce wiring complexity across temperature stages, but the isolation and operational frequency range reported to date are insufficient for typical cQED experiments.

Here, we demonstrate frequency reuse in an extensible solid-state multiqubit architecture. An extensible architecture harnessing frequency reuse has two key requirements: a method for distributing control pulses to multiple qubits with economical means to adapt the pulses for each qubit, and a multiqubit device containing

same-frequency qubits with relevant connectivity and sufficient isolation between same-frequency qubits. To this end, we show independent simultaneous control of two same-frequency qubits with a room-temperature vector switch matrix (VSM) that we have developed. The VSM allows tailoring of control pulses to individual qubit properties, and routing of the pulses to either one or both of the qubits using fast digital markers. We develop several different approaches to selective pulse broadcasting, including a simple scheme for implementing independent Clifford control on an arbitrary number of qubits with a constant overhead in time. The device for this experiment is designed to allow testing in a circuit with the correct connectivity of a relevant surface-code lattice [18, 19]. Using randomized benchmarking (RB), we show that all control schemes exceed the fidelity threshold for surface code and are dominated by qubit relaxation. We also develop a method for measuring leakage to the second-excited state directly within the context of RB [166, 167]. We characterize the limitations of our system and find no major obstacles to scaling up to larger implementations.

5.2 METHODS

To demonstrate frequency reuse, we focus on a particular implementation of the surface code based on repeated tiling of a four-qubit unit cell (Figure 5.1), where nearest-neighbor qubits are coupled via bus resonators [161].[1] Our device contains a small block of this design, consisting of two same-frequency transmon qubits (Q_T and Q_B), which are connected to a third qubit (Q_M) via separate bus resonators (Figure 5.1). Each qubit has a capacitively-coupled drive line for individual qubit control [168], a readout resonator coupled to a common feedline for frequency-division multiplexing readout [122, 169], and a flux-bias line for individual frequency tuning [25]. While Q_T and Q_B were designed to be identical, fabrication uncertainties resulted in a sweet-spot (maximum) frequency of Q_T that was 57 MHz higher than that of Q_B. With Q_B and Q_M kept at their respective sweet-spots (6.220 GHz and 6.550 GHz, respectively), Q_T was then flux tuned to match Q_B with an accuracy of ~ 50 kHz, determined using Ramsey measurements. The coherence times at the operating frequency can be found in Figure 5.9 in Section 5.5. Because of the transmon's weak anharmonicity [45], high-fidelity fast single-qubit control is achieved using the method of derivative-removal-via-adiabatic-gate (DRAG) pulsing, where the in-phase Gaussian pulse is combined with a quadrature derivative-of-Gaussian pulse [76, 77]. For each qubit, this requires independent amplitude control of the two constituent quadrature pulses.

The VSM was designed to accept multiple input pulses and selectively fan them out to multiple qubits with individual pulse tuning for each qubit (Figure 5.1). Our

[1] Same-frequency qubits are compatible with almost any architecture where the control pulses can be sufficiently selective, including transmons coupled by tuneable couplers or transmons that are capacitively coupled directly. To minimize residual driving, a larger frequency lattice can be chosen.

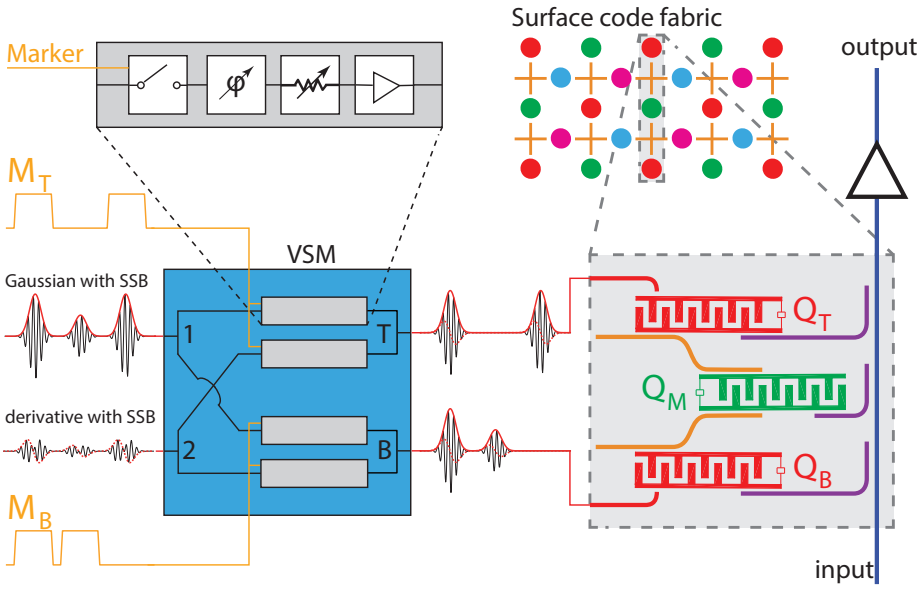

Figure 5.1: *Schematic of independent control of same-frequency qubits using a vector switch matrix (VSM). The device (grey box on the bottom right) connects two transmons with matched frequency (Q_T and Q_B: 6.220 GHz) indirectly through coupling buses and a third non-matched transmon (Q_M: 6.550 GHz). This provides the smallest relevant subunit of the four-frequency surface-code fabric illustrated above right (colors represent distinct qubit frequencies). The VSM (blue box) allows independent, simultaneous transmon control with tailored DRAG pulsing for each qubit through dedicated drive lines. The link between inputs and outputs can be switched on nanosecond timescales using the digital markers M_T and M_B (orange lines). Gaussian and derivative-of-Gaussian pulses are independently tuned in amplitude and phase for each input-output pair (top left).*

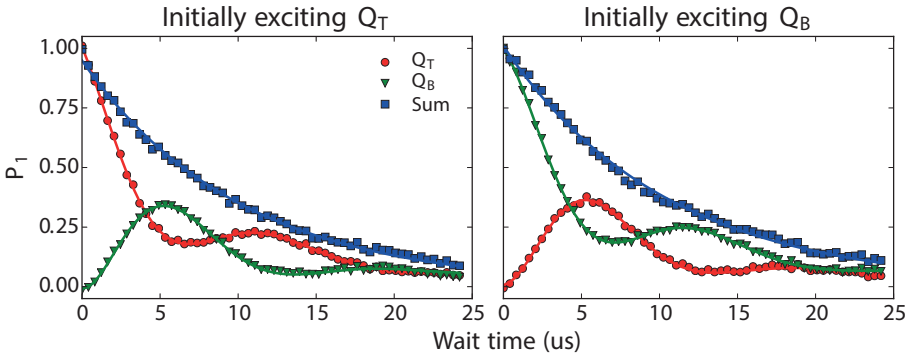

Figure 5.2: *Cross-coupling: Temporal evolution of a single excitation after initially exciting Q_T (a) or Q_B (b). Both qubits are measured simultaneously using multiplexed readout. The oscillations of population in both qubits are out of phase and have a common frequency. The sum of both populations shows approximately exponential decay with time constant 10.2(2) μs, which lies between the relaxation times of Q_T and Q_B.*

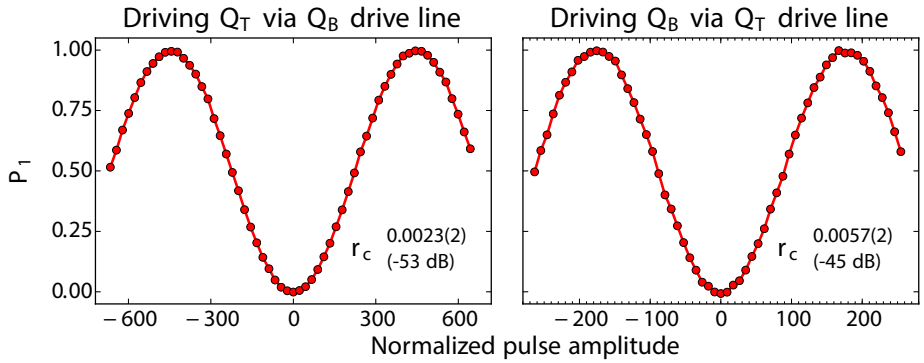

Figure 5.3: *Cross-driving: Rabi oscillations of Q_T (c) and Q_B (d) induced by pulses on the drive line of the other qubit. The pulse amplitude is normalized to the calibrated π-pulse amplitude required for the directly-coupled qubit, the normalization factor being the inverse of the cross-driving ratio r_c.*

prototype room-temperature 4×2 (four input, two output) VSM allows independent control of amplitude and phase for each of its input-output combinations. Fast marker-controlled digital switches enable routing of pulses to the qubits at nanosecond timescale, with approximately 50 dB isolation in the frequency range from 4 to 8 GHz (see Section 5.6.1 for VSM specifications). By directing the two consistuent pulses of DRAG control to two of the four inputs of the VSM, this allows independent, in-situ DRAG tuning for both same-frequency qubits using four AWG channels (two channels for IQ modulation of each constituent pulse).

There are several spurious sources of error that affect the gate fidelity in this architecture. Dominant on-chip sources include a residual qubit-qubit exchange interaction, resulting from coupling between the two qubits, and cross-driving, resulting from the spurious coupling of each drive line to the untargeted qubit. The dominant off-chip source is the finite isolation in the VSM. We briefly describe the methods used to quantify these sources.

To characterise the cross-coupling between Q_T and Q_B, we measure the evolution of excited-state populations after a single excitation is injected at one of the qubits with a π pulse. To place a tight upper bound on the interaction strength J, the qubit frequencies must be matched as closely as possible. We achieve an accuracy of around 50 kHz using Ramsey experiments, limited by a combination of factors: the resolution of the flux tuning, the fitting resolution limit imposed by qubit T_2 dephasing times, and also the frequency shifting induced by the qubit-qubit exchange interaction itself. From single-excitation swap experiments (Figure 5.2), we observe a residual exchange interaction of the form $J(\sigma_+^T\sigma_-^B + \sigma_-^T\sigma_+^B)$ [160] between Q_T and Q_B with strength $J/2\pi \leq 36 \pm 1$ kHz.

To characterize the residual on-chip cross-driving, we disconnect the VSM and send driving pulses through the drive line for one of either Q_T or Q_B, and compare the amplitude required to implement a π pulse on each same-frequency qubit

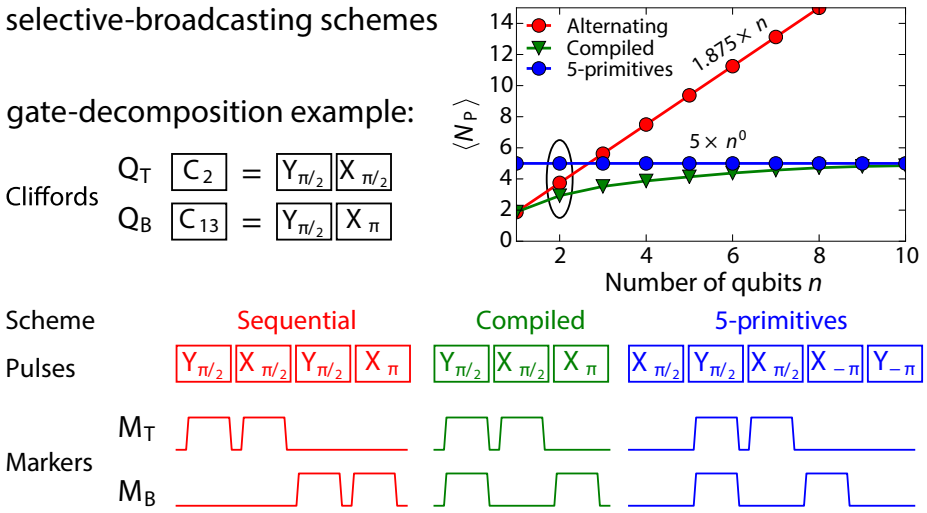

Figure 5.4: *Selective broadcasting schemes for simultaneous single-qubit control of multiple qubits. Main figure: Example of a single Clifford round for n=2 qubits targeting C_2 (C_{13}) in Q_T (Q_B) (C_j defined in Table 5.3 in Section 5.10). In the sequential scheme, the pulses implementing C_2 are directed to Q_T, after which the pulses implementing C_{13} are directed to Q_B. In the compiled scheme, the two Cliffords are realized concurrently using a pre-determined pulse sequence, with appropriate markers, which minimizes the total number of pulses, N_p (see Section 5.10.2 for the compilation algorithm). Finally, in the 5-primitives scheme, a fixed sequence of five pulses is repeated in each round (N_p=5). The targeted Cliffords are then applied simultaneously by selecting the appropriate subset of pulses for each qubit (see rTable 5.3 for the 5-primitives marker table). Top-right: Scaling of the average pulses per multiqubit combination of Cliffords, $\langle N_p \rangle$, versus qubit number n. The constant scaling achieved by the 5-primitives scheme provides a dramatic improvement over the linear scaling of the sequential scheme. While $\langle N_p \rangle$ is always lowest for the compiled scheme, pre-compiling the optimal pulse and marker combinations is impractical for $n \gtrsim 5$, and the improvement over the simpler 5-primitives scheme is negligible by $n \sim 10$.*

(Figure 5.3). For this test, pulses are first amplified and then attenuated using a step attenuator to allow the large amplitude range required. The results show that the cross-driving on our chip is asymmetric, being stronger when Q_B is driven using the drive line of Q_T than vice versa. Direct measurements of the internal VSM isolation reveal an additional leakage of around −57 dB and −54 dB on Q_T and Q_B, respectively (see Section 5.6.1), lower than the direct on-chip cross-driving.

The first critical test of our control architecture is to assess the VSM's ability to implement high-precision control of one qubit while leaving the other qubit idle. To do this, we use the standard technique of single-qubit RB based on Clifford gates [82, 170, 171], which allows the characterization of control performance independently of state preparation and measurement errors. After initializing all qubits in the ground state by relaxation, we use the VSM to selectively apply random sequences of Cliffords gates to only one of the same-frequency qubits, with

lengths m ranging from 1 to 800 gates and the results averaged for 50 different random sequences. We decompose each gate into the standard minimal sequence of π and $\pm\pi/2$ pulses around the x and y axes (16 ns pulses separated by a 4 ns buffer; $\tau_P = 20$ ns) (ref. 167), requiring on average $\langle N_p \rangle = 1.875$ pulses per Clifford. This is in contrast to so-called "atomic pulses" [172], where the 24 single-qubit Cliffords can each be implemented with a single pulse. After applying a final Clifford that inverts the cumulative effect of all m previous Cliffords, the driven qubit is ideally returned to the ground state, but as a result of imperfections such as gate errors and decoherence, the final ground-state population decays as a function of m. The decay rate can be related to the average fidelity per Clifford F_C (ref. 82, 170). In a strictly two-level system, the measured ground- and excited-state populations averaged over many sequences ($\langle P_0 \rangle$ and $\langle P_1 \rangle$) both converge to 0.5 for large m. For weakly anharmonic transmon qubits, leakage to the second-excited state can be an important additional source of gate error, which can lead to a shift of the asymptotic values away from 0.5. We address this issue by performing the RB protocol both with and without an additional final π pulse [173], which allows us to explicitly estimate the populations of the first three transmon states (see Section 5.8 for details).

The defining test of extensibility in our control architecture is to demonstrate the simultaneous, independent, single-qubit control over same-frequency qubits that is enabled by selective broadcasting using the VSM. We explore three paradigmatic schemes for implementing selective broadcasting of Cliffords on an arbitrary number of qubits n (Figure 5.4). In the most straightforward selective-broadcasting scheme, the individual qubits are driven sequentially, with each pulse being directed to one qubit at a time. This results in a linear scaling of the average number of pulses per Clifford round $\left(\langle N_p \rangle = 1.875 \times n\right)$. By contrast, the second paradigm takes best advantage of the VSM's capability to broadcast simultaneously to multiple qubits by compiling the constituent Clifford pulses to minimize N_p for each Clifford combination in the sequence. However, compiling pulses comes at the cost of an exponentially increasing compilation time with the number of qubits prior to running the sequence. This motivates our final broadcasting paradigm, where all Clifford gates can be implemented using the same fixed, ordered sequence of five pulse primitives (Figure 5.4). Independent Cliffords can be applied to all qubits, irrespective of n, by selectively directing the appropriate subset of pulses to each qubit, achieving a constant overhead in time for control of an arbitrary number of qubits.

5.3 RESULTS

To fully characterize our multiqubit frequency reuse control architecture, we assess both single-qubit and simultaneous multiqubit control using RB.

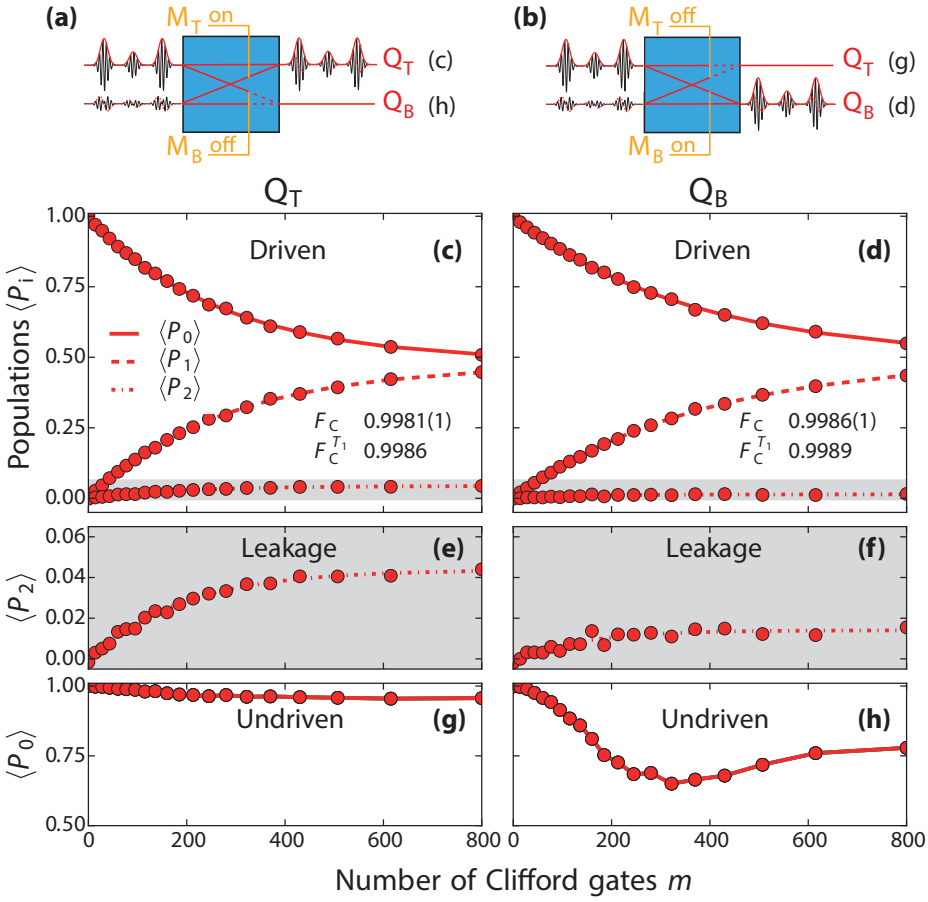

Figure 5.5: *Single-qubit control of same-frequency qubits using the VSM. (a,b) Schematics showing DRAG pulses routed exclusively to either* Q_T *or* Q_B *using the corresponding markers (always on or off). (c,d) Characterization of single-qubit control by randomized benchmarking (RB) of Clifford gates. Average populations of* Q_T *and* Q_B *in the ground, first- and second-excited states (*$\langle P_0\rangle$, $\langle P_1\rangle$ *and* $\langle P_2\rangle$*, respectively) as a function of the number of Clifford gates applied. Curves are best fits of single exponentials with offsets. Single-qubit Clifford fidelities for each qubit are extracted from the decay of ground-state populations. Both surpass the surface-code fault-tolerance threshold and are near* T_1*-only relaxation-limited performance. (e,f) Expanded plots of second-excited state leakage during RB. Curves are best fits according to Equation (5.2). (g,h) Cross-excitation of the undriven qubit resulting from control pulses applied to the driven qubit due to microwave leakage.*

5.3.1 *Individual qubit control*

We first implement the characterization of precision single-qubit control by driving one qubit at a time, and switching off the marker for the undriven qubit at the VSM [Figure 5.5(a,b)], in each case measuring the effect on both qubits simultaneously via multiplexed readout. From the RB data [Figure 5.5(c,d)], we extract the average Clifford fidelities for the two individually-driven qubits to be 0.9982(2) (Q_T) and 0.9986(2) (Q_B). We compare these values with the expected average Clifford fidelities assuming only T_1 decay [174]:

$$F_C^{T_1} \simeq \left[\frac{1}{6}\left(3 + 2e^{-\tau_P/2T_1} + e^{-\tau_P/T_1}\right)\right]^{\langle N_p \rangle}. \tag{5.1}$$

The similarity [Figure 5.5(c,d)] shows that the results are predominately limited by relaxation effects. The difference in performance between the two qubits is consistent with their different T_1 times.

From the measured leakage populations $\langle P_2 \rangle$, we extract per Clifford leakage rates κ_{CL} of $1.4(2) \times 10^{-4}$ (Q_T) and $3.9(4) \times 10^{-5}$ (Q_B) by fitting the following simple model to the data (see Section 5.8 for details):

$$\langle P_2[m] \rangle \simeq \kappa_{CL}\, T_{2\to1} \left(1 - e^{-\frac{m\langle N_p \rangle \tau_P}{T_{2\to1}}}\right), \tag{5.2}$$

where $T_{2\to1}$ is the second- to first-excited-state relaxation time. As these leakage rates are much smaller than the gate errors ($1-F_C$), it is reasonable to neglect them when estimating the Clifford fidelity.

We next explore the effect of the single-qubit control pulses on the undriven qubit [Figure 5.5(g,h)]. While Q_T remains largely unaffected when driving Q_B, a substantial deviation from the ground state is measured in Q_B when driving Q_T. As discussed in Section 5.2, there are several possible mechanisms for cross-excitation effects in the system: cross-coupling (higher-order quantum coupling mediated by the bus resonators and Q_M) and cross-driving (spurious driving of the idle channel by microwave leakage resulting from imperfect isolation either in the VSM or on chip). The symmetric swapping of excitation, measured using single-excitation swap experiments (Figure 5.2), is unlikely to explain the strong asymmetry in the amount of cross-excitation measured for the different qubits. Moreover, numerical simulations show that the observed effects are consistent with cross-driving alone (see Section 5.9). Direct, independent measurements of microwave isolation in both the VSM (Section 5.6.1) and on chip (Figure 5.3) indicate that the on-chip cross-driving dominates and is asymmetric, in agreement with results. The effect of cross-driving in the context of RB can be quantified using interleaved RB [175], where pulses on the driven qubit are interleaved with a random sequence of Cliffords applied to the undriven qubit. This yields an average idling fidelity for Q_B of 0.9986(5) (Section 5.9.1), consistent with the error due to additional T_1 decay, confirming that cross-excitation effects do not dominate the error per Clifford.

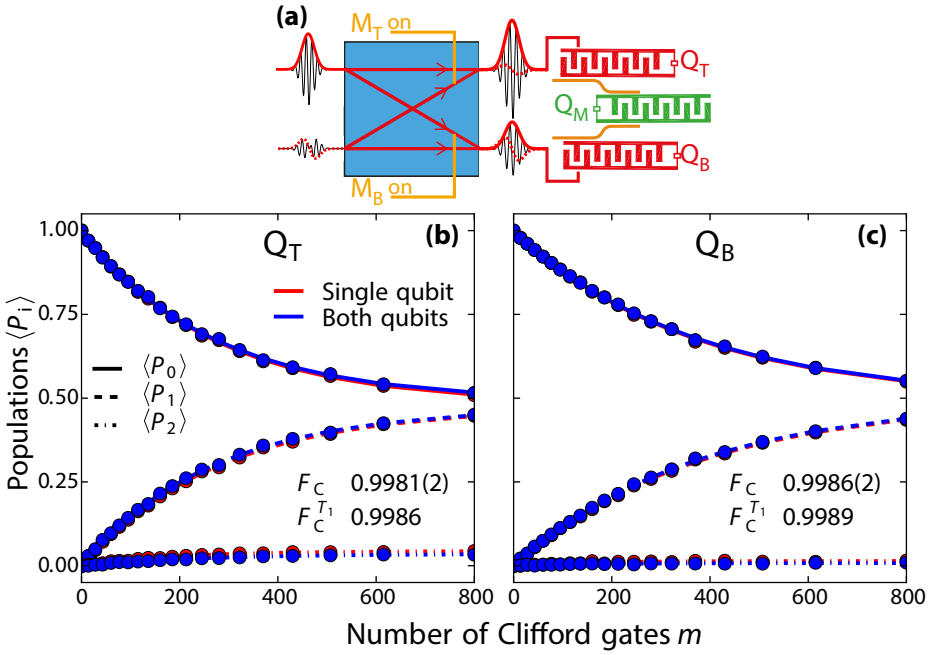

Figure 5.6: *Global broadcasting of DRAG pulses to same-frequency qubits. (a) Illustration of global broadcasting. Two simultaneous pulses, one with Gaussian envelope at input 1, and another with derivative-of-Gaussian envelope at input 2, are simultaneously directed to* Q_T *and* Q_B *(both markers always on). The insertion loss and phase shift of each pulse is separately optimized for each output to produce precision DRAG pulses for each qubit. (b,c) Comparison of single-qubit driving versus driving both qubits (broadcasting) by RB of Clifford gates composed from* $\pi/2$ *and* π *pulses [167]. Average population of* Q_T *and* Q_B *in the ground, first- and second-excited state (*$\langle P_0\rangle$, $\langle P_1\rangle$ *and* $\langle P_2\rangle$, *resp.) as a function of the number of Clifford gates applied. Curves are the best fits of single exponentials with offsets to the populations. The single-qubit Clifford-gate fidelity for each qubit is extracted from the decay of the corresponding ground-state population when using global broadcasting.*

5.3.2 *Global broadcasting*

Aside from single-qubit control and selective broadcasting, the VSM also allows global broadcasting of pulses to all qubits simultaneously by keeping the markers for both qubits on (Figure 5.6). While this does provide simultaneous control of Q_T and Q_B, marker control is needed to achieve independent control. Using RB, we measure the performance of both qubits when broadcasting the same Clifford sequences to both qubits, and compare the results with those obtained from individual single-qubit control (Figure 5.6). The global broadcasting RB measurements were alternated with the single-qubit RB measurements, and aside from marker settings all other settings were identical. Comparison of the results in Figure 5.6 show that the qubit gate performance does not depend on whether a single qubit is controlled, or both are controlled simultaneously through global broadcasting.

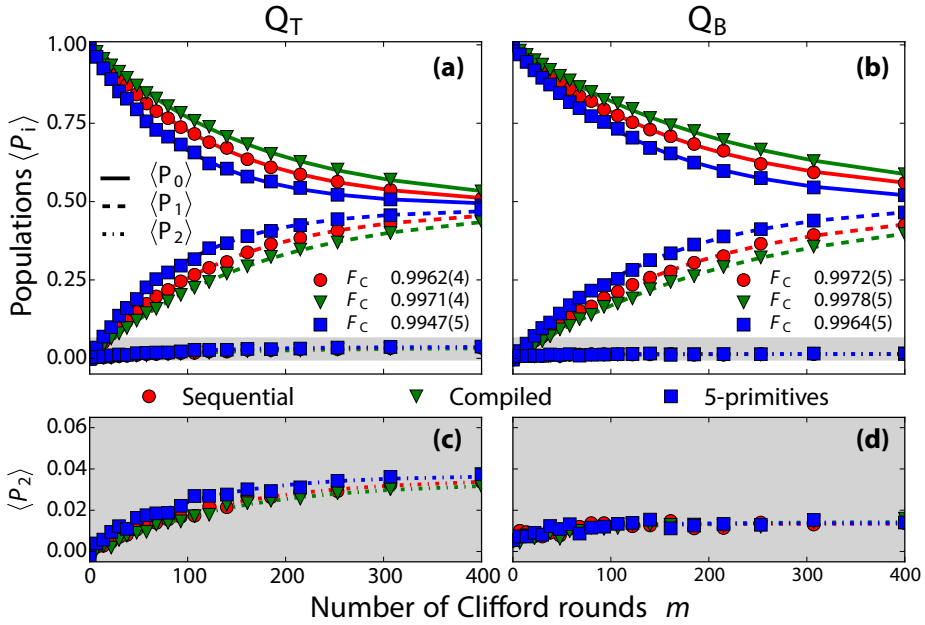

Figure 5.7: *Characterization of sequential, compiled and 5-primitives selective-broadcasting schemes by RB. (a,b) Evolution of the average transmon populations for* Q_T *(a) and* Q_B *(b) as a function of the number of Clifford rounds. Curves are the best fits of single exponentials with offsets. (c,d) Expanded plots of second-excited-state leakage during RB. (e) Average single-qubit Clifford-gate fidelities for* Q_T *and* Q_B *in each scheme, extracted from the decay of the corresponding ground-state population. All fidelities surpass the surface-code fault-tolerance threshold and closely track those expected for* T_1*-relaxation-limited performance.*

5.3.3 *Independent individual control using selective broadcasting*

To demonstrate the full functionality of our control architecture, we implement all three selective-broadcasting schemes and measure their performance using parallel single-qubit RB with independent Clifford sequences for each qubit. Figure 5.7 shows that the compiled scheme performs best, followed by the sequential and then 5-primitives schemes, consistent with the average number of pulses required for each (Figure 5.4). In all cases, the average fidelity per Clifford is still dominated by relaxation. The results are completely consistent with the values obtained in the test for isolated single-qubit control.

5.4 DISCUSSION

Our VSM allows efficient use of control equipment on same-frequency qubits. It enables high-precision single-qubit control of multiple qubits with a performance that surpasses the best known surface-code fault-tolerance threshold for single-qubit gates of ~ 0.99 (ref. 176–178), and is mainly limited by relaxation. Although the measurements show a nonnegligible amount of leakage from the computational subspace

after many pulses [Figure 5.5(e,f)], the corresponding leakage errors are outweighed by other gate errors. A significant amount of cross-excitation was measured in one qubit during the RB measurements [Figure 5.5(h)], which resulted primarily from on-chip cross-driving. In future experiments, this effect could be reduced by careful design of both the surface-code and physical chip layouts. In the first case, increasing the number of qubit frequencies used will result in larger lattice separations between same-frequency qubits. This will provide better effective isolation at the cost of increased design and hardware complexity. In the second case, circuit QED provides naturally good circuit isolation due to the superconducting ground plane, but optimizing the on-chip coupling network to minimize spurious driving will still be one of the key problems in scaling up to larger systems. In addition, here we show that cross-driving effects can be reduced even at the control level. Specifically, as demonstrated here with the 5-primitives pulse sequence, we choose a sequence of control pulses in such a way that leakage pulses partially or completely cancel out (see Section 5.9.2). This technique is not limited to RB, but could also be used to minimize cross-driving in quantum algorithms. By contrast with cross-driving, the measured cross-coupling (direct qubit-qubit quantum coupling) has no observable effect in the single-qubit RB measurements. Most likely, this is because rapid application of randomising Clifford pulses effectively decouples the cross-coupling dynamics. However, such a coupling may have a stronger effect in other contexts and may have to be addressed in future experiments.

We have introduced three selective broadcasting schemes for performing simultaneous, independent single-qubit RB on both qubits, in each case demonstrating performance that surpasses the fault-tolerance threshold for the surface code for both driven qubits. The naive sequential broadcasting approach still performs acceptably with two qubits, but scales poorly with increasing numbers of qubits. On the other hand, the compiled scheme by definition always minimizes the length of the pulse sequence, but at the cost of exponentially increasing difficulty of the compilation step. Moreover, our estimates suggest that the number of pulses per Clifford round rapidly asymptotes to a total of five pulses, which provides limited gains over our final scheme. Specifically, the 5-primitives scheme combines both scalability and simplicity of implementation (Figure 5.4), selecting the target Clifford by routing a subset of five primitive pulses using digital markers. This is the minimal set of pulses required to implement an arbitrary Clifford gate, and allows independent Cliffords to be applied to an arbitrary number of qubits with no additional overhead in the number of sequence pulses. On a technical level, marker-based selection of Clifford gates can be useful when fast feedback has to be applied on multiple qubits, as is often the case in quantum error correction protocols. Furthermore, by adding a sixth, non-Clifford gate to the five pulse primitives, this can be extended to achieve universal single-qubit control. We show that the fidelities are mainly limited by qubit relaxation for all broadcasting schemes, and are consistent with each other and with the single-qubit RB results once the average duration per Clifford round is taken

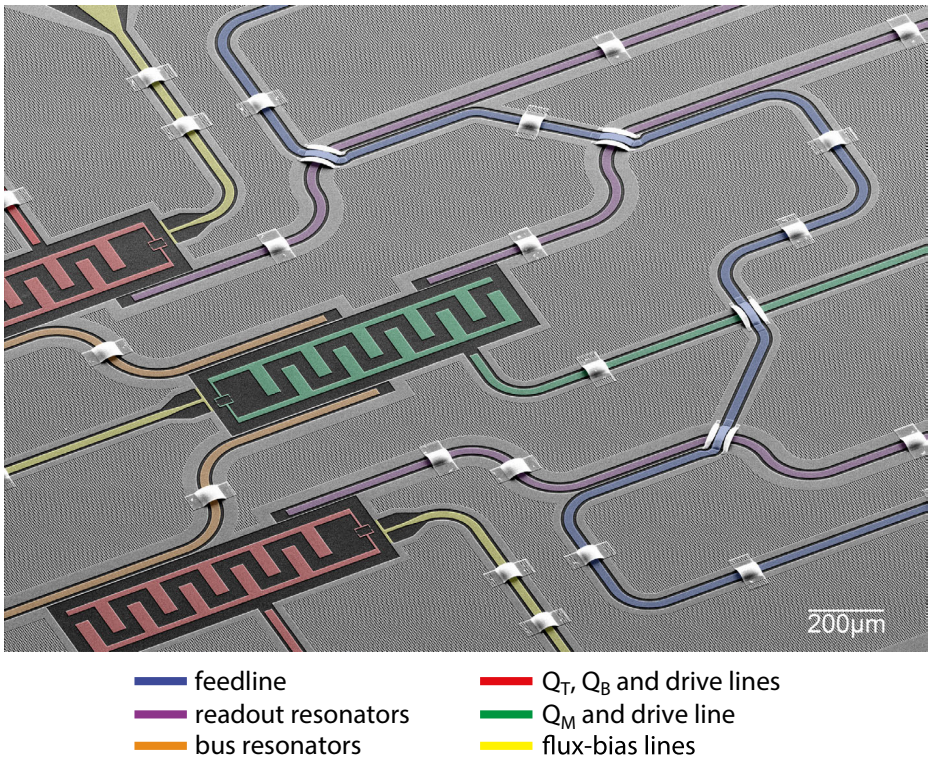

Figure 5.8: *Scanning electron micrograph (with added false colour) of a device twin to the one used in the experiment and fabricated in the same batch. Notably, the feedline crosses the three readout resonators and one of the qubit drive lines.*

into account. This confirms that selective pulse broadcasting does not decrease gate performance relative to that expected from the intrinsic pulse fidelities.

Combining the connectivity of our device, the VSM-based control, and the fixed pulse overhead of the 5-primitives broadcasting strategy, our experiment realizes the simplest element of an extensible qubit control architecture. While we do not yet see explicit savings in control hardware for two qubits, this design can be straightforwardly expanded to more same-frequency qubits without requiring any further microwave sources or arbitrary waveform generators. This experiment suggests that surface-code tiling with frequency reuse is a viable path towards large-scale quantum processors.

5.5 QUANTUM CHIP AND EXPERIMENTAL SETUP

5.5.1 *Chip design and fabrication*

Our quantum chip consists of three transmons (top: Q_T, middle (ancilla): Q_M, and bottom: Q_B) with dedicated voltage drive lines (D_T, D_M and D_B, respectively), flux-bias lines, and readout resonators. All readout resonators are capacitively coupled

Table 5.1: *Table of sweet-spot frequencies f_{max} and bias-point frequencies f_{bias} of the three qubits, as well as the fundamental frequencies f_{res} of their dedicated read-out resonators at the bias point. The qubits are tuned into the bias point by a combination of spectroscopy and standard Ramsey experiments.*

Qubit	f_{max} (GHz)	f_{bias} (GHz)	f_{res} (GHz)
Q_T	6.277	6.220	6.700
Q_M	6.551	6.551	6.733
Q_B	6.220	6.220	6.800

to one common feedline which crosses various on-chip components using airbridge crossovers. Qubits Q_T and Q_M are coupled by one bus resonator, and Q_M and Q_B by another (fundamental frequencies 4.9 and 5.0 GHz, respectively). All resonators are open-ended on the coupling side, and short-circuited at the other.

The chip fabrication method is similar to that in ref. 125, but with some important differences which we now explain. Rather than sapphire, we use a high-resistivity intrinsic silicon substrate prepared by HF dip and HMDS surface passivation before sputtering a 300-nm-thick film of NbTiN, as introduced in ref. 117. This change aims to improve the substrate-metal interface and thereby intrinsic quality factors for both resonators and qubits. After sputtering, the patterns are etched into the superconducting layer using reactive-ion etching with an SF_6/O_2 plasma. In contrast with the Al transmon capacitor plates commonly used, in this experiment we make them also from NbTiN, with an aim to improve the substrate-metal interface and avoid large AlO_x surfaces which may house unwanted two-level systems. Only the Josephson junctions are made by the standard technique of Al-AlO_x-Al double-angle evaporation. A further HF dip just prior to evaporation also helps to contact the junctions directly to the NbTiN capacitor plates. In ref. 125, air bridges were already used to cross the feedline over flux-bias lines on chip. Here, we extend this technique to allow the feedline to cross three readout resonators.

A key requirement for this experiment was the ability to match qubit frequencies without sacrificing coherence. Flux-bias lines allow easy compensation for mismatch, but at the cost of reduced coherence in the qubit detuned from its maximal frequency (coherence sweet spot [179]). We aimed for identical maximum frequencies of Q_T and Q_B, as determined by capacitor and junction geometries. The capacitors were easily matched in fabrication. We then selected the chip with the closest matching room-temperature resistance values for the relevant qubit junctions. The qubit and resonator frequencies are given in Table 5.1. The coherence times at the bias point can be found in Figure 5.9.

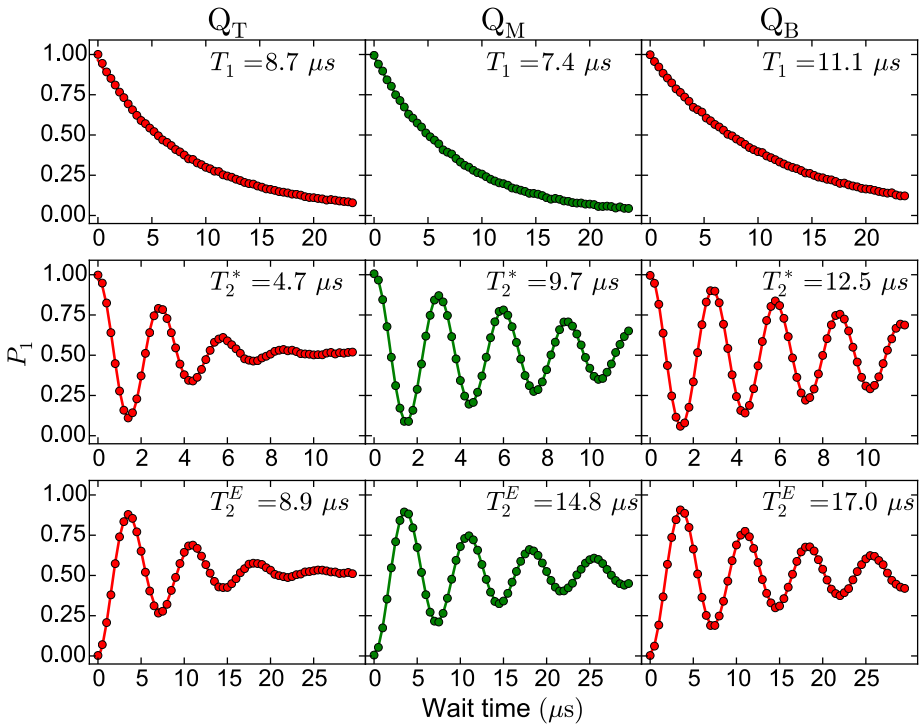

Figure 5.9: *Measurements of relaxation (T_1, top), Ramsey dephasing (T_2^*, middle) and echo dephasing ($T_{2,\text{echo}}$, bottom) times for the three qubits at the bias point. When measuring Q_T or Q_B, the other qubit is detuned by −50 MHz to suppress cross-coupling effects. Ramsey fringes for Q_T (middle, left panel) fit better to a Gaussian (shown) than an exponential decay, reflecting the susceptibility of Q_T to low-frequency flux noise away from its sweet-spot. P_1 denotes excited-state population.*

5.5.2 *Experimental Setup*

The chip is anchored to a copper cold-finger connected to the mixing chamber of a Leiden Cryogenics CS81 ^{3}He/^{4}He dilution refrigerator with 7 mK base temperature. A copper can seals the sample space, with an inner surface that is coated with a mixture of Stycast 2850 and silicon carbide granules (15 to 1000 nm diameter) used for infrared absorption [134]. The copper can is in turn magnetically shielded by an aluminum enclosure and two outer Cryophy enclosures (1 mm thick) [117].

A complete wiring schematic showing all cryogenic and room-temperature components is shown in Figure 5.10. The four analog channels of the Tektronix AWG5014C create the in-phase and in-quadrature pulses for Q_T and Q_B by single-sideband modulation of a common carrier. Because single-sideband modulation requires two AWG channels to modulate an IQ mixer, independent derivative-removal-via-adiabatic-gate (DRAG) tuning with the VSM therefore requires four AWG channels, irrespective of the number of qubits. The VSM can be scaled up to

many output channels, and direct hardware savings are realized as soon as three or more same-frequency qubits are driven by a single set of AWG inputs. These pulses are sent into ports 1 and 2 of the VSM. The VSM combines these pulses with individually tuned insertion loss and phase to each of two outputs (labelled T and B). Input-output combinations can be switched on nanosecond timescales using the gate inputs of the VSM, provided by digital markers of the AWG5014C. A second AWG5014C with the appropriate carrier frequency is used to excite transmons Q_T and Q_B to the second-excited state (Section 5.8), to pulse measurement tones, and to trigger the AlazarTech ATS9870 acquisition card.

5.6 VECTOR SWITCH MATRIX

5.6.1 *Measured isolation*

To characterize the isolation of the VSM in the range 4 to 8 GHz, we have measured the insertion loss between all input (1 and 2) and output ports (T and B) with static settings at the two gate inputs (Figure 5.11). Ideally, each gate activates (on state) and deactivates (off state) the link of both inputs 1 and 2 to one output, independent of the other gate. As shown in Figure 5.11, the typical relative isolation with the relevant gate in the off state is ~ 50 dB.

5.6.2 *Individual qubit tune-up*

The VSM enables independent control of the on/off state, insertion loss and phase for every input-output combination. We exploit this feature to perform DRAG-compensated pulses on Q_T and Q_B, that are individually tailored for each qubit. Different types of gate errors, such as non-ideal in-phase and in-quadrature amplitudes, can be distinguished using an AllXY sequence [180], consisting of 21 combinations of two pulses drawn from the set $\left\{I, X_\pi, Y_\pi, X_{\pi/2}, Y_{\pi/2}\right\}$ (Table 5.2). Figure 5.12 shows AllXY sequence results for Q_T and Q_B as the amplitude of each quadrature on Q_T is varied independently. While the AllXY signature of Q_T reveals changing levels of amplitude and phase errors, there is no noticeable change in the AllXY signature of Q_B. This demonstrates the use of the VSM for individual tune-up of pulses for same-frequency qubits.

5.7 PULSE-CALIBRATION ROUTINES

We tune up qubit pulses by alternating the calibration of in-phase and in-quadrature pulse amplitudes until a simultaneous optimum is found. The two calibration routines are discussed below.

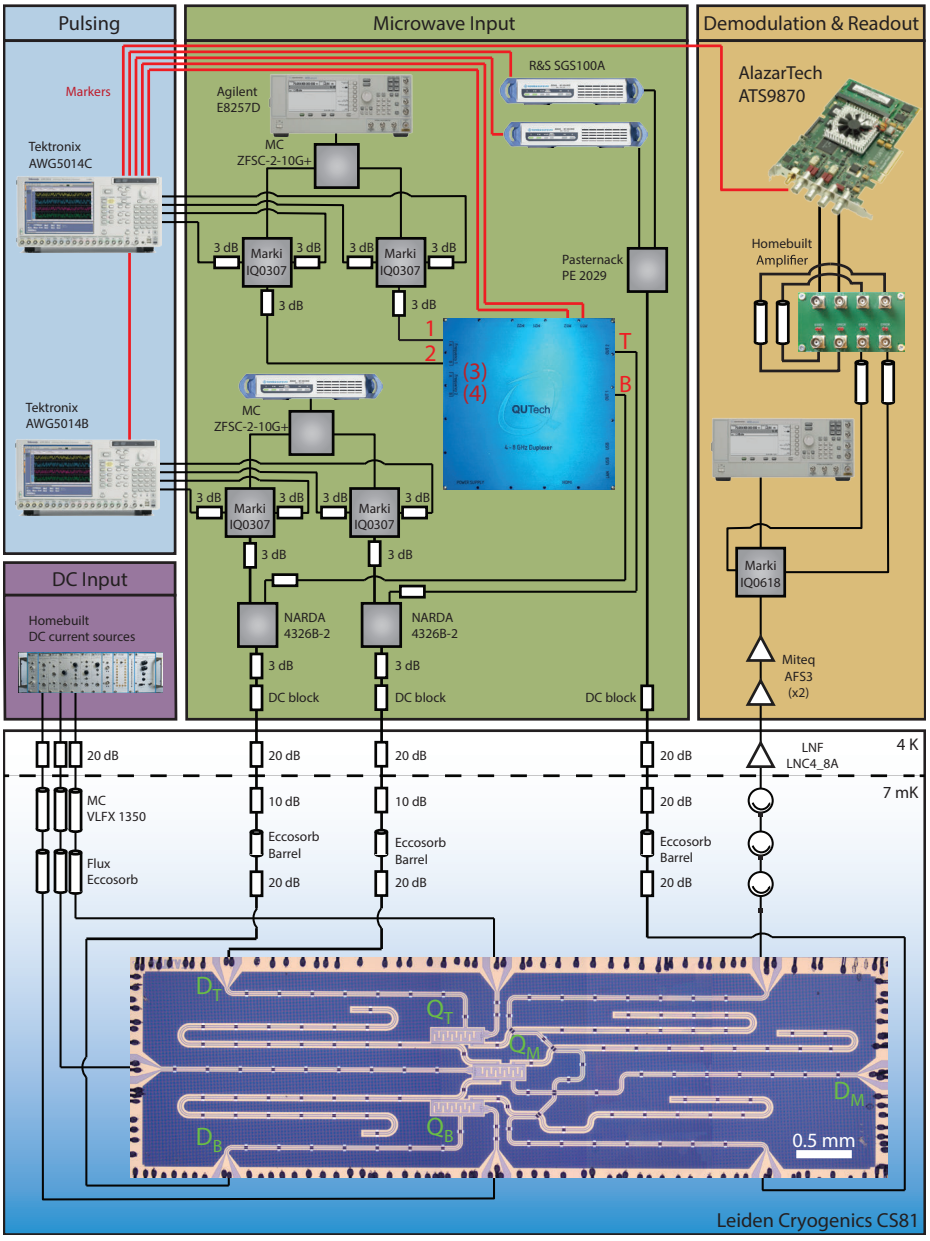

Figure 5.10: *Detailed schematic of the experimental setup and optical image of the chip (installed in a Leiden Cryogenics CS81 dilution refrigerator). Note that while our VSM has two pairs of analog inputs [(1,2) and (3,4)] and four gate inputs (activating links from each pair to each output), the pair (3,4) and its associated gate inputs are not used throughout this experiment.*

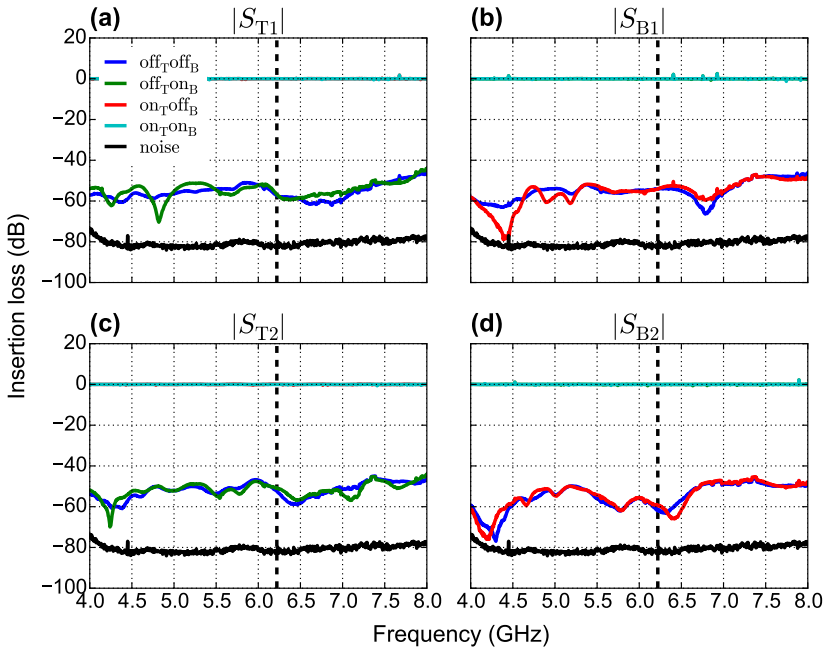

Figure 5.11: *Insertion loss between inputs and outputs of the VSM for four static combinations of the gate inputs. The insertion loss is measured relative to the level with both gate inputs activated ($\mathrm{on_T on_B}$). The black curves indicate the noise background in our scalar network analyzer measurement. The dashed vertical lines indicate the common frequency (*6.220 GHz*) of Q_T and Q_B at the bias point.*

ID	Ideal P_1	Pulses		ID	Ideal P_1	Pulses	
		First	Second			First	Second
1	0	I	I	12	0.5	Y_π	$Y_{\pi/2}$
2	0	X_π	X_π	13	0.5	X_π	$X_{\pi/2}$
3	0	Y_π	Y_π	14	0.5	$X_{\pi/2}$	X_π
4	0	X_π	Y_π	15	0.5	X_π	$X_{\pi/2}$
5	0	Y_π	X_π	16	0.5	$Y_{\pi/2}$	Y_π
6	0.5	I	$X_{\pi/2}$	17	0.5	Y_π	$Y_{\pi/2}$
7	0.5	I	$Y_{\pi/2}$	18	1	I	X_π
8	0.5	$X_{\pi/2}$	$Y_{\pi/2}$	19	1	I	Y_π
9	0.5	$Y_{\pi/2}$	$X_{\pi/2}$	20	1	$X_{\pi/2}$	$X_{\pi/2}$
10	0.5	$X_{\pi/2}$	Y_π	21	1	$Y_{\pi/2}$	$Y_{\pi/2}$
11	0.5	$Y_{\pi/2}$	X_π				

Table 5.2: *The 21 two-pulse combinations comprising the AllXY pulse sequence [180].*

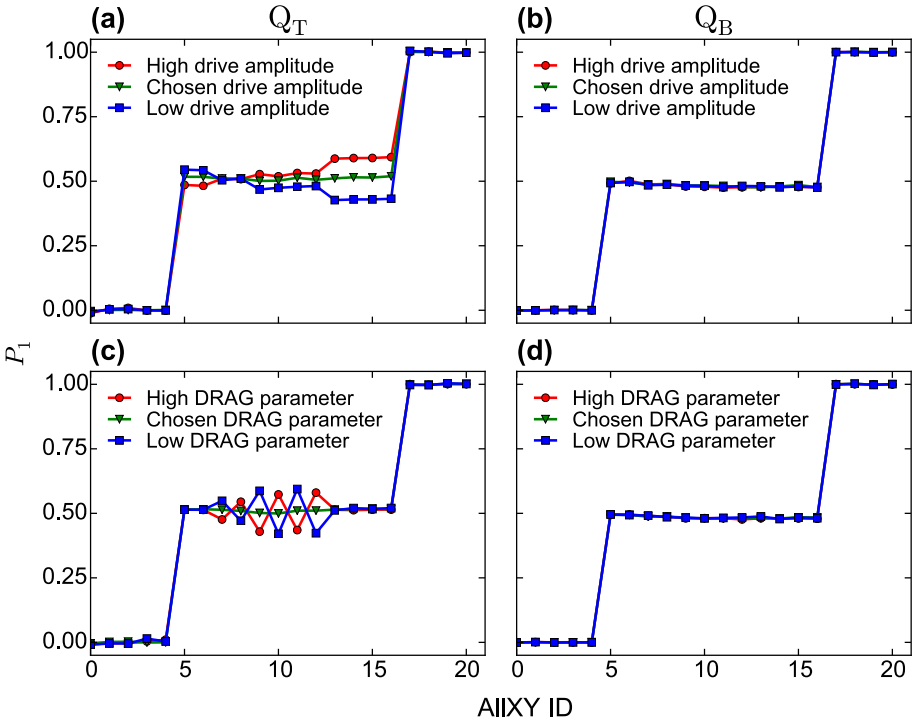

Figure 5.12: *AllXY results for* Q_T *(left) and* Q_B *(right), as the in-phase amplitude (top) or in-quadrature amplitude (bottom) of* Q_T *pulses is varied. During each measurement, both qubits are driven simultaneously, but read out individually. The AllXY results of* Q_B *all overlap independent of the setting on* Q_A*, showing independent control of pulse parameters for each qubit.*

5.7.1 *Accurate in-phase pulse amplitude calibration*

The in-phase quadrature amplitude is calibrated by first applying a $\pi/2$ pulse to the qubit, followed by a train of π pulses. The pulse sequence is $(X_\pi)^{2N} X_{\pi/2} |g\rangle$, where $|g\rangle$ is the qubit ground state and $N \in [0, 49]$. In the absence of gate errors and decoherence, the driven qubit would end on the equator of its Bloch sphere for all N. However, over- or under-driving produces a positive or negative initial slope on P_1 versus N, respectively (Figure 5.13). We choose the in-quadrature amplitude that minimizes the absolute slope.

5.7.2 *DRAG-parameter calibration*

To minimize phase errors resulting from the presence of the second- and higher-excited states, we optimize the scaling of the in-quadrature pulse. As in conventional DRAG [76, 77], we choose as the envelope of the in-quadrature pulse the derivative of the Gaussian envelope on the in-phase pulse. The DRAG scaling parameter is calibrated using the method detailed in ref. 180. Specifically, we measure the

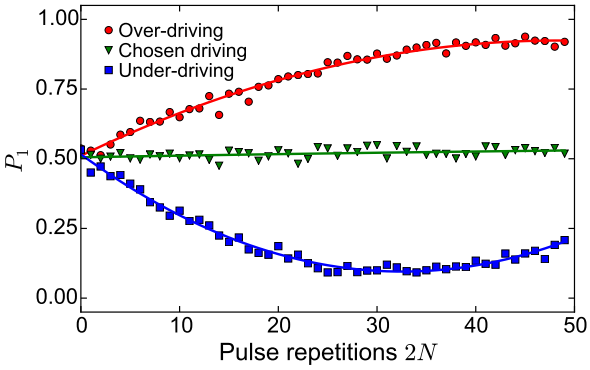

Figure 5.13: *Fine calibration of pulse amplitude by initial $\pi/2$ pulse, followed by $2N$ repeated π pulses. The initial slope determines if the qubit is over- (positive slope) or under-driven (negative slope).*

difference in excited-state population produced by the $Y_\pi X_{\pi/2}$ and $X_\pi Y_{\pi/2}$ pulse combinations (AllXY ID 10 and 11). Ideally, for both, the final qubit state would lie on the equator. However, any phase error shifts the final excited-state population in opposite directions in these cases. We choose the DRAG scaling parameter minimizing this shift.

5.8 LEAKAGE TO SECOND EXCITED STATE

Leakage is fundamentally different from unitary qubit errors. To quantify leakage, we monitor the populations P_i of the three lowest energy states ($i \in \{0, 1, 2\}$) during RB and calculate the average values $\langle P_i \rangle$ over all seeds. To do this, we calibrate the average signal levels V_i for the transmons in level i, by performing a Rabi experiment on the 1–2 transition with the qubit starting in $|1\rangle$ (Figure 5.14). The Rabi oscillation experiment is performed with and without a final X_π pulse on the 0–1 transition to confirm that we get a consistent picture. We use the calibrated π pulse on the 1–2 transition to obtain calibration points for the three state readout. Each RB measurement is then performed twice, the second time with an added final π pulse on the 0–1 transition. This final π pulse swaps P_0 and

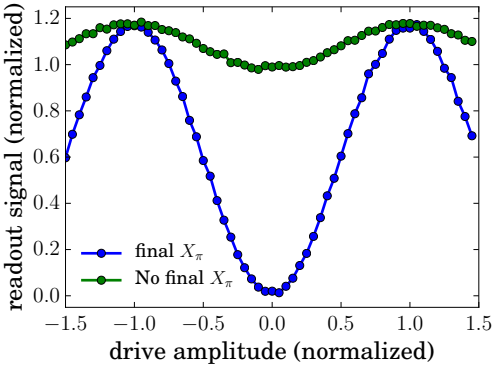

Figure 5.14: *Result of a Rabi measurement of the 1–2 transition with the qubit starting in $|1\rangle$. The readout signal is normalized such that 0 corresponds to the nominal ground state and 1 to the nominal first excited state. The $|2\rangle$ state clearly gives a readout signal close to but slightly beyond the $|1\rangle$ signal as expected.*

P_1, leaving P_2 unaffected. Under the assumption that higher levels are unpopulated ($P_0 + P_1 + P_2 = 1$),

$$\begin{bmatrix} V_0 - V_2 & V_1 - V_2 \\ V_1 - V_2 & V_0 - V_2 \end{bmatrix} \begin{bmatrix} P_0 \\ P_1 \end{bmatrix} = \begin{bmatrix} S - V_2 \\ S' - V_2 \end{bmatrix}, \tag{5.3}$$

where S (S') is the measured signal level without (with) final π pulse. The populations are extracted by matrix inversion. We measured leakage using the averaged readout signals, because in this experiment the single-shot readout fidelity was low, as no quantum limited amplifier was used. With good single shot fidelity, it is also possible to distinguish the $|2\rangle$ state in a single shot as done in [78]. In that case, performing each sequence a second time with a final π pulse is not necessary.

Measuring $\langle P_2 \rangle$ as a function of the number of Clifford gates allows us to estimate an average leakage per Clifford, κ_{CL}. Because the populations are ensemble averages over different random seeds, we assume that leakage of the average qubit-space populations to $\langle P_2 \rangle$ is incoherent, and, provided $\langle P_2 \rangle$ remains small (κ_{CL} small), we also assume that leakage is irreversible. We therefore model leakage using the following difference equation for $\langle P_2 \rangle$:

$$\langle P_2[m+1] \rangle - \langle P_2[m] \rangle \simeq \kappa_{\mathrm{CL}} - \frac{\tau_{\mathrm{CL}}}{T_{2\to1}} \langle P_2[m] \rangle, \tag{5.4}$$

where $T_{2\to1}$ is the second- to first-excited-state relaxation time and $\tau_{\mathrm{CL}} = \langle N_{\mathrm{p}} \rangle \tau_{\mathrm{P}}$ is the time per Clifford gate. Assuming no initial population in the second-excited state, the solution is Equation (5.2), which shows good agreement with measured data. We extract κ_{CL} by fitting Section 5.8 to $\langle P_2 \rangle$ data. $T_{2\to1}$ is obtained from the best-fit decay constant (not directly measured) and κ_{CL} from the best-fit prefactor.

5.9 CROSS-DRIVING EFFECTS

The isolated single-qubit control experiments [Figure 5.7(g,h)] show that significant spurious excitations can build up in the idling qubit over the course of the long gate sequences tested in RB (particularly in the case of idling $\mathrm{Q_B}$ while driving $\mathrm{Q_T}$). It may therefore initially be somewhat surprising that virtually the same individual qubit-control performance is achieved in both selective-broadcasting (Figure 5.7, and global-broadcasting (Figure 5.6) scenarios. As discussed above, the observed cross-excitation is unlikely to result from cross-coupling, primarily because a symmetrical quantum coupling should not result in strongly asymmetric effects on the different qubits. We show in Section 5.9.1 that the results are, however, consistent with the effects of cross-driving by numerically simulating RB with cross-driving under experimentally realistic conditions (using independently measured qubit and cross-driving parameters). Simulations are performed using QuTiP [143]. In Section 5.9.2, we show that the residual cross-driving effects can be largely compensated for by an appropriate choice of Clifford decompositions.

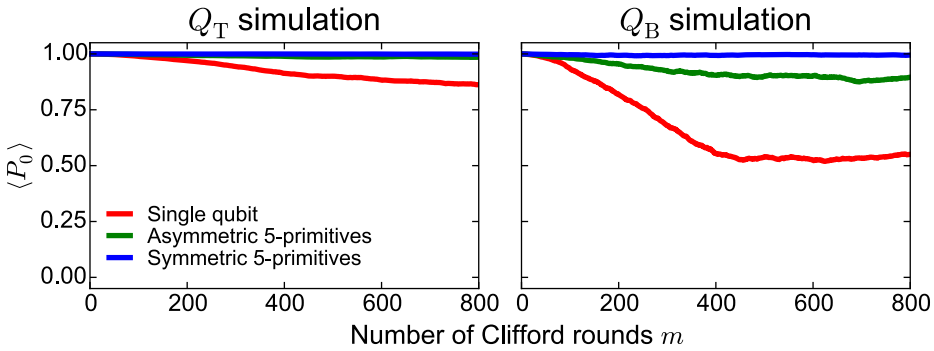

Figure 5.15: *Simulation of cross-driving effects during RB. The results shown are averaged over ten runs, using the single-qubit minimal-set decomposition (red), and using the selective-broadcasting asymmetric and symmetric 5-primitives schemes (green and blue, respectively). Cross-driving effects are largely suppressed in the 5-primitives schemes by choosing the five pulse primitives such that constituent pulses largely cancel out. The symmetric 5-primitives scheme further reduces cross-driving effects by alternating between the five pulse primitives and the inverse pulses.*

5.9.1 *Simulating cross-driving*

We model our system as two uncoupled qubits, Q_T and Q_B, subject to T_1 relaxation (with corresponding relaxation times) and cross-driving. We approximate the system dynamics using instantaneous unitary pulse operators from the standard Pauli set $\{X_\pi, Y_\pi, X_{\pm\pi/2}, Y_{\pm\pi/2}\}$ with 20 ns delays of T_1-only qubit relaxation between pulses implemented using a master equation. When applying a pulse to one qubit, cross-driving of the other qubit is implemented by applying a pulse with the same rotation axis, but with the original rotation angle multiplied by the relevant cross-driving ratio. We note that also trying to model the effects of qubit dephasing using a simple master equation does not produce RB data consistent with the experimental observations (Figure 5.5 and Figure 5.7). This reflects the non-uniform phase noise spectrum which affects the transmon qubit. The long RB pulse sequences consisting of π and $\pi/2$ pulses around the X and Y axes seem to provide some form of dynamical decoupling which makes the RB measurements robust to qubit dephasing. As will be seen, the experimental results can be well modelled using only T_1-type noise processes.

Randomized benchmarking is implemented by generating independent Clifford sequences for each qubit. We decompose Clifford gates using either the minimal set decomposition or one of the selective-broadcasting schemes. Figure 5.15 shows simulated results of cross-driving for the isolated single-qubit control scenario reported in Figure 5.3. In this section, we are only concerned with the red curves, which correspond to implementing single-qubit RB with the standard set of pulse decompositions [167]. These simulations can be compared directly with the curves in Figure 5.5. While the maximum excitation population observed in the simulations

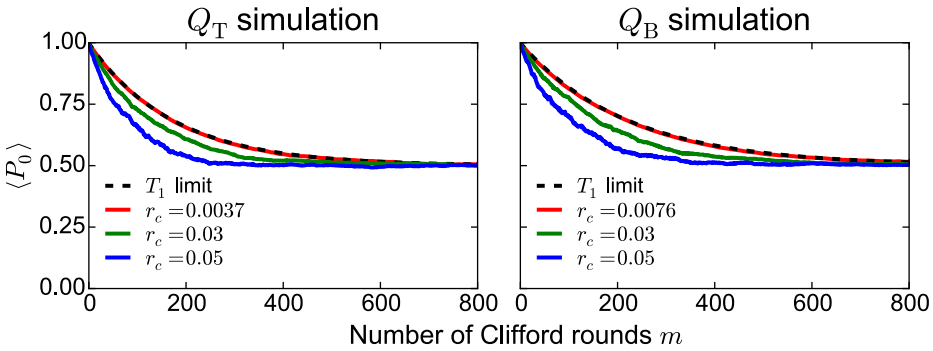

Figure 5.16: *Simulation of sequential (interleaved) RB for several cross-driving ratios. For each cross-driving ratio, 50 simulation runs were performed, using sequential RB up to* $m = 800$ *Clifford rounds. Under the cross-driving levels pertaining in our experiments (0.0037 and 0.0076 for* Q_T *and* Q_B*, respectively), the error per Clifford for the idling operation is dominated by the effects of* T_1 *relaxation as calculated from Equation* (5.1).

is larger than the value observed in the experiments, the simulations for both qubits show the same qualitative behaviour as the measured data. The quantitative difference may be explained by the fact that the direct measurements of cross-driving were made at a different time from the main measurement run and we observed some small fluctuations in cross-driving levels over time.

As discussed above, while the plots of cross-excitation during RB are useful diagnostics of the presence of a spurious cross-driving effect, they may give a misleading impression when presented in parallel with RB results. Although the decay curves look superficially similar, they should not be interpreted in the same way. By contrast, the technique of interleaved RB (IRB), which was introduced to enable rigorous quantification of the performance of individual gates, allows us to calculate a meaningful error per Clifford for the idling operation [175]. In IRB, the usual random sequence of Cliffords is alternated with identical repetitions of an individual gate. By comparing the interleaved decay rate with the decay rate for a standard RB measurement, it is possible to calculate a robust error per gate for the individual gate in question. In this context, the target gate is the nominal identity operation on one qubit which results from a random Clifford being applied to the other qubit. The IRB pulse sequence is therefore identical to the sequence implemented in the sequential selective-broadcasting scheme (see Figure 5.7). We use the formulas in reference 175 to calculate the idling error per Clifford, but for these simulations, the performance of sequential selective-broadcasting already provides a simple way to assess the performance of cross-excitation during idling. Figure 5.16 shows that idling performance as quantified by RB is limited mainly by T_1 relaxation. Finally, when identical gate sequences are being applied to both qubits, cross-driving will result in a small amount of over-driving on each qubit (overdriving ratio r_o), which

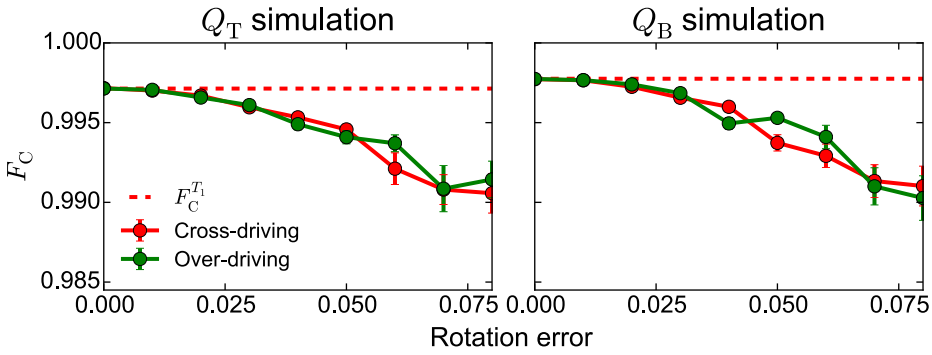

Figure 5.17: *Simulations of Clifford fidelity F_C as a function of the cross-driving ratio (r_c: red) and the relative over-driving rotation error (r_o-1: green). For each error type, 50 simulation runs were performed, using sequential RB on both qubits simultaneously up to $m = 800$ Clifford rounds, after which F_C was extracted from an exponential fit to averaged data. The T_1 limit [Equation (5.1)] is given by a horizontal dashed line. The data shows that F_C is first-order insensitive to both cross-driving and to over-rotations.*

would also look like an error in pulse rotation angle. Figure 5.17 shows that the Clifford error is insensitive to both cross-driving and over-driving to first order.

5.9.2 *Making pulse sequences robust to cross-driving*

We have already shown that cross-excitation does not have a dominant effect on single-qubit control in both global and selective broadcasting. We show here that any residual effect can be largely eliminated also while a qubit is idling by choosing robust pulse sequences for decomposing the Clifford gates.

If a qubit is idle, every pulse that is applied to the driven qubit rotates the idle qubit by an amount depending on the cross-driving ratio. The random application of successive pulses to the driven qubit can therefore be viewed as a random walk for the idle qubit. As we will discuss in more detail in Section 5.10, there are many ways to compose a given Clifford gate from a small set of standard rotations. By choosing the constituent pulses in such a way that their combined application largely cancels out, cross-driving effects can be greatly reduced. In the standard set of Clifford decompositions [167], the decompositions involve a majority of pulses rotating in the positive direction, biasing the random walk and producing a pronounced net cross-driving effect. This effect can be countered by choosing decompositions which minimize the bias. We have implemented this in the 5-primitives scheme, by choosing the first three pulses, $\{X_{\pi/2}, Y_{\pi/2}, X_{\pi/2}\}$, to be positive rotations, and the last two, $\{X_{-\pi}, Y_{-\pi}\}$, to move in the negative direction. Even though the pulse subset that is applied depends on the Clifford chosen, the pulses still largely cancel out after applying many Cliffords. Furthermore, as the single-qubit Clifford operations form a group, the inverse of all Cliffords also form the Clifford group. The complete inverse of the five pulse primitives, $\{X_{\pi}, Y_{\pi}, X_{-\pi/2}, Y_{-\pi/2}, X_{-\pi/2}\}$, can therefore also generate each

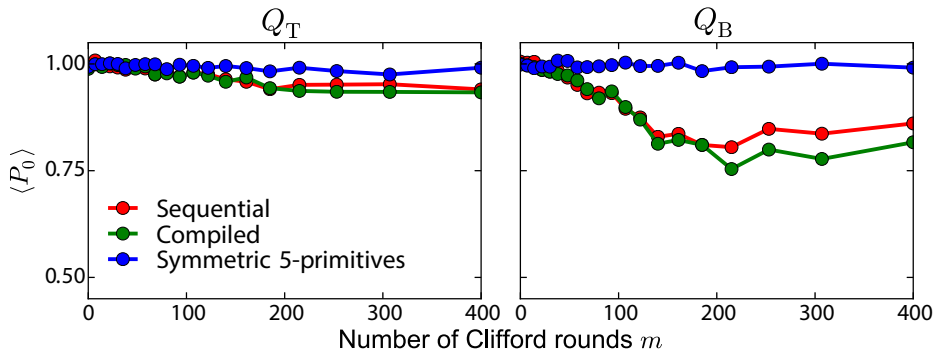

Figure 5.18: *Measured cross-driving results when performing selective broadcasting. Even though the selective broadcasting schemes are meant for multiple qubits, the markers of the measured qubit are turned off to measure cross-driving effects. The cross-driving effects of* Q_B *are stronger than for* Q_T*, in agreement with single-qubit results. With pulse decompositions whose cumulative effect largely cancels out, cross-driving is strongly reduced in the 5-primitives method.*

of the 24 Cliffords using an appropriate subset of the pulses. By alternating between the normal five-pulse primitives and the inverted five pulses, cross-driving effects can be further reduced. (In fact, we note that this exactly eliminates all cross-driving that occurs via leakage in the VSM, because all pulses are always present at that distribution stage.) We refer to this as the symmetric 5-primitives technique and this is the technique we implement in the main experiments described in Figure 5.7. Our simulations in Figure 5.15 show that the asymmetric 5-primitives technique already dramatically reduces the effect of cross-driving, and in the case of isolated single-qubit control, cross-driving is effectively eliminated completely using the symmetric 5-primitives scheme. This is also confirmed by measurements of cross-driving for the three selective-broadcasting schemes (Figure 5.18), where we implement the symmetric 5-primitives technique. While we have only demonstrated this technique for the 5-primitives scheme, it could also be relatively straightforwardly applied to the sequential scheme, but the far better scaling of the 5-primitives scheme make it more interesting for scaling up to larger system sizes.

5.10 CLIFFORD PULSE DECOMPOSITION

When using a selective broadcasting architecture to send pulse sequences to multiple qubits, pulses can be directed to any subset of the qubits, but distinct pulses may not be applied simultaneously. The decompositions of the 24 single-qubit Clifford gates into a minimal set of $\pi/2$ and π pulses and into the 5-primitives scheme are shown in Table 5.3. We note that the specific choice of pulse primitives in the 5-primitives scheme is not unique, but at least five are required (four pulses allow a maximum of 16 unique gate decompositions, compared with the 24 single-qubit Cliffords).

Clifford ID	Minimal set decomposition			5-primitives decomposition				
	First	Second	Third	$X_{\pi/2}$	$Y_{\pi/2}$	$X_{\pi/2}$	$X_{-\pi}$	$Y_{-\pi}$
1	I			0	0	0	0	0
2	$Y_{\pi/2}$	$X_{\pi/2}$		0	1	1	0	0
3	$X_{-\pi/2}$	$Y_{-\pi/2}$		1	1	0	1	0
4	X_{π}			0	0	0	1	0
5	$Y_{-\pi/2}$	$X_{-\pi/2}$		0	1	1	0	1
6	$X_{\pi/2}$	$Y_{-\pi/2}$		1	1	0	0	1
7	Y_{π}			0	0	0	0	1
8	$Y_{-\pi/2}$	$X_{\pi/2}$		0	1	1	1	1
9	$X_{\pi/2}$	$Y_{\pi/2}$		1	1	0	0	0
10	X_{π}	Y_{π}		0	0	0	1	1
11	$Y_{\pi/2}$	$X_{-\pi/2}$		0	1	1	1	0
12	$X_{-\pi/2}$	$Y_{\pi/2}$		1	1	0	1	1
13	$Y_{\pi/2}$	X_{π}		0	1	0	1	0
14	$X_{-\pi/2}$			0	0	1	1	0
15	$X_{\pi/2}$	$Y_{-\pi/2}$	$X_{-\pi/2}$	1	1	1	0	1
16	$Y_{-\pi/2}$			0	1	0	0	1
17	$X_{\pi/2}$			0	0	1	0	0
18	$X_{\pi/2}$	$Y_{\pi/2}$	$X_{\pi/2}$	1	1	1	0	0
19	$Y_{-\pi/2}$	X_{π}		0	1	0	1	1
20	$X_{\pi/2}$	Y_{π}		1	0	0	0	1
21	$X_{\pi/2}$	$Y_{-\pi/2}$	$X_{\pi/2}$	1	1	1	1	1
22	$Y_{\pi/2}$			0	1	0	0	0
23	$X_{-\pi/2}$	Y_{π}		1	0	0	1	1
24	$X_{\pi/2}$	$Y_{\pi/2}$	$X_{-\pi/2}$	1	1	1	1	0

Table 5.3: *Two decompositions of the 24 single-qubit Clifford gates. The first, taken from ref. 167, minimizes the number of $\pi/2$ and π pulses around the $\pm x$ and $\pm y$ axes. The second is our decomposition into 5 primitives. Pulses are applied from left to right.*

5.10.1 *Finding the optimal pulse sequence*

In compiled selective broadcasting, the total number of pulses required to implement single-qubit gates on all qubits of a multi-qubit system is minimized by searching all possible combinations of single-qubit Clifford decompositions and grouping together like pulses where possible. In this section, we introduce an algorithm for determining the shortest compiled pulse sequence implementing independent single-qubit Clifford gates on n qubits.

On average, there are approximately 38 distinct decompositions for each single-qubit Clifford gate, given the basis set of X and Y pulses: $\{I, X_{\pi}, Y_{\pi}, X_{\pm\pi/2}, Y_{\pm\pi/2}\}$, resulting in approximately 38^n different decompositions for a given n-qubit combi-

nation of Cliffords. Here, we only consider sequences of up to four pulses, because the 5-primitives decomposition identified in Table 5.3 already provides a recipe for decomposing an arbitrary n-qubit Clifford combination into five pulses. We do not include trivial decompositions where sequential pulses cancel out.

Given a particular choice of n Cliffords $\left(C_{\alpha_1}, \ldots, C_{\alpha_n}\right)$, where α_i is the Clifford ID for qubit i, we write a specific decomposition as $\left(\left(P_1^1, ..., P_{m_1}^1\right), ..., \left(P_1^n, ..., P_{m_n}^n\right)\right)$, where P_j^i is the jth of m_i pulses which implement C_{α_i}. While this already fixes the order in which pulses must be applied to individual qubits, we still have the freedom to choose in which order the distinct pulses are applied to different qubits. For each possible decomposition, we use the following recursive algorithm to search and minimize over all possible pulse orderings.

We first define an empty broadcasting sequence $\boldsymbol{P}_{\text{seq}}$ to store the compiled multi-qubit pulse sequence. In order to convert from parallel single-qubit pulse sequences to the single broadcasting sequence $\boldsymbol{P}_{\text{seq}}$, we define a vector of indices $\boldsymbol{\beta} = (\beta_1, \ldots, \beta_n)$ to store the current position in each single-qubit sequence. Initially, $\boldsymbol{\beta} = (1, ..., 1)$. At each instant, $\boldsymbol{P}_{\boldsymbol{\beta}} = (P_{\beta_1}^1, \ldots, P_{\beta_n}^n)$ contains the next pulses to be applied to each qubit. When $\beta_i = m_i + 1$, the pulse sequence for that qubit is completed, and so there is no P_{β_i} to be added to $\boldsymbol{P}_{\boldsymbol{\beta}}$. The recursive part of the algorithm then proceeds as follows:

1. Define $\boldsymbol{P}'_{\boldsymbol{\beta}}$ to be the set of distinct pulses in $\boldsymbol{P}_{\boldsymbol{\beta}}$.

   If: $\boldsymbol{P}'_{\boldsymbol{\beta}}$ is empty, store the number of pulses in $\boldsymbol{P}_{\text{seq}}$ and abort this recursion branch ($\boldsymbol{P}_{\text{seq}}$ is a completed pulse sequence such that all Cliffords are applied to the corresponding qubits).

   Else: Continue.

2. For each pulse P in $\boldsymbol{P}'_{\boldsymbol{\beta}}$, perform the following steps:

   (i) Append P to $\boldsymbol{P}_{\text{seq}}$;

   (ii) Copy indices $\boldsymbol{\beta}$ to $\boldsymbol{\beta}^{\text{new}} = \left(\beta_1^{\text{new}}, ..., \beta_n^{\text{new}}\right)$;

   (iii) For all indices i for which $P_{\beta_i}^i = P$, increase the index $\beta_i^{\text{new}} = \beta_i + 1$;

   (iv) Recursively loop to step 1 using the new indices $\boldsymbol{\beta}^{\text{new}}$ for $\boldsymbol{\beta}$.

After considering all possible pulse sequences and looping over all possible decompositions, choose the sequence with the minimum number of pulses N_{p} in $\boldsymbol{P}_{\text{seq}}$.

This algorithm determines the minimum number of pulses N_{p} required to implement a given n-qubit combination of single-qubit Clifford gates. However, this becomes prohibitively resource intensive as the number of qubits increases. It is therefore important to assess how the performance of the optimal compiled decomposition compares with the 5-primitives decomposition, which can be applied to any number of qubits without any extra overhead in resources (in neither calculation time nor sequence length). To do this, we use the average number of pulses $\langle N_{\text{p}} \rangle$ required per n-qubit combination of Cliffords (per Clifford).

Table 5.4: *The average number of pulses $\langle N_p \rangle$ required to perform one Clifford gate on each of n qubits in compiled selective broadcasting. Exact values were obtained for $1 \leq n \leq 5$ in under two hours, using the outlined optimizations. Approximate values were obtained for $5 \leq n \leq 10$ using random sampling. These results are plotted in Figure 5.4.*

Exact calculation		Random sampling	
n	$\langle N_p \rangle$	n	$\langle N_p \rangle$
1	1.875	5	4.139 (2)
2	2.925	6	4.380 (12)
3	3.521	7	4.570 (15)
4	3.874	8	4.721 (10)
5	4.137	9	4.808 (14)
		10	4.857 (24)

In the case of compiled selective broadcasting, finding $\langle N_p \rangle$ requires minimizing the sequence length for all 24^n possible Clifford combinations. This problem again scales exponentially with n. For example, for $n = 5$ qubits, this requires $24^5 \cdot 38^5 \approx 6.3 \cdot 10^{14}$ repetitions of the complete recursive search described above. Nevertheless, by employing a number of optimizations desribed in the next section, we have exactly calculated $\langle N_p \rangle$ for $1 \leq n \leq 5$ qubits in under 2 hours. Using random sampling (finding the shortest pulse sequence for a random sample of Clifford combinations), we also approximated $\langle N_p \rangle$ for $5 \leq n \leq 10$. Exact and approximate results for $n = 5$ agree. As shown in Table 5.4, the improvement offered by compiled selective broadcasting over the 5-primitives method is already less than one pulse per Clifford and continues to decrease rapidly. Considering how badly the resource overhead scales for increasing numbers of qubits for finding a compiled sequence, it is questionable whether compiling offers any significant benefit over using the prescriptive 5-primitives approach when scaling up to larger system sizes.

5.10.2 *Optimizations for the Clifford compilation algorithm*

In the first optimization, we place an upper bound N^{ub} on the pulse sequence length. The upper bound N^{ub} is given by the minimum number of pulses found so far that can compile a given Clifford combination. At each stage, the algorithm checks if the sum of the pulses in P_{seq} and all distinct pulses left is equal to or greater than N^{ub}. If this is the case, a shorter combination of pulses using P_{seq} is not possible, so we stop considering this sequence and proceed to the next one. Initially $N^{ub} = 5$, as the 5-primitives method proves that there is always a decomposition of an arbitrary number of Cliffords into 5 pulses. Note that, as the limit N^{ub} moves down, the frequency at which the algorithm stops considering sequences increases.

The second optimization relies on decompositions with fewer pulses being more likely to result in an optimal Clifford compilation. The decompositions of every Clifford are therefore arranged in ascending number of pulses. The first decompositions compared are then those with the minimum number of pulses; these have the highest probability of finding an optimal Clifford compilation. Even if an optimal Clifford compilation is not found, it is more likely that N^{ub} will be low. This optimization is especially effective in combination with the first optimization.

The third optimization places a lower bound N^{lb} on the number of pulses. For a given Clifford combination $\left(C_{\alpha_1}, \ldots, C_{\alpha_n}\right)$, N^{lb} is found by looking at the minimum number of pulses N_{p} previously found for all $n-1$ Clifford subsets. Since N_{p} for the n Cliffords can never be less than N_{p} for any of the $n-1$ Clifford subsets, the maximum length of the $n-1$ Clifford subsets therefore places a lower bound N^{lb} on N_{p} for the n Cliffords. This means that if a pulse sequence is found whose length is equal to N^{lb}, it is an optimal Clifford compilation, and all further search is aborted. This is in contrast to the first optimization, where only the particular sequence of pulses is aborted upon reaching N^{ub}. Furthermore, as n increases, it becomes increasingly likely that the lower bound is 5. In this case, $N^{\mathrm{lb}} = N^{\mathrm{ub}}$, and so the 5-primitives method is an optimal Clifford compilation. This optimization results in the largest gain in computation time, by several orders of magnitude.

In the fourth and most complicated optimization, all decompositions composed of three pulses or less are separated from those composed of four pulses. First, all combinations of Clifford decompositions composed of three pulses or less are compared. This reduces the average number of decompositions per Clifford, from 38 to 7, resulting in an exponentially reduced number of total decomposition combinations. It is, however, not always the case that the optimal Clifford compilation is found using only up to three pulses per decomposition; sometimes optimal Clifford compilations requires that one of the decompositions is composed of four pulses. However, after comparing decompositions of three pulses or less, these four-pulse decompositions only need to be considered when $N^{\mathrm{lb}} \leq 4$ and $N^{\mathrm{ub}} = 5$. If there is a sequence containing a four-pulse decomposition that outperforms any found using up to three-pulse decompositions and the 5-primitives method, the sequence must consist of four pulses. Only one Clifford then has a four-pulse decomposition, while all other Cliffords are subsets of these four pulses. We therefore loop, for every Clifford, over each of the four-pulse decompositions, and test whether every other Cliffords can be decomposed into a subset of these four pulses. This changes the comparison of four-pulse decompositions from scaling exponentially with n to scaling linearly.

The fifth and final optimization is only of use when all different Clifford combinations need to be considered to determine $\langle N_{\mathrm{p}} \rangle$. It stems from the observation that an optimal compilation for a certain Clifford combination $\left(C_{\alpha_1}, \ldots, C_{\alpha_n}\right)$ is the same as for any permutation of those Cliffords. We therefore only determine an optimal Clifford compilation when $\beta_1 \leq \cdots \leq \beta_n$. This reduces the number of calculations exponentially (81 times fewer computations for $n = 5$).

6

CHIP-TO-CHIP ENTANGLEMENT OF TRANSMON QUBITS USING ENGINEERED MEASUREMENT FIELDS

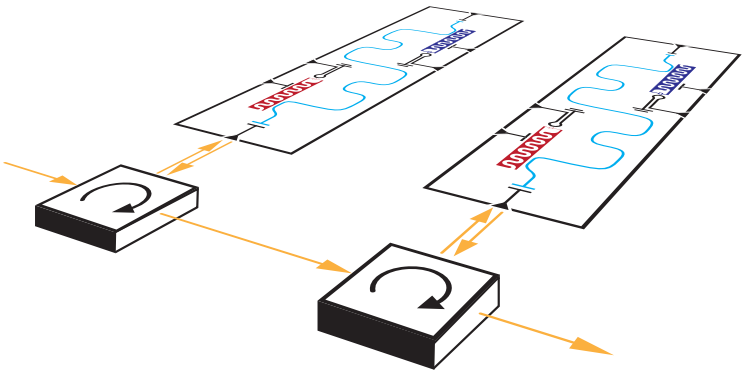

While the on-chip processing power in circuit QED devices is growing rapidly, it is an open challenge to establish high-fidelity quantum links between qubits on different chips. Here, we show entanglement between transmon qubits on different cQED chips with 49 % concurrence and 73 % Bell-state fidelity. We engineer a half-parity measurement by successively reflecting a coherent microwave field off two nearly-identical transmon-resonator systems. By ensuring the measured output field does not distinguish $|01\rangle$ from $|10\rangle$, unentangled superposition states are probabilistically projected onto entangled states in the odd-parity subspace. We use in-situ tunability and an additional weakly coupled driving field on the second resonator to overcome imperfect matching due to fabrication variations. To demonstrate the flexibility of this approach, we also produce an even-parity entangled state of similar quality, by engineering the matching of outputs for the $|00\rangle$ and $|11\rangle$ states. The protocol is characterized over a range of measurement strengths using quantum state tomography showing good agreement with a comprehensive theoretical model.

This chapter has been published with minor differences in *Physical Review B* **97**, 064508 (2018).

6.1 INTRODUCTION

The quest for large-scale quantum information processors is inspiring a multitude of architectures over a range of different qubit platforms that can be divided into two broad categories: monolithic [35, 161, 162, 192, 193] and modular [150, 194–196]. Monolithic architectures, in particular 2D lattices of qubits, are suitable for implementing the surface code [18, 19], but designers face challenges with fabrication yield, connectivity and cross-talk on large-scale devices. In contrast, modular architectures promise switchboard-like all-to-all connectivity, reduce design complexity and even correlated noise to the module scale, but face the challenge of distributing entanglement between nodes. While local entangling operations inevitably outperform their remote counterparts, the challenges of scaling up suggest that a future quantum computer will require a hybrid architecture, which balances local speed and fidelity with the benefits of modularity.

In circuit quantum electrodynamics (cQED) [160], entanglement distribution schemes have mainly relied on two mechanisms: Firstly, entanglement by measurement [181, 183] with either coherent [184, 185, 197] or Fock-states [182, 198], where a nonlocal entangling measurement is implemented by measuring photonic modes that have interacted with the qubits. Secondly, pitch-and-catch schemes [188, 199], where qubit-qubit entanglement is created by photons traveling from one qubit to another. A visual summary of the different protocols can be seen in Figure 6.1. This is by no means an exhaustive categorization – shaping the output photons could for example also help in Barrett-Kok style protocols. The Barrett-Kok protocol on the other hand does not necessarily require cavities as depicted in Figure 6.1, but they can enhance the efficiency of the protocol.

Since these protocols rely on photonic quantum information carriers, photon loss can limit either the achievable entanglement or the success rate. Modest entanglement can be bolstered by entanglement distillation to produce high-fidelity quantum links. Ultimately, the important figures of merit defining the performance of entanglement distribution protocols are entanglement generation rate and entanglement fidelity. Experiments have primarily focused on qubits embedded in separate 3D superconducting cavities [182, 184, 185], which allows separate fabrication and selection of qubits and cavities, and tuning of the cavity coupling to input ports. The effort to locally scale up to many-qubit experiments on the other hand has largely happened "on chip" [125, 153, 200, 201], where both qubits and resonators are patterned in superconducting thin films and where fast, high-fidelity multiqubit gates have been demonstrated [103]. In these 2D cQED devices, fabrication variability impedes the precise parameter matching required for many entanglement protocols, but these devices are arguably better suited for integration and scale-up. Therefore, generating rapid, high-fidelity entanglement chip-to-chip enables the exploration of interesting modular architectures in cQED.

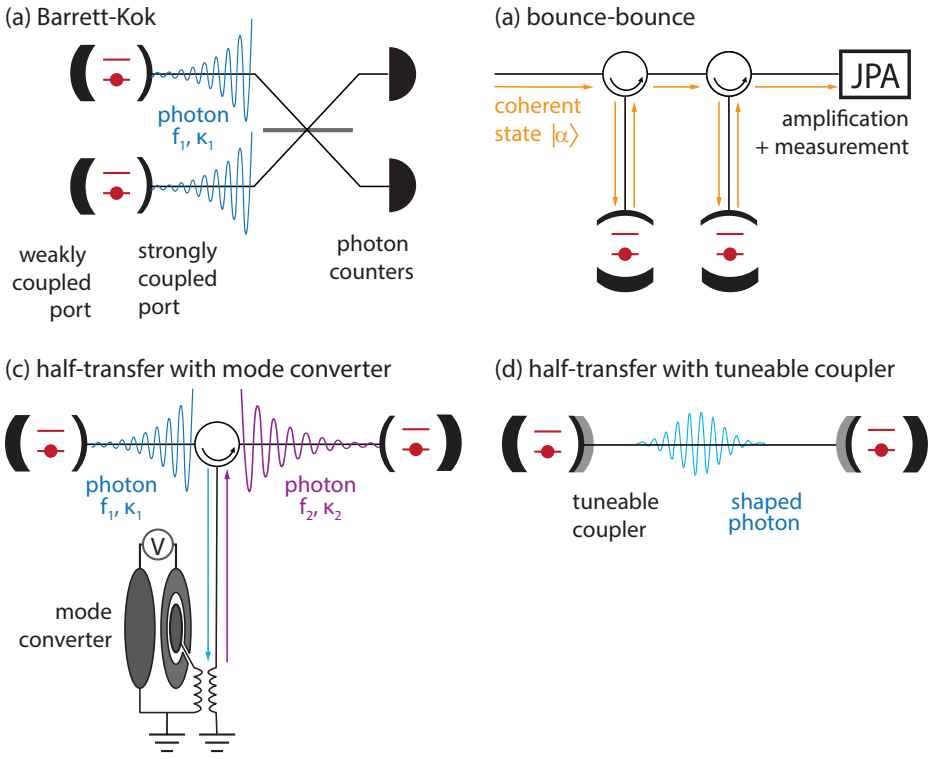

Figure 6.1: *Different schemes for remote two-qubit entanglement using traveling photons.* ***(a)*** *Barrett-Kok protocol, where qubits are made to emit into the cavity, photons leak out and are interfered on a beam splitter [181], realized in cQED using another transmon-cavity pair as a photon detector [182].* ***(b)*** *Bounce-bounce scheme as realized here [183], previously realized in cQED [184, 185].* ***(c)*** *Half transfer with a mode converter. First cavity-qubit pair is put into an equal superposition of having emitted a photon with the qubit in* $|0\rangle$ *and not having emitted with the qubit in* $|1\rangle$*. The emitted photon is reshaped to easily enter the second cavity where the entanglement is swapped to the qubit. Mode converters have been realized using electro-mechanical resonators [186], but entanglement has not yet been shown this way.* ***(d)*** *Half-transfer by controlling the emission and absorption process. Preliminary work using a SQUID-tunable coupling of the cavity to a feedline has shown the release and catch of photons [187, 188] Several recent experiments have tuned the coupling of the cavity via microwave drives and achieved entanglement between transmon qubits [189, 190] and cavity encoded qubits [191]. The latter scheme allows for error correction against photon loss.*

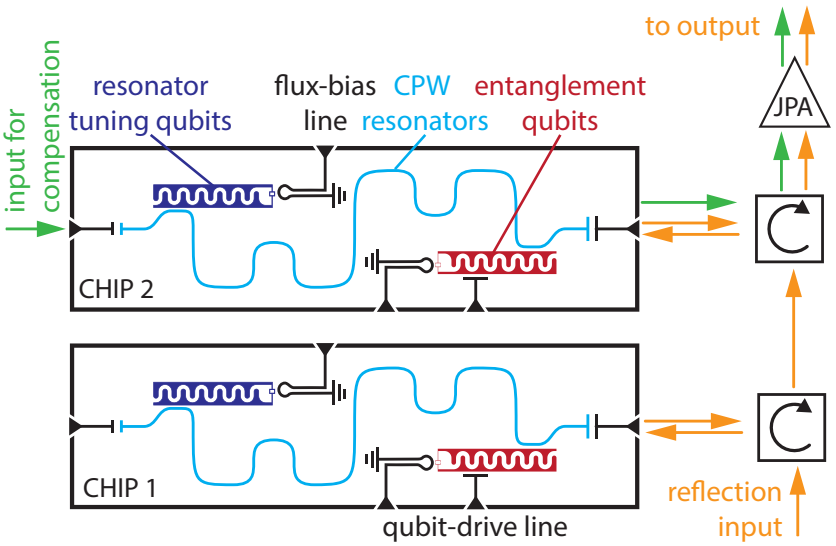

Figure 6.2: *Bounce-bounce entanglement setup. A microwave field (orange arrows) from the reflection input successively reflects on two CPW resonators (light blue) on separate chips via two circulators and is then amplified using a JPA. Each resonator is dispersively coupled to a transmon qubit (red). Additional tuning qubits (dark blue) are used to match the resonator frequencies via their dispersive shifts. A weakly-coupled input port to the resonator on the second chip is used to inject a compensation field (green arrow) to reduce distinguishability caused by a mismatch between parameters of different qubit-resonator systems.*

Here, we entangle two transmon qubits [45] on separate 2D-cQED chips by engineering a half-parity measurement using the bounce-bounce entanglement-by-measurement protocol [183–185]. A perfect odd half-parity measurement probabilistically projects a superposition state onto $|00\rangle$, $|11\rangle$ or an entangled superposition of $|01\rangle$ and $|10\rangle$. Distinguishability between $|01\rangle$ and $|10\rangle$, caused by differences between the two chips, leads to dephasing of the resulting entangled state and therefore degrades the entanglement. Two innovations make the protocol robust to fabrication variations. Firstly, adding resonator tuning qubits for frequency matching overcomes imperfect resonator frequency targeting. Secondly, we use an additional weakly-coupled port of the second resonator to apply a compensation pulse and reduce any distinguishability in the output fields for $|01\rangle$ and $|10\rangle$. We demonstrate the versatility of this technique by also matching the outputs for $|00\rangle$ and $|11\rangle$ to create an even-parity Bell state with similar performance. We characterize the performance of our protocol in aggregate by comparing the output states at different measurement strengths against a comprehensive model of the experiment.

6.2 EXPERIMENT OVERVIEW AND EXTENDED BOUNCE-BOUNCE PROTOCOL

The bounce-bounce approach to entanglement was proposed as a continuous two-qubit parity measurement in cavity quantum electrodynamics [183]. The qubit parity is mapped on a coherent state that successively reflects from two cavities and is then read out with a continuous homodyne measurement, leaving the two qubits entangled. Our setup [Figure 6.2] consists of two nominally identical chips each containing two transmon qubits both coupled to a coplanar waveguide (CPW) resonator. The two qubits in red will be entangled in the protocol. The $\lambda/2$ CPW resonator is coupled strongly to a feed line on one side and weakly on the other. This asymmetric coupling directs most of the photons on a single path that leads through the circulators to a Josephson parametric amplifier (JPA) [59], realizing a high-fidelity measurement of the output field. Details on the experimental setup and device fabrication can be found in Appendices 6.6 and 6.7.

In order to understand the measurement central to this experiment, it is useful to first consider the standard cQED measurement for a single qubit-resonator system in the dispersive limit [63]. In this limit, the qubit-resonator interaction simplifies to a qubit-dependent, dispersive shift χ of the resonator frequency. Under a coherent drive, the resonator therefore follows qubit-dependent coherent-state trajectories $|\alpha_i(t)\rangle$ with classical equations of motion for $\alpha_i(t)$ that depend on system parameters and the time-dependent drive. This entangles the resonator and qubit, creating the state $a|0\rangle|\alpha_0\rangle + b|1\rangle|\alpha_1\rangle$ for a qubit initially in $a|0\rangle + b|1\rangle$. As photons leak out of the resonator carrying qubit-state information, the qubit becomes more mixed, with coherence decaying according to the measurement-induced dephasing Γ_m:

$$\Gamma_m = 2\chi \int \mathrm{Im}\left[\alpha_0(t)\alpha_1^*(t)\right] \mathrm{d}t. \tag{6.1}$$

The dephasing seen by the qubit can be controlled by the coherent cavity drive, but the ability to infer the qubit state from the measured time-varying output signal, or transient, also depends on the noise added by the detection chain. Importantly, because the output field is directly related to the intracavity field, if the cavity starts and ends in the vacuum state, the dephasing can also be related to the measured average transient difference [71].

In a multi-qubit context, these concepts were generalized to realize entangling measurements [183, 202, 203]. For a joint measurement, selectively tuning the distinguishability between different state-dependent output transients can give dramatically different dephasing rates for different two-qubit coherence terms. For example, minimizing the dephasing between $|01\rangle$ and $|10\rangle$ creates a half-parity measurement that selectively preserves superpositions in the odd subspace, while giving distinct outcomes for $|00\rangle$ and $|11\rangle$. Thus, this measurement projects a separable superposition state to an entangled odd-parity Bell state with 50 % probability, with the corresponding measured outcome heralding successful entanglement generation. The phase of the odd-parity Bell state is determined by the initial superposition state.

In the bounce-bounce scheme, a perfect half-parity measurement requires identical qubit-cavity pairs and zero intra-cavity loss $1-\eta_l$. In 2D-cQED devices, however, fabrication variability makes precise parameter matching infeasible, and a more sophisticated approach is required. In our experiment, we introduced two techniques to mitigate these effects. Firstly, the variable dispersive shifts from two additional tuning qubits [dark blue in Figure 6.2] are used to match the fundamental frequencies of the two resonators [see Section 6.11 for details]. Secondly, to minimize any remaining transient distinguishability due to different resonator linewidths or dispersive shifts, we apply a compensation pulse to an additional, weakly coupled input port at the back of the second resonator [denoted by green arrows in Figure 6.2]. Effectively, interacting with only one resonator, this compensation pulse adds coherently to the reflected field from the bounce-bounce path [orange arrows in Figure 6.2] and can be shaped to conditionally displace the target trajectories to remove residual transient distinguishability.

For a given input pulse and system parameters, the optimal compensation pulse shape can be solved directly from the classical field equations in the Fourier domain [see Section 6.9 for detailed derivation]. In this approach, the qubit state dependent output field $y^{ij}(\omega)$ is a linear function of the reflection input field $\epsilon^s(\omega)$ and the transmission compensation field $\epsilon^w(\omega)$ via

$$y^{ij}(\omega) = H^{ij}_{\text{refl}}(\omega, \vec{p})\epsilon^s(\omega) + H^{j}_{\text{trans}}(\omega, \vec{p})\epsilon^w(\omega), \tag{6.2}$$

where $i,j \in \{0,1\}$ denote the state of the first and second qubit, and where $H^{ij}_{\text{refl}}(\omega, \vec{p})$ and $H^{j}_{\text{trans}}(\omega, \vec{p})$ are complex valued transfer functions that denote the individual system response to each input. The system parameter vector $\vec{p}$ consists of, for each chip, the resonator linewidth $\bar{\kappa} = \kappa^s + \kappa^w + \kappa^I$, with terms for the weakly and strongly coupled ports and the intrinsic losses, the dispersive shift χ, and the resonator-drive detuning Δ, as well as $1-\eta_l$ and ϕ, the interchip loss and acquired phase (see Table 6.1 for the measured values). This approach was tested by comparing predicted and measured output fields for various input fields [see Figure 6.18]. To ensure a measurement does not distinguish in the odd [even] subspace, we require $y^{01}(t) = y^{10}(t)$ [$y^{00}(t) = y^{11}(t)$] at all times. This gives a linear equation $\epsilon^w(\omega) = H^{\text{comp}}(\omega, \vec{p})\epsilon^s(\omega)$ where $H^{\text{comp}}(\omega, \vec{p})$ relates the transmission input to the reflection input. The classical solutions were then used to implement master equation (ME) and stochastic master equation (SME) models in the polaron frame incorporating the effect of qubit decoherence and post-selection on the measurement result, respectively [184, 203] [see Section 6.9 for details].

6.3 EXPERIMENTAL PULSE SEQUENCE AND COMPENSATION PULSE TUNE-UP

The experimental pulse sequence (Figure 6.3) is designed to faithfully characterize the entangling measurement using quantum state tomography (QST) with a joint readout [204, 205]. We first apply a projective measurement to be able to filter

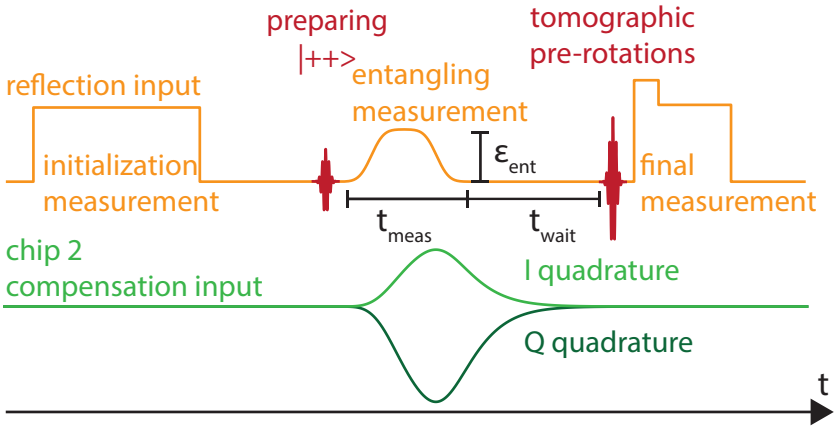

Figure 6.3: *Pulse scheme of the experiment. An initial measurement is used to condition on qubits in the ground state. Then, the entanglement qubits are prepared in the $|{+}{+}\rangle$ state. Entangling measurement pulses are applied through the reflection and compensation input. After waiting for the photons to leak out of the resonator, quantum state tomography is performed by applying an over-complete set of pre-rotations and a final measurement.*

out residual qubit excitations. While conditioning on the initial measurement reduces residual excitation, any remaining residual excitation can lead to an overestimate of the achieved entanglement by QST, an effect which we correct for (see Section 6.10). Next, we prepare the two qubits in the superposition state $|{+}{+}\rangle$, a tensor product with both qubits in the state $|+\rangle = (|0\rangle + |1\rangle)/\sqrt{2}$. Qubit gates are applied to the entanglement qubits via a capacitively coupled drive line (see Section 6.8 for qubit tune-up and performance). Then, we apply the entangling measurement, to probabilistically project the superposition state to an entangled state. To verify the entanglement, we perform QST by applying an overcomplete set of different pre-rotations on the qubits followed by a final measurement. All measurements consist of coherent microwave drives that populate the resonators with photons. The initial and final measurements are tuned for high single-shot fidelity (and avoiding measurement-induced excitations in case of the initial measurement).

The entanglement measurement strength can be varied either by changing the measurement amplitude or the duration, as marked in Figure 6.3. However, the simple equations of motion for the resonator state are only valid in the absence of qubit relaxation, thus the measurement time should be much shorter than the qubit lifetime T_1. As the shorter $T_1 = 9$ μs, we use a 300 ns measurement pulse with a smoothed square envelope to ease bandwidth requirements on the compensation pulse. The pulse is too short for the resonators to reach steady state. While the resonator-qubit system is in an entangled state with non-vacuum coherent states in the resonator, reliable gates on the qubits are not possible. Accordingly, the entangling protocol is only completed once the photons have left the resonators.

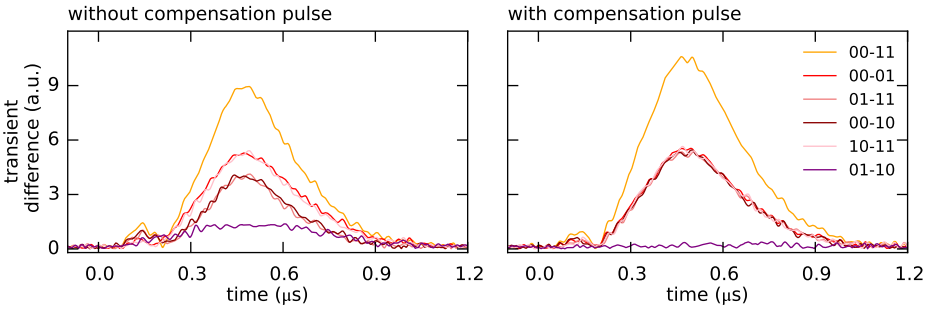

Figure 6.4: *Average output transient differences $|y_{ij} - y_{kl}|$ for different pairs of initial states with and without the compensation pulse. For the ideal half-parity measurement, the difference between the $|01\rangle$ and $|10\rangle$ outputs is zero at all times, which we realize with the compensation pulse. Additionally, the output difference for the other states is increased.*

We wait 700 ns for the resonators to empty before doing tomography, fixing the duration of the entangling protocol to 1 μs. Thus, measurement-independent qubit decoherence is fixed and the tomography as a function of measurement amplitude reveals the action of the measurement.

To realize the optimum compensation pulse $\epsilon^{W}(\omega)$ for an input $\epsilon^{S}(\omega)$, the parameters $\vec{p}$ need to be determined. Precise measurements are not straightforward for several parameters, such as κ_W and κ_I, the power difference of the two drives (due to small unknown differences in line attenuation and in the two mixers), η_I and the phase shift that the signal acquires between the two chips. To tune up the optimal compensation pulse, we minimize the transient difference between the odd (even) subspace $|01\rangle$ ($|00\rangle$) and $|10\rangle$ ($|11\rangle$) normalized by the sum of the other transient differences to keep the impact on readout fidelity to a minimum. This is optimized by iteratively varying $\vec{p}$ using a combination of hands-on and hands-off optimization [206].

We can look at the transient differences for all state pairs with and without compensation pulse (see Figure 6.4), to determine how well the compensation works. Just using the reflection input, there is still a mismatch between the output fields for $|01\rangle$ and $|10\rangle$ [difference $|y_{ij} - y_{kl}|$]. The improvement of the compensation pulse is two-fold, increasing the transient difference for the states we want to dephase and minimizing it for the subspace we want to preserve. The optimization is performed close to the optimal amplitude for entanglement after initial experiments. Since the transient-difference signal is noisy and affected by qubit relaxation, in future experiments it may prove more efficient to optimize on a qubit-based signal such as the dephasing itself or the acquired phase shift between the target states.

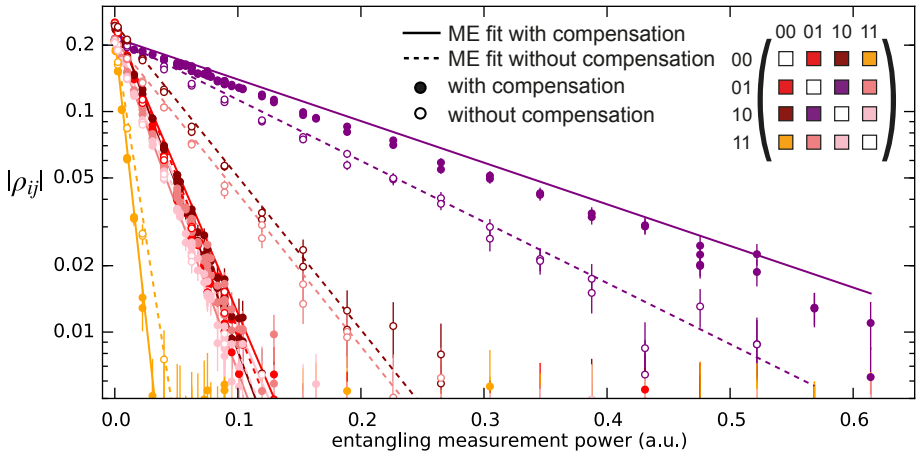

Figure 6.5: *Measurement-induced dephasing giving a decay of the coherence elements of the unconditioned density matrix as a function of measurement power. Dispersive readout gives exponential decay as a function of power as suggested by Equation (6.1). A master-equation model (see Section 6.9.3) is fitted to data with inter-chip loss* $1-\eta_\mathrm{l}$ *and amplitude scaling factor as only free parameters. Residual dephasing is largely explained by* $1-\eta_\mathrm{l} = 11.8$ *% (obtained from fit).*

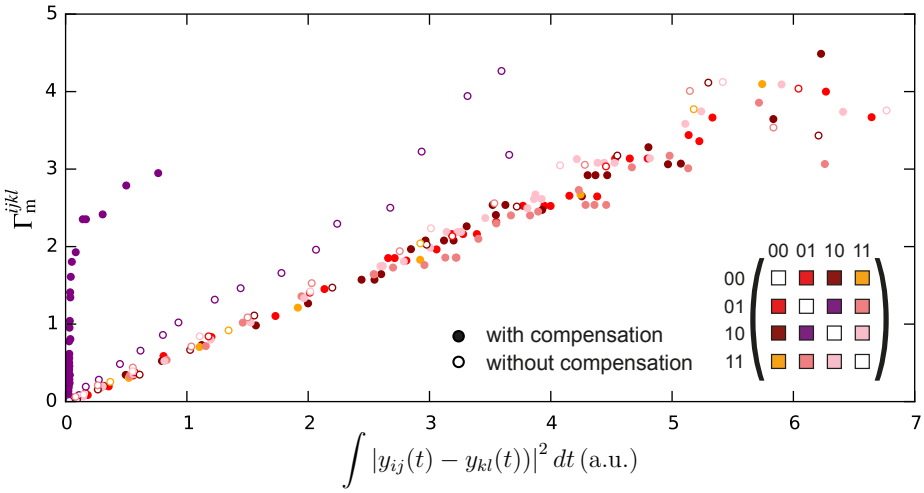

Figure 6.6: *Another way to look at the data from figures Figure 6.4 and Figure 6.5 is to plot the square of the time-integrated average transient difference agains the measurement-induced dephasing. Plotting the data like that reveals the linear relation between the measurement-induced dephasing and the squared integrated transient difference. The 01-10 transients remain fairly indistinguishable for a long time, but eventually the non-linearities lead to a breakdown of our transient matching. We attribute the residual dephasing despite the good transient matching to photon loss.*

6.4 EXPERIMENTAL RESULTS

We now confirm the effect of the transient matching on the qubits, using QST to reconstruct the density matrix after measurement. Measurement-induced dephasing leads to an exponential decay in the coherence elements of the density matrix as a function of measurement power as shown in Figure 6.5. Better transient matching with the compensation pulse results in reduced dephasing in the wanted subspace while enhancing the dephasing of the unwanted coherence elements over the entire amplitude range. Measurement power was rescaled for the independently measured mixer nonlinearity. We plot the ME simulation results (see Section 6.9) for both the compensation and no-compensation case, showing good agreement with the data. When fitting the ME we fixed the estimates for all parameters in $\vec{p}$ from independent measurements except for η_I and a scaling factor between the input power on the arbitrary waveform generator (AWG) that time-shapes a microwave carrier and the power that arrives at the experiment. We performed a single fit of the measurement-induced dephasing with the ME simulation to all 6 independent complex off-diagonal density matrix elements as a function of amplitude (populations remain constant). The full density matrix data and fits can be found in Figure 6.20 (Section 6.9).

Due to the finite $1-\eta_\mathrm{I}$, there is dephasing even for perfectly matched transients. To illustrate the dephasing even in the presence of matched transients with purely experimental data, we plot the integrated transient difference against the dephasing for different state pairs (Figure 6.6). In particular, for the compensation pulse we see the residual dephasing for matched transients which is due to the photon loss between the cavities. Similarly, without the compensation pulse, the 01-10 pairing shows more dephasing for the same transient difference, also due to photon loss. All other state pairs, where single-qubit dephasing contributions are dominant, show roughly the same linear behavior. We find that the datasets with and without compensation pulse are well described for $1-\eta_\mathrm{I} = 11.8$ % in the model. This power loss is partially explained by the circulators, which are specified to give 3-4 % , with the connectors to the printed circuit board (PCB) also likely to contribute significantly.

We now shift from looking only at the selective dephasing in the unconditional density matrix evolution to looking at the density matrix conditioned on the measurement outcome. The new variable to consider in this context is η_m, which determines the signal-to-noise ratio (SNR) for state determination based on the measurement outcome. We use the following entanglement measures as figures of merit: concurrence $\mathcal{C}$ [207], Bell-state fidelity $\mathcal{F}_\mathrm{B}$ and ebit rate, discussed below.

For good qubit readout at low photon numbers we require a low-noise amplifier. The amplifier is a JPA that we operate in phase-sensitive mode with a single strong pump tone (see Section 6.8 for tune-up procedure). This results approximately in a homodyne measurement that is effectively only sensitive along one quadrature, due

to the squeezing of the amplifier. The single-quadrature sensitivity puts an interesting constraint on the output fields: it penalizes having a signal that oscillates between quadratures. For this reason, it is beneficial to place the measurement tone at the symmetry point between the ground and excited state frequencies of the resonators. To simultaneously reach this condition for both resonators, they need to be lined up using the tuning qubits. This is irrelevant for the measurement-induced dephasing, as resonator frequency differences can be accounted for by the compensation pulse.

In addition to optimally employing the JPA and achieving the symmetric readout condition, digital processing of the output traces with integration weights is used to further increase the SNR. For a binary readout problem, the weight function for optimally distinguishing the states is the average transient difference in each quadrature (in the absence of qubit decay) [70]. In this case (Figure 6.4), the shape of the transient difference for different pairs of states is similar, such that we can economize. We used the mean of all transient differences for $|01\rangle$-$|00\rangle$, $|10\rangle$-$|00\rangle$, $|01\rangle$-$|11\rangle$, and $|10\rangle$-$|11\rangle$ as integration weights for the I and Q quadratures separately, giving a complex data point for each run of the experiment.

The binary decision whether a measurement result corresponds to the odd-subspace is a textbook classification problem. We relied on a machine-learning based approach [209], which proved more robust than an approach based on Gaussian fits and linear boundaries in phase space. We tried several standard classifiers from the scikit-learn python package [208], finding that the neural network classifier and the Radial Basis Function Suport Vector Machine (RBF SVM) show the best performance Figure 6.7. The calibration points for even (odd) parity are the red (blue) points. The color scale indicates the odd-subspace probability landscape learned by the neural network. Based on the comparison, we decided to use the neural network classifier because of the faster runtime as well as the intuitive looking probability landscape it extracts. The regularization parameter, which reduces overfitting, was swept to find a good value. For a given wanted percentage of data kept, the experimental runs with the highest odd-subspace probability were kept. Note that the classifier could also be trained on full single-shot traces, in which case the integration weights would be unnecessary.

The conditional density matrix evolution keeping 25 % of the data is shown in Figure 6.8**(a,b)** as a function of the measurement amplitude. As the measurement becomes stronger, the ability to threshold out the even subspace increases as shown by the reduction in even population and increase in odd populations. The wanted odd subspace coherence element first increases due to the selection, and is eventually limited by the measurement-induced dephasing. Qubit relaxation during measurement leads to a residual population in the $|00\rangle$ state. Note that early relaxation events will lead to $|00\rangle$ outcomes and will be filtered out. The data shows good agreement with an SME simulation with the same parameters as the ME simulation. The SME assumes a perfect signal-quadrature measurement with no squeezing as described

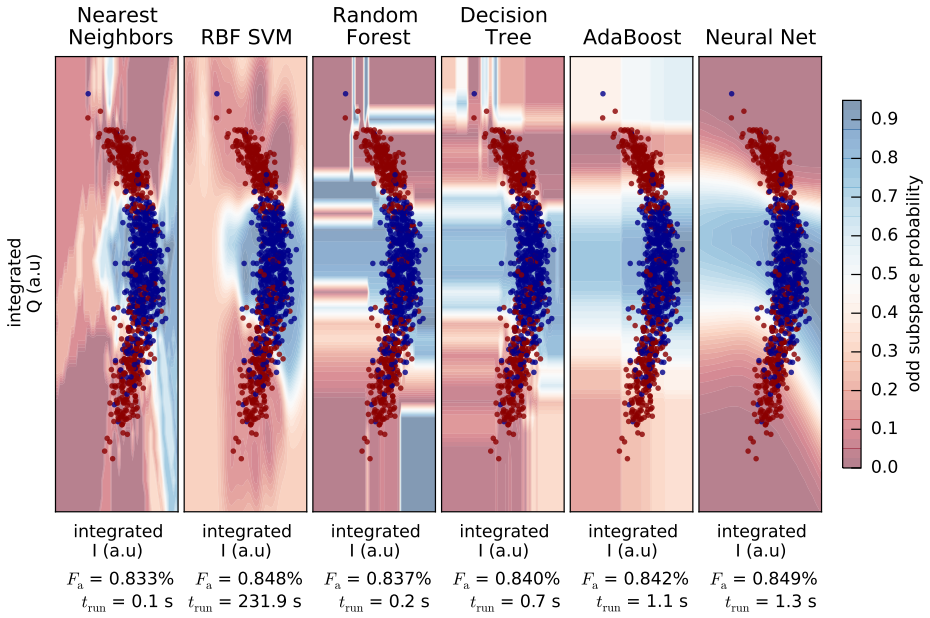

Figure 6.7: *Comparison of different classifiers from the scikit-learn python package [208]. Example data of integrated calibration-point output at optimum amplitude with even (red points) and odd (blue points) subspace data points. A neural network classifier is trained on calibration points giving a learned odd-subspace probability landscape (color scale).* 90 % *of the calibration data is used to train,* 10 % *is used to estimate the assignment fidelity* F_a*. Below we give* F_a *and runtime on the dataset* t_{run}*. The neural network classifier showed the best performance with a reasonable runtime. The classifier is used to select the fraction of data with the highest odd-subspace probability. Further optimization would probably also have lead to similar performance with another classifier choice. The main take-away message is that using existing packages for these kind of problems is often comparable if not superior to self-made algorithms that take a lot more time to develop.*

in [184, 203]. We find that $\eta_m = 50$ % gives good agreement with the experiment for the no-compensation case.

We now extract different entanglement measures from the conditioned density matrix keeping 25 % of the data [Figure 6.8**(c)**]. While $\mathcal{C}$ can be directly computed, $\mathcal{F}_B$ requires finding the odd (or even) Bell state with the highest overlap. A non-zero $\mathcal{C}$ signals entanglement, as does a $\mathcal{F}_B$ larger than 0.5. Both $\mathcal{F}_B$ and $\mathcal{C}$ peak at a common amplitude, which is characterized by a balance between good SNR and low measurement-induced dephasing in the odd-parity subspace. Improvements in η_m would shift the optimum to lower amplitudes and improve the result. The compensation pulse dataset clearly outperforms the no-compensation case but falls slightly below the theory which assumes a perfect compensation pulse. It is possible that the JPA tune-up gave a slightly lower η_m but the ME simulation in Figure 6.8**(c)** already shows signs of the sub-optimal compensation and the maximum $\mathcal{C}$ coincides for both cases. At high amplitudes, η_m likely starts to suffer from from the onset of

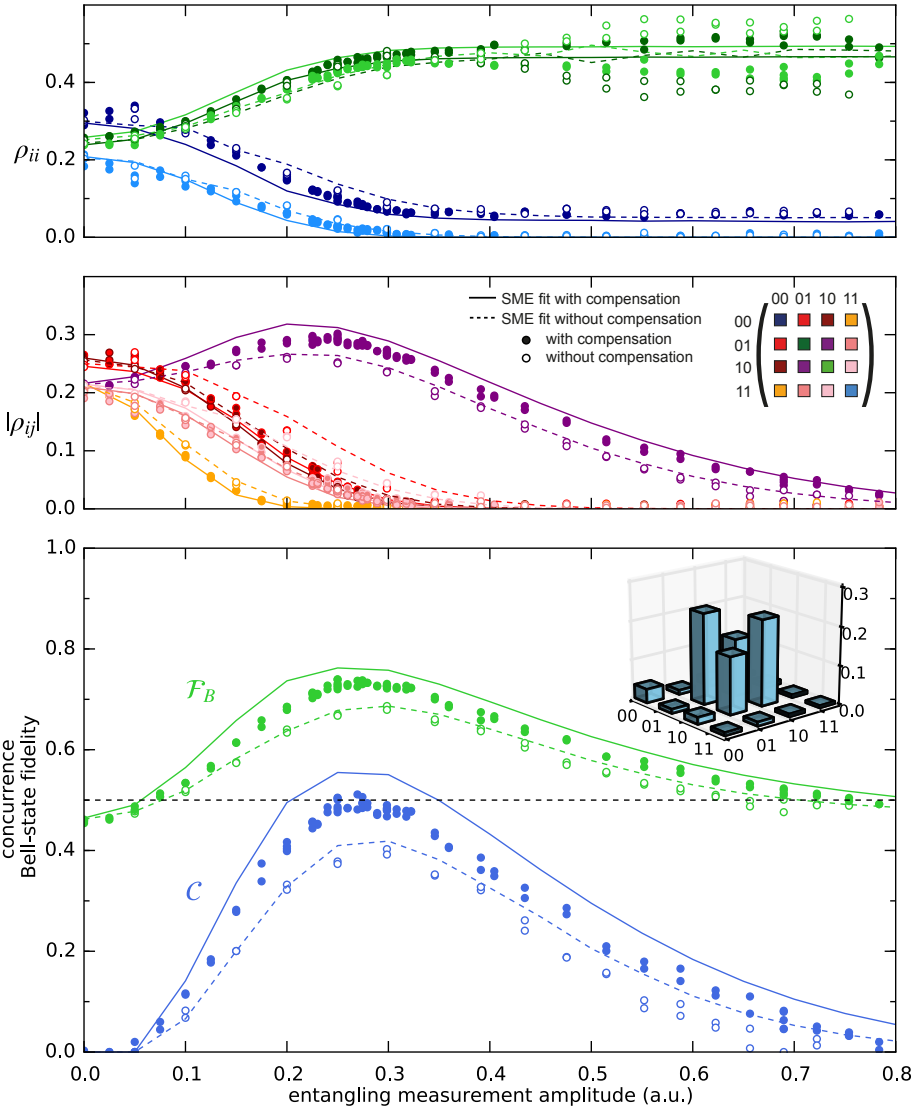

Figure 6.8: ***(a, b)*** *Evolution of the conditional density matrix ρ as a function of measurement amplitude with and without the compensation pulse. We keep 25 % of the data based on the measurement outcome. SME simulation (see Section 6.9.4) using the ME parameters with $\eta_m = 50$ % shows good agreement with the data.* ***(c)*** *Concurrence $\mathcal{C}$ and Bell-state fidelity $\mathcal{F}_B$ as a function of measurement amplitude comparing both cases. Inset shows $|\rho|$ with compensation at optimum amplitude.*

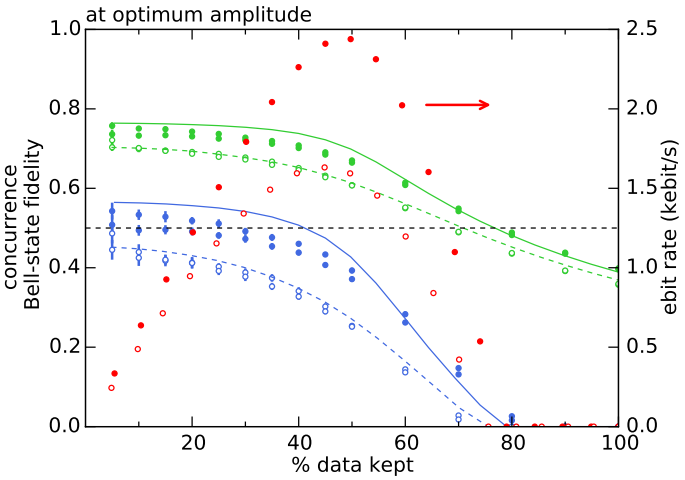

Figure 6.9: *$\mathcal{C}$ and $\mathcal{F}_B$ at the optimum amplitude as a function of data kept with and without the compensation pulse. We also compute the ebit rate (red) as described in the text.*

compression in the JPA. We reach an optimum $\mathcal{C} = 0.49 \pm 0.01$ and $\mathcal{F}_B = 0.731 \pm 0.003$ with the compensation pulse, and $\mathcal{C} = 0.40 \pm 0.01$ and $\mathcal{F}_B = 0.683 \pm 0.003$ without. The error bars are derived from Monte Carlo simulations based on a coin-toss model of multinomial sampling statistics. Point-by-point fluctuations seem to exceed the statistical errors, possibly due to JPA related fluctuations in quantum efficiency, drift in qubit coherence time and thermal excitations.

It is also interesting to look at the entanglement measures at the optimum amplitude as a function of the data kept when selecting on the entangling measurement (Figure 6.9). In addition to $\mathcal{C}$ and $\mathcal{F}_B$, we also compute the ebit rate, which is the product of the logarithmic negativity [210], the fraction of the data we keep and the experimental repetition rate of 10 kHz. The logarithmic negativity gives an upper bound for the distillable entanglement of a state [211]. The ebit rate is a relatively conservative estimate of an actually achievable entanglement rate, as the entire experimental sequence takes less than 5 μs including an initialization measurement, which in principle could be combined with active feedback for faster qubit initialization [72], and the QST. Thus, repetition rates on the order of 200 kHz should be achievable, corresponding to ebit rates around 40 kebit/s, comparable to qubit coherence times. The ebit rate peaks when keeping 50 % of the data, which corresponds to $\mathcal{C} = 0.38 \pm 0.01$ and $\mathcal{F}_B = 0.668 \pm 0.003$.

As mentioned in Section 6.3, by simply changing the form of the compensation pulse, it can be used to minimize the measurement-induced dephasing for any pair of states. To demonstrate this, we also implemented the compensation pulse that produces identical output for $|00\rangle$ and $|11\rangle$. In this case, the compensation pulse has to be stronger, as we match the two states that are naturally most distinguishable. While the transient matching in Figure 6.10 is comparable to the odd case, the measurement-induced dephasing shows a stronger deviation from the model. This is most likely due to mixer imperfections, such as skewness and non-linearity, which

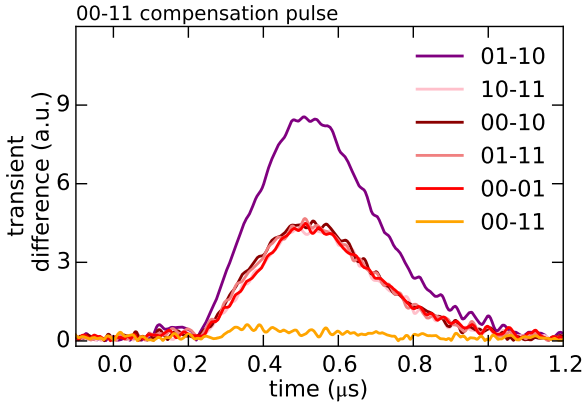

Figure 6.10: *Transient differences for the even subspace at optimum concurrence.*

were not independently calibrated for both mixers. These effects were likely more detrimental with higher mixer voltages for the even compensation pulse, but probably also contributed to not reaching the optimum in the odd case. Nonetheless, we realize an even-parity entangled state almost matching the odd-parity performance and again outperforming the no-compensation case reaching a $\mathcal{C} = 0.47 \pm 0.01$ and $\mathcal{F}_B = 0.732 \pm 0.005$ when keeping 25 % of the data. Our model predicts identical performance for the even and odd case assuming an optimally tuned compensation pulse.

6.5 CONCLUSION

We have shown that the bounce-bounce scheme can be implemented in a 2D-circuit QED setup, achieving remote entanglement for superconducting qubits that is competitive with the state of the art. The two chips in the experiment are not identical: tuning qubits are used to match the resonator frequencies. The resonator linewidths are significantly different but the additional compensation pulse allows the matching of the transients to realize either an odd or an even half-parity measurement. The experiment is not limited by the resonator linewidth as a steady state of the resonators is never reached. It is also not currently limited by qubit decoherence, however, it would be possible to include an echo pulse between two weak measurements in order to cancel slow noise on our qubits as T_2^* is generally smaller than $T_{2,\text{echo}}$ in these devices. Our current implementation leaves room for improvement in the limiting η_l and η_m.

Managing the photon loss to improve the achieved entanglement is difficult, but there are several obvious improvements. One circulator can be removed without compromising performance, as done in [185]. Developments of on-chip circulators [212] and better parametric amplifiers might lead to improvements in η_l and η_m, respectively. The loss could also be managed with quantum-error-correction-like protocols that make use of ancilla qubits [213].

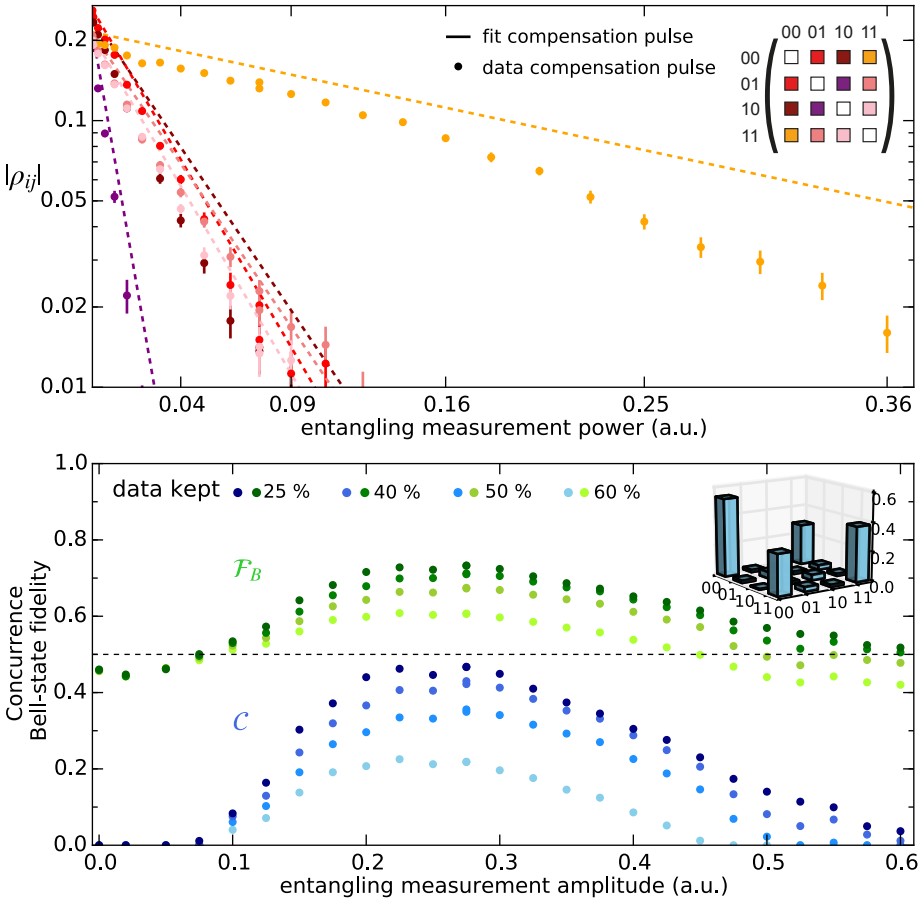

Figure 6.11: ***(a)*** *Measurement-induced dephasing for the even-subspace compensation pulse.* ***(b)*** *Concurrence (blue points) and even-Bell-state fidelity (green points) as a function of amplitude for different amounts of data kept. Inset shows the best even-Bell-state density matrix keeping 25 % of the data.*

A current maximum of 50 % success probability would either require several pairs of qubits where the protocol is performed in parallel or several entangling attempts. The protocol can be sped up employing faster ramp-up and ramp-down pulses. An entanglement generation time 1 μs would be promising for quantum network operation given qubits with demonstrated $\sim$ 50 μs coherence times. With further improvements, a cQED realization of entanglement distillation [214, 215] should come within reach. Also, in this two-qubit/two-cavity bounce-bounce configuration, entanglement generation via bath engineering [216–218] and feedback-control schemes [219] can be further explored to achieve steady-state entanglement.

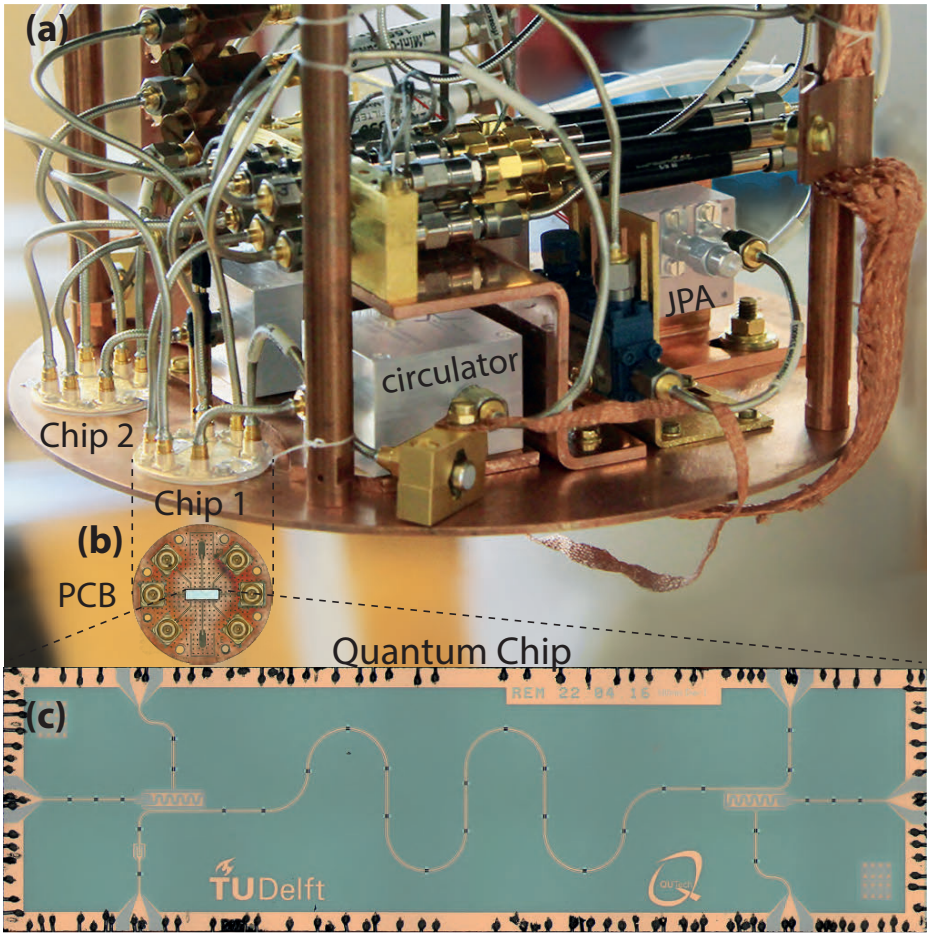

Figure 6.12: *Photographs of the setup.* ***(a)*** *Cold finger of the dilution refrigerator with the 2 chips, circulators and JPA.* ***(b)*** *Bird's eye view of the PCB.* ***(c)*** *Microscope image of the 7 mm × 2 mm chip.*

6.6 EXPERIMENTAL SETUP

Both chips were attached to the cold finger of a Leiden Cryogenics CF-650 dilution refrigerator as seen in Figure 6.12. The temperature of the cold finger during the experiment was around 35 mK. For radiation shielding, the entire setup is enclosed within a copper can coated with a mixture of Stycast 2850 and silicon carbide granules (15 to 1000 nm diameter) used for infrared absorption [134]. To shield against external magnetic fields, the copper can is enclosed by an aluminum can and two Cryophy cans. The magnetic shielding might be compromised as we placed circulators close to the samples to reduce cable length. SQUID loop offsets were not negligible for the qubits, such that we cannot exclude the presence of a slight external magnetic field.

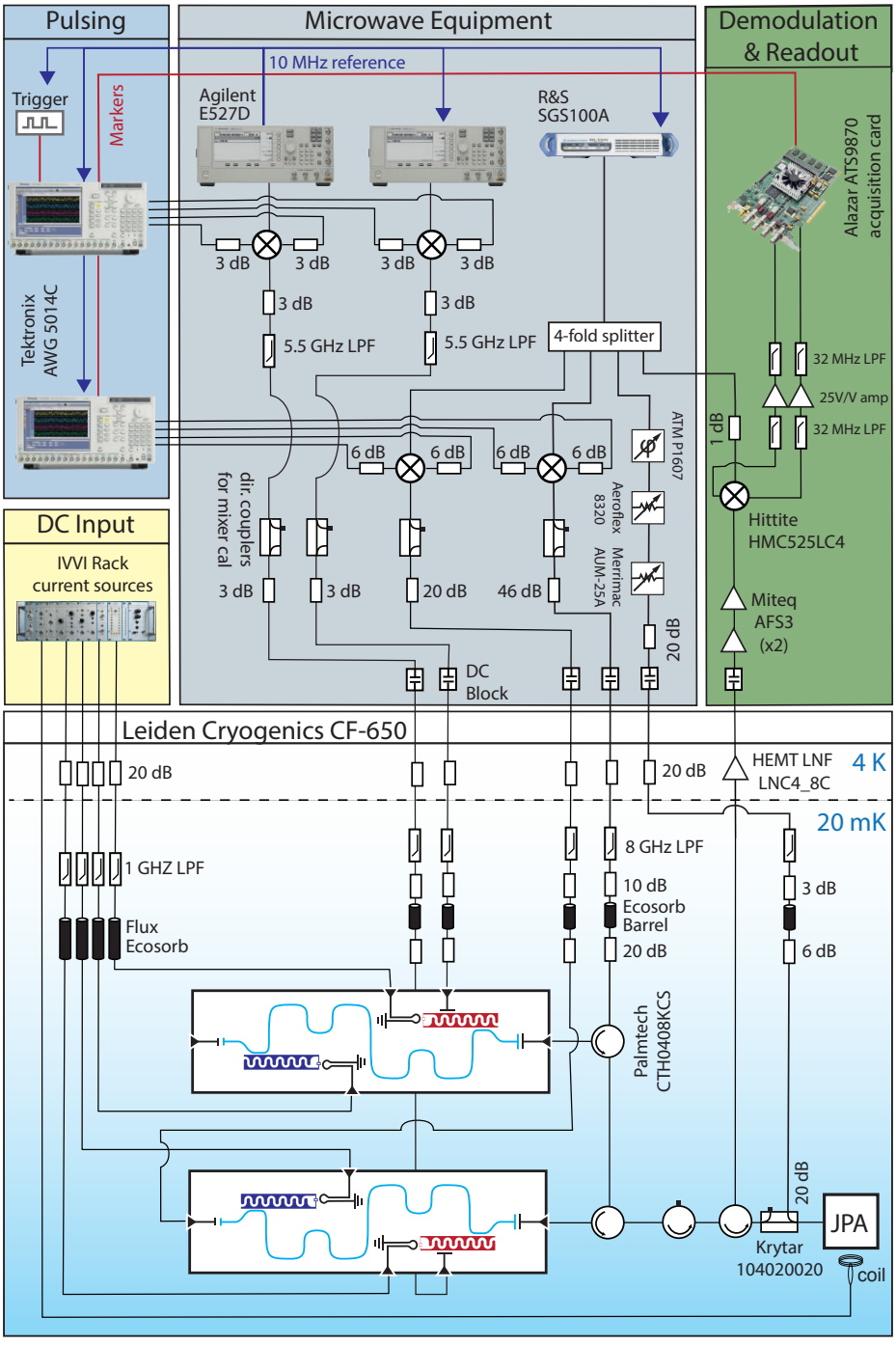

Figure 6.13: *Detailed schematic of the experimental setup.*

Table 6.1: *Key device parameters and designed target values. Large difference in resonator κ is either an effect of the wire-bonds or an effect of sample packaging. For both qubits, χ is given at the upper sweet spot, where they are operated throughout the experiment.*

Parameter	Target	Chip 1	Chip 2
$f_{r,bare}$	6.27 GHz	6.344 GHz	6.339 GHz
$\kappa/2\pi$	2 MHz	3.01 MHz	4.53 MHz
$f_{q,max}$	5.57 GHz	5.23 GHz	5.24 GHz
E_c/h	280 MHz	293 MHz	293 MHz
$\chi/2\pi$	-1 MHz	-335 kHz	-335 kHz

A detailed wiring diagram of the experiment can be found in Figure 6.13. Microwave lines are filtered using $\sim$ 60 dB of attenuation using both commercial cryogenic attenuators and home-made Eccosorb filters for infrared absorption. Flux-bias lines are also filtered using commercial low-pass filters and Eccosorb filters with a stronger absorption, in principle allowing for fast control of qubit frequencies, even though in this experiment only static biasing was used. The JPA is mounted with an additional circulator to prevent leakage of the resonant pump tone back to the experiment. This can be improved in future experiments, as double-pumping or pump-canceling schemes could have been used in place of the additional circulator, likely improving the quantum efficiency.

6.7 DEVICE FABRICATION AND PARAMETERS

The devices were fabricated with the same process as those in [49]. Device parameters can be found in Table 6.1. Bare resonator frequencies are close to the target frequency, resonator targeting is discussed in more detail in Section 6.11. The difference in κ_c between the two chips with identical base-layer patterns that come from the same die is surprising and suggests that either wire-bonds or packaging play a role. Likely this is also the cause of the κ_c value being off target.

The qubit frequencies are well matched for this pair of devices. Usually Josephson junction fabrication leads to an expected relative spread of several percent in qubit frequencies [133]. Pairs of matching qubits can be selected from the room-temperature resistances of the Josephson junctions [132], which in this case differed by 1 %. However, the absolute frequencies were not on target, due to systematic shifts in the junction parameters between different fabrication runs. Reducing the statistical spread and systematic variations between Josephson junction fabrication runs remains an outstanding challenge for future many-qubit devices.

6.8 QUBIT TUNEUP AND PERFORMANCE

A plot of the qubit frequencies as a function of flux through their SQUID loops is shown in Figure 6.14. For this dataset, two-tone spectroscopy was performed after decoupling the flux bias lines from an initial 2 % on-chip crosstalk to $<$ 0.2 %

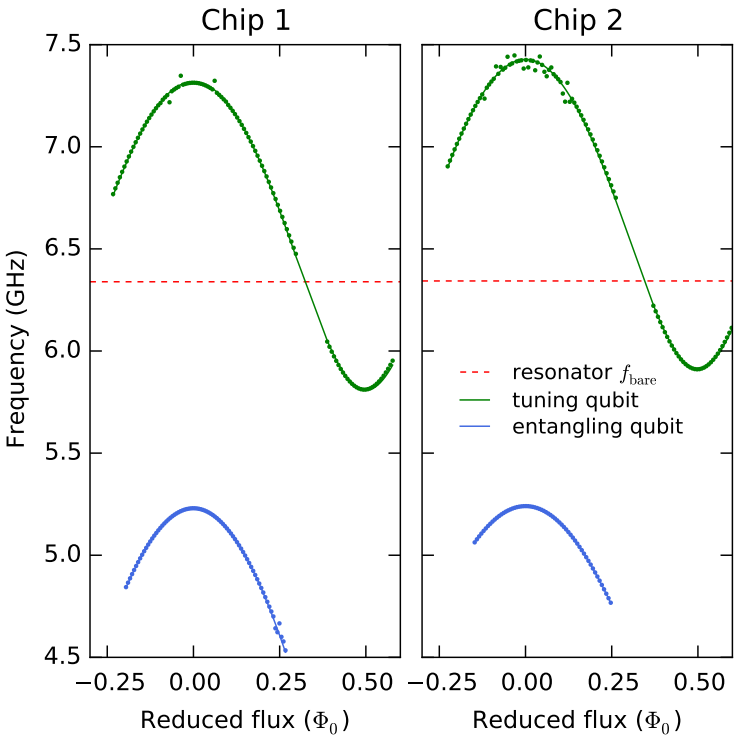

Figure 6.14: *Flux-dependent frequency for the qubits in the experiment. Points are qubit frequencies extracted from spectroscopy. The lines are fits based on the flux dependence on an assymetric-SQUID transmon qubit.*

using a compensation matrix. All qubits in the experiment have SQUID loops with asymmetric Josephson junctions, leading to a top and bottom sweet-spot and reducing the sensitivity to flux noise. For the entanglement qubits, the bottom sweet-spot is estimated to be at ~ 4 GHz.

Single-qubit rotations on the entanglement qubits were implemented using DRAG pulses [76, 77] using the first AWG. A sideband modulation of -100 MHz was used to put the carrier leakage above the qubit frequency. Gaussian pulses comprise 4σ with a total duration of 20 ns. The AllXY sequence [220] was used to tune up the DRAG parameter. T_1, T_2^* and $T_{2,\mathrm{echo}}$ measurements, as well as AllXY sequences and readout fidelity measurements were performed interleaved with the experimental runs in order to monitor performance. The cross-driving isolation from chip 1 to chip 2 was estimated to be larger than 30 dB by trying to measure a Rabi oscillation on the chip 2 qubit through the drive-line of the chip 1 qubit. During this procedure, the chip 1 qubit frequency was detuned. The isolation from chip 2 to chip 1 should be ~ 40dB larger due to the directionality of the circulators, but this was not confirmed by measurement, as we could not provide the additional 40dB of power for the pulses.

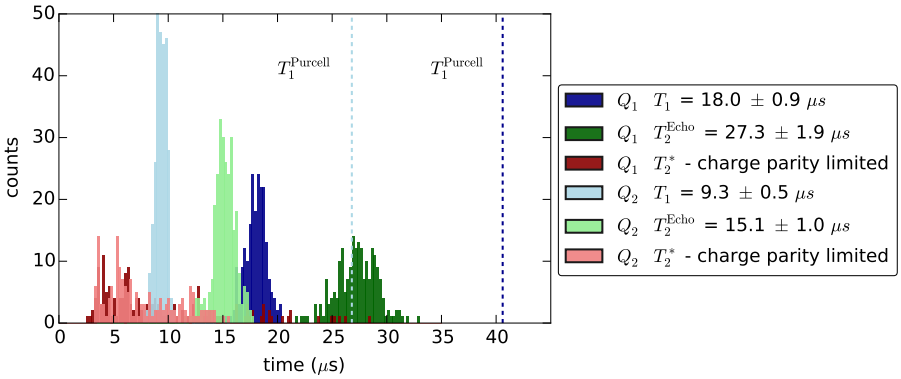

Figure 6.15: *Coherence-time histograms for the entanglement qubits at operating point. Data was taken intermittently over a* 24 h *interval with almost 300 data points per quantity. During the experiment, coherence times were monitored and the AllXY sequence [180] was measured to quickly monitor gate quality.*

The entanglement qubits were operated at their flux sweet-spots which maximized coherence and dispersive shift. Histograms of repeated coherence-time measurements at the operating point can be found in Figure 6.15. T_1 was a factor ~ 2 below the Purcell limit $T_1^{\text{Purcell}} = \Delta^2/g^2\kappa$ for both qubits, with dielectric loss likely to be the other limiting factor. The charging energy of the transmon $E_C/h = 293$ MHz was higher than the design value. The resulting maximum charge-parity splitting was measured to be $\approx$ 66 kHz from the beating pattern measured in Ramsey experiments. However, this frequency uncertainty does not become a limiting factor on the timescale of the experiment. We also report the coherence times as a function of frequency (Figure 6.16).

One microwave source was split four ways to generate the carriers for the bounce-bounce and compensation input, the JPA pump tone and the local oscillator for demodulation. Readout pulses were defined using the second AWG. The qubit readout using the JPA was optimized for separation between all four computational states. A sequence preparing all four states with subsequent readout was used and single shots were collected. We then optimized JPA pump power, flux-bias setting and pump phase, minimizing the overlap between the resulting probability distributions [221]. Single-shot fidelities for the final readout for each individual qubit were generally on the order of 95-99 %. A quantum efficiency $\eta_m = 50$ % gives good agreement between the SME simulation and the experimental data in Figure 6.8. This is below the limit expected from photon loss according to component specifications but consistent with reported values in other experiments [184, 222]. In principle, $\eta_m = 100$ % can be achieved, but finite JPA gain and bandwidth as well as photon loss on the way to the JPA (for this setup 25 % loss is expected from component specifications) limit the quantum efficiency. Using a phase-insensitive, higher-bandwidth amplifier such as the traveling wave parametric amplifier [61] would

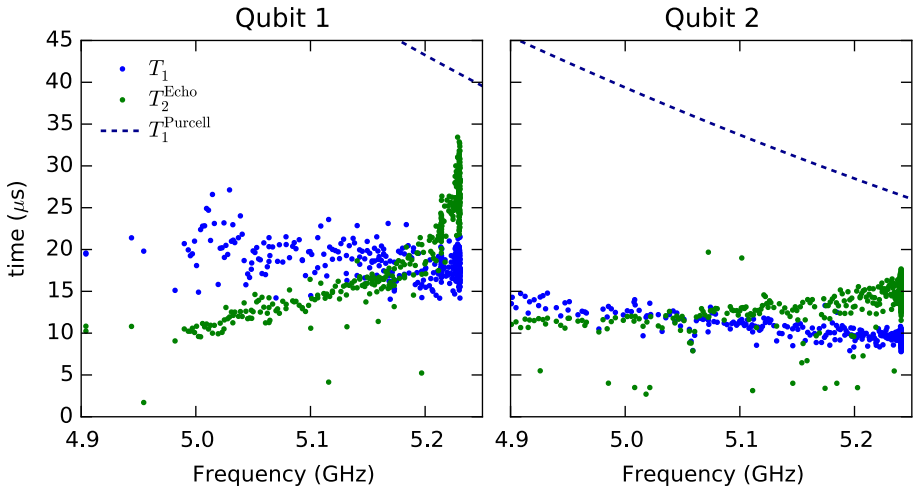

Figure 6.16: *Frequency dependend coherence times for the entanglement qubits. For both qubits the T_1 is not merely explained by the Purcell effect, dielectric loss likely has a strong contribution. Measurements like this are important to exclude isolated drops in T_1 as reported in [103]. This figure also illustrates the fact, that qubits can not be tuned more than $\sim$ 200 MHz without severely compromising coherence times.*

result in imposing a 50 % upper-limit on the achievable quantum efficiency by that definition making the protocol more sensitive to loss between the chips - the residual source of measurement-induced dephasing.

In future experiments, it would be helpful to fully calibrate the mixer non-linearity and skewness across the experimental range or use step attenuators in order to realize more linear sweeps of the readout power. Mixer imperfections impact the experiment in several ways but can in principle be completely corrected. We did cancel the carrier leakage of the mixers in the experiments using fixed DC voltages, to prevent additional photon shot noise. In addition, there is non-linearity in the output power, which manifests in our mixers as reduced output at high voltages. We only corrected this effect in post-processing when we realized the severity. Thus, the compensation pulses, where two mixers with different amplitudes were involved, would no longer have been perfect at all amplitudes. Another effect that would start playing a role in the compensation cases is mixer skewness, which we did not account for. In future experiments all these things can be measured and fixed by adjusting the AWG pulses.

6.9 COMPREHENSIVE MODELING OF THE EXPERIMENT

We now describe the modeling for this experiment both for the output fields and the density matrix evolution. It is natural to begin with the classical equations of motion in Section 6.9.1, since the full two qubit two cavity ME can be reduced to a qubit

only ME using the resonator field solutions and a polaron transformation [203]. The classical equations of motion are also used to derive the compensation pulse in Section 6.9.2. We then describe the ME in Section 6.9.3 and finally add a stochastic term to model post-selection of the measurement results in Section 6.9.4.

6.9.1 *Classical equations of motion*

In the dispersive regime and in the absence of qubit relaxation, the resonator field modeling reduces to qubit state dependent harmonic oscillators. We generally work in a rotating frame of the coherent measurement drive. Making use of the cascaded nature of our system we can derive the Heisenberg equation of motion for the system using input-output theory [223]. Taking the expectation value immediately we end up with the following set of classical qubit-state-dependent coupled linear differential equations

$$\begin{aligned}
\dot{\alpha}^{\pm}(t) &= \left(-i(\Delta_1 \pm \chi_1) - \frac{1}{2}\overline{\kappa}_1\right)\alpha^{\pm}(t) + \sqrt{\kappa_1^{s}}\epsilon^{s}(t) \\
z^{\pm}(t) &= \sqrt{\kappa_1^{s}}\alpha^{\pm}(t) - \epsilon^{s}(t) \\
\dot{\beta}^{\pm\pm}(t) &= \left(-i(\Delta_2 \pm \chi_2) - \frac{1}{2}\overline{\kappa}_2\right)\beta^{\pm\pm}(t) \\
&\quad + \sqrt{\kappa_2^{s}\eta_l}e^{i\phi}z^{\pm}(t) + \sqrt{\kappa_2^{w}}\epsilon^{w}(t) \\
y^{\pm\pm}(t) &= -\sqrt{\kappa_2^{s}\eta_l}e^{i\phi}z^{\pm}(t) + \sqrt{\kappa_2^{s}}\beta^{\pm\pm}(t),
\end{aligned} \tag{6.3}$$

where the qubit $0(1)$ state is denoted by $+(-)$, $\alpha^{\pm}, \beta^{\pm\pm}$ denote the two qubit-state-dependent coherent states inside resonator 1 and 2 respectively, $z(t)$ denotes the reflected output field of resonator 1, $y(t)$ denotes the monitored output field after reflection off both resonators. Driving fields $\epsilon^{s}(t)$, $\epsilon^{w}(t)$ are the reflection input at the strongly-coupled resonator ports and the transmission input at the weakly-coupled port of the second resonator, respectively. The system parameters are the resonator linewidths $\overline{\kappa}_i = \kappa_i^{s} + \kappa_i^{w} + \kappa_i^{I}$ with contributions from the two ports and the intrinsic loss, the dispersive shifts χ_i, the resonator detunings from the measurement tone Δ_i. Between the chips, the field undergoes a power loss $1-\eta_l$ and a phase shift ϕ.

The above set of equations describes a linear time invariant system, so it can be readily solved in the Fourier domain. The solutions are written using transfer functions (shown schematically in Figure 6.17) for the single-qubit-resonator systems as

$$\begin{aligned}
\alpha^{\pm}(\omega) &= H_1^{\pm}(\omega)\,\epsilon^{s}(\omega) \\
z^{\pm}(\omega) &= H_{1R}^{\pm}(\omega)\,\epsilon^{s}(\omega) \\
\beta^{\pm\pm}(\omega) &= \sqrt{\eta_l}e^{i\phi}H_2^{\pm}(\omega)\,H_{1R}^{\pm}(\omega)\,\epsilon^{s}(\omega) + \sqrt{\frac{\kappa_2^{w}}{\kappa_2^{s}}}H_2^{\pm}\epsilon^{w}(\omega) \\
y^{\pm\pm}(\omega) &= \sqrt{\eta_l}e^{i\phi}H_{1R}^{\pm}(\omega)\,H_{2R}^{\pm}\epsilon^{s}(\omega) + \sqrt{\kappa_2^{w}}H_2^{\pm}(\omega)\,\epsilon^{w}(\omega),
\end{aligned} \tag{6.4}$$

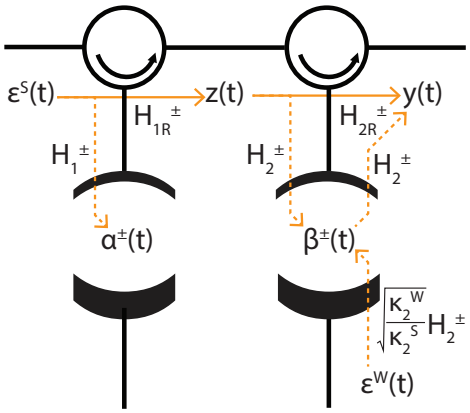

Figure 6.17: *Schematic of the system with arrows indicating the transfer functions that relate fields at different positions to eac other.*

where $H_j^{\pm}(\omega) = \frac{\sqrt{\kappa_j^s}}{i\omega + i(\Delta_j \pm \chi_j) + \frac{1}{2}\overline{\kappa_j}}$, $j \in \{1,2\}$ are the transfer functions into resonator 1 and 2 and $H_{jR}^{\pm}(\omega) = \sqrt{\kappa_j^s} H_j^{\pm}(\omega) - 1$ is the transfer function after reflection from them. This approach shows clearly that cascading systems entails a simple multiplication of their transfer functions.

We use these equations to fit the measured output transients at the optimum entangling measurement amplitude. The results for all three cases can be found in Figure 6.18. To further compare experiment and model, we can look at the integrated output power which is to a good approximation qubit state independent. This is shown in Figure 6.19**(a)**. For low powers, particularly up to the point of maximum $\mathcal{C}$, we find good agreement with theory. The no-compensation case shows the expected linear behavior. For the odd-compensation case we find deviations at high powers while the even compensation case shows a general systematic deviation from linearity, likely due to mixer imperfections. Using the fitted amplitude scaling factor from the ME (Section 6.9.3), we can use the qubits as photon-meters and estimate the photon numbers in the resonators as a function of input power for both resonators, found in Figure 6.19**(b)** and **(c)**.

For this work, we did not attempt active ramp-up and ring-down pulses for the resonators as done in [68, 69], but the transfer function mechanism provides a simple way to do this. The transfer functions relate the drive to the resonator fields. Any ansatz for the driving field at the strong port with enough free parameters can be used derive a pulse where the resonator photon numbers are ramped up and reset to zero faster than the resonators ring-up and ring-down time. The number of parameters necessary is given by the number of different qubit states for which the ramp-up and ramp-down is supposed to work.

6.9.2 *Compensating pulse solution*

Using the compensation pulse to limit measurement-induced dephasing was already suggested in [203]. Here, we expand on the conceptual solution we presented to

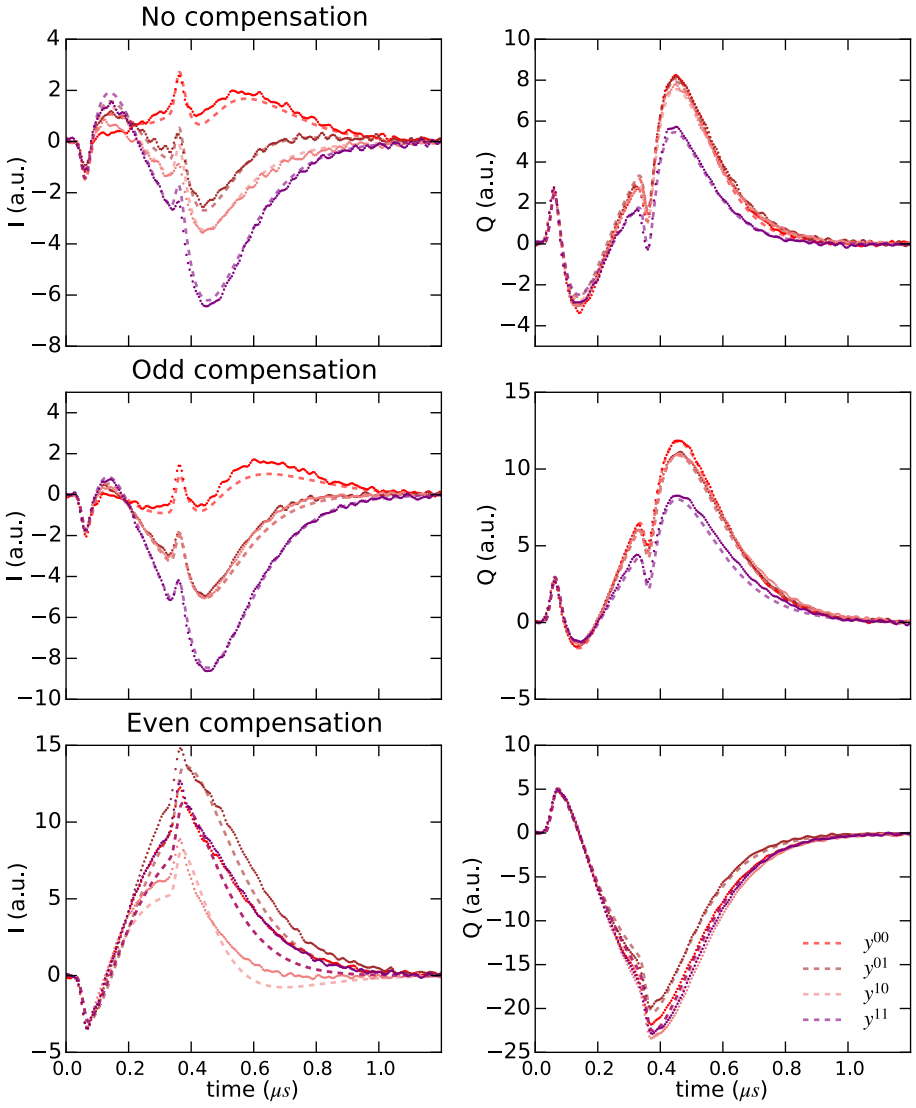

Figure 6.18: *Output transients and model fits for the uncompensated, the odd-compensation and the even compensation case, each at maximum-concurrence amplitude. The signal was rotated to maximize the difference of the matched states in the I-quadrature for visual clarity.*

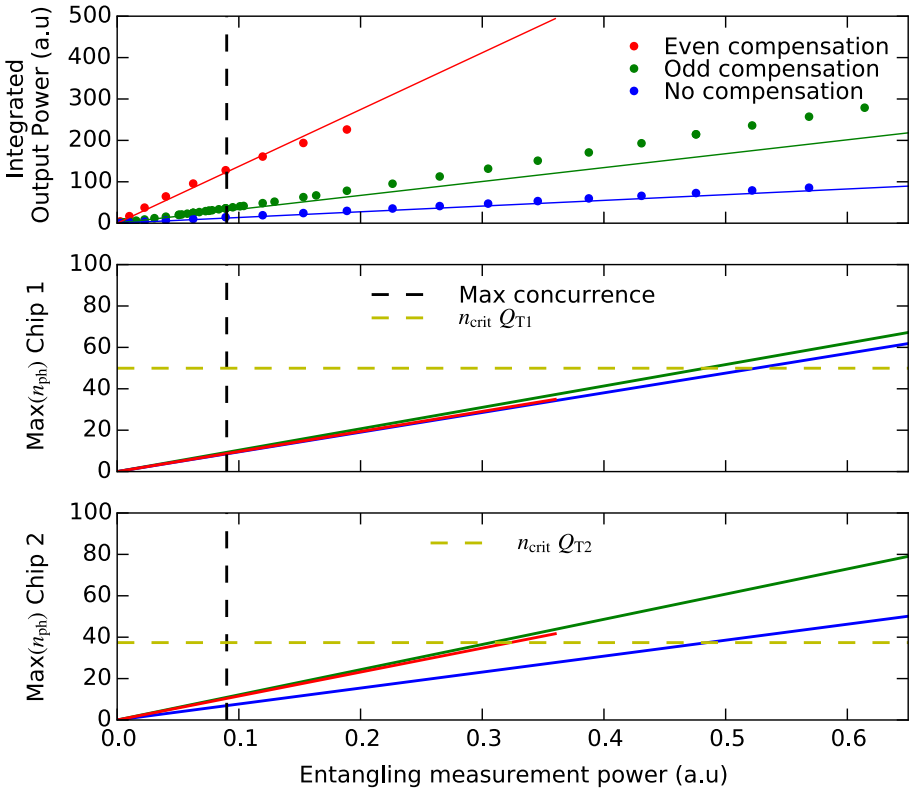

Figure 6.19: ***(a)*** *Integrated output power in experiment (dots) and theory (lines) for the three cases to confirm the modeling of the output fields. We again find the best agreement for the no-compensation case. In the relevant regime up to the concurrence maximum we find good agreement.* ***(b)*** *and* ***(c)*** *maximum photon numbers in each resonators extracted from the model for all three cases. Critical photon number imposed by the tuning qubit Q_{Ti} on chip i is marked by the horizontal line for each resonator (see Section 6.11).*

the compensation pulse in Equation (6.2). By sending a drive through the weak input port simultaneously with the existing pulse in the strong port, we can make nearly any pair of the four classical output states equal by solving $y^{kl}(\omega) = y^{mn}(\omega)$, where y is the qubit state dependent output field of Equation (6.4); k, m denote the state of the first qubit and l, n of the second qubit. Solving this, we can obtain a general expression for the weak compensation measurement field $\epsilon^{w}_{kl,mn}(\omega)$ as a function of the strong port measurement field $\epsilon^{s}(\omega)$ and the desired pair of matching output states $|kl\rangle$ and $|mn\rangle$

$$\begin{aligned} \epsilon^{w}(\omega) &= H^{comp}(\omega)\epsilon^{s}(\omega) \\ H^{comp}(\omega) &= \frac{\sqrt{\eta_1}e^{i\phi}\left(H^{k}_{aR}(\omega)H^{l}_{bR}(\omega) - H^{m}_{aR}(\omega)H^{n}_{bR}(\omega)\right)}{\sqrt{\kappa^{w}_{2}}\left(H^{n}_{2}(\omega) - H^{l}_{2}(\omega)\right)}. \end{aligned} \tag{6.5}$$

Using this simple relation allows us to reduce dephasing of the two-qubit density matrix element $\rho_{kl,mn}$ and therefore create an odd $(y^{01}(\omega) = y^{10}(\omega))$ or even $(y^{00}(\omega) = y^{11}(\omega))$ parity state robust to fabrication variations in the chips. The full parity measurement is a special case in this context, where two pairs of states are always matched, leading to an entangled state independent of the measurement result [224]. This is only possible with another symmetry in the system. We could not achieve a parity measurement with our devices. The number of free parameters available with two driving fields does not allow us to satisfy $y^{00}(\omega) = y^{11}(\omega)$ and $y^{01}(\omega) = y^{10}(\omega)$ simultaneously.

An intuitive way to approach the parity measurement problem is the qubit dependent steady-state phase shift. The steady-state phase for reflection on a single cavity as a function of the qubit state and the cavity detuning from the measurement frequency Δ is given by [225]

$$\phi^{\pm}(\Delta) = 2\arctan\left[\frac{2(\Delta \pm \chi)}{\kappa}\right]. \tag{6.6}$$

The qubit-dependent phase shift $\left|\phi^{+} - \phi^{-}\right|$ contains the measurement information and $\left|\phi^{+} - \phi^{-}\right| = 180^{\circ}$ can be achieved if 2χ is not smaller than κ by adjusting the frequency of the measurement tone. But making the phase shifts 180° for two different cavities simultaneously is more difficult. Phase shifts from successive cavities add up, and if the qubit-dependent phase shift is 180° for both, $|00\rangle$ and $|11\rangle$ will acquire 0° and 360°, while $|01\rangle$ and $|10\rangle$ will acquire 180°, which looks suggestively like a parity condition. But an identical steady-state phase shift does not mean that the transients are identical. That requires Δ and κ to be the same as well. For identical qubit-cavity systems and a measurement in the symmetry condition, $2\chi = \kappa$ for both chips (leading to a steady-state phase shift of 180° for each cavity), will yield a perfect parity measurement.

6.9.3 *Master equation model*

As derived in [203], in the dispersive regime we can fully model the average evolution of the qubit states using a qubit-only ME:

$$\begin{aligned} \dot{\rho} &= \sum_{ijkl} a_{ijkl}(t)\, P_{ij}\rho(t)\, P_{kl} + \mathcal{L}_d\rho(t) \\ a_{ijkl}(t) &= 2i\chi_1(1-\delta_{ik})\left((-1)^i \alpha^k \alpha^{*i}\right) \\ &\quad + 2i\chi_2(1-\delta_{jl})\left((-1)^i \beta^{kl}\beta^{*ij}\right), \end{aligned} \tag{6.7}$$

where $P_{ij} = |ij\rangle\langle ij|$ are the two qubit projection operators, δ_{ij} the Kronecker delta function, $\mathcal{L}_d$ is given by standard Lindblad type $\mathcal{D}[A]\rho = A\rho A^{\dagger} - \frac{1}{2}\left(A^{\dagger}A\rho + \rho A^{\dagger}A\right)$ phenomenological qubit dissipation (with rate γ^i) and dephasing (with rate γ_{ϕ}^i) operators $\mathcal{L}_d = \sum_{i=1}^{2}\gamma_{\phi}^i\mathcal{D}\left[\sigma_z^i\right] + \gamma^i\mathcal{D}\left[\sigma_-^i\right]$. Adding the qubit relaxation operators makes this equation no longer exact but is still reasonably valid in the limit

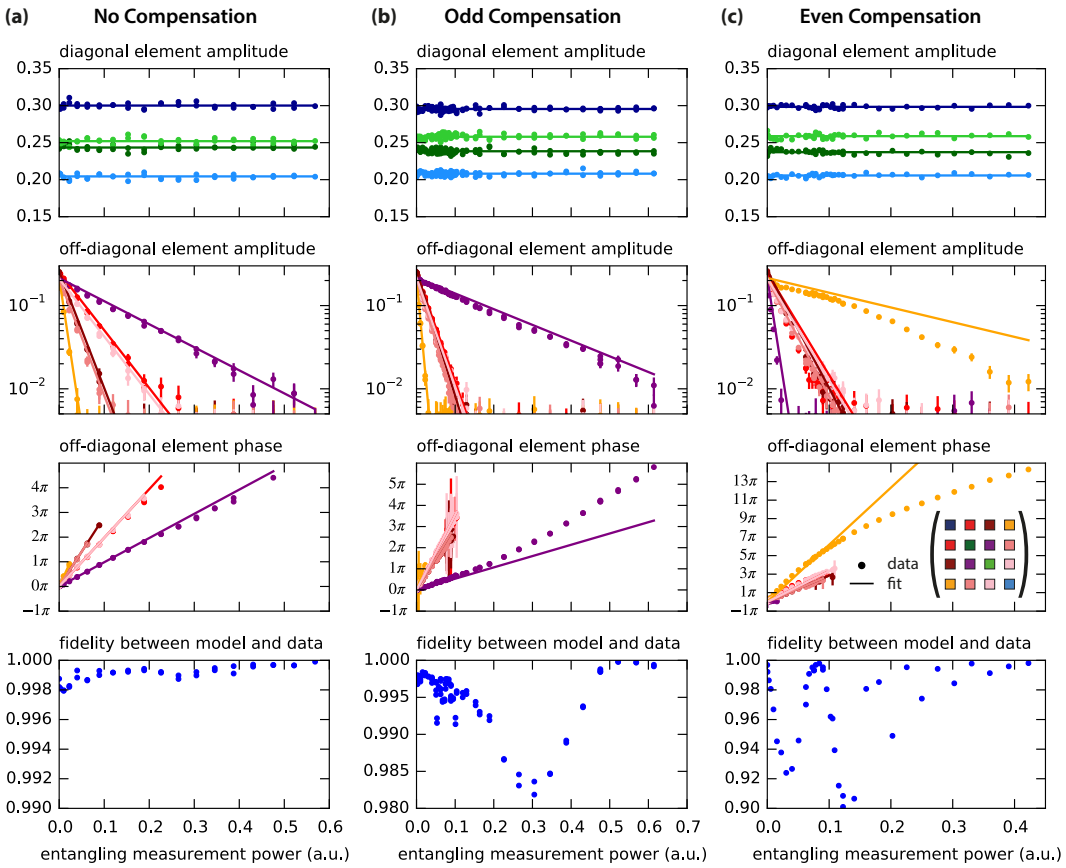

Figure 6.20: *Master equation fits for the three cases: no-compensation* ***(a)****, the odd compensation* ***(b)*** *and the even compensation* ***(c)****. Populations are used to fit the* T_1 *Lindblad operators and do not show a dependence on the measurement power. For the off-diagonal density matrix, amplitude and phase are plotted independently. The phase is only plotted if the amplitude of the off-diagonal density matrix elements is above 0.01. This no compensation case shows the best agreement between theory and experiment, while the odd and even compensation pulse cases deviate at larger amplitudes.*

$\kappa_1^s, \kappa_2^s \gg \chi_1, \chi_2$ [203]. Since the resonators are traced out in this equation during the measurement process, we can see a trajectory with possible non-Markovian revival of coherence due to entangled photons leaking out of the resonators. Once the approximation breaks down, the cavities would have to be simulated in the Fock basis, leading to increased computational complexity.

In order to fit the master equation model to the experimental data we take several steps. As predicted by the model, the qubit populations are constant as a function of measurement power. They only depend on the qubit T_1 dissipation due to the $\gamma^i \mathcal{D}\left[\sigma_-^i\right]$ terms, which are fitted to the diagonal terms, since they fluctuate slightly between datasets. The density matrix at zero measurement power can be

used to estimate γ_ϕ^i. We used a fit to extract the scaling factor between the AWG voltage at room temperature and the power that arrives at the experiment, as well as the inter-chip loss, fixing the other system parameters. The results can be found in Figure 6.20. We find excellent agreement with theory for the no-compensation case, for the other two cases we simply applied the compensation in the model without re-fitting. This shows good agreement with no additional fitting parameters. Similar to the integrated output power, agreement for the two compensation cases is considerably worse, which we attribute mostly to mixer imperfections that were not properly accounted for. While we believe this is the main source of mismatch, we also reach the limits of the dispersive approximation due to the tuning qubits (see Section 6.11). These effects could be included in a full two-qubit/two-cavity master equation including higher-order terms, but this would be computationally much more involved.

6.9.4 *Stochastic Master equation simulation*

The JPA in phase-insensitive mode, due to the squeezing, can be modeled as reading out a single quadrature of the output field. Thus, we can define the angle θ along which we read out. We approximate the imperfect readout due to photon loss up to the JPA and finite gain and bandwidth with a single quantity, the quantum efficiency of the measurement η_m. Modeling single runs of a homodyne measurement with angle θ and quantum efficiency η_m requires us to add another superoperator $\mathcal{L}_\mathrm{m}$ to the right-hand side of Equation (6.7) adding the stochastic measurement dynamics to the ME. This allows us to calculate the density matrix conditioned on the measurement result. This gives a stochastic differential equation in Itô form [226] and $\mathcal{L}_\mathrm{m}$ is given by [203]

$$\mathcal{L}_\mathrm{m}\rho = \sqrt{\eta_\mathrm{m}}\xi(t)\left[M\rho + \rho M^\dagger - \mathrm{Tr}\left(M\rho + \rho M^\dagger\right)\rho\right], \tag{6.8}$$

where $M = e^{i\theta}\left(-\sqrt{\kappa_1^s\eta_l}\Pi_1 + \sqrt{\kappa_2^s}\Pi_2\right)$, $\Pi_1(t) = \sum_{i,j} P_{ij}\alpha^{ij}(t)$, $\Pi_2(t) = \sum_{i,j} P_{ij}\beta^{ij}(t)$ are resonator-state-dependent qubit projection operators, $\xi(t)\,dt = dW$ is a white noise process satisfying $E[dW] = 0$ and $E[dW(t)\,dW(s)] = \delta(t-s)\,dt$ and dW is a Wiener increment. The measured output voltage corresponding to such a trajectory is given by [203]

$$V(t) = \sqrt{\eta_\mathrm{m}}\mathrm{Re}(\langle M\rangle) + \xi(t). \tag{6.9}$$

This was used to simulate the measurement including post-selection and to generate the theory curves for Figure 6.11.

Although simulating the SME allows comparing individual trajectories at each point in time, we only looked at the qubit-only density matrix at a time where the resonators were back to the vacuum state. Only at this point in time are the qubits a useful resource for remote information processing schemes. Studying the trajectories themselves, on the other hand, is performed in more detail in [184, 185], which will be relevant for real-time feedback schemes.

6.10 QUANTUM STATE TOMOGRAPHY AND SPAM ERRORS

In this experiment, we diagnose the entanglement, the key figure of merit, via QST. QST allows us to reconstruct the density matrix from which the entanglement measures are computed. Our QST procedure consists of two steps. First we do a set of calibration measurements with known input states to determine the observable $\hat{M}_0$ that corresponds to our final measurement. For a joint dispersive readout, the measurement operator for a d-dimensional Hilbert space is of the simple form $\hat{M}_0 = \sum_{k=0}^{d-1} a_k P_k$ with $P_k = |k\rangle\langle k|$ [25]. The coefficients a_k can be directly read out from computational basis state inputs, e.g. $a_k = \mathrm{Tr}\left(\hat{M}_0 P_k\right)$. The aim is the reconstruction of an unknown ρ using the now known measurement operator $\hat{M}_0$. We can reduce this to a simple linear algebra problem where we need to estimate the $d^2 - 1$ independent basis coefficients of ρ by measuring the expectation values $\langle \hat{M}_i \rangle = \mathrm{Tr}\left(\hat{M}_i \rho\right)$ of at least $d^2 - 1$ orthogonal measurement operators $\hat{M}_i$. Only then we can solve the resulting system of equations. The measurement operators $\hat{M}_i$ can be effectively obtained from $\hat{M}_0$ by rotating ρ before measurement using that the trace is invariant under cyclic permutations $\mathrm{Tr}\left(\hat{R}_i \hat{M}_0 \hat{R}_i^{\dagger} \rho\right) = \mathrm{Tr}\left(\hat{M}_0 \hat{R}_i^{\dagger} \rho \hat{R}_i\right)$. Thus by rotating our input state before measurement we effectively measure in different bases.

In this experiment, we used the cardinal set (an overcomplete set of 36 single qubit rotations: $\left\{I, X, X_{\pi/2}, X_{-\pi/2}, Y_{\pi/2}, Y_{-\pi/2}\right\}^{\times 2}$) on both qubits. The 36 rotations together with 4 calibration points (each repeated 5 times) were measured sequentially and the whole sequence was repeated 12800 times. We binned the measurement outcomes based on the calibration points, where one bin was mostly comprised of outcomes corresponding to $|00\rangle$ and another to those of $|11\rangle$. Using proper normalization, the counts in bin n for rotation i corresponded to the expectation value $\langle \hat{M}_i^n \rangle$ of the bin operator $\hat{M}_i^n$. This resulted in an overcomplete set of $36 \times 2 = 72$ equations with 15 unknowns and was solved by performing standard maximum likelihood techniques with physicality constraints [227–229].

While QST is a widely used way to confirm entanglement, its accuracy is limited by state-preparation and measurement (SPAM [230]) errors. SPAM errors mainly impact the measurement operator, and thus arise in step 1, the calibration process. They likely exceed the errors due to imperfect qubit gates. In order to test our state preparation and tomography for self consistency, we prepared the 36 two-qubit cardinal states, performed tomography and compared the fidelity to the ideal state (Figure 6.21). We find a mean fidelity of 99 %.

Assuming the initial state to be perfectly $|00\rangle$ is an approximation. The histograms of the measurement outcomes projected on one quadrature given in Figure 6.22**(a)** clearly show multiple peaks which coincide with the average outcomes for the other computational states. We conditioned on an additional initial measure-

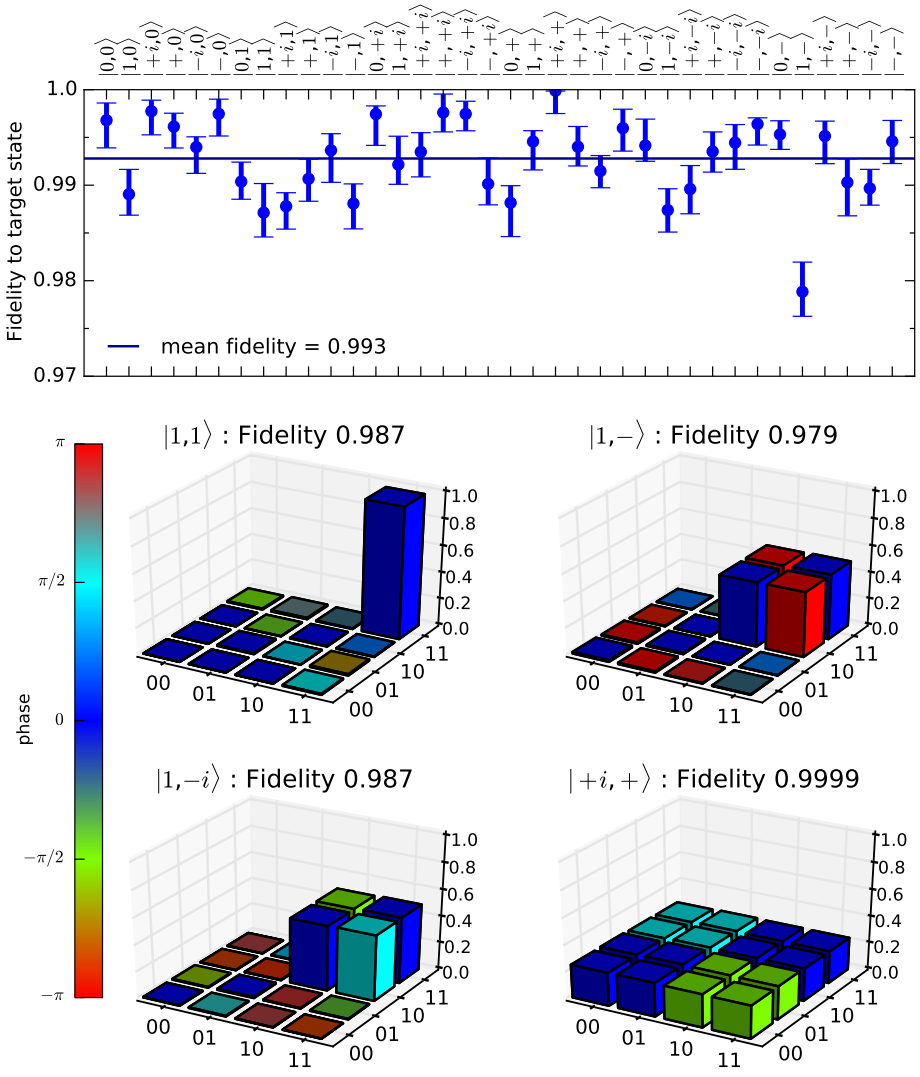

Figure 6.21: *Quantum state tomography of the 36 two-qubit cardinal states. Below several reconstructed density matrices are shown. This set of states was used to confirm that our tomography procedure was producing reasonable results. he mean fidelity of 99 %. Due to the readout condition for this dataset, the thermal excitation correction could not be applied here, as the readout histograms did not permit distinguishing thermal excitations between qubit 1 and qubit 2.*

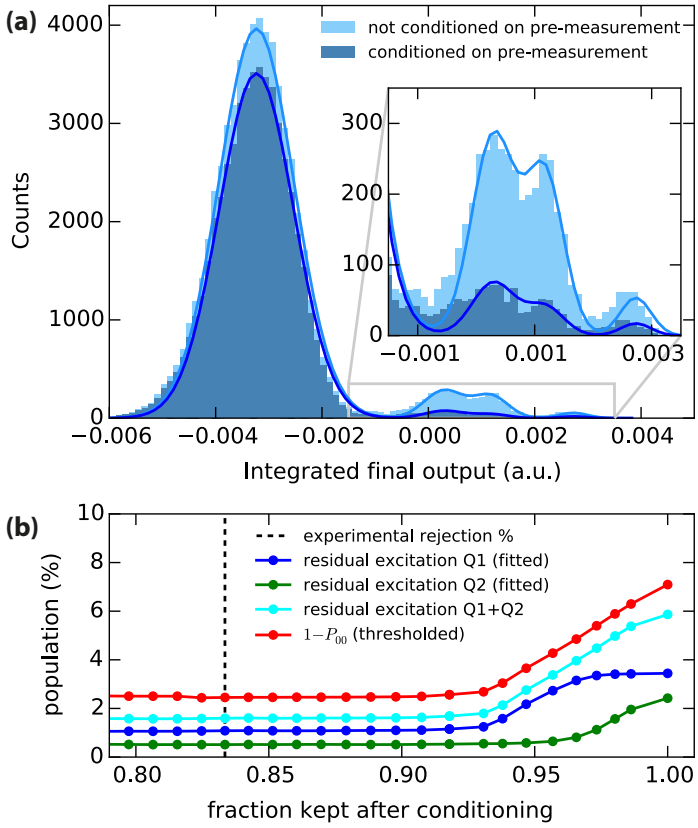

Figure 6.22: ***(a)*** *Histogram of single-shot measurements of the system in the nominal ground state reveals additional peaks that coincide with the* $|01\rangle$, $|10\rangle$ *and* $|11\rangle$ *calibration points.* ***(b)*** *A multi-Gaussian fit can be used to estimate the residual populations of the two qubits for different conditioning on the pre-measurement. The conditioning on the ground state can bring down the residual populations to about* 1 % *(*0.5 %*) for qubit 1 (2) by rejecting* 10 % *of the experimental runs. In practice the rejection rate was closer* $15-17$ % *indicated by the vertical line. A simple threshold estimate of the excited state population gives a slightly higher estimate. The constant offset could be due to tuning qubit excitations.*

ment to reduce the residual excitation. The results after post-selection are shown in Figure 6.22**(b)** giving an estimated decrease of 6 % to less than 2 % total excitation in both qubits. Re-excitation times calculated from T_1 and the measured excitation fraction suggest that the conditioning should be limited to reducing the residual excitation to ~ 0.5 %.

The conditioning on the ground state paradoxically decreases the amount of entanglement in the tomography outcome. As an example, for the run giving the highest entanglement keeping 25 % of the data, the extracted density matrix without conditioning resulted in $\mathcal{C} = 0.58 \pm 0.01$ and $\mathcal{F}_{\mathrm{B}} = 0.761 \pm 0.004$. After conditioning, the same dataset resulted in $\mathcal{C} = 0.57 \pm 0.01$ and $\mathcal{F}_{\mathrm{B}} = 0.755 \pm 0.004$. Reducing

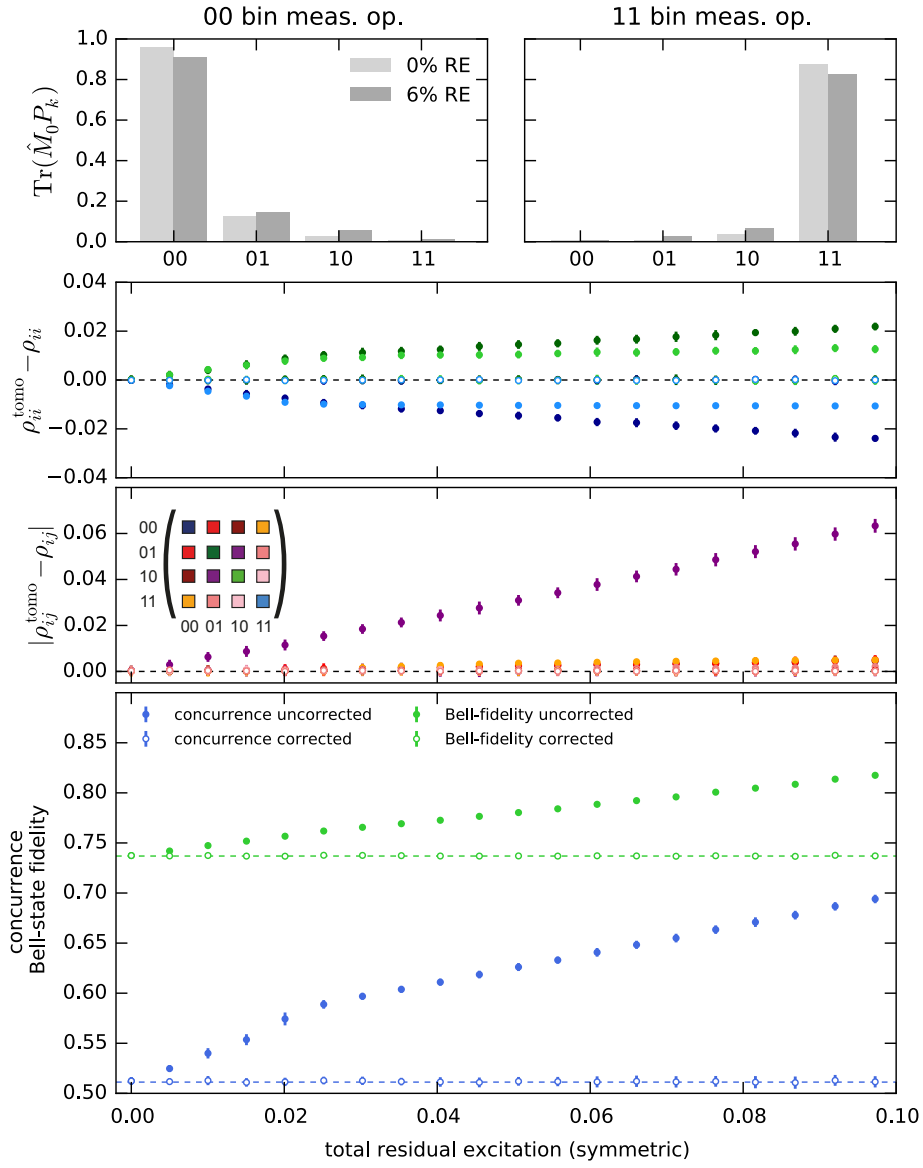

Figure 6.23: *Simulation of the effects of residual excitations on quantum state tomography. Tomography runs are simulated giving the resulting ρ^{tomo} for an underlying density matrix ρ corresponding to the highest concurrence state.* ***(a)*** *Change in measurement expectation values for the computational states without residual excitation (RE) and with 6 % total RE symmetrical on both qubits.* ***(b)*** *and* ***(c)*** *Change in populations and absolute coherence elements of the reconstructed density matrix as a function of total RE (filled markers). Taking into account known RE and fixing the measurement operators leads to the correct reconstruction of the density matrix (open markers).* ***(d)*** *Change entanglement measures as a function of total RE (filled markers), reconstructions taking the RE into account (open markers) lead to the correct values (lines). Statistical error bars are on the order of the marker size.*

the amount of residual excitation should have increased $\mathcal{C}$ if the QST was accurate, because the conditioning should increase the purity of the initial state, which in turn would reduce the mixture in the final state. This suggests that SPAM errors related to the residual excitation skew the QST result.

Monte Carlo simulations of QST reproduce the effect, pointing to the flawed assumption of pure calibration points which are in reality mixed by residual excitation as seen in Figure 6.23. This skews the measurement operators obtained from calibration and artificially boosts the purity of the estimated density matrix. For the optimum entangled state this results in a significant increase in $\mathcal{C}$. Simulations also showed that beyond the limit of reducing residual excitation by conditioning, tomography can be further improved by taking the known mixture of the calibration points into account. We can then correct the calibration of the measurement operators by assuming mixed input states $\tilde{P}_{ij}$ instead of pure projectors P_{ij}, which for $|00\rangle$ becomes

$$\begin{aligned}\tilde{P}_{00} = &\left(1-p_{e_{01}}\right)\left(1-p_{e_{10}}\right)P_{00} + p_{e_{01}}\left(1-p_{e_{10}}\right)P_{01} \\ &+p_{e_{10}}\left(1-p_{e_{01}}\right)P_{10} + p_{e_{01}}p_{e_{10}}P_{11},\end{aligned} \tag{6.10}$$

where $p_{e_{01}}$ is the excitation fraction in qubit 2, $p_{e_{10}}$ the excitation fraction of qubit 1, and P_{ij} the projector onto state $|ij\rangle$. In simulation [Figure 6.23] the correction leads to a more precise estimate of the density matrix given an accurate estimate of the residual excitation. Systematic errors in tomography due to residual excitation likely exceed the statistical counting errors.

Correcting for the estimated residual excitations, the conditioning on the initial measurement now increases the entanglement as expected from $\mathcal{C} = 0.46 \pm 0.01$ and $\mathcal{F}_B = 0.71 \pm 0.003$ to $\mathcal{C} = 0.51 \pm 0.01$ and $\mathcal{F}_B = 0.734 \pm 0.005$. The main data was corrected for the estimated residual excitation in each experimental run, which remained ~ 1 % on both qubits after conditioning.

6.11 THE ROLE OF THE TUNING QUBITS

While the mismatch in κ_c for the two chips was significant, this is an effect that can be fully corrected with the compensation pulse without affecting the performance of the protocol. Differences in χ between the two chips could also be compensated without sacrificing performance. However, resonator frequency mismatch has different implications and would have a strong impact on achievable entanglement. The measurement-induced dephasing due to frequency mismatch could be eliminated using the compensation field, but the quantum efficiency would suffer. This is due to the measurement with a phase-insensitive, low-bandwidth JPA, which is optimal in the symmetric readout condition. For either qubit-resonator system which is not symmetrically driven, meaning that the measurement tone is halfway between the resonator frequencies for $|0\rangle$ and $|1\rangle$, the output information is not confined to one quadrature. Any information in the de-amplified quadrature is lost, therefore realizing

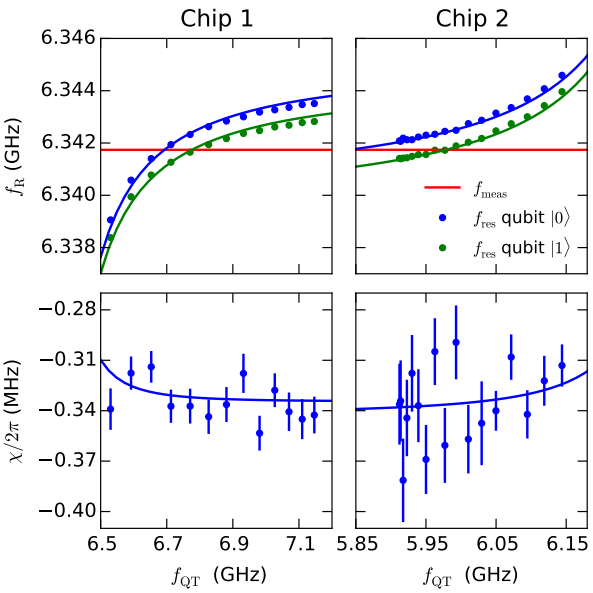

Figure 6.24: *Matching resonator frequencies via the dispersive shifts of the tuning qubits. Resonator transmission is measured for the respective entanglement qubit in $|0\rangle$ and $|1\rangle$ and frequencies f_R are extracted from Lorentzian fits for both cases. They are plotted against the tuning qubit frequencies f_{QT}. Tuning qubit frequency can be varied by changing the DC flux through its bias line. The two frequencies can be used to extract χ. Tuning qubits have no measurable effect on the χ of the entangling qubits in this tuning range, as expected from the qutrit Tavis-Cummings model.*

the symmetric driving condition simultaneously for both resonators is essential for maximizing the quantum efficiency.

Making identical microwave resonators to MHz precision is technically conceivable but challenging, partially due to the choice of niobium titanium nitride (NbTiN) film as the base superconductor. The thin film was sputtered with the Nordico tool from [130]. NbTiN is a high-kinetic-inductance superconductor due to the low charge carrier density, which leads to a strong dependence on the film thickness. Therefore, the two bare resonator frequencies are not identical within the linewidth κ_i. The additional qubits are used to shift their respective resonators via their Lamb shift, allowing us to match the resonator frequencies at the cost of introducing additional Kerr-nonlinearity.

Tunable low-loss CPW-resonators have also been demonstrated using kinetic inductance [231] or via SQUID loops [232, 233]. Each of the tuning methods leads to Kerr-nonlinearity in the resonator. The effect of the tuning qubit on the ideal qubit-resonator system can be modeled via the Tavis-Cummings Hamiltonian [234]. Tuning qubits were designed with top and bottom sweet spots sitting above and below the resonator respectively. As seen in Figure 6.24, the resonator frequency as a function of tuning-qubit frequency is well described by the model. Our measurements were not accurate enough to resolve the small change in the χ of the entanglement-qubit in the range we measured. At the operating points, T_1 of the tuning qubits was found to be 3.9 μs and 4.1 μs for chip 1 and 2 respectively. The critical photon numbers $n_{crit} = \Delta^2/4g^2$ calculated from the entanglement-qubit frequency and coupling are 193 and 188 for chip 1 and chip 2 respectively, a factor ~ 10 above the maximum photon numbers we reach in the protocol at the optimum

entanglement amplitude. The non-linearity from the tuning qubits can be inferred, using the qubit and bare-resonator frequencies and the coupling constants obtained from the fit above. While photon numbers never reach n_{crit} of the entanglement qubits, they do for the tuning qubits. We calculate $n_{\mathrm{crit}} = 50$ and 37 for chips 1 and 2, respectively. An additional unwanted effect is that residual excitations of the tuning-qubits would lead to additional noise in the readout signal, but it should not be correlated with the state of the entanglement-qubits, and should therefore not skew the tomography result.

7 CONCLUSION AND OUTLOOK

Above you see a picture of the PCB used in the experiments reported in this thesis and a PCB for a 49-qubit quantum processor designed and made in a collaboration between QuTech and Intel[1]. It is obvious that eventually the connectors will make way for a different solution that allows bringing in more control wires. This is one of the many problems that have to be solved in order to make large-scale superconducting quantum computers. Indeed, the main question to answer in the next few years is how a large-scale quantum computer will look like. In this conclusion, I will summarize the main results of this thesis. I will put them in the context of a large-scale quantum computer and try to point out interesting future research. Also, I will give personal summaries of other experiments where I was involved in a supporting role, which underline the versatility of cQED experiments and the rich physics that can be studied with these tools.

[1] Large PCB picture courtesy of Intel Corporation.

7.1 THE BICAMERAL COMPUTER?

As I was writing this thesis, I was reading Dan Brown's recent bestseller *Origin* [235]. (spoiler alert) The book plays on the common trope of evil AI, a computer going rogue and committing several murders. In the beginning, a computer passes a Turing test, giving the protagonist a tour through an art museum only to reveal his true nature and showcase his own artwork. The computer attributes his extraordinary "synthetic intelligence" to his bicameral mind: his hardware is a quantum computer that is connected to a powerful supercomputer[2]. The book is a Dan Brown page turner, but it doesn't contain too many straight-out falsehoods concerning quantum computing, mostly "truthful hyperbole". The mentioned combination of classical and quantum computer parts is very important, the quantum computer requires a classical interface. Powerful classical computing is an essential part of quantum error correction and variational quantum eigensolvers use classical optimization on quantum results to calculate spectra of Hamiltonians [236]. While my work has only been tangentially related to this (Chapter 4), a large effort in Qutech is devoted to creating the right way to integrate quantum computers with classical computers and making them as useful and programmable. I have come to see the quantum computer as a hardware accelerator, like a GPU, rather than like something that we today experience as a "computer"[3]. Thus, the poetic image of a computer that imitates the bicameralism of the human brain contains a small grain of truth.

In terms of the scientific content, Dan Brown greatly exaggerates the near-term (and possibly long-term) power of the quantum computer. The connection he makes to artificial intelligence is circumstantial today, but the application of quantum computers for optimization and linear algebra problems in machine learning is actively being explored [237, 238], so that is not an outlandish idea. That being said, a fluent conversation about diverse topics with a quantum computer is likely still a few years away, if it ever happens. In the book the classical-quantum hybrid computer is used to further our understanding by running simulations and I think Dan Brown's assessment is on the money. But his example is extreme: simulating a time-lapse Miller-Urey experiment, million years of evolution of a few liters of primordial soup, in order to prove that life can arise without a creator. It would require a computer with as many qubits as the primordial soup has relevant quantum degrees of freedom – I will not try to guess this number but I think it is beyond even the wildest proposals for practical quantum computers. However, polymers in solutions can also be modeled semi-classically. A quantum-classical hybrid simulation for similar much smaller systems might give interesting insight in the future.

Probably we won't answer the big human questions right away, but quantum computer simulations will probably shed light on some open problems in chem-

[2] The existing MareNostrum supercomputer located in the Torre Girona chapel in Barcelona - a location to Dan Brown's liking.

[3] A universal tool with an operating system, higher-level programming languages and most importantly today: a web browser

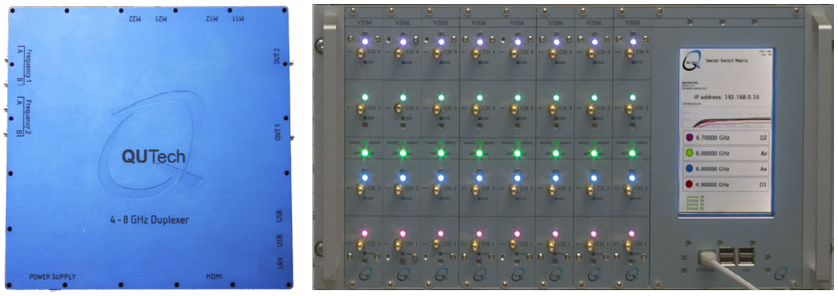

Figure 7.1: *2 frequency input, 2 qubit output VSM prototype and 4 frequency input, 32 qubit output final device aimed to save hardware for the 17 and 49-qubit surface code chips. Two prototypes have been produced so far and are being integrated into experiments.*

istry [239, 240] and material science [241]. They will do so in a matter similar to the primordial soup example, as the simulated systems give us more access to parameters and allow regimes that we cannot easily access and vary in experiment. So my take-away messages from the Dan Brown bestseller are: Quantum and classical computers will form hybrid computing systems. Quantum simulations will be among the first key applications. The quantum computing community clearly has the world's attention and quantum computing is capturing people's imaginations. This in turn means that we have to be responsible, managing expectations and carefully explaining what our computers can and cannot do. In my opinion, our field's efforts are not misrepresented more in this lurid bestseller than in an average quantum computing article in a respected newspaper or popular-science magazine. This concerns me.

7.2 HOW WILL A LARGE-SCALE SUPERCONDUCTING QUANTUM COMPUTER LOOK LIKE?

Dan Brown describes the quantum computer as being located in a dilution refrigerator and it is named E-Wave, one-upping D-Wave who are building superconducting quantum computers. Thus, he probably envisions a superconducting quantum computer. In Chapter 1, I explained the ongoing effort to push to 50 qubits and more, now I'd like to relate the experiments in Chapter 5 and Chapter 6 to this effort.

7.2.1 *Scalability and economics*

In our selective broadcasting experiment we demonstrated a control architecture for our future many-qubit quantum processors, that can greatly save expensive hardware (fast pulsing equipment and microwave sources). While we do not yet show an actual reduction in the control hardware in our proof of principle experiment, it would already pay off economically for the 17-qubit experiment, which could already show an improved quantum memory. Conventionally, this would require about as many

microwave sources as qubits and twice as many AWG channels. Both microwave sources and the fast DACs (Digital to Analog Converters) in the AWGs are expensive, currently the control hardware for a single qubit costs $\sim 15,000$€. A three-frequency VSM version could use six AWG channels and three microwave sources for the 17-qubit lattice, approximately bringing the cost for single qubit control down by a factor of three. Furthermore, a 49-qubit distance-five surface code lattice could use almost the same hardware with more fanout.

In addition to the reduction in control hardware, the repeating frequency layout also reduces the design complexity: once a unit cell with performance past the fault-tolerance threshold has been designed and realized, one simply has to copy-paste it to make an arbitrarily sized lattice. If control lines are accessing the chip plane from above or below, designing such a scalable unit cell is possible [35]. To date, no such scalable design has shown the required performance.

The problem of residual cross-coupling between same-frequency qubits mediated by multiple bus resonators and other qubits might need to be considered. We measured a residual exchange coupling of $J/2\pi = 36$ kHz. For surface-code devices, the coupling will most probably be stronger than the one that we measured, because for a three-frequency surface code, two sets of resonators and different-frequency qubits connect the same-frequency qubits instead of one set. Our current architecture [35] would result in many same-frequency qubits with residual couplings along a line. The qubit transitions for n qubits along the line would be split by the coupling to yield 2^{n-1} levels within $2J$. This splitting would not be enough to yield problems for single-qubit driving, as our pulses are much wider in frequency, but the effect of the slow entangling process between the same-frequency qubits on surface-code performance is difficult to predict. In case it proves to be a limiting factor, a larger frequency-unit-cell would have to be chosen.

However, same-frequency qubits put stringent requirements on the fabrication, as near-identical qubits are necessary for the scheme to work. Before we run into the limits of fan-out at room temperature, there are other problems to solve at that scale, namely the cooling power of dilution refrigerators, wiring solutions and fabrication yield[4].

The important take-away message from the experiment is that building a quantum computer is not only a physics challenge, but it is also an engineering challenge to come up with an extensible, economical system design. Quantum hardware, classical electronics and cryogenic engineering come together and a holistic approach to the system is necessary for building even a medium-scale quantum processor. In our current architecture [35], this result only improves the hardware scaling for single qubit gates, but it could be used for an architecture where two-qubit gates are microwave gates as well [108]. Similar hardware saving strategies could be used for low-frequency flux pulses that currently provide the fastest two-qubit gates,

[4] With current yield for Josephson junctions, resonators and on-chip lines, the chance of having a 50-qubit chip with all components working is likely $\sim 10\%$.

provided a set of pulse primitives is found that can be combined through a VSM style device without compromising tuneability.

7.2.2 *Entanglement with "flying" photons*

Whether the future superconducting quantum computer will use "flying" or transient photons as links between qubits is an interesting question that goes beyond economics. Current quantum processors are mainly confined to one chip where qubits are either directly coupled or coupled with bus resonators. This naturally leads to 2D arrays, the connectivity required for surface code and we are soon going to see the first publications realizing this on a small scale. "Flying" photonic interconnects however would lead to a different kind of quantum processor distributed between different chips or 3D cavities. At microwave frequencies, together with a cold switching matrix that would route the photons to the different qubit-cavity modules they could provide almost arbitrary connectivity. While currently, the entanglement we produce is not competitive with on-chip entangled states, improvements in the wiring, especially eliminating lossy connectors and circulators could make this approach more viable. With some improvements, distributed systems offer higher connectivity and isolation as well as the ease of picking and choosing from a larger fabrication run when putting them together. This might make them competitive with monolithic on-chip systems. In addition to our work presented in Chapter 6, the other experiments that were published almost simultaneously with our result [189–191] are deterministic entanglement schemes based on half transfer of photons from one cavity to the other that could more easily be scaled up, as they do not require a high-fidelity readout chain.

Nonetheless, our experiment compares well with other superconducting implementations of remote entanglement, especially when taking two points into account: Firstly, the entanglement rate we report is limited by our low repetition rate and could be easily increased by a factor ~ 20 with the implementation of real-time feedback for initializing the qubits [72]. Secondly, we had one more circulator than the other recent experiments [189–191], removing it to improve the loss between the cavities should provide an easy path towards Bell-state fidelities of $\sim 80\%$ with our method. Removing the circulators results in a finite length of cable connecting the chips, a low-Q communication mode. Parametric driving of transmon qubits can realize a sideband interaction with this communication mode that can also be used to generate chip-to-chip entanglement as demonstrated in [261]. The reduced losses between the chips leads to better Bell-state fidelities.

A broader comparison of remote entanglement experiments can be found in Figure 7.2, which was adapted with permission from [190]. It compares entanglement rates and different measures of bipartite entanglement that were achieved with different qubit platforms. Currently superconducting setups achieve some of the best entanglement rates. However, comparing the achieved entanglement, be it expressed

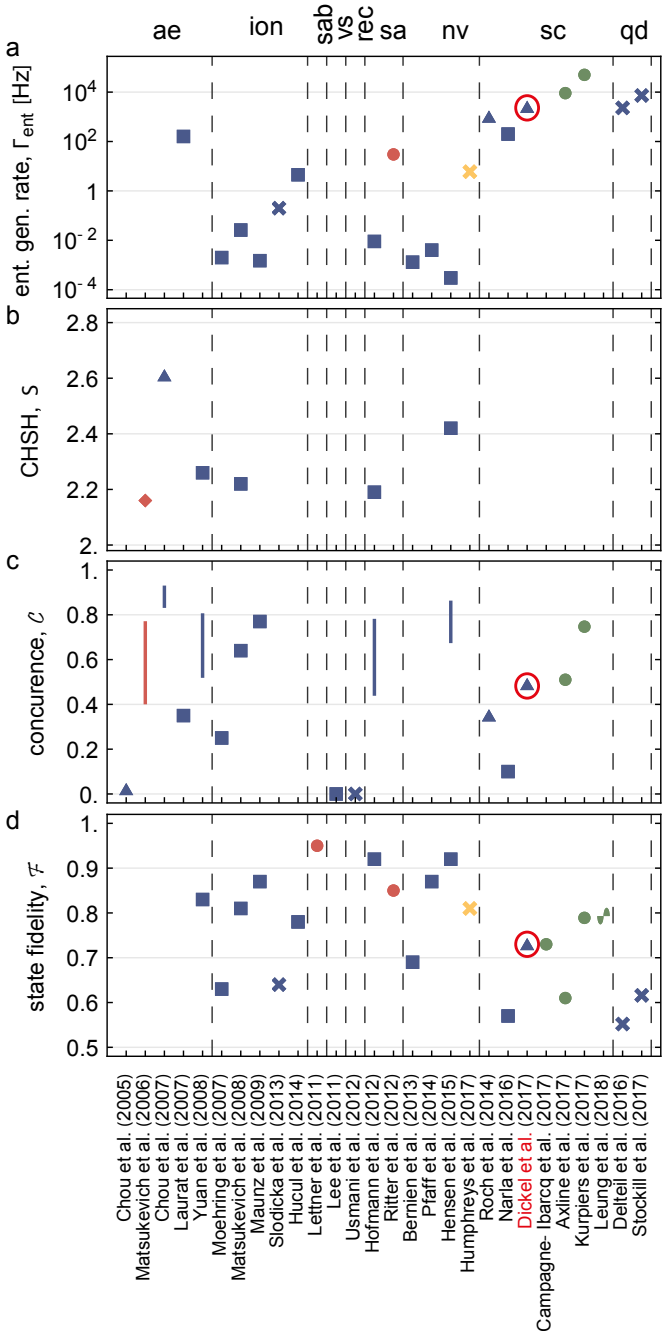

Figure 7.2: *Comparison of different remote entanglement experiments across hardware platforms (our result highlighted by red circles) giving main figures of merit:* ***(a)*** *entanglement generation rates,* ***(b)*** *CHSH, S parameter in the context of a Bell test,* ***(c)*** *concurrence,* ***(d)*** *entangled state fidelity. The experiments are sorted by physical system: atomic ensembles (ae) [242–246], trapped ions (ion) [247–251], single atom - Bose Einstein condensate (sab) [252], vibrational state of diamonds (vs) [253], rare-earth crystals (rec) [254] single atoms (sa) [255, 256], nitrogen-vacancy (nv) center [257–260], superconducting circuits (sc) [50, 182, 184, 189–191, 261] and quantum dots (qd) [262, 263]. The colors indicate probabilist unheralded (red), probabilist heralded (blue), deterministic unheralded (green) implementations. A probabilistic protocol can be made almost deterministic with repeat until success strategies (yellow). The plot markers indicate different schemes to realize the remote interaction: measurement induced (triangle), interference of two single photons on beam splitter (squares), single photon emission and detection (cross), direct transfer with shaped photons (circles) and sideband interaction with a low-Q communication mode (sine-wave). Figure used with permission [190].*

in terms of CHSH inequality [264], or in terms of concurrence or Bell-state fidelity, the ionic, atomic and NV-center results are still superior, partly because of longer coherence times.

Purely photonic entanglement is not included in Figure 7.2 and the distance between the entangled qubits is not compared. When it comes to distance, purely photonic experiments are still outperforming experiments with stationary qubits. Pairs of entangled photons to date also show some of the strongest CHSH violations in loophole-free Bell tests [265, 266] and have recently demonstrated long-distance entanglement through submarine optical fibers [267] and up to satellites [268]. Thus, for communication purposes, photonic systems at optical and telecom wavelengths remain very promising. But stationary qubits allow the implementation of quantum repeaters and will eventually be more useful in many quantum network protocols. For superconducting qubits, long-distance applications will only come within reach if the microwave photons can be faithfully converted to telecom-wavelength photons that can be transmitted over longer distances. While there are attempts to realize this frequency conversion, for example [269, 270], currently conversion efficiencies are much too low.

7.2.3 *Direct syndrome measurements for error correction*

The entanglement-by-measurement approach we realized in Chapter 6 could also be generalized to achieve direct parity measurements. Generalizing this to a multi-qubit parity measurement, one could realize error correcting schemes without the need for ancilla qubits [271]. In our experiment, we only explored the static Jaynes-Cummings Hamiltonian, where the qubit states are fixed during measurements, but a combination of driving the qubits and resonators could make such approaches less demanding in terms of fabricating systems with natural symmetries. Thus, the number of elements on chip for a surface code lattice could be cut in half. The drawback is that the ancilla qubits in the isotropic surface code lattice can be used, for example swapped with the data qubits to eliminate leakage or do gates on the code, which would not be possible in an architecture with direct syndrome measurements.

Paradoxically, theoretical proposals requiring symmetries of the hardware is a symptom of a more general problem: most quantum computer architectures put strong constraints on the quantum hardware, while not challenging the control electronics as much or venturing into Hamiltonians that are hard to model. Navigating the vast space of multi-qubit-multi-cavity systems with both qubit and resonator drives might yield robust schemes for entanglement that do not require fabrication precision beyond the current state of the art.

7.3 ENTANGLING MEASUREMENTS AND FEEDBACK

Another experiment we left unexplored for lack of time, was to combine the entangling measurement of Chapter 6 with direct feedback on the qubits as for example

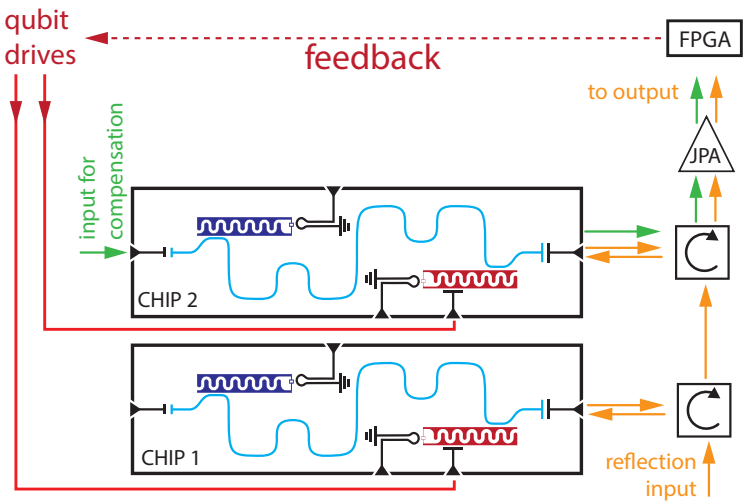

Figure 7.3: *Schematic for a feedback loop added to the entanglement experiment reported in Chapter 6. This would open interesting possibilities, either to increase the rate of the experiment, applying digital $Y_{\pi/2}$-Pulses in case the $|00\rangle$ or $|11\rangle$ results can be inferred from the readout trace and starting over or exploring a more analog approach applying rotations proportional to the signal mismatch from the target outcome.*

suggested in [219]. The hardware would be largely the same as in the Chapter 6 experiment, but an FPGA with data demodulation would be used to realize a feedback loop as sketched in Figure 7.3. The qubit drives would be a function of the deviation from the odd-subspace voltage, driving the system out of the 00 and 11 state. Under certain conditions, the interplay of measurement and feedback driving can lead to steady state entanglement.

Another way to achieve steady state entanglement is a bath engineering approach [217]. The system is driven, such that the only steady state is an entangled state. In direct experimental comparison for two qubits in the same cavity [272] bath engineering outperformed the feedback approach, because the bath engineering approach is not hurt by a quantum efficiency < 1. Comparing the approaches in the two-qubit-two-cavity case would be an interesting experiment to perform.

7.4 A PERSONAL VIEW ON OTHER EXPERIMENTS OF MY PHD

The experiments reported in Chapter 5 and Chapter 6 are the main experiments I performed during my PhD, but I played supporting roles in several other experiments. The opportunity to peek into different experiments was a privilege, as I could familiarize myself with the challenges of studying different Josephson junctions, looking deeper into circuit quantization, and looking into quantum simulations. These experiments also reside in different abstraction layers in the spectrum of cQED from hardware to quantum algorithms, thus requiring different experimental skills: in the

case of the readout experiment and the Rabi simulation, it required careful tuning to optimize performance, while the nanowire transmons and the tuneable coupler required an open mind in exploring the physics of these devices. I will now briefly summarize the four experiments.

Active resonator reset in the nonlinear dispersive regime of circuit QED [71] was related to the chip-to-chip entanglement work as both papers use dispersive readout and explore non-trivial readout pulse shapes to control the measurements. Where the chip-to-chip entanglement optimizes a pulse shape for two-qubit readout to make two of the four basis states indistinguishable, this work focuses on single-qubit readout and engineers pulses that empty the resonator as fast as possible after the measurement. While the readout resonator is occupied, accurate gates on the qubit are not possible. Without engineered pulses, the measurement time is limited by the ringdown time of the resonator. We show that we can decrease the depletion time of the measurement by 6 inverse resonator linewidths.

In addition, the experiment was performed in a regime of readout power where the dispersive approximation breaks down, which is a difficult regime to simulate. It was known from previous work, that a high-fidelity transmon readout can be achieved at surprisingly high measurement powers where the Jaynes-Cummings Hamiltonian should no longer be accurate [273]. In our case, the measurement power exceeds the critical photon number n_{crit} by two orders of magnitude. Nonetheless, repeated measurements imitating the ancilla cycle of surface code give good agreement with a model assuming a non-demolition measurement. The comparison with [274] is interesting because their study of the transmon resonator system as two coupled ladders suggests that at high measurement powers, the transmon can be excited into higher states via processes involving several photons. But at small transmon-resonator detuning $|\Delta|$, as realized in our experiment, quantum non-demolition measurements might be possible at higher photon numbers, because these transitions are more unlikely. It would also have been interesting to use depletion techniques to make the entanglement protocol in Chapter 6 faster or even explore the entangling measurement in the high-power regime.

Experimentally simulating the dynamics of quantum light and matter at deep-strong coupling [49] concerned the Rabi model which is the parent Hamiltonian of the dispersive Jaynes-Cummings Hamiltonian that the cQED community so heavily relies upon.[5] A visual summary of the main results can be found in Figure 7.4. The standard quantum Rabi model [275] describes the coupling of a two-level atom (energy $\hbar\Omega^{\text{R}}$) to a quantum harmonic field mode (energy $\hbar\omega^{\text{R}}$) by a field-dipole interaction (energy $\hbar g^{\text{R}}$):

$$\frac{H_{\text{R}}}{\hbar} = -\frac{\Omega^{\text{R}}}{2}\sigma_z + \omega^{\text{R}} a^\dagger a + g^{\text{R}}\left(a + a^\dagger\right)\left(\sigma_+ + \sigma_-\right). \tag{7.1}$$

[5] The Rabi model is more general than the Jaynes Cummings Hamiltonian introduced in Chapter 2, which already neglects the excitation-non-conserving terms $a\sigma_-$ and $a^\dagger\sigma_+$.

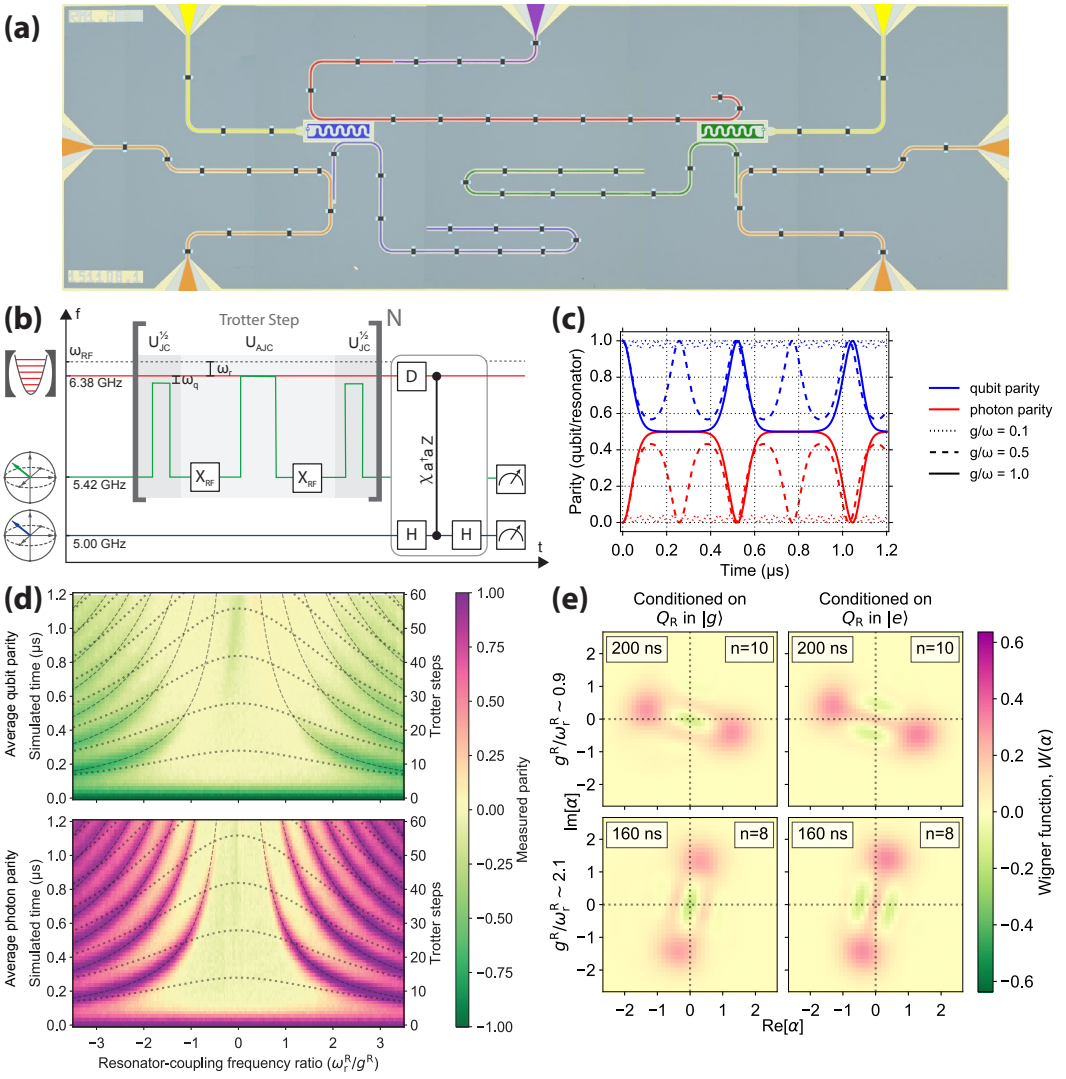

Figure 7.4: *Figure summary of the Rabi Model simulation experiment.* ***(a)*** *False-color microscope image of the device with two qubits (blue and green) and the Rabi-model resonator (red). Qubits have individual readout resonators.* ***(b)*** *Experimental scheme. The simulation trotter step consists of three flux-pulses, where the Rabi-qubit (green) is pulsed near resonance with the Rabi-resonator, and X_π-pulses. The resulting effective Hamiltonian corresponds to the Rabi-Hamiltonian with coupling that can be tuned into the deep-strong coupling regime.* ***(c)*** *Qubit and resonator parity dynamics with varying coupling strength.* ***(d)*** *Heat maps of the qubit and resonator parity varying the relative coupling and simulated time.* ***(e)*** *Wigner tomography. Using the Wigner-qubit (blue), the resonator state can be reconstructed conditioned on the state of the Rabi qubit. The resulting qubit dependent cat-states confirm qubit-resonator entanglement.*

Realizing this Hamiltonian where g^R is dominant with respect to Ω^R and ω^R is challenging. In cQED, "qubits" generally have higher levels that need to be taken into account once the coupling to a resonator becomes very big [276]. So far only spectroscopic signatures of this regime have been achieved in cQED [277, 278]. Our experiment aimed at exploring the dynamics in this challenging regime. The experiment is a quantum simulation that relies upon the fact that the full Rabi Hamiltonian can be decomposed into two JC-like interactions [279]:

$$H_R(g^R, \omega^R, \Omega^R) = H_{JC}(g, \Delta_r, \Delta_q^{JC}) + H_{AJC}(g, \Delta_r, \Delta_q^{AJC}), \tag{7.2}$$

where $H_{AJC} = \sigma_x H_{JC} \sigma_x$, is a Jaynes-Cummings evolution sandwiched between two bit flip operations on the qubit, that generates the counter-rotating interaction terms. The effective Rabi parameters $g^R = g$, $\omega^R = 2\Delta_r$ and $\Omega^R = \Delta_q \equiv \Delta_q^{JC} - \Delta_q^{AJC}$ are not related to the natural circuit frequencies, but defined relative to a nearby rotating frame ($\Delta = \omega - \omega_{RF}$), and can be arbitrarily small. This makes it possible to simulate a Rabi model Hamiltonian in the ultra-strong and deep strong coupling regimes, where g^R is the dominant term using a physical system that is far from ultra-strongly coupled. The detailed experimental scheme including this Trotter step can be found in Figure 7.4**(b)**. Our simulation starts in the state $|1\rangle_q \otimes |0\rangle_r$, an eigenstate of the uncoupled system. While the total parity in the system is conserved, the dynamics lead to the build up of photons in the resonator and interesting dynamics in the individual parities of the resonator and the qubit. Figure 7.4**(c)** shows the theoretically predicted qubit and resonator parity dynamics for three different coupling strengths, while Figure 7.4**(d)** shows our quantum simulation of the dynamics results sweeping the relative coupling , the strongest coupling being in the center of the plot. The deep-strong coupling between the qubit and resonator also leads to interesting qubit-resonator entanglement, which we showed by reconstructing the resonator state conditioned on the qubit state [Figure 7.4**(e)**]. Instead of only using the resonator as a means to read out the qubit, another qubit was used as a means to reconstruct the quantum state of a resonator via Wigner tomography.

Getting insight into the field of quantum simulation with a simulation that has analog and digital components was fascinating. The digital part of the simulation is the Trotter step, breaking up the time evolution and constructing the hard-to-realize Rabi Hamiltonian from simple Jaynes-Cummings dynamics and bit flips on the qubit. The analog part of this simulation is the fact that the resonator is simulated by a resonator, instead of a resonator state being encoded in many qubits. This enabled a more complex simulation without excessive use of quantum hardware. The method can be extended to simulate Dicke models [280] with more than one qubit ultra-strongly coupled to the resonator, systems that can be difficult to simulate classically. The Rabi model we simulate is still solvable in all parameter regimes.

Evolution of nanowire transmon qubits and their coherence in a magnetic field [281] was a continuation of our groups work on semiconductor-superconductor hybrid qubits, where a nanowire Josephson junction was used to make a transmon

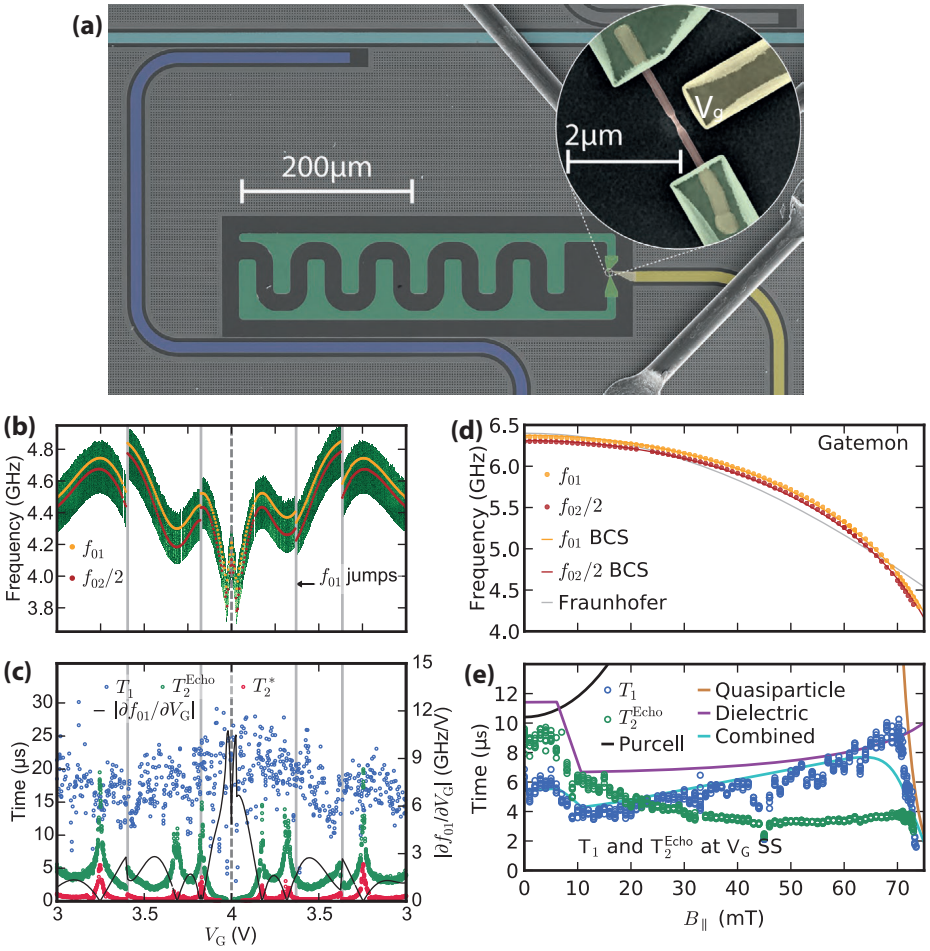

Figure 7.5: ***(a)*** *Picture of a nanowire transmon device with zoom in on the junction region.* ***(b)*** *Dependence of the transmon frequency on gate voltage. We observe a mix of reproducible continuous changes as well as random and sometimes reproducible jumps.* ***(c)*** T_1, T_2 *and* $T_{2,\mathrm{echo}}$ *as a function of the gate voltage. Coherence time is correlated with the frequency sensitivity to the voltage. (note that these qubits outperform many Al-AlO_x-Al-junction qubits reported in this thesis)* ***(d)*** *Frequency dependence on magnetic field applied parallel to the chip plane. Qubit* f_{01} *and* $f_{02}/2$ *are well described b a closing of the BCS gap.* ***(e)*** T_1 *and* $T_{2,\mathrm{echo}}$ *as a function of the applied field. We find that the overall behavior is modeled well by the Purcell effect, a field dependent dielectric loss and a quasiparticle contribution.*

qubit [282, 283]. We showed several nanowire transmons with coherence times comparable to their counterparts with Al-AlO_x-Al junctions. A visual summary of the main results can be found in Figure 7.5. The picture of the device shows the nanowire in place of the usual Al-AlO_x-Al junctions with a side gate that can be used to change the properties of the junction. As good contact between the superconductor and semiconductor is important, indium arsenide nanowires with an epitaxially grown aluminum shell were used to make these devices [284, 285]. The junction was created by removing the aluminum shell in a small section of the nanowire. In these junctions, only few channels contribute to the Josephson effect, such that the current-phase relationship is modified with interesting consequences for the transmon Hamiltonian. This data can best be obtained from SQUID-loop transmons, fitting the flux dependence of the transmon levels (data not included in summary).

The nanowire junctions lead to voltage-tuneable Josephson energies. Voltage-gate tuneable transmon qubits were named gatemons in the tradition of branding any transmon innovation [283].[6] However, this also means that gatemon qubits are charge sensitive. We studied the additional charge noise these junctions are subject to, seeing a switching behavior that we attribute to nearby charge traps coupling to the junction. The plot of frequency vs applied gate voltage in Figure 7.5**(b)** shows clear sweet spots, where the frequency gradient with applied voltage is low and qubit coherence [Figure 7.5**(c)**] increases accordingly.

In addition, we studied the magnetic field behavior of the nanowire devices. Currently, due to the thick aluminum layer, the junctions have critical fields on the order of $\sim 80\text{mT}$ as seen in in Figure 7.5**(d)** and **(e)**, where the qubit frequency and coherence properties are plotted against the field. The qubit frequency reduction is well described by a closing BCS gap. We used a single-axis magnet, with fields roughly aligned in plane with the superconducting film to avoid vortices, but the field direction with respect to the nanowire could not yet be studied here. Future devices with thinner aluminum layers should sustain fields up to $\sim 200\text{mT} - 500\text{mT}$, which would enable investigating the origin of flux noise as well as the study of spin-orbit physics inside the nanowire junctions.

Tuneable hopping and nonlinear cross-Kerr interactions in a high-coherence superconducting circuit [51] was an exploration of coupling two transmon qubits via a third transmon-like circuit in order to realize tuneable qubit-qubit coupling for analog quantum simulations. The main results are summarized in Figure 7.6, which shows the circuit diagram and illustrates the tuneable coupling by a series of avoided crossings for different coupler settings. In the crucial region, where the linear hopping interaction between transmons can be turned off and the current through the capacitor and inductor cancel out [Figure 7.6 (d)], the non-linear terms of the coupler dominate the remaining interaction. These terms include cross-Kerr ($a^\dagger a b^\dagger b$), correlated hopping [$(a^\dagger a + b^\dagger b)(a^\dagger b + b^\dagger a)$] and pair-tunneling ($a^\dagger a^\dagger b b + a a b^\dagger b^\dagger$)

[6] So far this has given rise to the Xmon [127], gmon [104],the gatemon and the starmon [35].

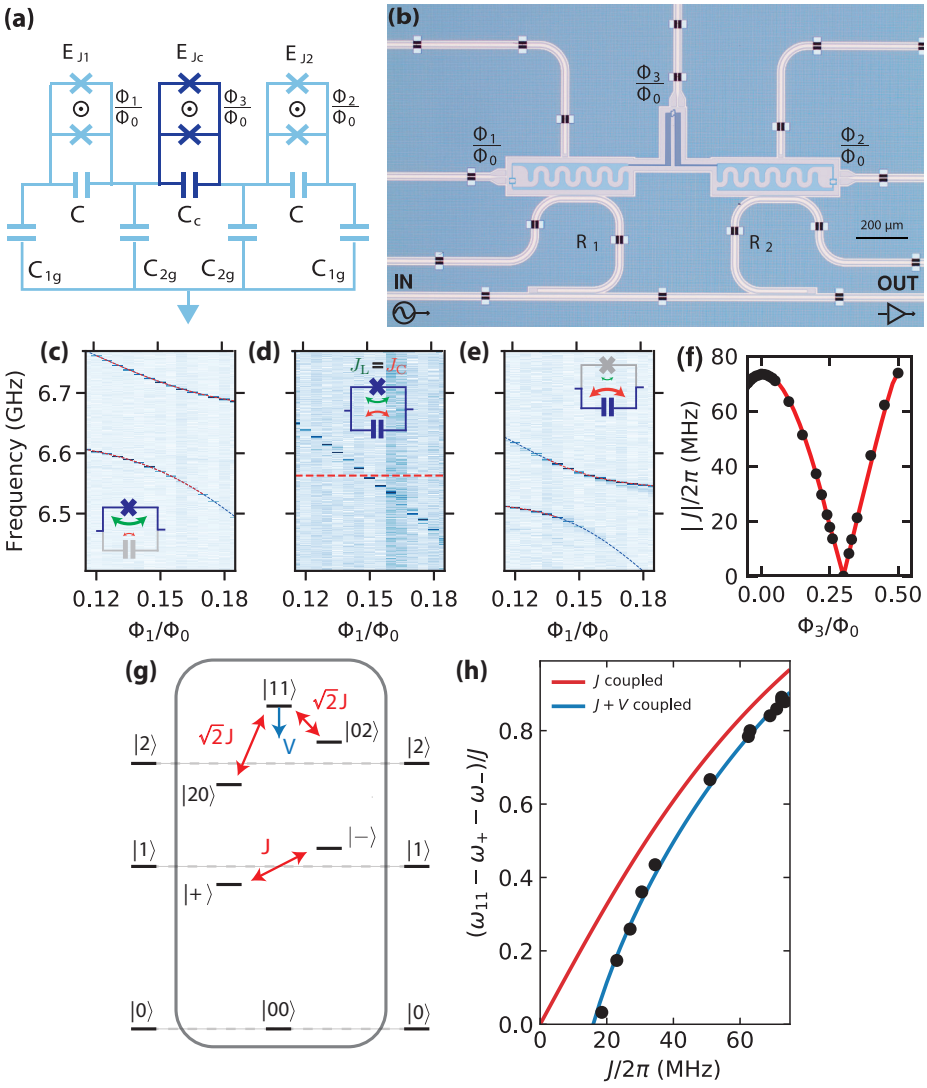

Figure 7.6: ***(a)*** *Circuit diagram for the tuneable coupler.* ***(b)*** *False-color microscope picture of the chip. Flux-bias lines for the 3 SQUID loops are indicated, as well as the readout resonators (R_1 and R_2) and the feedline at the bottom.* ***(c, d and e)*** *Avoided crossings between the qubits, for different coupler-bias settings showing the change in the qubit-qubit couping.* ***(f)*** *Coupling as a function of coupler bias as determined from the avoided crossings* ***(g)*** *Level diagram of the system including the higher excited states of the two transmons. In the more complete picture, it becomes clear that the repulsion of the higher levels plays a role in the coupler action.* ***(h)*** *Modelling the effect of the higher levels. A plot of $(\omega_{11}+\omega_{+}+\omega_{-}-\omega_{11})/J$ agains J assuming only hopping interactions (red) and taking into account the nonlinear cross-Kerr coupling (blue) shows that the latter describes our data well.*

processes. However, higher levels of the coupler also cross the relevant region in case of this particular device. We were able to show this by modeling the circuit including the higher levels and finding a good correspondence with our measured spectrum. Using a full theoretical model, we show that the circuit can be adapted, mostly by adjusting the capacitances, to push the higher levels of the coupler out of the relevant region.

Therefore, we realize an interesting building block for analog simulations with transmon chains and 2D-arrays both in the qubit subspace and higher excitation manifolds. In driven dissipative scenarios, the formation of crystalline phases of light can be observed [286]. A recent experiment with tunably-coupled resonators also exploits this interaction to show photon ordering as a function of the coupling [287].

ACKNOWLEDGEMENTS

Apart from the science, these acknowledgments are the most important part of this thesis. These few pages have to hold four years worth of thankyous but one comes first: **Leo**, thank you for taking me on as your PhD student. That decision has profoundly impacted my life and lead to more than 4 years in Delft that were fantastic. In German, we say Doktorvater – literally doctor father – and our relationship has at times been as passionate as a family relationship. Please know that I have more affection for you than I usually admit. Our personalities are opposites in the worst case and complementary in the best case. Your strengths have inspired me to try to overcome my flaws: my rash judgment, my lack of focus and wavering dependability – sometimes successfully. Your example as a scientist has taught me standards that I hope to maintain in the future. Maybe it is fair to say that the first quality that comes to mind when thinking of you is not patience, but I am most grateful for your patience with me. In addition, you did not give up on helping me with my English punctuation, especially improving my hyphenation. Last but not least, we played together in the QuTech band and you – fittingly – set the tempo from behind the drum set or playing rhythm guitar.

I would also thank the **leadership of QuTech** for creating this unique environment. You have made all this science possible, but more importantly, you have brought this diverse cast of characters together. Even if I have my reservations about the transition from QT to QuTech, as any member of an organization that more than doubles in size likely has, I am inspired by the ambitious roadmap goals and the determined effort to reach them. My generation of PhD students is one that did not have to worry about resources and I am grateful for that and I hope to have been mindful of that fact most of the time.

I would like to thank the members of the committee for evaluating my thesis, it is comforting to know that some readership is guaranteed and I hope you do not find it too dull. **Ronald**, thanks for being my second promotor and a mediating influence towards the end of my PhD. Your "I already have a PhD" catchphrase has always motivated me to get one as well. **Barbara**, I am glad that you are on the committee, because your class in Aachen was one of my gateway drugs to quantum information and computation. **Hans**, it also meant a lot to me that you agreed to be part of my committee. I really enjoyed talking you into writing for the QuTech blog and am thankful that you were frequently around QT and QuTech always happy to discuss and share your knowledge.

Being a part of the DiCarlo group was an honor and a pleasure because of the people that constitute it. But lets be honest here, when I talked about interesting

physics that can be studied with these tools in Chapter 7, I was also talking about some of you guys. Let me thank the cast in order of appearance (according to my recollection).

I would like to begin with the group that I joined more than four years ago, which is very different from the group now. **Diego**, you impressed me from the beginning with your knowledge, dedication and focus. I am grateful that you taught me the basics in the cleanroom and in the lab. The project we started together took me much longer than we anticipated, but eventually it was a partial success. **Alessandro**, you are the constant in this story because you are the only member that has been around since I joined. You made me feel at home in the group from the beginning and taught me a great deal of cleanroom technique and tricks. You are also the only person mentioned here that I threatened with physical violence. Thanks for being my friend despite that and keep having crazy ideas and making them a reality. I would also like to thank you for your help in fabricating the chips for the thesis cover. **Gijs**, in the beginning I might have smoked many cigarettes just because of the accompanying conversations with you. You seem to have the happy and full life as a scientist figured out, which has always given me hope. Thanks for teaching me lots of stuff and more importantly for your friendship. **Olli**, as the least Finnish Finn I have met so far, you have finished quite a bit of impressive science in your short time in Delft. Also, you brought **Visa** to Delft, who played the drums in the first instance of the QT band that I was part of.

After I joined, the group gradually grew with many new people joining and occupying the new big labspace after the move from F033 to QClab. **Stefano**, you helped me run the first randomized benchmarking sequences and you took over my chip design code and pushed it to design a 17 qubit chip. Your sense of humor has often helped me cope with the scientific and social challenges of the lab. I hope you will like working with the competition! **Nathan**, I have never had a short conversation with you, but most of them were worth it. Of all the post docs, you had the biggest impact on my formation as a scientist. Your comments on the draft of this thesis were a huge help in completing it. I'm happy that Jasmin and I became friends with you, **Mim**, **Freddy** and **Berti** (I'm still a bit affraid of holding babies...) and I hope we can visit you in Australia soon. Also, I wish you all the best for starting your own research group of course. **Florian**, I wish we could have started our PhDs together instead of a year apart, because you are the ideal labmate. I often wished I was as dependable as you are. But you are not only a great lab mate but also a good friend and I am honored that you will be my paranymph. Good luck with finishing your project and pushing transmons to higher fields. **Ramiro**, I still remember the day when Leo and I interviewed you for a master project. You had an immediate impact on the group with your positive attitude and you should work to maintain it even when things get frustrating. Maybe you can teach me Latin dancing in the future and I will gain more confidence and positive attitude! I am proud of our history and it is fitting that we went from master student and

supervisor, to friends, colleagues and now you are my paranymph. **Adriaan**, let me start by apologizing for sometimes referring to you as the GIT git. We have realized a nice architecture for measurements together and you have been at the center of it. I have not always been an easy collaborator and didn't have as much time to contributing to the core of PyCQED as I would have liked. I hope that you can run optimizations on a 17 qubit surface code soon. **Niels**, you are a machine in the lab, I wish I had your focus and determination, but I'm happy to have also seen your human side. I wish you and **Anne-Marije** all the best for finding the balance between work and life in QuTech. **Marios**, it kinda broke my heart that you switched groups, but I am happy that you seem happier now. Thanks for many discussions that make me happy to be a physicist. You and **Electra** have started on a much bigger adventure than a PhD with **Antigoni**. I wish you all the best for both. **Jacob**, you are the oldest of us, but probably also the healthiest and without a doubt the wisest person in the DiCarlo group. Thanks for all your effort to make the group better that goes beyond just programming our firmware and optimizing rack wiring. **Duije**, thanks for designing the VSM and the QuTech mixers. You have given me an idea of the intricacies of analog microwave design and were always happy to explain the details of your work. **Wouter**, your work of building our own AWG has demystified the hardware a little bit, but also shown how difficult it is to design a working model. **Nadia**, you have drawn many a funky transmon capacitor and given them cool names. Thanks for explaining some of the intricacies of electrostatic and dynamic simulations. I hope you guys make the control hardware for surface 17 a reality. When it comes to bridging the gap between physics and engineering, who better than **Xiang** (or master Fu) to turn himself into a living bridge. Our conversations have made the concepts of "hardware programming" more clear to me and helped me understand how computer scientists approach architectures in a concrete way. Thus, the value of working in an interdisciplinary field is partially to gain a broad education. **Thijs**, thank you for seeming much more naive than you are while occasionally being much more naive than we think to keep us on our toes. **Dave**, you were our company man. While we never officially worked together, I feel that we always had things to talk about, be it fabrication ideas, US politics or music. Finishing this thesis, I feel that I have reached the state of enlightenment summarized in your song "Adios". **Jules**, I like your enthusiasm and appreciate your advice for the blog article. Hopefully one day I can buy some Delft Instruments from you and Niels. **Brian**, as our resident experimental theorist, you have taken many responsibilities. From fridges, to measurements, to simulations you seem to do it all. Thankfully you also usually have time to explain things to me that I don't understand. It was always cool to have you, **Tom**, and **Xavi** around looking into decoders for the surface code devices and finding out what kind of performance we will need. **Nandini**, we had been friends for a few years when you joined the group and I really enjoy spending more time together at work and sitting across from you in the office. Your explanations of chemistry and biology have helped look

beyond the narrow quantum-computing horizon a little bit. **Tom v.d.R.**, while you were never a member of the group, you spent quite some time with us and gave me the opportunity to learn about traveling wave parametric amplifiers and think about making Josephson junctions without the Dolan bridge. I wish you good luck with testing the limits of quantum mechanics in our systems.

I would like to thank all of my master students: **Serwan**, **Ramiro**, **Sarwan** and **Jaap**. I have learned at least as much from you as you have learned from me. Most of you are better at coding than I am and it made our work so much easier that I didn't have to teach it to you! Without you, I would not have achieved the results presented in this thesis. All of you have started your own PhDs now or are about to do so, which makes me proud in a patronizing way, and I wish you success and more importantly fun along the way. I'd also like to thank all the other master and bachelor students who came through the group for all the interesting work, the discussions and being part of the team: **Myles**, **Kian**, **Bart**, **Rick**, **Sjoerd**, **Oscar**, **Livio**, **Malay**, **Joep**, **René** and **Marc**.

For the theory support in the entanglement project, I'd like to thank **Ben** and **Felix**. **Ben**, thanks for helping me understand the intricacies of SME simulations (which might still be work in progress for both of us). I hope that you will die on Mars, just not on impact! **Felix**, you are the DRAG-king of transmon physics. It was fun to work with you and meet at conferences!

Good science requires good technical support, a maxim that has been carried over from QT to QuTech. Whenever I had an electronics question or a technical problem, **Raymond Sr** was always the first person to ask, because of his clear explanations and problem solving skills. Thank you, Raymond! But you also created a team with **Raymond Jr** and **Marijn**, that puts the tech in QuTech. **Marijn**, sorry that I never managed to get to the feedback experiment that you prepared the FPGA for. I'd also like to thank **DEMO** for providing custom solutions and helping with fridge wiring.

When it comes to the more heavy hardware, pumps, fridges, liquid nitrogen and machining, I'd like to thank **Remco** (always in tune on the guitar), **Jelle**, **Mark**, **Siebe**, **Niko**, **Jason** and **Olaf**. Without your support experiments in QuTech would not be running smoothly. Thanks for keeping the cooling water flowing and keeping things cool even during power outages. I'd also like to thank **Giorgio Frossati** and his team at **Leiden Cryogenics** for building all fridges I worked with during my PhD and providing quick solutions whenever problems arose. I mostly worked with the Leiden fridge that was lovingly named *La Ferrari*. Even though *La Ferrari* is to my knowledge the oldest dry fridge in QClab, it was often photographed by journalists and a picture even made it into the quantum manifesto [288], a European Union strategy paper. It needed some maintenance from time to time but has been reliable and will hopefully continue to be a vessel for cool experiments for a long time.

For keeping the cleanroom running, I'd like to thank the **Kavli Nanolab Team**. Having 24/7 access to the equipment is very helpful and you guys usually manage

to keep the machines up. I'm sorry for not labeling every beaker and not honoring every reservation. Here, I'd also like to thank **David** and **Akira** for providing the NbTiN film for virtually all experiments I participated in. You also always have interesting different views on our experiments and it inspires me that you use similar hardware to look at the stars.

On the administrative side of QuTech, I'd like to thank **Marja**, **Yuki**, **Chantal** and all the other secretaries for streamlining the ordering, booking of flights and other paperwork. I probably needed more help with paperwork than the average PhD student. **Joanna**, thanks for all the reminders to register my working hours in the system and sorry for all the times I forgot.

I would also like to thank my office mates from the beginning of the PhD: **Ilse**, **Fei**, **Diego** and later **Florian**. As to the latter half of my PhD, my office mates were basically **all of QuTech**. If I would try to mention everyone who has had an impact on me in these years, I would have to add a few pages to these acknowledgments. Thanks to all for being part of this amazing institute which is a textbook example of an emergent phenomenon. The growth of the last years has illustrated that more is different, but in terms of science, I think we are proving that more is more. All of us are constantly exposed to excellent quantum science across different hardware and this diversity is a unique strength. For someone like me, discussing my favorite science (and non-scientific topics) with smart people is like heroin and I often could not tear myself away from those discussions to actually achieve scientific results. But it has not been for nothing, all of these micro-interactions have impacted my view on science (and life in general). I have no doubt there is a lot of cutting-edge science coming from the several QClabs in the future and I'm looking forward to reading about it. So farewell QuTech, continue to be more than the sum of your parts!

A PhD in QuTech also made it possible to be part of the institute blog and band. These extracurricular activities have made my life here much richer. For the blog, I'd like to thank the initial editing team **Suzanne**, **Jonas**, **James** and **Adriaan**. You guys started something and I hope it will continue to promote and explain our science to a bigger audience. For all the fun we had with all the instances of the recently named **Q2** band, I'd like to thank **Bas**, **Hannes**, **Machiel**, **Visa**, **Maaike**, **John**, **Jonas**, **James**, **Leo**, **Ruud**, **Marina**, **Remco**, **Nathan**, **Dave**, **Peter**, **Gertjan**, **Victoria**, **Hans**, **Romy**, **Connor**, **Joe**, **Floor**, **Matteo**, **Jelle** and **Timo**.

A special thanks goes to **Gary Steele** and the **Lab of Steele** for giving me a scientific home in Delft while waiting to defend this thesis. The last few month of working together with **Mario(s)** have given me a different look at cQED and a quick introduction to mechanical oscillators of different shapes and sizes. It was also an opportunity to get to know the non-QuTech part of **QN**. I'd like to thank the people of **QN** for all the cool science and fun activities besides work during my PhD and in the last six month. At the skiing and sailing trips it was also always fun

to party with the **BN** people and listen to their talks even if they are a bit closer to the stamp-collecting side of science.

Thanks to all the people who have made the Delftse Dada Jam music nights fun and productive: **Jochen**, **Albert**, **Tolga**, **Ege**, **Holger**, **Steven**, **Giordano**, **Anna**, **Jonas**, **Christopher**, **Romy**, **Will**, **Floor**, **Federico**, **Rob**, **Filip** and **Avradeep** (and many more who I have not mentioned by name). The jam nights were a big part of my social life in Delft and playing music with many different people has inspired me and given me a unique creative outlet. Thanks to the **Pickwick Club** for writing some poetry together and drinking Pastis, because we are a pretentious bunch. I want to thank **Giannis** and **Esther** for all the pitas, the lamb chops, the greek music nights and your friendship. You guys know that the stomach is the way to the heart! Maybe most important for enjoying my time in Delft was **Oude Langendijk 24A**, the house next to where Vermeer's house used to be. Apart from my parents house I never lived in one house for so long. I'd like to thank my previous house mates **Francesco**, **Inigo** and **Faik**, but particularly now with **Deniz** and **Raj**, our household has really become a surrogate family.

I'd like to thank my friends from Germany who have supported me all the way to here. **Aynur**, we have been friends for most of our lives and I'm happy you visited me in Delft so often! **Pia**, you, Jasmin and me have been through quite a lot by now, but I'm sure we can always have a good time together! The Aachen crowd: **Jens**, **Betzi** and **Lotte**, **Pascal**, **Franzi**, **Susanne**, **Marcia**, **Martin**, **Zeus**, **Tim** and **Gregor**. Many of you helped me study and develop as a physicist or as a musician, but most importantly as a person. We have to try to continue the tradition of Christmas dinners in Aachen.

Without my **family**, I would not be who I am today. My curiosity has been my main driving force to become a scientist and you have nurtured it from an early age. You have supported me both financially and emotionally through the long studies to become a scientist. You have always provided a safety net and a home in Herten. My in-law's house in Witten has now also become another home for me and lying in the hammock in the garden has always been a good way to detach from science for a while.

Jasmin, für mich bist Du immer nur *die* Frau. Thank you for putting up with these four years of me living my science dream. Without your support, I would not have made it. My hope stems from the fact that we are pursuing a richer, more important dream together (with **Twickers**).

CURRICULUM VITÆ

Christian Dickel

26.06.1988 Born in Herten, Germany.

EDUCATION

1998–2007 Secondary School
Städtisches Gymnasium Herten, Germany (1998–2004)
Winton Woods High School, Cincinnati, USA (2004–2005)
Städtisches Gymnasium Herten, Germany (2005–2007)

2007-2013 Undergraduate in Physics
Rheinisch-Westfälische Technische Hochschule (2007-2010)
Université libre de Bruxelles (2010-2011)
Rheinisch-Westfälische Technische Hochschule (2011-2013)
Master end project:
Thesis: Nuclear Spin Mediated Landau-Zener Transitions in Double Quantum Dots
Advisor: Prof. dr. H. Bluhm

2013-2018 PhD. Physics
Technische Universiteit Delft
Thesis: Scalability and modularity for transmon-based quantum processors
Advisor: Prof. dr. L. Di Carlo

LIST OF PUBLICATIONS

7. M. Kounalakis, **C. Dickel**, N. K. Langford, A. Bruno, G. A. Steele, *Tuneable hopping and nonlinear cross-Kerr interactions in a high-coherence superconducting circuit*, NPJ Quantum Information **4**, 38 (2018).

6. **C. Dickel**, J. J. Wesdorp, N. K. Langford, S. Peiter, R. Sagastizabal, A. Bruno, B. Criger, F. Motzoi, L. DiCarlo, *Chip-to-chip entanglement of transmon qubits using engineered measurement fields*, Physical Review B **97**, 064508 (2018).

5. F. Luthi, T. Stavenga, O. W. Enzing, A. Bruno, **C. Dickel**, N. K. Langford, M. A. Rol, T. S. Jespersen, J. Nygård, P. Krogstrup, L. DiCarlo, *Evolution of nanowire transmon qubits and their coherence in a magnetic field*, Physical Review Letters **120**, 100502 (2018).

4. N. K. Langford, R. Sagastizabal, M. Kounalakis, **C. Dickel**, A. Bruno, F. Luthi, D. J. Thoen, A. Endo, L. DiCarlo, *Experimentally simulating the dynamics of quantum light and matter at deep-strong coupling*, Nature Communications **8**, 1715 (2017).

3. C. C. Bultink, M. A. Rol, T. E. O'Brien, X. Fu, B. C. S. Dikken, **C. Dickel**, R. F. L. Vermeulen, J. C. de Sterke, A. Bruno, R. N. Schouten, and L. DiCarlo, *Active Resonator Reset in the Nonlinear Dispersive Regime of Circuit QED*, Physical Review Applied **6**, 034008 (2016).

2. S. Asaad*, **C. Dickel***, N. K. Langford, S. Poletto, A. Bruno, M. A. Rol, D. Deurloo, L. DiCarlo, *Independent, extensible control of same-frequency superconducting qubits by selective broadcasting*, NPJ Quantum Information **2**, 16029 (2016).

1. **C. Dickel**, S. Foletti, V. Umansky, H. Bluhm, *Characterization of S–T+ transition dynamics via correlation measurements*, Physical Review B **92**, 125402 (2015).

ADC	analog to digital converter
AllXY	experimental sequence with different two-pulse combinations of qubit rotations around the x and y axis (see Table 5.2)
AWG	arbitrary waveform generator
a ($a^\dagger$)	annihilation (creation) operator of a harmonic oscillator. In case of two cavities, b ($b^\dagger$) are used for the second one.
α	anharmonicity of a transmon qubit ($\omega_{01} - \omega_{12}$)
C_i	ith Clifford gate, group indexed according to Table 5.3
CPW	coplanar waveguide
cQED	circuit quantum electrodynamics
$\mathcal{C}$	concurrence
Δ	denotes frequency differences, e.g. $\Delta = \omega_q - \omega_r$
$\mathcal{D}$	dissipation Lindblad operator
DRAG	derivative removal by adiabatic gate, single-qubit control pulses minimizing leakage aptly named in [76]
e	elementary charge
E_C	charging energy of a transmon qubit
E_J	Josephson energy of a transmon qubit
f	used for frequencies, e.g. f_{01} and f_{12} are the transition frequencies between $\|0\rangle$ and $\|1\rangle$ ($\|1\rangle$ and $\|2\rangle$)
f_{max}	maximum frequency of a transmon qubit
$\mathcal{F}_B$	maximum fidelity of a given state to a Bell state
F_C	Clifford fidelity from randomized benchmarking
$F_C^{T_1}$	T_1-limit on Clifford fidelity
Γ_m	measurement induced dephasing
g	qubit-resonator coupling
HF	hydrofluoric acid, used for oxide removal
I_c	critical current of a Josephson junction
J	qubit-qubit exchange interaction
κ	resonator linewidth

L_J	Josephson inductance
$\mathcal{L}$	Lindblad operators
$\hat{M}$	measurement operators in tomography
ME	master equation
NbTiN	niobium titanium nitride
ω	angular frequency as written in Hamiltonian terms. $\omega = 2\pi f$
P_i	population in state i
n_{crit}	critical resonator photon number of the dispersive regime.
$n_{\text{crit,Kerr}}$	critical resonator photon number where the intrinsic nonlinearity or non-linearity inherited from a qubit is no longer negligible.
Φ_0	superconducting flux quantum
PCB	printed circuit board
Q	resonator quality factor $Q = f_{res}/2\pi\kappa$
QST	quantum state tomography
RB	randomized benchmarking
ρ	density matrix
SME	stochastic master equation
SNR	signal-to-noise ratio
SPAM	state-preparation and measurement errors [230]
SQUID	superconducting quantum interference device, a loop with two Josephson junctions
σ_i	Pauli Matrices with index $i \in \{x, y, z\}$
σ_+, σ_-	qubit raising and lowering operators, $\sigma_+ = \|1\rangle\langle 0\|$ and $\sigma_- = \|1\rangle\langle 0\|$
T_1	qubit lifetime
T_2^*	qubit dephasing time as measured in a Ramsey experiment
$T_{2,\text{echo}}$	qubit dephasing time with a single symmetric Hahn-echo pulse
VSM	vector switch matrix
χ	dispersive shift in the dispersive Jaynes-Cummings Hamiltonian
X, Y, Z	qubit rotations around the respective axis with angles as prefactor, e.g. $X_{\pi/2}$

REFERENCES

[1] R. Landauer. *Information is physical*. Physics Today, **25**, 1991. (see page: 2)

[2] R. K. Bassett. *To the Digital Age: Research Labs, Start-up Companies, and the Rise of MOS Technology*. Johns Hopkins University Press, Baltimore, MD, USA, 2002. (see page: 2)

[3] G. E. Moore. *Cramming more components onto integrated circuits, reprinted from electronics, volume 38, number 8, april 19, 1965, pp.114 ff.* IEEE Solid-State Circuits Society Newsletter, **11** (3), 33–35, 2006. (see page: 2)

[4] R. P. Feynman. *Simulating physics with computers*. International Journal of Theoretical Physics, **21** (6-7), 467–488, 1982. (see page: 2)

[5] R. Landauer. *Is quantum mechanics useful?* Phil. Trans. R. Soc. Lond. A, **353** (1703), 367–376, 1995. (see page: 2)

[6] R. Landauer. *Advanced technology and truth in advertising*. Physica A: Statistical Mechanics and its Applications, **168** (1), 75–87, 1990. (see page: 3)

[7] H. Bernien, S. Schwartz, A. Keesling, H. Levine, A. Omran, H. Pichler, S. Choi, A. S. Zibrov, M. Endres, M. Greiner, *et al*. *Probing many-body dynamics on a 51-atom quantum simulator*. Nature, **551** (7682), 579, 2017. (see page: 4)

[8] J. Zhang, G. Pagano, P. W. Hess, A. Kyprianidis, P. Becker, H. Kaplan, A. V. Gorshkov, Z.-X. Gong, and C. Monroe. *Observation of a many-body dynamical phase transition with a 53-qubit quantum simulator*. Nature, **551** (7682), 601, 2017. (see page: 4)

[9] J. Preskill. *Quantum Computing in the NISQ era and beyond*. Quantum, **2**, 79, 2018. (see page: 4)

[10] P. W. Shor. *Scheme for reducing decoherence in quantum computer memory*. Phys. Rev. A, **52**, R2493–R2496, 1995. (see page: 5)

[11] M. Born. *Quantenmechanik der stoßvorg□nge*. Zeitschrift für Physik, **38** (11-12), 803–827, 1926. (see page: 5)

[12] D. Gottesman. *Class of quantum error-correcting codes saturating the quantum hamming bound*. Phys. Rev. A, **54**, 1862–1868, 1996. (see pages: 5, 6)

[13] D. P. DiVincenzo. *The physical implementation of quantum computation*. Fortschritte der Physik, **48**, 771, 2000. (see page: 5)

[14] R. Laflamme, C. Miquel, J. P. Paz, and W. H. Zurek. *Perfect quantum error correcting code*. Phys. Rev. Lett., **77**, 198, 1996. (see page: 5)

[15] C. H. Bennett, D. P. DiVincenzo, J. A. Smolin, and W. K. Wootters. *Mixed-state entanglement and quantum error correction*. Phys. Rev. A, **54**, 3824, 1996. (see page: 5)

[16] A. M. Steane. Error correcting codes in quantum theory. Phys. Rev. Lett., **77**, 793, 1996. (see page: 5)

[17] D. Aharonov and M. Ben-Or. *Fault-tolerant quantum computation with constant error*. In *Proceedings of the twenty-ninth annual ACM symposium on Theory of computing*, pages 176–188. ACM, 1997. (see page: 6)

[18] S. B. Bravyi and A. Y. Kitaev. *Quantum codes on a lattice with boundary*. arXiv:quant-ph/9811052, 1998. (see pages: 6, 59, and 88)

[19] A. G. Fowler, M. Mariantoni, J. M. Martinis, and A. N. Cleland. *Surface codes: Towards practical large-scale quantum computation*. Phys. Rev. A, **86**, 032 324, 2012. (see pages: 6, 59, and 88)

[20] P. W. Shor. *Polynomial-time algorithms for prime factorization and discrete logarithms on a quantum computer*. SIAM Journal on Computing, **26**, 1484, 1997. (see page: 6)

[21] I. L. Chuang, L. M. K. Vandersypen, X. Zhou, D. W. Leung, and S. Lloyd. *Experimental realization of a quantum algorithm*. Nature, **393**, 143–146, 1998. (see page: 7)

[22] L. M. K. Vandersypen, M. Steffen, G. Breyta, C. S. Yannoni, M. H. Sherwood, and I. L. Chuang. *Experimental realization of Shor's quantum factoring algorithm*. Nature, **414**, 883–887, 2001. (see page: 7)

[23] S. Guide, M. Riebe, G. P. T. Lancaster, C. Becher, J. Eschner, H. Häffner, F. Schmidt-Kaler, I. L. Chuang, and R. Blatt. *Implementation of the Deutsch-Jozsa algorithm on an ion-trap quantum computer*. Nature, **421**, 48–50, 2003. (see page: 7)

[24] P. G. Kwiat, J. R. Mitchell, P. D. D. Schwindt, and A. G. White. *Grover's search algorithm: an optical approach*. J. Mod. Opt., **47**, 257–266, 2000. (see page: 7)

[25] L. DiCarlo, J. M. Chow, J. M. Gambetta, L. S. Bishop, B. R. Johnson, D. I. Schuster, J. Majer, A. Blais, L. Frunzio, S. M. Girvin, and R. J. Schoelkopf. *Demonstration of two-qubit algorithms with a superconducting quantum processor*. Nature, **460**, 240, 2009. (see pages: 7, 26, 28, 31, 42, 59, and 116)

[26] T. Watson, S. Philips, E. Kawakami, D. Ward, P. Scarlino, M. Veldhorst, D. Savage, M. Lagally, M. Friesen, S. Coppersmith, *et al.* *A programmable two-qubit quantum processor in silicon*. Nature, 2018. (see page: 7)

[27] J. Cramer, N. Kalb, M. A. Rol, B. Hensen, M. Markham, D. J. Twitchen, R. Hanson, and T. H. Taminiau. *Repeated quantum error correction on a continuously encoded qubit by real-time feedback*. Nat. Commun., **5**, 11 526, 2016. (see page: 7)

[28] S. Debnath, N. M. Linke, C. Figgatt, K. A. Landsman, K. Wright, and C. Monroe. *Demonstration of a small programmable quantum computer with atomic qubits*. Nature, **536**, 63, 2016. (see pages: 7, 55)

[29] IBM Quantum Experience. (see pages: 7, 55)

[30] M. Mohseni, P. Read, H. Neven, S. Boixo, V. Denchev, R. Babbush, A. Fowler, V. Smelyanskiy, and J. Martinis. *Commercialize quantum technologies in five years*. Nature News, **543** (7644), 171, 2017. (see page: 7)

[31] J. Preskill. *Quantum computing and the entanglement frontier*. arXiv:1203.5813, 2012. (see page: 7)

[32] T. Häner and D. S. Steiger. *0.5 petabyte simulation of a 45-qubit quantum circuit*. In *Proceedings of the International Conference for High Performance Computing, Networking, Storage and Analysis*, page 33. ACM, 2017. (see page: 7)

[33] E. Pednault, J. A. Gunnels, G. Nannicini, L. Horesh, T. Magerlein, E. Solomonik, and R. Wisnieff. *Breaking the 49-qubit barrier in the simulation of quantum circuits*. arXiv:1710.05867, 2017. (see page: 7)

[34] T. O'brien, B. Tarasinski, and L. DiCarlo. *Density-matrix simulation of small surface codes under current and projected experimental noise*. npj Quantum Information, **3** (1), 39, 2017. (see page: 8)

[35] R. Versluis, S. Poletto, N. Khammassi, B. Tarasinski, N. Haider, D. J. Michalak, A. Bruno, K. Bertels, and L. DiCarlo. *Scalable quantum circuit and control for a superconducting surface code*. Phys. Rev. Appl., **8**, 034021, 2017. (see pages: 8, 38, 42, 88, 126, and 135)

[36] B. D. Josephson. *Possible new effects in superconductive tunnelling*. Phys. Lett., **1** (7), 251–253, 1962. (see page: 13)

[37] J. M. Martinis, M. H. Devoret, and J. Clarke. *Energy-level quantization in the zero-voltage state of a current-biased josephson junction*. Phys. Rev. Lett., **55**, 1543–1546, 1985. (see page: 14)

[38] B. Yurke and J. S. Denker. *Quantum network theory*. Phys. Rev. A, **29**, 1419–1437, 1984. (see page: 14)

[39] G. Burkard, R. H. Koch, and D. P. DiVincenzo. *Multilevel quantum description of decoherence in superconducting qubits*. Phys. Rev. B, **69**, 064503, 2004. (see page: 14)

[40] U. Vool and M. Devoret. *Introduction to quantum electromagnetic circuits*. International Journal of Circuit Theory and Applications, **45** (7), 897–934, 2017. (see page: 14)

[41] D. Ristè, C. C. Bultink, M. J. Tiggelman, R. N. Schouten, K. W. Lehnert, and L. DiCarlo. *Millisecond charge-parity fluctuations and induced decoherence in a superconducting transmon qubit*. Nat. Commun., **4**, 1913, 2013. (see pages: 15, 31)

[42] C. Wang, Y. Y. Gao, I. M. Pop, U. Vool, C. Axline, T. Brecht, R. W. Heeres, L. Frunzio, M. H. Devoret, G. Catelani, L. I. Glazman, and R. J. Schoelkopf. *Measurement and control of quasiparticle dynamics in a superconducting qubit*. Nat. Commun., **5**, 5836, 2014.

[43] K. Serniak, M. Hays, G. de Lange, S. Diamond, S. Shankar, L. Burkhart, L. Frunzio, M. Houzet, and M. Devoret. *Hot non-equilibrium quasiparticles in transmon qubits*. arXiv:1803.00476, 2018. (see pages: 15, 23)

[44] Y. Nakamura, Y. Pashkin, and J. Tsai. *Coherent control of macroscopic quantum states in a single-Cooper-pair box*. Nature, **398**, 786, 1999. (see page: 15)

[45] J. Koch, T. M. Yu, J. Gambetta, A. A. Houck, D. I. Schuster, J. Majer, A. Blais, M. H. Devoret, S. M. Girvin, and R. J. Schoelkopf. *Charge-insensitive qubit design derived from the Cooper pair box*. Phys. Rev. A, **76**, 042319, 2007. (see pages: 15, 16, 19, 59, and 90)

[46] R. C. Jaklevic, J. Lambe, A. H. Silver, and J. E. Mercereau. *Quantum interference effects in josephson tunneling*. Phys. Rev. Lett., **12**, 159–160, 1964. (see page: 16)

[47] J. E. Zimmerman and A. H. Silver. *Macroscopic quantum interference effects through superconducting point contacts*. Phys. Rev., **141**, 367–375, 1966. (see page: 16)

[48] M. Hutchings, J. B. Hertzberg, Y. Liu, N. T. Bronn, G. A. Keefe, M. Brink, J. M. Chow, and B. Plourde. *Tunable superconducting qubits with flux-independent coherence*. Phys. Rev. Appl., **8** (4), 044003, 2017. (see pages: 17, 41)

[49] N. K. Langford, R. Sagastizabal, M. Kounalakis, C. Dickel, A. Bruno, F. Luthi, D. Thoen, A. Endo, and L. DiCarlo. *Experimentally simulating the dynamics of quantum light and matter at deep-strong coupling*. Nature Communications, **8**, 1715, 2017. (see pages: 17, 31, 39, 105, and 131)

[50] C. Dickel, J. J. Wesdorp, N. K. Langford, S. Peiter, R. Sagastizabal, A. Bruno, B. Criger, F. Motzoi, and L. DiCarlo. *Chip-to-chip entanglement of transmon qubits using engineered measurement fields*. Phys. Rev. B, **97**, 064508, 2018. (see pages: 50, 128)

[51] M. Kounalakis, C. Dickel, A. Bruno, N. K. Langford, and G. A. Steele. *Tuneable hopping and nonlinear cross-kerr interactions in a high-coherence superconducting circuit*. npj Quantum Information, **4** (1), 2018. (see pages: 17, 28, and 135)

[52] A. Wallraff, D. I. Schuster, A. Blais, L. Frunzio, R.-S. Huang, J. Majer, S. Kumar, S. M. Girvin, and R. J. Schoelkopf. *Strong coupling of a single photon to a superconducting qubit using circuit quantum electrodynamics*. Nature, **431**, 162–167, 2004. (see page: 17)

[53] X. Mi, J. Cady, D. Zajac, P. Deelman, and J. Petta. *Strong coupling of a single electron in silicon to a microwave photon*. Science, page aal2469, 2016.

[54] N. Samkharadze, G. Zheng, N. Kalhor, D. Brousse, A. Sammak, U. Mendes, A. Blais, G. Scappucci, and L. Vandersypen. *Strong spin-photon coupling in silicon*. Science, **359** (6380), 1123–1127, 2018. (see page: 17)

[55] E. T. Jaynes and F. W. Cummings. *Comparison of quantum and semiclassical radiation theories with application to the beam maser*. Proceedings of the IEEE, **51** (1), 89–109, 1963. (see page: 17)

[56] P. A. M. Dirac. *A new notation for quantum mechanics*. Mathematical Proceedings of the Cambridge Philosophical Society, **35** (3), 416–418, 1939. (see page: 18)

[57] F. Yan, S. Gustavsson, A. Kamal, J. Birenbaum, A. P. Sears, D. Hover, T. J. Gudmundsen, D. Rosenberg, G. Samach, S. Weber, *et al*. *The flux qubit revisited to enhance coherence and reproducibility*. Nature communications, **7**, 12964, 2016. (see pages: 19, 27)

[58] H. T. Friis. *Noise figures of radio receivers*. Proceedings of the IRE, **32** (7), 419–422, 1944. (see page: 21)

[59] M. A. Castellanos-Beltran, K. D. Irwin, G. C. Hilton, L. R. Vale, and K. W. Lehnert. *Amplification and squeezing of quantum noise with a tunable Josephson metamaterial*. Nat. Phys., **4** (12), 929, 2008. (see pages: 21, 91)

[60] S. Boutin, D. M. Toyli, A. V. Venkatramani, A. W. Eddins, I. Siddiqi, and A. Blais. *Effect of higher-order nonlinearities on amplification and squeezing in josephson parametric amplifiers*. Phys. Rev. Applied, **8**, 054030, 2017. (see page: 21)

[61] C. Macklin, K. O'Brien, D. Hover, M. E. Schwartz, V. Bolkhovsky, X. Zhang, W. D. Oliver, and I. Siddiqi. *A near–quantum-limited josephson traveling-wave parametric amplifier*. Science, **350** (6258), 307–310, 2015. (see pages: 21, 107)

[62] A. Eddins, J. Kreikebaum, D. Toyli, E. Levenson-Falk, A. Dove, W. Livingston, B. Levitan, L. Govia, A. Clerk, and I. Siddiqi. *High-efficiency measurement of an artificial atom embedded in a parametric amplifier*. arXiv:1806.05276, 2018. (see page: 21)

[63] J. Gambetta, A. Blais, M. Boissonneault, A. A. Houck, D. I. Schuster, and S. M. Girvin. *Quantum trajectory approach to circuit QED: Quantum jumps and the Zeno effect*. Phys. Rev. A, **77** (1), 012112, 2008. (see pages: 21, 22, and 91)

[64] A. Frisk Kockum, L. Tornberg, and G. Johansson. *Undoing measurement-induced dephasing in circuit QED*. Phys. Rev. A, **85**, 052318, 2012. (see page: 21)

[65] T. Walter, P. Kurpiers, S. Gasparinetti, P. Magnard, A. PotoČnik, Y. Salathé, M. Pechal, M. Mondal, M. Oppliger, C. Eichler, and A. Wallraff. *Rapid High-Fidelity Single-Shot Dispersive Readout of Superconducting Qubits*. Phys. Rev. Appl., **7** (5), 054020, 2017. (see page: 22)

[66] E. Jeffrey, D. Sank, J. Y. Mutus, T. C. White, J. Kelly, R. Barends, Y. Chen, Z. Chen, B. Chiaro, A. Dunsworth, A. Megrant, P. J. J. O'Malley, C. Neill, *et al*. *Fast accurate state measurement with superconducting qubits*. Phys. Rev. Lett., **112**, 190504, 2014. (see page: 22)

[67] M. D. Reed, B. R. Johnson, A. A. Houck, L. DiCarlo, J. M. Chow, D. I. Schuster, L. Frunzio, and R. J. Schoelkopf. *Fast reset and suppressing spontaneous emission of a superconducting qubit*. Appl. Phys. Lett., **96** (20), 203 110, 2010. (see page: 22)

[68] D. T. McClure, H. Paik, L. S. Bishop, M. Steffen, J. M. Chow, and J. M. Gambetta. *Rapid driven reset of a qubit readout resonator*. Phys. Rev. Appl., **5**, 011 001, 2016. (see pages: 22, 110)

[69] C. C. Bultink, M. A. Rol, T. E. O'Brien, X. Fu, B. C. S. Dikken, C. Dickel, R. F. L. Vermeulen, J. C. de Sterke, A. Bruno, R. N. Schouten, and L. DiCarlo. *Active resonator reset in the nonlinear dispersive regime of circuit qed*. Phys. Rev. Appl., **6**, 034 008, 2016. (see pages: 22, 38, 50, and 110)

[70] C. A. Ryan, B. R. Johnson, J. M. Gambetta, J. M. Chow, M. P. da Silva, O. E. Dial, and T. A. Ohki. *Tomography via correlation of noisy measurement records*. Phys. Rev. A, **91**, 022 118, 2015. (see pages: 22, 97)

[71] C. C. Bultink, B. Tarasinski, N. Haandbæk, S. Poletto, N. Haider, D. J. Michalak, A. Bruno, and L. DiCarlo. *General method for extracting the quantum efficiency of dispersive qubit readout in circuit qed*. Applied Physics Letters, **112** (9), 092 601, 2018. (see pages: 23, 91, and 131)

[72] D. Ristè, J. G. van Leeuwen, H.-S. Ku, K. W. Lehnert, and L. DiCarlo. *Initialization by measurement of a superconducting quantum bit circuit*. Phys. Rev. Lett., **109**, 050 507, 2012. (see pages: 23, 100, and 127)

[73] J. Raftery, A. Vrajitoarea, G. Zhang, Z. Leng, S. Srinivasan, and A. Houck. *Direct digital synthesis of microwave waveforms for quantum computing*. arXiv:1703.00942, 2017. (see page: 24)

[74] J. Kelly, R. Barends, B. Campbell, Y. Chen, Z. Chen, B. Chiaro, A. Dunsworth, A. G. Fowler, I.-C. Hoi, E. Jeffrey, A. Megrant, J. Mutus, C. Neill, *et al.* *Optimal quantum control using randomized benchmarking*. Phys. Rev. Lett., **112**, 240 504, 2014. (see page: 25)

[75] M. A. Rol, C. C. Bultink, T. E. O'Brien, S. R. de Jong, L. S. Theis, X. Fu, F. Luthi, R. F. L. Vermeulen, J. C. de Sterke, A. Bruno, D. Deurloo, R. N. Schouten, F. K. Wilhelm, *et al.* *Restless tuneup of high-fidelity qubit gates*. Phys. Rev. Applied, **7**, 041 001, 2017. (see pages: 25, 27, and 50)

[76] F. Motzoi, J. M. Gambetta, P. Rebentrost, and F. K. Wilhelm. *Simple pulses for elimination of leakage in weakly nonlinear qubits*. Phys. Rev. Lett., **103**, 110 501, 2009. (see pages: 25, 59, 75, 106, and 149)

[77] J. M. Chow, L. DiCarlo, J. M. Gambetta, F. Motzoi, L. Frunzio, S. M. Girvin, and R. J. Schoelkopf. *Optimized driving of superconducting artificial atoms for improved single-qubit gates*. Phys. Rev. A, **82**, 040 305, 2010. (see pages: 25, 59, 75, and 106)

[78] Z. Chen, J. Kelly, C. Quintana, R. Barends, B. Campbell, Y. Chen, B. Chiaro, A. Dunsworth, A. G. Fowler, E. Lucero, E. Jeffrey, A. Megrant, J. Mutus, *et al.* *Measuring and suppressing quantum state leakage in a superconducting qubit*. Phys. Rev. Lett., **116**, 020 501, 2016. (see pages: 26, 77)

[79] E. L. Hahn. *Spin echoes*. Phys. Rev., **80**, 580–594, 1950. (see page: 26)

[80] L. Viola and S. Lloyd. *Dynamical suppression of decoherence in two-state quantum systems*. Phys. Rev. A, **58**, 2733–2744, 1998. (see page: 26)

[81] R. M. Lutchyn, L. I. Glazman, and A. I. Larkin. *Kinetics of the superconducting charge qubit in the presence of a quasiparticle*. Phys. Rev. B, **74**, 064 515, 2006. (see page: 26)

[82] E. Knill, D. Leibfried, R. Reichle, J. Britton, R. B. Blakestad, J. D. Jost, C. Langer, R. Ozeri, S. Seidelin, and D. J. Wineland. *Randomized benchmarking of quantum gates*. Phys. Rev. A, **77**, 012 307, 2008. (see pages: 26, 62, and 63)

[83] R. Barends, J. Kelly, A. Veitia, A. Megrant, A. G. Fowler, B. Campbell, Y. Chen, Z. Chen, B. Chiaro, A. Dunsworth, I.-C. Hoi, E. Jeffrey, C. Neill, *et al*. *Rolling quantum dice with a superconducting qubit*. Phys. Rev. A, **90**, 030 303, 2014. (see page: 26)

[84] R. Blume-Kohout, J. K. Gamble, E. Nielsen, K. Rudinger, J. Mizrahi, K. Fortier, and P. Maunz. *Demonstration of qubit operations below a rigorous fault tolerance threshold with gate set tomography*. Nat. Commun., **8**, 14 485, 2017. (see page: 27)

[85] G. Feng, J. J. Wallman, B. Buonacorsi, F. H. Cho, D. K. Park, T. Xin, D. Lu, J. Baugh, and R. Laflamme. *Estimating the coherence of noise in quantum control of a solid-state qubit*. Phys. Rev. Lett., **117**, 260 501, 2016. (see page: 27)

[86] M. A. Nielsen and I. L. Chuang. *Quantum computation and quantum information*. 2000. (see page: 27)

[87] J. Clarke and F. K. Wilhelm. *Superconducting quantum bits*. Nature, **453** (7198), 1031, 2008. (see page: 27)

[88] J. E. Mooij, T. P. Orlando, L. Levitov, L. Tian, C. H. van der Wal, and S. Lloyd. *Josephson persistent-current qubit*. Science, **285** (5430), 1036–1039, 1999. . (see page: 27)

[89] T. P. Orlando, J. E. Mooij, L. Tian, C. H. van der Wal, L. S. Levitov, S. Lloyd, and J. J. Mazo. *Superconducting persistent-current qubit*. Phys. Rev. B, **60**, 15 398–15 413, 1999. (see page: 27)

[90] V. S. Denchev, S. Boixo, S. V. Isakov, N. Ding, R. Babbush, V. Smelyanskiy, J. Martinis, and H. Neven. *What is the computational value of finite-range tunneling?* Phys. Rev. X, **6**, 031 015, 2016. (see page: 27)

[91] R. Harris, Y. Sato, A. J. Berkley, M. Reis, F. Altomare, M. H. Amin, K. Boothby, P. Bunyk, C. Deng, C. Enderud, S. Huang, E. Hoskinson, M. W. Johnson, *et al*. *Phase transitions in a programmable quantum spin glass simulator*. Science, **361** (6398), 162–165, 2018. . (see page: 27)

[92] J. Q. You, X. Hu, S. Ashhab, and F. Nori. *Low-decoherence flux qubit*. Phys. Rev. B, **75**, 140 515, 2007. (see page: 27)

[93] M. Steffen, S. Kumar, D. P. DiVincenzo, J. R. Rozen, G. A. Keefe, M. B. Rothwell, and M. B. Ketchen. *High-coherence hybrid superconducting qubit*. Phys. Rev. Lett., **105**, 100 502, 2010. (see page: 27)

[94] V. E. Manucharyan, J. Koch, L. I. Glazman, and M. H. Devoret. *Fluxonium: Single cooper-pair circuit free of charge offsets*. Science, **326** (5949), 113–116, 2009. . (see page: 27)

[95] I. M. Pop, K. Geerlings, G. Catelani, R. J. Schoelkopf, L. I. Glazman, and M. H. Devoret. *Coherent suppression of electromagnetic dissipation due to superconducting quasiparticles*. Nature, **508** (7496), 369–72, 2014. (see page: 27)

[96] Y.-H. Lin, L. B. Nguyen, N. Grabon, J. San Miguel, N. Pankratova, and V. E. Manucharyan. *Demonstration of protection of a superconducting qubit from energy decay*. Phys. Rev. Lett., **120**, 150 503, 2018. (see page: 27)

[97] P. Brooks, A. Kitaev, and J. Preskill. *Protected gates for superconducting qubits*. Phys. Rev. A, **87**, 052 306, 2013. (see page: 27)

[98] P. Groszkowski, A. Di Paolo, A. Grimsmo, A. Blais, D. Schuster, A. Houck, and J. Koch. *Coherence properties of the 0-π qubit*. New Journal of Physics, **20** (4), 043 053, 2018. (see page: 27)

[99] N. Didier, J. Bourassa, and A. Blais. *Fast quantum nondemolition readout by parametric modulation of longitudinal qubit-oscillator interaction*. Phys. Rev. Lett., **115**, 203 601, 2015. (see page: 28)

[100] S. Richer, N. Maleeva, S. T. Skacel, I. M. Pop, and D. DiVincenzo. *Inductively shunted transmon qubit with tunable transverse and longitudinal coupling*. Phys. Rev. B, **96**, 174 520, 2017. (see page: 28)

[101] J. Majer, J. M. Chow, J. M. Gambetta, B. R. Johnson, J. A. Schreier, L. Frunzio, D. I. Schuster, A. A. Houck, A. Wallraff, A. Blais, M. H. Devoret, S. M. Girvin, and R. J. Schoelkopf. *Coupling superconducting qubits via a cavity bus*. Nature, **449**, 443, 2007. (see page: 28)

[102] M. Steffen, M. Ansmann, R. C. Bialczak, N. Katz, E. Lucero, R. McDermott, M. Neeley, E. M. Weig, A. N. Cleland, and J. M. Martinis. *Measurement of the entanglement of two superconducting qubits via state tomography*. Science, **313**, 1423, 2006. (see page: 28)

[103] R. Barends, J. Kelly, A. Megrant, A. Veitia, D. Sank, E. Jeffrey, T. C. White, J. Mutus, A. G. Fowler, B. Campbell, Y. Chen, Z. Chen, B. Chiaro, *et al*. *Superconducting quantum circuits at the surface code threshold for fault tolerance*. Nature, **508** (7497), 500, 2014. (see pages: 28, 88, and 108)

[104] Y. Chen, C. Neill, P. Roushan, N. Leung, M. Fang, R. Barends, J. Kelly, B. Campbell, Z. Chen, B. Chiaro, A. Dunsworth, E. Jeffrey, A. Megrant, *et al*. *Qubit architecture with high coherence and fast tunable coupling*. Phys. Rev. Lett., **113**, 220 502, 2014. (see pages: 28, 135)

[105] D. C. McKay, S. Filipp, A. Mezzacapo, E. Magesan, J. M. Chow, and J. M. Gambetta. *Universal gate for fixed-frequency qubits via a tunable bus*. Phys. Rev. Applied, **6**, 064 007, 2016. (see page: 28)

[106] P.-M. Billangeon, J. S. Tsai, and Y. Nakamura. *Circuit-qed-based scalable architectures for quantum information processing with superconducting qubits*. Phys. Rev. B, **91**, 094 517, 2015. (see page: 28)

[107] S. Richer and D. DiVincenzo. *Circuit design implementing longitudinal coupling: A scalable scheme for superconducting qubits*. Phys. Rev. B, **93**, 134 501, 2016. (see page: 28)

[108] J. M. Chow, A. D. Córcoles, J. M. Gambetta, C. Rigetti, B. R. Johnson, J. A. Smolin, J. R. Rozen, G. A. Keefe, M. B. Rothwell, M. B. Ketchen, and M. Steffen. *Simple all-microwave entangling gate for fixed-frequency superconducting qubits*. Phys. Rev. Lett., **107**, 080 502, 2011. (see pages: 28, 126)

[109] P. Bertet, C. J. P. M. Harmans, and J. E. Mooij. *Parametric coupling for superconducting qubits*. Phys. Rev. B, **73**, 064 512, 2006. (see page: 28)

[110] P. Roushan, C. Neill, A. Megrant, Y. Chen, R. Babbush, R. Barends, B. Campbell, Z. Chen, B. Chiaro, A. Dunsworth, *et al*. *Chiral ground-state currents of interacting photons in a synthetic magnetic field*. Nature Physics, **13** (2), 146, 2017. (see page: 28)

[111] S. Caldwell, N. Didier, C. Ryan, E. Sete, A. Hudson, P. Karalekas, R. Manenti, M. Reagor, M. da Silva, R. Sinclair, *et al*. *Parametrically-activated entangling gates using transmon qubits*. arXiv:1706.06562, 2017. (see page: 28)

[112] R. Naik, N. Leung, S. Chakram, P. Groszkowski, Y. Lu, N. Earnest, D. McKay, J. Koch, and D. Schuster. *Random access quantum information processors using multimode circuit quantum electrodynamics*. Nature communications, **8** (1), 1904, 2017. (see page: 28)

[113] H. Paik, D. I. Schuster, L. S. Bishop, G. Kirchmair, G. Catelani, A. P. Sears, B. R. Johnson, M. J. Reagor, L. Frunzio, L. I. Glazman, S. M. Girvin, M. H. Devoret, and R. J. Schoelkopf. *Observation of high coherence in Josephson junction qubits measured in a three-dimensional circuit QED architecture*. Phys. Rev. Lett., **107**, 240501, 2011. (see page: 30)

[114] C. Rigetti, J. M. Gambetta, S. Poletto, B. L. T. Plourde, J. M. Chow, A. D. Córcoles, J. A. Smolin, S. T. Merkel, J. R. Rozen, G. A. Keefe, M. B. Rothwell, M. B. Ketchen, and M. Steffen. *Superconducting qubit in a waveguide cavity with a coherence time approaching 0.1 ms*. Phys. Rev. B, **86**, 100506, 2012. (see page: 30)

[115] D. I. Schuster, A. A. Houck, J. A. Schreier, A. Wallraff, J. M. Gambetta, A. Blais, L. Frunzio, J. Majer, M. H. Devoret, S. M. Givin, and R. J. Schoelkopf. *Resolving photon number states in a superconducting circuit*. Nature, **445**, 515, 2007. (see page: 30)

[116] A. A. Houck, J. A. Schreier, B. R. Johnson, J. M. Chow, J. Koch, J. M. Gambetta, D. I. Schuster, L. Frunzio, M. H. Devoret, S. M. Girvin, and R. J. Schoelkopf. *Controlling the spontaneous emission of a superconducting transmon qubit*. Phys. Rev. Lett., **101**, 080502 (pages 4), 2008. (see page: 30)

[117] A. Bruno, G. de Lange, S. Asaad, K. L. van der Enden, N. K. Langford, and L. DiCarlo. *Reducing intrinsic loss in superconducting resonators by surface treatment and deep etching of silicon substrates*. Appl. Phys. Lett., **106**, 182601, 2015. (see pages: 31, 38, 70, and 71)

[118] R. W. Heeres, B. Vlastakis, E. Holland, S. Krastanov, V. V. Albert, L. Frunzio, L. Jiang, and R. J. Schoelkopf. *Cavity state manipulation using photon-number selective phase gates*. Phys. Rev. Lett., **115**, 137002, 2015. (see page: 31)

[119] D. Gottesman, A. Kitaev, and J. Preskill. *Encoding a qubit in an oscillator*. Phys. Rev. A, **64**, 012310, 2001. (see page: 31)

[120] N. Ofek, A. Petrenko, R. Heeres, P. Reinhold, Z. Leghtas, B. Vlastakis, Y. Liu, L. Frunzio, S. M. Girvin, L. Jiang, M. Mirrahimi, M. H. Devoret, and R. J. Schoelkopf. *Extending the lifetime of a quantum bit with error correction in superconducting circuits*. Nature, **536**, 441, 2016. (see page: 31)

[121] M. Göppl, A. Fragner, M. Baur, R. Bianchetti, S. Filipp, J. M. Fink, P. J. Leek, G. Puebla, L. Steffen, and A. Wallraff. *Coplanar waveguide resonators for circuit quantum electrodynamics*. Journal of Applied Physics, **104** (11), 113904, 2008. (see pages: 32, 33)

[122] J. P. Groen, D. Ristè, L. Tornberg, J. Cramer, P. C. de Groot, T. Picot, G. Johansson, and L. DiCarlo. *Partial-measurement backaction and nonclassical weak values in a superconducting circuit*. Phys. Rev. Lett., **111**, 090506, 2013. (see pages: 36, 59)

[123] O.-P. Saira, J. P. Groen, J. Cramer, M. Meretska, G. de Lange, and L. DiCarlo. *Entanglement genesis by ancilla-based parity measurement in 2D circuit QED*. Phys. Rev. Lett., **112**, 070502, 2014.

[124] V. Vesterinen, O.-P. Saira, A. Bruno, and L. DiCarlo. *Mitigating information leakage in a crowded spectrum of weakly anharmonic qubits*. arXiv:cond-mat/1405.0450, 2014. (see page: 58)

[125] D. Ristè, S. Poletto, M. Z. Huang, A. Bruno, V. Vesterinen, O. P. Saira, and L. DiCarlo. *Detecting bit-flip errors in a logical qubit using stabilizer measurements*. Nat. Commun., **6**, 6983, 2015. (see pages: 36, 42, 58, 70, and 88)

[126] D. Rosenberg, D. Kim, R. Das, D. Yost, S. Gustavsson, D. Hover, P. Krantz, A. Melville, L. Racz, G. Samach, *et al.* *3d integrated superconducting qubits*. npj Quantum Information, **3** (1), 42, 2017. (see page: 38)

[127] R. Barends, J. Kelly, A. Megrant, D. Sank, E. Jeffrey, Y. Chen, Y. Yin, B. Chiaro, J. Mutus, C. Neill, P. O'Malley, P. Roushan, J. Wenner, *et al.* *Coherent Josephson qubit suitable for scalable quantum integrated circuits*. Phys. Rev. Lett., **111**, 080502, 2013. (see pages: 38, 135)

[128] J. M. Gambetta, C. E. Murray, Y. K. K. Fung, D. T. McClure, O. Dial, W. Shanks, J. W. Sleight, and M. Steffen. *Investigating surface loss effects in superconducting transmon qubits*. IEEE Transactions on Applied Superconductivity, **27** (1), 1–5, 2017. (see page: 38)

[129] J. B. Chang, M. R. Vissers, A. D. Córcoles, M. Sandberg, J. Gao, D. W. Abraham, J. M. Chow, J. M. Gambetta, M. B. Rothwell, G. A. Keefe, M. Steffen, and D. P. Pappas. *Improved superconducting qubit coherence using titanium nitride*. Appl. Phys. Lett., **103**, 012602, 2013. (see page: 38)

[130] D. J. Thoen, B. G. C. Bos, E. Haalebos, T. Klapwijk, J. Baselmans, and A. Endo. *Superconducting nbtin thin films with highly uniform properties over a ∅ 100 mm wafer*. IEEE T. Appl. Supercon., **27** (4), 1–5, 2017. (see pages: 38, 121)

[131] G. J. Dolan. *Offset masks for lift-off photoprocessing*. Appl. Phys. Lett., **31**, 337, 1977. (see page: 39)

[132] V. Ambegaokar and A. Baratoff. *Tunneling between superconductors*. Phys. Rev. Lett., **10**, 486–489, 1963. (see pages: 40, 105)

[133] I. M. Pop, T. Fournier, T. Crozes, F. Lecocq, I. Matei, B. Pannetier, O. Buisson, and W. Guichard. *Fabrication of stable and reproducible submicron tunnel junctions*. J. Vac. Sci. Technol. B, **30**, 010607, 2012. (see pages: 41, 105)

[134] R. Barends, J. Wenner, M. Lenander, Y. Chen, R. C. Bialczak, J. Kelly, E. Lucero, P. O'Malley, M. Mariantoni, D. Sank, H. Wang, T. C. White, Y. Yin, *et al.* *Minimizing quasiparticle generation from stray infrared light in superconducting quantum circuits*. Appl. Phys. Lett., **99**, 113507, 2011. (see pages: 43, 71, and 103)

[135] S. Krinner, S. Storz, P. Kurpiers, P. Magnard, J. Heinsoo, R. Keller, J. Luetolf, C. Eichler, and A. Wallraff. *Engineering cryogenic setups for 100-qubit scale superconducting circuit systems*. arXiv:1806.07862, 2018. (see page: 43)

[136] D. F. Santavicca and D. E. Prober. *Impedance-matched low-pass stripline filters*. Meas. Sci. Technol., **19**, 087001, 2008. (see page: 44)

[137] D. H. Slichter, O. Naaman, and I. Siddiqi. *Millikelvin thermal and electrical performance of lossy transmission line filters*. Applied Physics Letters, **94** (19), 192508, 2009. . (see page: 44)

[138] F. Yan, D. Campbell, P. Krantz, M. Kjaergaard, D. Kim, J. L. Yoder, D. Hover, A. Sears, A. J. Kerman, T. P. Orlando, S. Gustavsson, and W. D. Oliver. *Distinguishing coherent and thermal photon noise in a circuit quantum electrodynamical system*. Phys. Rev. Lett., **120**, 260504, 2018. (see page: 44)

[139] Z. Wang, S. Shankar, Z. Minev, P. Campagne-Ibarcq, A. Narla, and M. Devoret. *Cavity attenuators for superconducting qubits*. arXiv:1807.04849, 2018. (see page: 44)

[140] E. Jones, T. Oliphant, P. Peterson, *et al.* *SciPy: Open source scientific tools for Python*, 2001. [Online; accessed 06.04.2018]. (see page: 48)

[141] J. D. Hunter. Matplotlib: A 2d graphics environment. Computing In Science & Engineering, **9** (3), 90–95, 2007. (see page: 48)

[142] M. Newville, T. Stensitzki, D. B. Allen, and A. Ingargiola. *LMFIT: Non-Linear Least-Square Minimization and Curve-Fitting for Python¶*, 2014. (see page: 48)

[143] J. Johansson, P. Nation, and F. Nori. *Qutip: An open-source python framework for the dynamics of open quantum systems*. Computer Physics Communications, **183** (8), 1760–1772, 2012. (see pages: 48, 77)

[144] R. Heeres, P. de Groot, and M. Schaafsma. *Qtlab*. (see page: 50)

[145] A. Johnson, G. Ungaretti, *et al.* *QCoDeS*, 2016. (see page: 50)

[146] S. Asaad, C. Dickel, S. Poletto, A. Bruno, N. K. Langford, M. A. Rol, D. Deurloo, and L. DiCarlo. *Independent, extensible control of same-frequency superconducting qubits by selective broadcasting*. npj Quantum Inf., **2**, 16029, 2016. (see page: 50)

[147] M. Rol, C. Dickel, S.Asaad, N. Langford, C. Bultink, R. Sagastizabal, N. Langford, G. de Lange, X. Fu, S. de Jong, F. Luthi, and W. Vlothuizen. *Pycqed*, 2016. (see page: 51)

[148] X. Fu, M. A. Rol, C. C. Bultink, J. van Someren, N. Khammassi, I. Ashraf, R. F. L. Vermeulen, J. C. de Sterke, W. J. Vlothuizen, R. N. Schouten, C. G. Almudever, L. DiCarlo, and K. Bertels. *An experimental microarchitecture for a superconducting quantum processor*. In *Proceedings of the 50th Annual IEEE/ACM International Symposium on Microarchitecture*, pages 813–825. ACM, 2017. (see page: 55)

[149] X. Fu, L. Riesebos, M. Rol, J. van Straten, J. van Someren, N. Khammassi, I. Ashraf, R. Vermeulen, V. Newsum, K. Loh, *et al.* *eqasm: An executable quantum instruction set architecture*. arXiv:1808.02449, 2018. (see page: 55)

[150] C. Monroe and J. Kim. *Scaling the ion trap quantum processor*. Science, **339** (6124), 1164–1169, 2013. (see pages: 58, 88)

[151] D. D. Awschalom, L. C. Bassett, A. S. Dzurak, E. L. Hu, and J. R. Petta. *Quantum spintronics: Engineering and manipulating atom-like spins in semiconductors*. Science, **339** (6124), 1174–1179, 2013. (see page: 58)

[152] M. H. Devoret and R. J. Schoelkopf. *Superconducting circuits for quantum information: An outlook*. Science, **339** (6124), 1169–1174, 2013. (see page: 58)

[153] J. Kelly, R. Barends, A. Fowler, A. Megrant, E. Jeffrey, T. White, D. Sank, J. Mutus, B. Campbell, Y. Chen, *et al.* *State preservation by repetitive error detection in a superconducting quantum circuit*. Nature, **519** (7541), 66–69, 2015. (see pages: 58, 88)

[154] A. D. Córcoles, E. Magesan, S. J. Srinivasan, A. W. Cross, M. Steffen, J. M. Gambetta, and J. M. Chow. *Demonstration of a quantum error detection code using a square lattice of four superconducting qubits*. Nat. Commun., **6**, 6979, 2015. (see page: 58)

[155] J. M. Hornibrook, J. I. Colless, I. D. Conway Lamb, S. J. Pauka, H. Lu, A. C. Gossard, J. D. Watson, G. C. Gardner, S. Fallahi, M. J. Manfra, and D. J. Reilly. *Cryogenic control architecture for large-scale quantum computing*. Phys. Rev. Appl., **3**, 024010, 2015. (see page: 58)

[156] C. Knoernschild, X. L. Zhang, L. Isenhower, A. T. Gill, F. P. Lu, M. Saffman, and J. Kim. *Independent individual addressing of multiple neutral atom qubits with a micromirror-based beam steering system*. Applied Physics Letters, **97** (13), 134101, 2010. . (see page: 58)

[157] C. Weitenberg, M. Endres, J. F. Sherson, M. Cheneau, P. Schauss, T. Fukuhara, I. Bloch, and S. Kuhr. *Single-spin addressing in an atomic mott insulator*. Nature, **471** (7338), 319–324, 2011.

[158] S. Crain, E. Mount, S. Baek, and J. Kim. *Individual addressing of trapped 171yb+ ion qubits using a microelectromechanical systems-based beam steering system*. Appl. Phys. Lett., **105** (18), 181115, 2014.

[159] T. Xia, M. Lichtman, K. Maller, A. W. Carr, M. J. Piotrowicz, L. Isenhower, and M. Saffman. *Randomized benchmarking of single-qubit gates in a 2d array of neutral-atom qubits*. Phys. Rev. Lett., **114**, 100503, 2015. (see page: 58)

[160] A. Blais, R.-S. Huang, A. Wallraff, S. M. Girvin, and R. J. Schoelkopf. *Cavity quantum electrodynamics for superconducting electrical circuits: An architecture for quantum computation*. Phys. Rev. A, **69**, 062320, 2004. (see pages: 58, 61, and 88)

[161] D. P. DiVincenzo. *Fault-tolerant architectures for superconducting qubits*. Physica Scripta, (T137), 014020, 2009. (see pages: 58, 59, and 88)

[162] F. Helmer, M. Mariantoni, A. Fowler, J. Von Delft, E. Solano, and F. Marquardt. *Cavity grid for scalable quantum computation with superconducting circuits*. Europhys. Lett., **85** (5), 50007, 2009. (see page: 88)

[163] J. Ghosh, A. G. Fowler, and M. R. Geller. *Surface code with decoherence: An analysis of three superconducting architectures*. Phys. Rev. A, **86**, 062318, 2012. (see page: 58)

[164] J. Gambetta and J. Smolin. *Frequency arrangement for surface code on a superconducting lattice*, 2014. US Patent App. 13/827,326. (see page: 58)

[165] R. Schutjens, F. A. Dagga, D. J. Egger, and F. K. Wilhelm. *Single-qubit gates in frequency-crowded transmon systems*. Phys. Rev. A, **88**, 052330, 2013. (see page: 58)

[166] T. Chasseur and F. K. Wilhelm. *Complete randomized benchmarking protocol accounting for leakage errors*. Phys. Rev. A, **92**, 042333, 2015. (see page: 59)

[167] J. M. Epstein, A. W. Cross, E. Magesan, and J. M. Gambetta. *Investigating the limits of randomized benchmarking protocols*. Phys. Rev. A, **89**, 062321, 2014. (see pages: 59, 63, 66, 78, 80, and 82)

[168] A. Fragner, M. Göppl, J. M. Fink, M. Baur, R. Bianchetti, P. J. Leek, A. Blais, and A. Wallraff. *Resolving vacuum fluctuations in an electrical circuit by measuring the Lamb shift*. Science, **322**, 1357–1360, 2008. (see page: 59)

[169] M. Jerger, S. Poletto, P. Macha, U. Hübner, E. Il'ichev, and A. V. Ustinov. *Frequency division multiplexing readout and simultaneous manipulation of an array of flux qubits*. Appl. Phys. Lett., **101** (4), 042604, 2012. (see page: 59)

[170] E. Magesan, J. M. Gambetta, and J. Emerson. *Scalable and robust randomized benchmarking of quantum processes*. Phys. Rev. Lett., **106**, 180504, 2011. (see pages: 62, 63)

[171] E. Magesan, J. M. Gambetta, and J. Emerson. *Characterizing quantum gates via randomized benchmarking*. Phys. Rev. A, **85**, 042311, 2012. (see page: 62)

[172] B. R. Johnson, M. P. da Silva, C. A. Ryan, S. Kimmel, J. M. Chow, and T. A. Ohki. *Demonstration of robust quantum gate tomography via randomized benchmarking*. New Journal of Physics, **17** (11), 113019, 2015. (see page: 63)

[173] D. Ristè, C. C. Bultink, K. W. Lehnert, and L. DiCarlo. *Feedback control of a solid-state qubit using high-fidelity projective measurement*. Phys. Rev. Lett., **109**, 240502, 2012. (see page: 63)

[174] E. Magesan, private communication. (see page: 65)

[175] E. Magesan, J. M. Gambetta, B. R. Johnson, C. A. Ryan, J. M. Chow, S. T. Merkel, M. P. da Silva, G. A. Keefe, M. B. Rothwell, T. A. Ohki, M. B. Ketchen, and M. Steffen. *Efficient measurement of quantum gate error by interleaved randomized benchmarking*. Phys. Rev. Lett., **109**, 080505, 2012. (see pages: 65, 79)

[176] R. Raussendorf and J. Harrington. *Fault-tolerant quantum computation with high threshold in two dimensions*. Phys. Rev. Lett., **98**, 190504, 2007. (see page: 67)

[177] A. G. Fowler, A. M. Stephens, and P. Groszkowski. *High-threshold universal quantum computation on the surface code*. Phys. Rev. A, **80**, 052312, 2009.

[178] D. S. Wang, A. G. Fowler, and L. C. L. Hollenberg. *Surface code quantum computing with error rates over 1%*. Phys. Rev. A, **83**, 020302, 2011. (see page: 67)

[179] J. A. Schreier, A. A. Houck, J. Koch, D. I. Schuster, B. R. Johnson, J. M. Chow, J. M. Gambetta, J. Majer, L. Frunzio, M. H. Devoret, S. M. Girvin, and R. J. Schoelkopf. *Suppressing charge noise decoherence in superconducting charge qubits*. Phys. Rev. B, **77**, 180502, 2008. (see page: 70)

[180] M. Reed. *Entanglement and quantum error correction with superconducting qubits*. PhD Dissertation, Yale University, 2013. (see pages: 72, 74, 75, and 107)

[181] S. D. Barrett and P. Kok. *Efficient high-fidelity quantum computation using matter qubits and linear optics*. Phys. Rev. A, **71**, 060310, 2005. (see pages: 88, 89)

[182] A. Narla, S. Shankar, M. Hatridge, Z. Leghtas, K. M. Sliwa, E. Zalys-Geller, S. O. Mundhada, W. Pfaff, L. Frunzio, R. J. Schoelkopf, and M. H. Devoret. *Robust concurrent remote entanglement between two superconducting qubits*. Phys. Rev. X, **6**, 031036, 2016. (see pages: 88, 89, and 128)

[183] J. Kerckhoff, L. Bouten, A. Silberfarb, and H. Mabuchi. *Physical model of continuous two-qubit parity measurement in a cavity-QED network*. Phys. Rev. A, **79**, 024305, 2009. (see pages: 88, 89, 90, and 91)

[184] N. Roch, M. E. Schwartz, F. Motzoi, C. Macklin, R. Vijay, A. W. Eddins, A. N. Korotkov, K. B. Whaley, M. Sarovar, and I. Siddiqi. *Observation of measurement-induced entanglement and quantum trajectories of remote superconducting qubits*. Phys. Rev. Lett., **112**, 170501, 2014. (see pages: 88, 89, 92, 98, 107, 115, and 128)

[185] A. Chantasri, M. E. Kimchi-Schwartz, N. Roch, I. Siddiqi, and A. N. Jordan. *Quantum trajectories and their statistics for remotely entangled quantum bits*. Phys. Rev. X, **6**, 041052, 2016. (see pages: 88, 89, 90, 101, and 115)

[186] A. Reed, K. Mayer, J. Teufel, L. Burkhart, W. Pfaff, M. Reagor, L. Sletten, X. Ma, R. Schoelkopf, E. Knill, *et al.* *Faithful conversion of propagating quantum information to mechanical motion*. Nature Physics, **13** (12), 1163, 2017. (see page: 89)

[187] Y. Yin, Y. Chen, D. Sank, P. J. J. O'Malley, T. C. White, R. Barends, J. Kelly, E. Lucero, M. Mariantoni, A. Megrant, C. Neill, A. Vainsencher, J. Wenner, *et al.* *Catch and release of microwave photon states*. Phys. Rev. Lett., **110**, 107001, 2013. (see page: 89)

[188] J. Wenner, Y. Yin, Y. Chen, R. Barends, B. Chiaro, E. Jeffrey, J. Kelly, A. Megrant, J. Y. Mutus, C. Neill, P. J. J. O'Malley, P. Roushan, D. Sank, *et al.* *Catching time-reversed microwave coherent state photons with 99.4% absorption efficiency*. Phys. Rev. Lett., **112**, 210501, 2014. (see pages: 88, 89)

[189] P. Campagne-Ibarcq, E. Zalys-Geller, A. Narla, S. Shankar, P. Reinhold, L. Burkhart, C. Axline, W. Pfaff, L. Frunzio, R. J. Schoelkopf, and M. H. Devoret. *Deterministic remote entanglement of superconducting circuits through microwave two-photon transitions*. Phys. Rev. Lett., **120**, 200501, 2018. (see pages: 89, 127, and 128)

[190] P. Kurpiers, P. Magnard, T. Walter, B. Royer, M. Pechal, J. Heinsoo, Y. Salathé, A. Akin, S. Storz, J.-C. Besse, *et al.* *Deterministic quantum state transfer and remote entanglement using microwave photons*. Nature, **558** (7709), 264, 2018. (see pages: 89, 127, and 128)

[191] C. J. Axline, L. D. Burkhart, W. Pfaff, M. Zhang, K. Chou, P. Campagne-Ibarcq, P. Reinhold, L. Frunzio, S. Girvin, L. Jiang, *et al.* *On-demand quantum state transfer and entanglement between remote microwave cavity memories*. Nature Physics, **14**, 1, 2018. (see pages: 89, 127, and 128)

[192] C. D. Hill, E. Peretz, S. J. Hile, M. G. House, M. Fuechsle, S. Rogge, M. Y. Simmons, and L. C. L. Hollenberg. *A surface code quantum computer in silicon*. Science Advances, **1** (9), 2015. (see page: 88)

[193] R. Li, L. Petit, D. P. Franke, J. P. Dehollain, J. Helsen, M. Steudtner, N. K. Thomas, Z. R. Yoscovits, K. J. Singh, S. Wehner, L. M. K. Vandersypen, J. S. Clarke, and M. Veldhorst. *A crossbar network for silicon quantum dot qubits*. Science Advances, **4** (7), 2018. . (see page: 88)

[194] N. H. Nickerson, Y. Li, and S. C. Benjamin. *Topological quantum computing with a very noisy network and local error rates approaching one percent*. Nat. Commun., **4**, 1756, 2013. (see page: 88)

[195] K. Nemoto, M. Trupke, S. J. Devitt, A. M. Stephens, B. Scharfenberger, K. Buczak, T. Nöbauer, M. S. Everitt, J. Schmiedmayer, and W. J. Munro. *Photonic architecture for scalable quantum information processing in diamond*. Phys. Rev. X, **4**, 031 022, 2014.

[196] T. Brecht, W. Pfaff, C. Wang, Y. Chu, L. Frunzio, M. H. Devoret, and R. J. Schoelkopf. *Multilayer microwave integrated quantum circuits for scalable quantum computing*. npj Quantum Information, **2**, 16 002, 2016. (see page: 88)

[197] A. Roy, L. Jiang, A. D. Stone, and M. Devoret. *Remote entanglement by coherent multiplication of concurrent quantum signals*. Phys. Rev. Lett., **115**, 150 503, 2015. (see page: 88)

[198] C. Ohm and F. Hassler. *Measurement-induced entanglement of two transmon qubits by a single photon*. New Journal of Physics, **19** (5), 053 018, 2017. (see page: 88)

[199] W. Pfaff, C. J. Axline, L. D. Burkhart, U. Vool, P. Reinhold, L. Frunzio, L. Jiang, M. H. Devoret, and R. J. Schoelkopf. *Controlled release of multiphoton quantum states from a microwave cavity memory*. Nat. Phys., **13**, 882–887, 2017. (see page: 88)

[200] C. Song, K. Xu, W. Liu, C.-p. Yang, S.-B. Zheng, H. Deng, Q. Xie, K. Huang, Q. Guo, L. Zhang, P. Zhang, D. Xu, D. Zheng, *et al.* *10-qubit entanglement and parallel logic operations with a superconducting circuit*. Phys. Rev. Lett., **119**, 180 511, 2017. (see page: 88)

[201] M. Takita, A. W. Cross, A. D. Córcoles, J. M. Chow, and J. M. Gambetta. *Experimental demonstration of fault-tolerant state preparation with superconducting qubits*. Phys. Rev. Lett., **119**, 180 501, 2017. (see page: 88)

[202] L. Tornberg and G. Johansson. *High-fidelity feedback-assisted parity measurement in circuit QED*. Phys. Rev. A, **82** (1), 012 329, 2010. (see page: 91)

[203] F. Motzoi, K. B. Whaley, and M. Sarovar. *Continuous joint measurement and entanglement of qubits in remote cavities*. Phys. Rev. A, **92**, 032 308, 2015. (see pages: 91, 92, 98, 109, 110, 113, 114, and 115)

[204] J. M. Chow, L. DiCarlo, J. M. Gambetta, A. Nunnenkamp, L. S. Bishop, L. Frunzio, M. H. Devoret, S. M. Girvin, and R. J. Schoelkopf. *Detecting highly entangled states with a joint qubit readout*. Phys. Rev. A, **81**, 062 325, 2010. (see page: 92)

[205] S. Filipp, P. Maurer, P. J. Leek, M. Baur, R. Bianchetti, J. M. Fink, M. Göppl, L. Steffen, J. M. Gambetta, A. Blais, and A. Wallraff. *Two-qubit state tomography using a joint dispersive readout*. Phys. Rev. Lett., **102**, 200 402, 2009. (see page: 92)

[206] J. A. Nelder and R. Mead. *A simplex method for function minimization*. The Computer Journal, **7** (4), 308–313, 1965. (see page: 94)

[207] W. K. Wootters. *Entanglement of formation of an arbitrary state of two qubits*. Phys. Rev. Lett., **80**, 2245–2248, 1998. (see page: 96)

[208] F. Pedregosa, G. Varoquaux, A. Gramfort, V. Michel, B. Thirion, O. Grisel, M. Blondel, P. Prettenhofer, R. Weiss, V. Dubourg, J. Vanderplas, A. Passos, D. Cournapeau, *et al.* *Scikit-learn: Machine learning in Python*. Journal of Machine Learning Research, **12**, 2825–2830, 2011. (see pages: 97, 98)

[209] E. Magesan, J. M. Gambetta, A. D. Córcoles, and J. M. Chow. *Machine learning for discriminating quantum measurement trajectories and improving readout*. Phys. Rev. Lett., **114**, 200501, 2015. (see page: 97)

[210] R. Horodecki, P. Horodecki, M. Horodecki, and K. Horodecki. *Quantum entanglement*. Rev. Mod. Phys., **81**, 865, 2009. (see page: 100)

[211] G. Vidal and R. F. Werner. *Computable measure of entanglement*. Phys. Rev. A, **65**, 032314, 2002. (see page: 100)

[212] B. J. Chapman, E. I. Rosenthal, J. Kerckhoff, B. A. Moores, L. R. Vale, J. A. B. Mates, G. C. Hilton, K. Lalumière, A. Blais, and K. W. Lehnert. *Widely tunable on-chip microwave circulator for superconducting quantum circuits*. Phys. Rev. X, **7**, 041043, 2017. (see page: 101)

[213] A. Roy, A. D. Stone, and L. Jiang. *Concurrent remote entanglement with quantum error correction against photon losses*. Phys. Rev. A, **94**, 032333, 2016. (see page: 101)

[214] D. Deutsch, A. Ekert, R. Jozsa, C. Macchiavello, S. Popescu, and A. Sanpera. *Quantum privacy amplification and the security of quantum cryptography over noisy channels*. Phys. Rev. Lett., **77**, 2818–2821, 1996. (see page: 102)

[215] C. H. Bennett, G. Brassard, S. Popescu, B. Schumacher, J. A. Smolin, and W. K. Wootters. *Purification of noisy entanglement and faithful teleportation via noisy channels*. Phys. Rev. Lett., **76**, 722–725, 1996. (see page: 102)

[216] S. Shankar, M. Hatridge, Z. Leghtas, K. M. Sliwa, A. Narla, U. Vool, S. M. Girvin, L. Frunzio, M. Mirrahimi, and M. H. Devoret. *Autonomously stabilized entanglement between two superconducting quantum bits*. Nature, **504** (7480), 419–22, 2013. (see page: 102)

[217] F. Motzoi, E. Halperin, X. Wang, K. B. Whaley, and S. Schirmer. *Backaction-driven, robust, steady-state long-distance qubit entanglement over lossy channels*. Phys. Rev. A, **94**, 032313, 2016. (see page: 130)

[218] M. E. Kimchi-Schwartz, L. Martin, E. Flurin, C. Aron, M. Kulkarni, H. E. Tureci, and I. Siddiqi. *Stabilizing entanglement via symmetry-selective bath engineering in superconducting qubits*. Phys. Rev. Lett., **116**, 240503, 2016. (see page: 102)

[219] L. Martin, F. Motzoi, H. Li, M. Sarovar, and K. B. Whaley. *Deterministic generation of remote entanglement with active quantum feedback*. Phys. Rev. A, **92**, 062321, 2015. (see pages: 102, 130)

[220] M. D. Reed. *Entanglement and Quantum Error Correction with Superconducting Qubits*. PhD Dissertation, Yale University, 2013. (see page: 106)

[221] A. Bhattacharyya. *On a measure of divergence between two multinomial populations*. Sankhya: the indian journal of statistics, **7**, 401–406, 1946. (see page: 107)

[222] G. de Lange, D. Ristè, M. J. Tiggelman, C. Eichler, L. Tornberg, G. Johansson, A. Wallraff, R. N. Schouten, and L. DiCarlo. *Reversing quantum trajectories with analog feedback*. Phys. Rev. Lett., **112**, 080501, 2014. (see page: 107)

[223] D. F. Walls and G. J. Milburn. *Quantum optics*. Springer Science & Business Media, 2007. (see page: 109)

[224] D. Ristè, M. Dukalski, C. A. Watson, G. de Lange, M. J. Tiggelman, Y. M. Blanter, K. W. Lehnert, R. N. Schouten, and L. DiCarlo. *Deterministic entanglement of superconducting qubits by parity measurement and feedback*. Nature, **502** (7471), 350–354, 2013. (see page: 113)

[225] S. Barzanjeh, D. P. DiVincenzo, and B. M. Terhal. *Dispersive qubit measurement by interferometry with parametric amplifiers*. Phys. Rev. B, **90**, 134515, 2014. (see page: 113)

[226] C. Gardiner and P. Zoller. *Quantum Noise*. Springer, Berlin, Germany, 3rd edition, 2004. (see page: 115)

[227] D. F. V. James, P. G. Kwiat, W. J. Munro, and A. G. White. *Measurement of qubits*. Phys. Rev. A, **64**, 052312, 2001. (see page: 116)

[228] S. Boyd. *Convex Optimization*. Cambridge University Press, 1st edition, 2004.

[229] N. K. Langford. *Errors in quantum tomography: diagnosing systematic versus statistical errors*. New J. Phys., **15** (3), 035003, 2013. (see page: 116)

[230] T. Jones and M. Palin. Spam. Monty Python's Flying Circus, 1970. (see pages: 116, 150)

[231] M. R. Vissers, J. Gao, D. S. Wisbey, D. A. Hite, C. C. Tsuei, A. D. Corcoles, M. Steffen, and D. P. Pappas. *Low loss superconducting titanium nitride coplanar waveguide resonators*. Appl. Phys. Lett., **97** (23), 232509, 2010. (see page: 121)

[232] M. Sandberg, C. M. Wilson, F. Persson, T. Bauch, G. Johansson, V. Shumeiko, T. Duty, and P. Delsing. *Tuning the field in a microwave resonator faster than the photon lifetime*. Appl. Phys. Lett., **92** (20), 203501, 2008. (see page: 121)

[233] T. Yamamoto, K. Inomata, M. Watanabe, K. Matsuba, T. Miyazaki, W. D. Oliver, Y. Nakamura, and J. S. Tsai. *Flux-driven josephson parametric amplifier*. Appl. Phys. Lett., **93** (4), 042510, 2008. (see page: 121)

[234] M. Tavis and F. W. Cummings. *Exact solution for an n-molecule-radiation-field hamiltonian*. Phys. Rev., **170**, 379–384, 1968. (see page: 121)

[235] D. Brown. *Origin*. Transworld Publishers London, 2017. (see page: 124)

[236] A. Peruzzo, J. McClean, P. Shadbolt, M.-H. Yung, X.-Q. Zhou, P. J. Love, A. Aspuru-Guzik, and J. L. O'brien. *A variational eigenvalue solver on a photonic quantum processor*. Nature communications, **5**, 4213, 2014. (see page: 124)

[237] D. Ristè, M. P. Da Silva, C. A. Ryan, A. W. Cross, A. D. Córcoles, J. A. Smolin, J. M. Gambetta, J. M. Chow, and B. R. Johnson. *Demonstration of quantum advantage in machine learning*. npj Quantum Information, **3** (1), 16, 2017. (see page: 124)

[238] J. Otterbach, R. Manenti, N. Alidoust, A. Bestwick, M. Block, B. Bloom, S. Caldwell, N. Didier, E. S. Fried, S. Hong, *et al.* *Unsupervised machine learning on a hybrid quantum computer*. arXiv:1712.05771, 2017. (see page: 124)

[239] P. J. J. O'Malley, R. Babbush, I. D. Kivlichan, J. Romero, J. R. McClean, R. Barends, J. Kelly, P. Roushan, A. Tranter, N. Ding, B. Campbell, Y. Chen, Z. Chen, *et al.* *Scalable quantum simulation of molecular energies*. Phys. Rev. X, **6**, 031007, 2016. (see page: 125)

[240] A. Kandala, A. Mezzacapo, K. Temme, M. Takita, M. Brink, J. M. Chow, and J. M. Gambetta. *Hardware-efficient variational quantum eigensolver for small molecules and quantum magnets*. Nature, **549** (7671), 242, 2017. (see page: 125)

[241] B. Bauer, D. Wecker, A. J. Millis, M. B. Hastings, and M. Troyer. *Hybrid quantum-classical approach to correlated materials*. Phys. Rev. X, **6**, 031 045, 2016. (see page: 125)

[242] C. Chou, H. de Riedmatten, D. Felinto, S. Polyakov, S. van Enk, and H. Kimble. *Measurement-induced entanglement for excitation stored in remote atomic ensembles*. Nature, **438**, 828–832, 2005. (see page: 128)

[243] D. N. Matsukevich, T. Chanelière, S. D. Jenkins, S.-Y. Lan, T. A. B. Kennedy, and A. Kuzmich. *Entanglement of remote atomic qubits*. Phys. Rev. Lett., **96**, 030 405, 2006.

[244] C.-W. Chou, J. Laurat, H. Deng, K. S. Choi, H. de Riedmatten, D. Felinto, and H. J. Kimble. *Functional quantum nodes for entanglement distribution over scalable quantum networks*. Science, **316** (5829), 1316–1320, 2007.

[245] J. Laurat, K. S. Choi, H. Deng, C. W. Chou, and H. J. Kimble. *Heralded entanglement between atomic ensembles: Preparation, decoherence, and scaling*. Phys. Rev. Lett., **99**, 180 504, 2007.

[246] Z.-S. Yuan, Y.-A. Chen, B. Zhao, S. Chen, J. Schmiedmayer, and J.-W. Pan. *Experimental demonstration of a bdcz quantum repeater node*. Nature, **454** (7208), 1098, 2008. (see page: 128)

[247] D. L. Moehring, P. Maunz, S. Olmschenk, K. C. Younge, D. N. Matsukevich, L.-M. Duan, and C. Monroe. *Entanglement of single-atom quantum bits at a distance*. Nature, **449** (7158), 68–71, 2007. (see page: 128)

[248] D. N. Matsukevich, P. Maunz, D. L. Moehring, S. Olmschenk, and C. Monroe. *Bell inequality violation with two remote atomic qubits*. Phys. Rev. Lett., **100**, 150 404, 2008.

[249] P. Maunz, S. Olmschenk, D. Hayes, D. N. Matsukevich, L.-M. Duan, and C. Monroe. *Heralded quantum gate between remote quantum memories*. Phys. Rev. Lett., **102**, 250 502, 2009.

[250] L. Slodička, G. Hétet, N. Röck, P. Schindler, M. Hennrich, and R. Blatt. *Atom-atom entanglement by single-photon detection*. Phys. Rev. Lett., **110**, 083 603, 2013.

[251] D. Hucul, I. Inlek, G. Vittorini, C. Crocker, S. Debnath, S. Clark, and C. Monroe. *Modular entanglement of atomic qubits using photons and phonons*. Nature Physics, **11** (1), 37, 2015. (see page: 128)

[252] M. Lettner, M. Mücke, S. Riedl, C. Vo, C. Hahn, S. Baur, J. Bochmann, S. Ritter, S. Dürr, and G. Rempe. *Remote entanglement between a single atom and a bose-einstein condensate*. Phys. Rev. Lett., **106**, 210 503, 2011. (see page: 128)

[253] K. C. Lee, M. R. Sprague, B. J. Sussman, J. Nunn, N. K. Langford, X.-M. Jin, T. Champion, P. Michelberger, K. F. Reim, D. England, D. Jaksch, and I. A. Walmsley. *Entangling macroscopic diamonds at room temperature*. Science, **334** (6060), 1253–1256, 2011. (see page: 128)

[254] I. Usmani, C. Clausen, F. Bussières, N. Sangouard, M. Afzelius, and N. Gisin. *Heralded quantum entanglement between two crystals*. Nature Photonics, **6** (4), 234, 2012. (see page: 128)

[255] J. Hofmann, M. Krug, N. Ortegel, L. Gérard, M. Weber, W. Rosenfeld, and H. Weinfurter. *Heralded entanglement between widely separated atoms*. Science, **337** (6090), 72–5, 2012. (see page: 128)

[256] S. Ritter, C. Nölleke, C. Hahn, A. Reiserer, A. Neuzner, M. Uphoff, M. Mücke, E. Figueroa, J. Bochmann, and G. Rempe. *An elementary quantum network of single atoms in optical cavities*. Nature, **484** (7393), 195–200, 2012. (see page: 128)

[257] H. Bernien, B. Hensen, W. Pfaff, G. Koolstra, M. Blok, L. Robledo, T. Taminiau, M. Markham, D. Twitchen, L. Childress, and R. Hanson. *Heralded entanglement between solid-state qubits separated by three metres*. Nature, **497**, 86–90, 2013. (see page: 128)

[258] W. Pfaff, B. Hensen, H. Bernien, S. B. van Dam, M. S. Blok, T. H. Taminiau, M. J. Tiggelman, R. N. Schouten, M. Markham, D. J. Twitchen, and R. Hanson. *Unconditional quantum teleportation between distant solid-state quantum bits*. Science, **345** (6196), 532–535, 2014.

[259] B. Hensen, H. Bernien, A. E. Dréau, A. Reiserer, N. Kalb, M. S. Blok, J. Ruitenberg, R. F. Vermeulen, R. N. Schouten, C. Abellán, *et al.* *Loophole-free bell inequality violation using electron spins separated by 1.3 kilometres*. Nature, **526** (7575), 682–686, 2015.

[260] P. C. Humphreys, N. Kalb, J. P. Morits, R. N. Schouten, R. F. Vermeulen, D. J. Twitchen, M. Markham, and R. Hanson. *Deterministic delivery of remote entanglement on a quantum network*. Nature, **558** (7709), 268, 2018. (see page: 128)

[261] N. Leung, Y. Lu, S. Chakram, R. K. Naik, R. Earnest, R. Ma, K. Jacos, A. N. Cleland, and D. I. Schuster. *Deterministic bidirectional communication and remote entanglement generation between superconducting quantum processors*. arXiv:1804.02028, 2016. (see pages: 127, 128)

[262] A. Delteil, Z. Sun, W.-b. Gao, E. Togan, S. Faelt, and A. ImamoĞlu. *Generation of heralded entanglement between distant hole spins*. Nature Physics, **12** (3), 218, 2016. (see page: 128)

[263] R. Stockill, M. J. Stanley, L. Huthmacher, E. Clarke, M. Hugues, A. J. Miller, C. Matthiesen, C. Le Gall, and M. Atatüre. *Phase-tuned entangled state generation between distant spin qubits*. Phys. Rev. Lett., **119**, 010503, 2017. (see page: 128)

[264] J. F. Clauser, M. A. Horne, A. Shimony, and R. A. Holt. *Proposed experiment to test local hidden-variable theories*. Phys. Rev. Lett., **23**, 880–884, 1969. (see page: 129)

[265] M. Giustina, M. A. M. Versteegh, S. Wengerowsky, J. Handsteiner, A. Hochrainer, K. Phelan, F. Steinlechner, J. Kofler, J.-A. Larsson, C. Abellán, W. Amaya, V. Pruneri, M. W. Mitchell, *et al.* *Significant-loophole-free test of bell's theorem with entangled photons*. Phys. Rev. Lett., **115**, 250401, 2015. (see page: 129)

[266] L. K. Shalm, E. Meyer-Scott, B. G. Christensen, P. Bierhorst, M. A. Wayne, M. J. Stevens, T. Gerrits, S. Glancy, D. R. Hamel, M. S. Allman, K. J. Coakley, S. D. Dyer, C. Hodge, *et al.* *Strong loophole-free test of local realism*. Phys. Rev. Lett., **115**, 250402, 2015. (see page: 129)

[267] S. Wengerowsky, S. K. Joshi, F. Steinlechner, J. R. Zichi, S. Dobrovolskiy, R. van der Molen, J. W. Los, V. Zwiller, M. A. Versteegh, A. Mura, *et al.* *In-field entanglement distribution over a 96 km-long submarine optical fibre*. arXiv:1803.00583, 2018. (see page: 129)

[268] J. Yin, Y. Cao, Y.-H. Li, S.-K. Liao, L. Zhang, J.-G. Ren, W.-Q. Cai, W.-Y. Liu, B. Li, H. Dai, *et al.* *Satellite-based entanglement distribution over 1200 kilometers*. Science, **356** (6343), 1140–1144, 2017. (see page: 129)

[269] R. W. Andrews, R. W. Peterson, T. P. Purdy, K. Cicak, R. W. Simmonds, C. A. Regal, and K. W. Lehnert. *Bidirectional and efficient conversion between microwave and optical light*. Nature Physics, **10** (4), 321, 2014. (see page: 129)

[270] A. Higginbotham, P. Burns, M. Urmey, R. Peterson, N. Kampel, B. Brubaker, G. Smith, K. Lehnert, and C. Regal. *Harnessing electro-optic correlations in an efficient mechanical converter*. Nature Physics, page 1, 2018. (see page: 129)

[271] D. P. DiVincenzo and F. Solgun. *Multi-qubit parity measurement in circuit quantum electrodynamics*. New Journal of Physics, **15** (7), 075001, 2013. (see page: 129)

[272] Y. Liu, S. Shankar, N. Ofek, M. Hatridge, A. Narla, K. M. Sliwa, L. Frunzio, R. J. Schoelkopf, and M. H. Devoret. *Comparing and combining measurement-based and driven-dissipative entanglement stabilization*. Phys. Rev. X, **6**, 011022, 2016. (see page: 130)

[273] M. D. Reed, L. DiCarlo, B. R. Johnson, L. Sun, D. I. Schuster, L. Frunzio, and R. J. Schoelkopf. *High-fidelity readout in circuit quantum electrodynamics using the Jaynes-Cummings nonlinearity*. Phys. Rev. Lett., **105**, 173601, 2010. (see page: 131)

[274] D. Sank, Z. Chen, M. Khezri, J. Kelly, R. Barends, B. Campbell, Y. Chen, B. Chiaro, A. Dunsworth, A. Fowler, *et al.* *Measurement-induced state transitions in a superconducting qubit: Beyond the rotating wave approximation*. Physical review letters, **117** (19), 190503, 2016. (see page: 131)

[275] I. Rabi. *On the process of space quantization*. Phys. Rev., **49** (4), 324, 1936. (see page: 131)

[276] V. E. Manucharyan, A. Baksic, and C. Ciuti. *Resilience of the quantum rabi model in circuit qed*. Journal of Physics A: Mathematical and Theoretical, **50** (29), 294001, 2017. (see page: 133)

[277] P. Forn-Díaz, J. García-Ripoll, B. Peropadre, J.-L. Orgiazzi, M. Yurtalan, R. Belyansky, C. Wilson, and A. Lupascu. *Ultrastrong coupling of a single artificial atom to an electromagnetic continuum in the nonperturbative regime*. Nat. Phys., 2016. (see page: 133)

[278] F. Yoshihara, T. Fuse, S. Ashhab, K. Kakuyanagi, S. Saito, and K. Semba. *Superconducting qubit–oscillator circuit beyond the ultrastrong-coupling regime*. Nat. Phys., 2016. (see page: 133)

[279] A. Mezzacapo, U. Las Heras, J. Pedernales, L. DiCarlo, E. Solano, and L. Lamata. *Digital quantum rabi and dicke models in superconducting circuits*. Sci. Rep., **4**, 7482, 2014. (see page: 133)

[280] R. H. Dicke. *Coherence in spontaneous radiation processes*. Phys. Rev., **93** (1), 99, 1954. (see page: 133)

[281] F. Luthi, T. Stavenga, O. W. Enzing, A. Bruno, C. Dickel, N. K. Langford, M. A. Rol, T. S. Jespersen, J. Nygård, P. Krogstrup, and L. DiCarlo. *Evolution of nanowire transmon qubits and their coherence in a magnetic field*. Phys. Rev. Lett., **120**, 100502, 2018. (see page: 133)

[282] G. de Lange, B. van Heck, A. Bruno, D. J. van Woerkom, A. Geresdi, S. R. Plissard, E. P. A. M. Bakkers, A. R. Akhmerov, and L. DiCarlo. *Realization of microwave quantum circuits using hybrid superconducting-semiconducting nanowire josephson elements*. Phys. Rev. Lett., **115**, 127002, 2015. (see page: 135)

[283] T. W. Larsen, K. D. Petersson, F. Kuemmeth, T. S. Jespersen, P. Krogstrup, J. Nygård, and C. M. Marcus. *Semiconductor-nanowire-based superconducting qubit*. Phys. Rev. Lett., **115**, 127001, 2015. (see page: 135)

[284] P. Krogstrup, N. L. B. Ziino, W. Chang, S. M. Albrecht, M. H. Madsen, E. Johnson, J. Nygård, C. M. Marcus, and T. S. Jespersen. *Epitaxy of semiconductor–superconductor nanowires*. Nat. Mater., **14**, 2015. (see page: 135)

[285] W. Chang, S. M. Albrecht, T. S. Jespersen, F. Kuemmeth, P. Krogstrup, J. Nygård, and C. M. Marcus. *Hard gap in epitaxial semiconductor–superconductor nanowires*. Nat. Nanotechnol., **10**, 2015. (see page: 135)

[286] J. Jin, D. Rossini, R. Fazio, M. Leib, and M. J. Hartmann. *Photon solid phases in driven arrays of nonlinearly coupled cavities*. Phys. Rev. Lett., **110**, 163605, 2013. (see page: 137)

[287] M. C. Collodo, A. PotoČnik, S. Gasparinetti, J.-C. Besse, M. Pechal, M. Sameti, M. J. Hartmann, A. Wallraff, and C. Eichler. *Observation of the crossover from photon ordering to delocalization in tunably coupled resonators*. arXiv:1808.00889, 2018. (see page: 137)

[288] A. De Touzalin, C. Marcus, F. Heijman, I. Cirac, R. Murray, and T. Calarco. *Quantum manifesto: A new era of technology*. European Comission, 2016. (see page: 142)

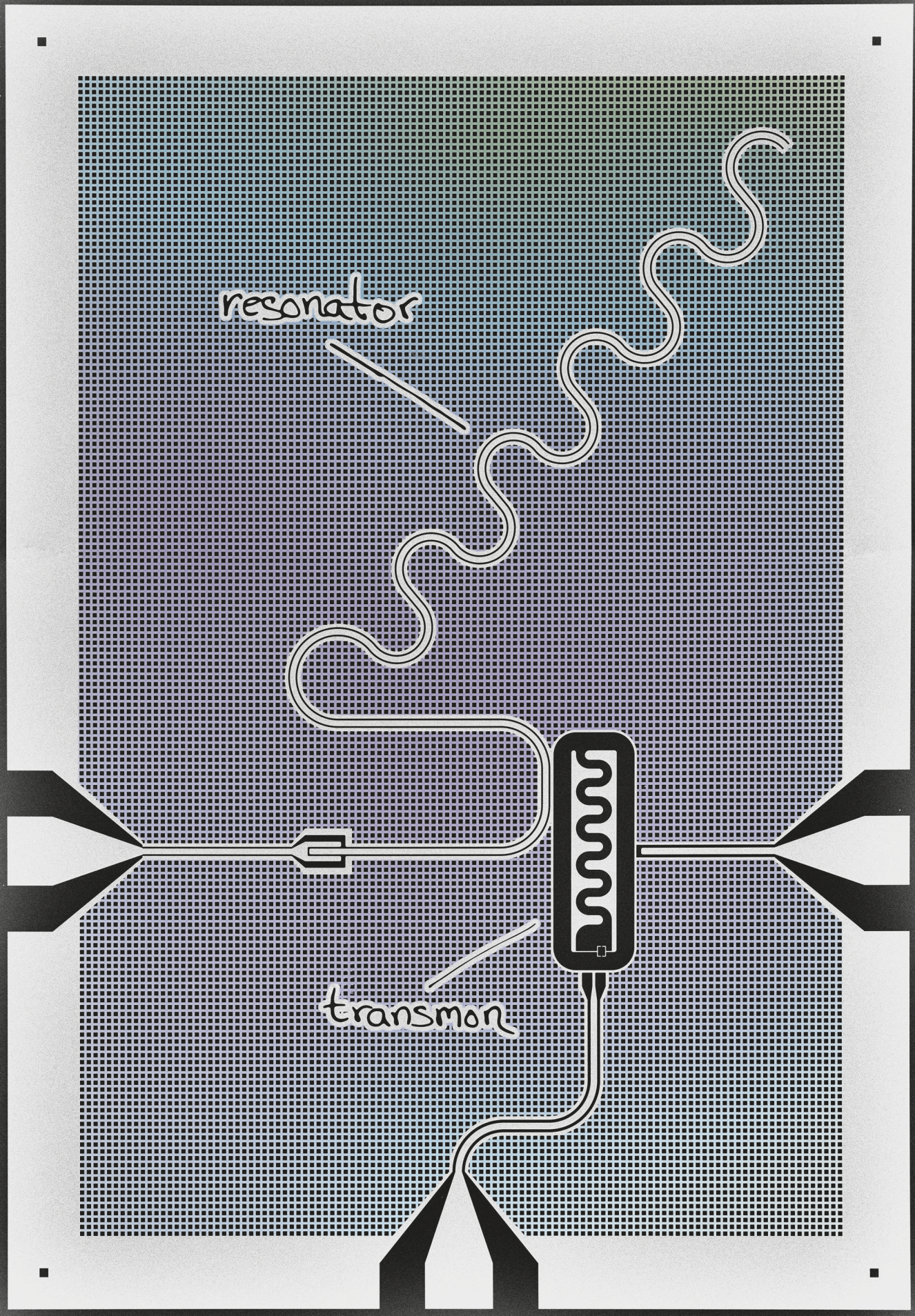
resonator
transmon